

École Doctorale des Sciences Chimiques — EDC222

UMR 7006

THÈSE

présentée par

Sven JANDURA

soutenue le 11 Septembre 2024

pour obtenir le grade de **Docteur de l'Université de Strasbourg**

Discipline/S spécialité: **Physique**

Optimized Quantum Gates for Neutral Atom Quantum Computers

Thèse dirigée par

Pr. PUPILLO Guido

Professeur, Université de Strasbourg

Rapporteurs

Pr. PICHLER Hannes

Professeur, Universität Innsbruck

Pr. MORIGI Giovanna

Professeur, Universität des Saarlands

Autres membres du jury

Pr. PFAU Tilman

Professeur, Universität Stuttgart

Optimizing Quantum Gates for Neutral Atom Quantum Computers

Résumé

Les atomes neutres sont récemment apparus comme une plate-forme compétitive pour l'informatique quantique. Le développement de portes quantiques intriquées de haute fidélité est la clé du succès de cette plateforme. Dans cette thèse, nous développons plusieurs protocoles nouveaux et optimisés pour l'implémentation de portes quantiques à deux et plusieurs qubits sur des atomes neutres. Nous introduisons la famille des protocoles temps-optimaux, qui implémentent une porte quantique donnée aussi rapidement que possible en appliquant une impulsion laser unique avec une phase dépendant du temps. Nous explorons également les protocoles de portes qui sont particulièrement robustes face à certaines sources d'erreurs expérimentales, et les portes qui sont optimisées pour leur utilisation dans un code de correction d'erreur quantique. Enfin, nous proposons deux nouveaux protocoles pour implémenter des portes multi-qubits non-locales sur des atomes neutres couplés à un mode de cavité commun qui peut être implémenté simplement par un pilotage classique de la cavité. Les résultats de cette thèse permettent d'obtenir des portes quantiques plus simples, de meilleure qualité et plus robustes sur des atomes neutres, et constituent une étape vers la réalisation de la vision d'un ordinateur quantique.

Mots-clés: Informatique quantique, atomes neutres, atomes de Rydberg, portes quantiques, contrôle optimal quantique

Abstract

Neutral atoms have recently emerged as a competitive platform for quantum computing. The development of high fidelity entangling quantum gates is a key to success of this platform. In this thesis, we develop several new and optimized protocols for the implementation of two- and multi-qubit quantum gates on neutral atoms. We introduce the family of time-optimal protocols, which implement a given quantum gate as fast as possible by applying a single laser pulse with a time-dependent phase. We also explore gate protocols which are particularly robust against certain experimental error sources, and gates which are optimized for their use in a quantum error correction code. Finally, we propose two new protocols to implement non-local multi-qubit gates on neutral atoms coupled to a common cavity mode which can be implemented simply by a classical drive of the cavity. The results of this thesis allow for simpler, higher quality, and more robust quantum gates on neutral atoms, and constitute a step towards realizing the vision of a quantum computer.

Keywords: Quantum Computing, Neutral Atoms, Rydberg Atoms, Quantum Gates, Quantum Optimal Control

Contents

Acknowledgements	ix
Résumé de la Thèse en Français	xi
1 Introduction	1
2 Introduction to Quantum Computing with Neutral Atoms	5
2.1 Storing Qubits in Atoms	7
2.2 Atom-Light Interaction	10
2.3 Trapping Atoms in Optical Tweezers	13
2.4 Single Qubit Operations	14
2.4.1 Qubit Initialization	15
2.4.2 Single Qubit Gates	15
2.4.3 Qubit Readout	16
2.5 Two- and Multi-Qubit Gates	17
2.5.1 Van der Waals Interaction between Rydberg States	17
2.5.2 The π - 2π - π Protocol	19
2.5.3 The Levine-Pichler Protocol	20
2.5.4 Other Gate Protocols	22
3 Time-Optimal Two- and Multi-Qubit Gates on Rydberg Atoms	23
3.1 Problem Formulation	24
3.1.1 Level Scheme and Hamiltonian	24
3.1.1.1 General Case	24
3.1.1.2 Permutation Symmetric Case	26
3.1.1.3 The Rydberg Blockade Limit	27
3.1.2 Time-Optimal Problem and Gate Fidelity	28
3.1.3 Symmetry Operations	29
3.2 Gradient Ascent Pulse Engineering (GRAPE)	31
3.2.1 General Algorithm	31
3.2.2 Application to Rydberg Atoms	33
3.3 Time-Optimal CZ Gate for a Perfect Rydberg Blockade	35
3.4 Time-Optimal CZ Gate for Finite Interaction Strengths	38
3.5 Time-Optimal C-Phase Gates	42
3.6 Time-Optimal Multi-Controlled C_kZ Gates	43
3.6.1 Rydberg Blockade Limit	45
3.6.2 Finite Interaction Strengths	47
3.6.3 Phase on $ 0\dots 0\rangle$ instead of $ 1\dots 1\rangle$	48
3.7 A Protocol to Generate GHZ States	49
3.8 Conclusion	51

4	Mathematical Structure of Time-Optimal Pulses	53
4.1	General formulation of the PMP	54
4.2	Proof Sketch	56
4.3	Formulation of the PMP for Quantum Optimal Control Problems	58
4.4	Application of the PMP to Time-Optimal Gates on Rydberg Atoms	59
4.5	Semi-Analytical Pulses for Two-Qubit Gates	63
4.6	Extension to Three-Qubit C_2Z Gates	67
4.7	Conclusion	69
4.A	Discussion of Abnormal Solutions	69
5	Robust Gate Protocols	73
5.1	Minimizing Rydberg Decay	75
5.2	Robustness to Interaction Strength Variations	78
5.3	Amplitude- and Detuning-Robust Pulses	81
5.3.1	Amplitude Robust pulses	82
5.3.2	Detuning Robust Pulses	84
5.3.3	Stark Shift Robust Pulses	84
5.4	Doppler Robust Pulses	86
5.4.1	Design of Doppler Robust Pulses	86
5.4.2	Reversing the Doppler Shift	89
5.5	Infidelities in a Realistic Error Model	91
5.6	Conditional Infidelity and Logical Error Rate	93
5.7	Conclusion	95
5.A	Gate Error for a CZ and C_2Z Error in Second Order in $1/B$	96
5.B	Pulse Most Robust against Detuning Errors	98
5.C	Modulation of the Trapping Potential	101
5.D	Comparing Switch and Wait Method of Doppler Shift Reversal	102
5.D.1	Robustness to Trap Inhomogeneities and Anharmonicity	103
5.D.2	Performance without Trap Modulation	104
5.D.3	Comparison between Switch and Wait Method	105
6	Surface Code Stabilizer Measurements for Rydberg Atoms	107
6.1	Introduction to Quantum Error Correction with Surface Codes	108
6.2	Stabilizer Measurement Schemes for Rydberg Atoms	111
6.3	The Data-Ancilla Blockade Model	113
6.4	The All-to-All Blockade Model	116
6.5	Conclusion	117
6.A	Numerical Calculation of Error Probabilities	117
6.B	Decomposition of Error Probabilities into Decay Events	118
6.C	Propagation of $ r\rangle \langle 1 $ Errors under V_{CZ}	119
6.C.1	Symmetric Protocols	119
6.C.2	The π - 2π - π Protocol	120
6.D	Error Analysis for the SIM protocol	121
6.D.1	Fit of the Logical Error Rates	121
6.D.2	Analytical Discussion	122
6.E	Propagation of a $ r\rangle \langle 1 $ Error on a Spectator Qubit under All-to-All Blockade	123
6.F	Comparison between TO and π - 2π - π Gate under All-to-All Blockade	124

7	Non-Local Multi-Qubit Gates via a Driven Cavity	127
7.1	Setup	129
7.2	Protocol A	131
7.2.1	Basis Transformation on the Cavity	131
7.2.2	Basis Transformation on the Qubits and Derivation of the Effective Hamiltonian	132
7.2.3	Implementation of a Quantum Gate	133
7.2.4	Performance in the Presence of Losses	135
7.2.5	CZ gate: Numerical Results	136
7.3	Protocol B	137
7.3.1	Loss Free Case	138
7.3.2	Performance in the Presence of Losses	138
7.3.3	CZ Gate: Numerical Results	139
7.3.4	Implementation of Arbitrary Phase Gates	139
7.4	Fidelity Estimates in Realistic Systems	141
7.4.1	Neutral Atoms Coupled to an Optical Cavity	141
7.4.2	Rydberg Atoms Coupled to a Microwave Cavity	142
7.4.3	Polar Molecules Coupled to a Microwave Cavity	142
7.5	Conclusion	143
7.A	Supporting Calculations for Protocol A	144
7.A.1	First Basis Transformation on the Cavity	144
7.A.2	Second Basis Transformation on the Qubits	145
7.A.3	Analytic Solution of Time Evolution under H_{eff}	147
7.A.4	Calculation of the Fidelity in the Limit $T \rightarrow \infty$	149
7.A.5	Effects of Coupling Inhomogeneities on the Fidelity	150
7.B	Supporting Calculations for Protocol B	151
7.B.1	Eigenenergies of H in Perturbation Theory	151
7.B.2	Effect of Losses	152
7.B.3	Effects of Coupling Inhomogeneities on the Fidelity	153
7.B.4	Using Protocol B for Arbitrary Phase Gates	154
8	Conclusions and Outlook	157
	Bibliography	159

Acknowledgements

I had the great fortune of working with many amazing people during the last years, and without them, this thesis would not exist. First and foremost I would like to thank my supervisor Guido Pupillo, who has always supported me in my research with his expertise and enthusiasm, who pushed me in right direction by asking the right questions, and who gave me the freedom to explore my own ideas. I would also like to thank my colleagues in the Quantum Matter Theory group in Strasbourg for all the insightful scientific discussions and the many after-work and weekend activities which I will keep in good memory: Johannes Schachenmayer, Guido Masella, Francesco Mattiotti, Hugo Perrin, David Wellnitz, Camille Le Calonnec, Vineesha Srivastava, Tanul Gupta, Tatiana Bepalova, Ruben Daraban, and Matteo Bergonzoni. Special thanks go to my office mates David Hagenmüller, Guillermo Preissert, and Laura Pecorari, who always managed to lighten my mood when I was stuck on a problem. I would further like to thank Shannon Whitlock and all members of the Exotic Quantum Matter group for giving me an exposure to the experimental techniques used in neutral atom quantum computing and for patiently answering all of my questions. The many discussions with Shannon always helped me to separate relevant from irrelevant ideas. This thesis also would not have been possible without the support of the administrative staff at the European Centre for Quantum Science, in particular Annia Bertrand and Anna Guyon, who have demonstrated an immense patience with me and were always able to accommodate my requests.

I had the great pleasure to collaborate with many outstanding scientists at other universities. In particular, I would like to thank Jeff Thompson and all members of his Ytterbium experiment at Princeton University for the experimental realization of some of the ideas presented in this thesis, for the many fruitful discussions on robust gate protocols and erasure conversion, and for their hospitality during my two visits to Princeton. Jeff's advise was incredibly valuable to me, and I am very grateful for his mentorship. I would also like to thank Gavin Brennen from Macquarie University for the collaboration on cavity mediated quantum gates, and Adam Kaufman and his group at JILA for their collaboration on protocols to generate Schrödinger cat states. Furthermore, I would like to thank Frank Wilhelm Mauch, Shai Machnes, and the whole PGI-12 group at Jülich research center for teaching me a lot about quantum optimal control, and for their hospitality during my three-month stay in Jülich. Finally, I would like to thank Felipe Herrera from the Universidad de Santiago de Chile and Dominique Sugny and Stephane Guerin from the Université de Bourgogne for many fruitful discussions and for their hospitality during my visit to their institutions.

During my doctorate I was a Marie Skłodowska-Curie fellow in the Innovative Training Network (ITN) of Molecular Quantum Simulations (MOQS). I would like to thank all the other fellows and supervisors for the great time that I had, both scientifically and socially, during our regular training weeks. I would in particular like to thank Juliane Sauer for her great organization of the network and for her patience with all of us.

Last, but definitely not least, I would like to thank my family and my friends, who have always supported me on my journey. Thank you for always being there for me.

Résumé de la Thèse en Français

L'invention de l'ordinateur dans la seconde moitié du XXe siècle a révolutionné tous les aspects de notre monde moderne, depuis les applications scientifiques et industrielles jusqu'à l'adoption généralisée de l'ordinateur personnel et l'essor de l'internet. Cependant, malgré l'existence de superordinateurs géants, il existe encore un grand nombre de problèmes de calcul importants sur le plan scientifique ou économique dont la solution est impossible ou peu pratique sur les machines actuelles. Il s'agit notamment de problèmes de chimie informatique, liés à la science des matériaux et à la découverte de médicaments, de problèmes d'optimisation combinatoire avec des applications en logistique et en recherche opérationnelle, et de problèmes financiers.

Les ordinateurs quantiques promettent de résoudre certains de ces problèmes plus rapidement que n'importe quel appareil classique en utilisant des algorithmes qui exploitent des phénomènes quantiques tels que l'intrication et la superposition [1-4]. En outre, d'autres technologies quantiques telles que la détection quantique [5] et la cryptographie quantique [6] offrent de grandes améliorations dans leurs domaines respectifs et peuvent être réalisées avec des éléments de construction similaires à ceux d'un ordinateur quantique. Alors que les ordinateurs quantiques sont restés pendant longtemps un concept largement théorique, les deux dernières décennies ont été marquées par un effort scientifique et industriel important pour développer une machine de démonstration de principe. Cependant, malgré les progrès impressionnants réalisés ces dernières années, la nature fondamentalement fragile de l'information quantique fait de la réalisation physique de l'informatique quantique une tâche ardue, et tous les ordinateurs quantiques existants sont trop petits, en termes de nombre de bits quantiques (qubits), et trop défectueux, en termes de taux d'erreur par opération, pour permettre une accélération des problèmes de calcul pertinents dans la pratique. Il est donc nécessaire de développer des méthodes nouvelles et améliorées pour mettre en œuvre des calculs quantiques de meilleure qualité sur un plus grand nombre de qubits.

Plusieurs technologies différentes sont actuellement étudiées en tant que candidates pour une plateforme de calcul quantique. Historiquement, les circuits supraconducteurs [7] et les ions piégés [8] ont été deux des premières plateformes à démontrer des calculs quantiques de principe à petite échelle. Dans ces plateformes, les bits quantiques sont encodés dans le courant d'un circuit supraconducteur et dans l'état électronique et nucléaire des ions piégés, respectivement. Cependant, ces dernières années, la plateforme prometteuse et en plein essor des atomes neutres piégés a atteint une performance qui est, selon de nombreuses mesures, comparable à celle des circuits supraconducteurs et des ions piégés [9-11]. Dans cette plateforme, des atomes individuels sont piégés dans des réseaux réguliers de pinces optiques, et des bits quantiques sont stockés dans l'état électronique et nucléaire de chaque atome.

L'état des atomes peut être manipulé avec une grande fidélité en appliquant des impulsions laser ou micro-ondes sur ou près de la résonance avec une transition dans les atomes. Pour mettre en œuvre une porte quantique sur deux atomes ou plus, les propriétés extrêmes des états dits *Rydberg* [12] sont exploitées. Les états de Rydberg sont des états très excités d'un atome, dans lesquels il existe une très grande séparation entre l'électron le plus externe et le noyau. En raison de la grande polarisation des états de Rydberg, il existe une forte interaction de van der Waals entre les atomes adjacents. Cette interaction est de plusieurs ordres de grandeur plus importante que pour les atomes dans l'état fondamental, de sorte que les portes quantiques sur deux atomes ou plus peuvent être mises en œuvre en couplant les états fondamentaux de ces atomes à un état de Rydberg, tandis que les atomes spectateurs qui ne sont pas impliqués dans la porte ne sont pas affectés par l'interaction de van der Waals. La manière dont l'interaction de van der Waals entre les états de Rydberg est utilisée pour mettre en œuvre une porte quantique donnée est décrite par un *protocole de porte*. Les différents protocoles de porte présentent des avantages et des inconvénients en termes de fidélité, de durée et de robustesse de la porte.

Dans cette thèse, nous proposons plusieurs nouveaux protocoles de portes quantiques sur deux qubits ou plus qui sont *optimaux*, et nous explorons plusieurs notions différentes d'optimalité. Pour trouver des protocoles de porte optimaux, nous utilisons une combinaison de techniques analytiques et de méthodes numériques de contrôle optimal quantique. Les principaux résultats de cette thèse peuvent être structurés selon différentes notions d'optimalité :

- i) Protocoles optimaux en temps.* La vitesse est une notion simple de l'optimalité. Comme les effets négatifs de nombreuses imperfections expérimentales sont réduits pour des durées de porte courtes, la recherche de protocoles de porte rapides est d'un grand intérêt pratique. Dans cette thèse, nous utilisons des méthodes numériques et analytiques de contrôle optimal quantique pour développer une famille de protocoles *temps-optimaux*. Tous ces protocoles ont une structure simple et ne nécessitent qu'une seule impulsion laser avec une phase laser dépendant du temps pour être appliquée sur les atomes. L'exemple le plus important de protocoles de portes optimales en fonction du temps est la porte CZ (controlled-Z) optimale en fonction du temps, qui est désormais couramment utilisée dans de nombreuses expériences [13-17]. Outre la porte CZ, nous trouvons des protocoles optimaux en termes de temps pour les portes de phase contrôlées générales à deux qubits, les portes multicontrôlées et pour la génération d'états de Greenberger-Horne-Zeilinger (GHZ). Nous analysons également la structure mathématique des protocoles optimaux en termes de temps à l'aide du principe du maximum de Pontryagin et nous constatons que la forme de l'impulsion laser utilisée pour mettre en œuvre les protocoles optimaux en termes de temps peut être décrite par une simple équation différentielle.
- ii) Protocoles robustes.* Si les principales sources d'erreur affectant une porte sont connues, les protocoles de porte peuvent être conçus pour être aussi robustes que possible contre ces sources d'erreur. Nous développons des protocoles de

porte pour la porte CZ qui minimisent l'erreur due à la désintégration de Rydberg, à une valeur finie de la force d'interaction entre les atomes, aux fluctuations d'amplitude du laser de Rydberg et aux désaccordages du laser dus à un décalage Doppler résultant du mouvement thermique des atomes. Nous analysons ensuite le compromis entre les différentes sources d'erreur pour des paramètres réalistes de qubits stockés dans des atomes de ^{171}Yb .

iii) Protocoles minimisant le taux d'erreur logique. En raison de la nature fragile de l'information quantique, les erreurs dans un calcul quantique sont inévitables. Pour atténuer ces erreurs, le cadre du *calcul quantique tolérant aux défauts (FTQC)* a été développé [19]. Le FTQC permet de coder un *qubit logique* en plusieurs qubits physiques et utilise la redondance pour détecter et corriger les erreurs de calcul. Dans le contexte de la FTQC, le taux d'erreur avec lequel le qubit logique subit une défaillance, appelé *taux d'erreur logique*, devient une mesure plus importante que le taux d'erreur des portes individuelles au niveau physique. Nous montrons, pour l'exemple du code de surface [21], que les protocoles de portes qui minimisent le taux d'erreur logique diffèrent sensiblement de ceux qui minimisent le taux d'erreur physique. Nous identifions les erreurs de fuite de Rydberg comme la source de cette divergence et nous développons des protocoles de porte qui réduisent les effets de ces erreurs.

Outre l'utilisation de l'interaction de van der Waals entre les états de Rydberg, il est également possible d'implémenter des portes quantiques sur deux atomes ou plus en coupant les atomes à un mode commun d'une cavité optique ou micro-onde. Cette méthode présente l'avantage de permettre une connectivité "tout-à-tout" et des portes non locales entre les qubits, mais elle se traduit généralement par des taux d'erreur plus élevés au niveau des portes. Dans cette thèse, nous proposons également deux nouvelles familles de protocoles de portes pour les atomes couplés à une cavité. Contrairement à de nombreux travaux antérieurs, ces protocoles peuvent être mis en œuvre simplement par une commande classique du mode de la cavité, sans qu'aucun adressage des atomes ne soit nécessaire. Cela ouvre de nouvelles possibilités expérimentales de mise en œuvre de portes quantiques via des cavités optiques.

Dans ce qui suit, nous donnons un aperçu de chacun des principaux résultats de la thèse.

Portes temporelles optimales à deux et plusieurs qubits sur des atomes de Rydberg

Les portes quantiques qui peuvent créer un enchevêtrement entre deux ou plusieurs qubits sont un composant crucial de toute architecture informatique quantique. Pour la plate-forme de l'atome neutre, la méthode la plus populaire pour mettre en œuvre

des portes sur deux qubits ou plus consiste à coupler un état de base de calcul de chaque atome à un ou plusieurs états de Rydberg à l'aide d'un laser, puis à utiliser la forte interaction de van der Waals entre les atomes de Rydberg pour générer l'intrication. Un grand nombre de protocoles de porte différents, présentant des avantages et des inconvénients différents, peuvent être utilisés à cette fin. [18, 64, 108-110, 112, 113, 115-118, 121-127]. Le choix de l'un de ces protocoles de porte qui permettra d'obtenir la plus grande fidélité de la porte dans une expérience dépend des détails de la configuration expérimentale et des sources d'erreur dominantes. Toutefois, deux propriétés d'un protocole de porte sont particulièrement souhaitables : *i)* Le protocole de porte ne doit nécessiter que des lasers de contrôle globaux s'adressant simultanément à tous les atomes. Cela réduit considérablement la complexité expérimentale par rapport aux protocoles qui nécessitent un adressage individuel des atomes. *ii)* Le protocole de porte doit être rapide car, indépendamment du modèle d'erreur exact, de nombreuses sources d'erreur peuvent être atténuées par des durées de porte courtes. C'est donc une question fondamentale que de trouver le protocole le plus rapide possible, appelé *temps-optimal* [128-131], le protocole de porte global le plus rapide possible qui met en œuvre une porte quantique donnée.

Dans le chapitre 3 de cette thèse, nous répondons à cette question pour la porte controlled-Z (CZ) et plusieurs de ses généralisations sur deux qubits ou plus. Nous supposons un schéma de niveau simple dans lequel nous modélisons chaque atome comme un système à trois niveaux composé des deux états de base de calcul et d'un état de Rydberg [64]. Un laser avec une fréquence de Rabi *dépendante du temps* $\Omega(t)$ couplant l'un des états de base de calcul à l'état de Rydberg est ensuite utilisée pour mettre en œuvre la porte souhaitée. Alors qu'une variété d'impulsions différentes $\Omega(t)$ peut mettre en œuvre la même porte, nous utilisons la méthode de contrôle optimal quantique de l'ingénierie des impulsions à ascension de gradient (GRAPE) [132] pour sélectionner celle qui est optimale en termes de temps.

Pour la porte CZ, nous constatons que le protocole optimal en termes de temps est environ 10% plus rapide que le protocole le plus rapide connu auparavant, le protocole de Levine-Pichler [18]. Plus important encore, l'impulsion optimale en fonction du temps peut être mise en œuvre à l'aide d'une impulsion *smooth* $\Omega(t)$, alors que le protocole LP nécessite un saut discontinu dans la phase du laser. Cela simplifie considérablement la mise en œuvre expérimentale du protocole temps-optimal par rapport au protocole LP. C'est cette caractéristique du protocole temps-optimal qui a conduit à son adoption généralisée dans de nombreuses expériences [13, 14, 16, 17], atteignant des fidélités jusqu'à 99,5% [13], la fidélité la plus élevée actuellement rapportée pour la plate-forme de l'atome neutre.

Les principaux résultats pour la porte CZ sont résumés dans la Fig. 1. La Fig. 1(a) montre l'infidélité minimale de la porte en fonction de la durée de l'impulsion, telle que trouvée par la méthode de contrôle optimal quantique GRAPE en optimisant sur la phase du laser dépendant du temps (cercles bleus). Dans la limite des petites durées d'impulsion, l'infidélité minimale est de l'ordre de 0,4, ce qui correspond à l'infidélité de la simple application de l'opération d'identité. Avec l'augmentation de la durée d'impulsion, l'infidélité minimale de la porte diminue, avant d'atteindre

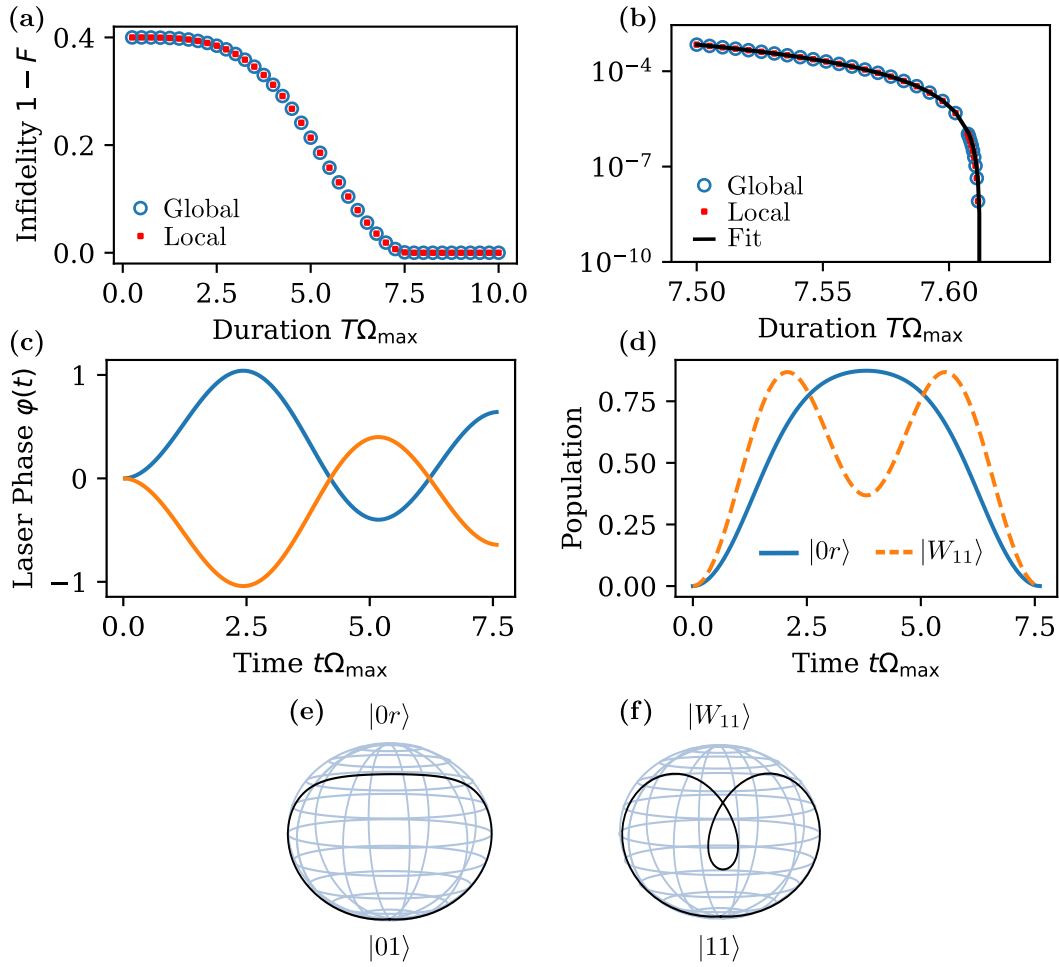


Figure 1 : Porte CZ optimale dans le temps. (a) Infidélité minimale $1 - F$ d'une porte CZ telle que trouvée par GRAPE pour des durées d'impulsion $0 \leq T\Omega_{\max} \leq 10$. Les cercles bleus (carrés rouges) montrent l'infidélité pour une impulsion globale (locale). (b) Zoom et ajustement de l'infidélité près du temps optimal $T_*\Omega_{\max} = 7.612$. (c) Deux impulsions différentes $\varphi(t)$ (liées par conjugaison complexe ou inversion temporelle) trouvées par GRAPE à la durée optimale T_* . (d) Population des états $|0r\rangle$ et $|W_{11}\rangle$ sous l'impulsion optimale en fonction du temps lorsque l'on commence respectivement à $|01\rangle$ et $|11\rangle$. (e/f) Trajectoire de $|\psi_{01}\rangle$ et $|\psi_{11}\rangle$ sur la sphère de Bloch pendant l'impulsion optimale en fonction du temps.

zéro autour de $T_*\Omega_{\max} \approx 7.6$, où Ω_{\max} représente l'amplitude de la fréquence de Rabi du laser. Pour des durées d'impulsion $T > T_*$, l'infidélité de la porte reste nulle. Pour déterminer T_* avec plus de précision, nous utilisons à nouveau GRAPE pour trouver l'infidélité pour $7.5 \leq T\Omega_{\max} \leq 7.65$, illustré sur la Fig. 1(b) avec l'infidélité en échelle logarithmique. Grâce à un ajustement décrit dans la Sec. 3.3, nous obtenons $T_*\Omega_{\max} = 7,612$ [ligne noire dans la Fig. 1(b)].

La Fig. 1(c) montre les deux phases différentes $\varphi(t)$ que nous obtenons à $T = T_*$. L'impulsion obtenue dépend du point de départ aléatoire de l'optimisation. Les deux impulsions peuvent être transformées l'une en l'autre par inversion temporelle [$\bar{\varphi}(t) = \varphi(T-t)$] ou par conjugaison complexe [$\bar{\varphi}(t) = -\varphi(t)$], de sorte que, jusqu'aux

opérations de symétrie, l'impulsion optimale du point de vue temporel est unique. Il est intéressant de noter que l'impulsion est invariante en cas d'inversion temporelle et de conjugaison complexe, de sorte qu'il n'y a que deux et non quatre impulsions temporelles optimales distinctes. Contrairement à la porte LP, la phase laser de l'optimum temporel est une fonction continue du temps sans aucun saut de phase. Sa dépendance temporelle est similaire à celle d'un cosinus, un fait que nous étudierons en détail dans le chapitre 4.

Pour comprendre comment l'impulsion agit sur les états initiaux $|01\rangle$ et $|0r\rangle$, nous considérons la population $|\langle 0r|\psi_{01}(t)\rangle|^2$ et $|\langle W_{11}|\psi_{11}(t)\rangle|^2$ des états $|0r\rangle$ et $|W_{11}\rangle$, respectivement, dans la Fig. 1(d). La population de $|0r\rangle$ augmente jusqu'à $t = T/2$ puis diminue jusqu'à 0 jusqu'à $t = T$, tandis que la population de $|W_{11}\rangle$ augmente jusqu'à $t \approx T/4$, puis diminue à nouveau jusqu'à $t = T/2$, suivie d'une augmentation symétrique jusqu'à $t \approx 3T/4$ et d'une chute jusqu'à 0 à $t = T$.

Les Figs. 1(e) et (f) montrent l'évolution de $|\psi_{01}\rangle$ et $|\psi_{11}\rangle$ sur la sphère de Bloch traversée par $|01\rangle$ et $|0r\rangle$ ainsi que $|11\rangle$ et $|W_{11}\rangle$, respectivement. Il est intéressant de noter que $|\psi_{11}\rangle$ présente un chemin auto-intersecté.

Enfin, nous examinons ce qui se passe lorsque nous levons la contrainte d'une impulsion globale et que nous autorisons des impulsions différentes $\Omega_1(t) \neq \Omega_2(t)$ sur les deux atomes. De manière analogue au cas global, nous calculons l'infidélité minimale en fonction de T à l'aide de GRAPE (carrés rouges dans les Figs. 1(a/b)). Il est intéressant de noter que l'infidélité minimale coïncide exactement avec celle d'une impulsion globale, ce qui montre que l'adressage individuel des atomes n'apporte aucune accélération pour une porte CZ. Nous constatons également que les impulsions $\Omega_1(t)$ et $\Omega_2(t)$ coïncident avec l'impulsion globale $\Omega(t)$ jusqu'à une phase constante.

Bien que la porte CZ soit la porte d'intrication de deux qubits la plus cruciale sur la plate-forme de Rydberg, nous utilisons également notre méthodologie temps-optimal pour trouver des impulsions qui mettent en œuvre des portes de phase contrôlées arbitraires sur deux qubits, ou des portes de phase sur trois qubits ou plus, telles que des portes Z multi-contrôlées ($C_k Z$) ou des portes CZ simultanées sur plusieurs paires de qubits. Dans tous les cas, nous trouvons des formes d'impulsion lisses et faciles à mettre en œuvre $\Omega(t)$. Le cas de trois qubits ou plus est particulièrement pertinent, car les plateformes de Rydberg permettent l'implémentation native de telles portes [18, 107, 116], mais avant notre travail, aucun protocole de porte *global* n'était connu.

Structure mathématique des impulsions optimales en fonction du temps

Dans le chapitre 3, nous trouvons l'impulsion optimale en termes de temps qui met en œuvre une porte CZ sur les atomes de Rydberg en utilisant la méthode de contrôle

quantique optimal numérique de GRAPE. Il est intéressant de noter que l'impulsion a une structure assez simple, la phase laser $\varphi(t)$ ressemble approximativement à la forme d'un sinus. La structure simple de l'impulsion optimale en temps n'est pas surprenante, puisque le problème de contrôle optimal que nous résolvons est également assez simple : Il consiste simplement à piloter deux systèmes différents à deux niveaux dont l'hamiltonien dépend d'un seul paramètre de contrôle, la phase du laser φ .

La nature simple du problème de contrôle optimal permet de l'aborder avec des méthodes analytiques. Dans ce chapitre 4 de cette thèse, nous utilisons le principe du maximum de Pontryagin (PMP) [158, 159] pour obtenir une forme semi-analytique de la phase laser optimale en temps $\varphi(t)$. Plus précisément, nous prouvons que pour toute porte C-Phase optimale en temps sur deux atomes dans la limite du blocage de Rydberg, le désaccord $\Delta = d\varphi/dt$ est donné par une solution de

$$\frac{1}{2}\dot{\Delta}^2 + V(\Delta) = 0 \quad \Delta(0) = 0 \quad (1)$$

avec

$$V(\Delta) = \frac{1}{8}\Delta^4 + c_2\Delta^2 + c_1\Delta + c_0 \quad (2)$$

pour certains coefficients c_2, c_1, c_0 . En d'autres termes, le désaccord Δ a la même dépendance fonctionnelle au temps que la position d'une particule classique de masse 1 et d'énergie 0 oscillant dans le potentiel quartique $V(\Delta)$. De plus, nous montrons qu'au temps final T , l'impulsion optimale en temps satisfait $\Delta(T) = 0$, ce qui correspond au retour de la particule à sa position initiale.

Notre résultat ne fait aucune déclaration sur les paramètres c_2, c_1, c_0 , qui doivent encore être déterminés numériquement. Ainsi, au lieu des $M \gg 1$ paramètres requis dans GRAPE en faisant un Ansatz constant par morceaux de $\varphi(t)$ avec M impulsions, cette approche semi-analytique caractérise les impulsions optimales en temps par seulement trois paramètres. De manière analogue, nous démontrons que pour les portes C_2Z à trois qubits, les impulsions optimales pour le temps peuvent être décrites par seulement sept paramètres.

Protocoles de portes robustes

L'une des orientations les plus importantes pour le développement continu des processeurs quantiques à atomes neutres est l'amélioration de la fidélité des portes à deux et plusieurs qubits. Dans les chapitres 3 et 4, nous relevons ce défi en trouvant les protocoles de porte les plus rapides possibles, optimaux en termes de temps. Étant donné que de nombreuses sources d'erreur sont moins préjudiciables pour des durées d'impulsion plus courtes, cette approche offre un protocole de porte d'une grande fidélité, indépendamment du modèle d'erreur exact. Pour les portes quantiques basées sur l'effet de blocage de Rydberg, cependant, les principales sources d'erreur sont souvent bien comprises et représentent une grande partie de l'infidélité

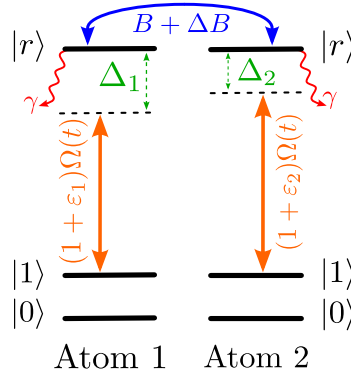


Figure 2 : Le schéma des niveaux et les sources d’erreur étudiés dans ce chapitre. Chaque atome est modélisé comme un système à trois niveaux avec les états $|0\rangle$, $|1\rangle$ et $|r\rangle$. Il existe une interaction de van der Waals qui déplace l’énergie de l’état des deux atomes dans $|r\rangle$, et un couplage laser global $|1\rangle$ et $|r\rangle$ avec une fréquence de Rabi $\Omega(t)$. Les sources d’erreur prises en compte dans ce chapitre sont indiquées dans des couleurs différentes : La désintégration de l’état de Rydberg (rouge), les incertitudes sur la force d’interaction (bleu), les déviations de l’amplitude laser attendue (orange), et les désaccordages laser (vert).

observée expérimentalement [13, 14, 105]. Il est donc possible de développer des protocoles de porte qui sont robustes contre ces sources d’erreur spécifiques, au prix d’être plus longs que le protocole optimal en termes de temps.

Dans le chapitre 5, nous considérons plusieurs sources d’erreur pertinentes en pratique et utilisons une combinaison de raisonnement analytique et de méthodes de contrôle optimal pour trouver des protocoles de porte avec une robustesse accrue à leur égard. Nous considérons le même schéma de niveau que dans les chapitres 3 et 4, avec deux ou trois atomes, chacun étant modélisé comme un système à trois niveaux avec des états de base de calcul $|0\rangle$ et $|1\rangle$ et un état de Rydberg auxiliaire $|r\rangle$, une interaction de van der Waals symétrique $B \sum_{j < k} |r_j r_k\rangle \langle r_j r_k|$, et un laser global avec une fréquence de Rabi (complexe) dépendant du temps $\Omega(t)$ couplant les états $|1\rangle$ et $|r\rangle$. Tout au long de ce chapitre, nous supposons que, au moins en l’absence d’imperfections, nous avons $B = \infty$, de sorte que l’excitation simultanée de plus de deux atomes à l’état de Rydberg est impossible. Nous considérons maintenant quatre sources d’erreur, à savoir une durée de vie finie de l’état de Rydberg, une force d’interaction finie incertaine B , et des incertitudes dans l’amplitude et le désaccord du laser global. Le schéma des niveaux et les sources d’erreur sont représentés sur la Fig. 2.

Les résultats de ce chapitre concernant la robustesse des protocoles de porte vis-à-vis de ces sources d’erreur peuvent être résumés comme suit :

- i) Décroissance de Rydberg.* Les états de Rydberg ont une durée de vie finie γ limitée par l’émission spontanée vers des états de basse altitude et le couplage à d’autres états de Rydberg dû au rayonnement du corps noir. La désintégration de l’état de Rydberg au cours d’une porte entraîne une erreur. Nous constatons

que, tant pour la porte CZ que pour la porte C_2Z , les impulsions optimales en temps sont presque optimales pour atténuer cette source d'erreur. Nous identifions les impulsions qui minimisent l'erreur due à la désintégration de Rydberg, et montrons que l'infidélité ne peut être réduite que de moins de 1% pour la porte CZ et de moins de 10% pour la porte C_2Z par rapport aux impulsions optimales en fonction du temps.

- ii) Incertitudes dans les forces d'interaction.* La force d'interaction B est souvent finie et n'est pas connue exactement, car elle dépend de la distance interatomique des atomes, qui fluctue avec le mouvement des atomes dans la pince optique. Bien que nous montrions dans la Sec. 3.4 qu'il est possible d'implémenter une porte CZ et une porte C_2Z exactement à des forces d'interaction finies, ces protocoles ne sont conçus que pour fonctionner à une force d'interaction spécifique B . Ici, nous trouvons plutôt des protocoles de porte qui implémentent un CZ et un C_2Z exactement seulement à $B = \infty$, mais dont l'infidélité augmente aussi lentement que possible avec $1/B$. Cela rend ces portes avantageuses si la force d'interaction est grande mais inconnue.
- iii) Les déviations de l'amplitude du laser.* Au lieu de la fréquence de Rabi attendue $\Omega(t)$, les atomes peuvent subir une fréquence de Rabi $(1 + \varepsilon_i)\Omega(t)$, avec différents ε_i pour différents atomes. Ces fluctuations d'un tir à l'autre peuvent être dues soit à des fluctuations de l'intensité du laser, soit à des fluctuations de la position de l'atome par rapport au centre du faisceau laser, par exemple en raison du mouvement de l'atome dans le piège. Nous utilisons des techniques de contrôle optimal quantique pour trouver une forme d'impulsion $\Omega(t)$ pour une porte CZ qui réduit l'effet des fluctuations d'intensité de plus de deux ordres de grandeur, au prix d'une durée d'impulsion plus longue.
- iv) Détonation du laser.* Diverses sources d'erreur peuvent conduire à un désaccord Δ_i du laser et de la transition $|1\rangle \leftrightarrow |r\rangle$. Les sources de désaccord les plus importantes sont les champs électriques parasites, qui déplacent l'énergie de l'état de Rydberg, les déplacements Doppler de la fréquence du laser dus au mouvement thermique des atomes dans le piège, et les fluctuations de l'amplitude du laser global (voir *iii*), qui, en raison du décalage de Stark résultant du couplage à d'autres états non résonants, affectent également les énergies des états $|1\rangle$ et $|r\rangle$. Nous constatons que pour des désaccordages arbitraires Δ_i , seule une petite amélioration de la robustesse par rapport à l'impulsion optimale en temps peut être obtenue. Pour les désaccords résultant de décalages Doppler, nous constatons cependant qu'en inversant le signe du décalage Doppler au milieu de l'impulsion, il est possible d'améliorer la robustesse contre cette erreur de plusieurs ordres de grandeur. De même, pour les désaccords dus à un décalage de Stark induit par le laser global, nous pouvons utiliser la corrélation entre les écarts d'amplitude et le désaccouplement du laser pour concevoir des impulsions robustes.

Nous considérons d'abord les quatre sources d'erreur ci-dessus séparément. Cependant, dans une expérience réelle, les quatre sources d'erreur sont présentes en même

temps, et le protocole de porte idéal établit un compromis entre la robustesse contre chacune d'entre elles. Pour mieux comprendre ce compromis, nous considérons les paramètres réalistes d'une expérience ^{171}Yb [85], et nous constatons que pour des écarts ou désaccords d'amplitude laser moyens ou importants, les impulsions robustes contre ces sources d'erreur sont plus performantes que l'impulsion optimale en temps, alors que pour des écarts ou désaccords d'amplitude laser faibles, l'impulsion optimale en temps, qui minimise essentiellement les erreurs dues à la désintégration de Rydberg, devient le meilleur choix. Toutefois, il a récemment été proposé [20, 162] et démontré expérimentalement [14] que dans les qubits métastables, les erreurs de désintégration de Rydberg peuvent être converties en erreurs dites *erasure*, qui sont beaucoup plus simples à corriger dans un code de correction d'erreurs que d'autres erreurs. En tenant compte de cela, nous trouvons de manière surprenante une large gamme d'imperfections pour lesquelles l'utilisation d'impulsions robustes contre les déviations d'amplitude ou les désaccordages augmente l'infidélité de la porte, mais diminue le taux d'erreurs logiques, par rapport à l'impulsion optimale en termes de temps. Cela démontre que la fidélité de la porte et le taux d'erreur logique peuvent différer de manière significative, et que l'optimisation des portes spécifiquement pour l'optimisation au niveau logique peut apporter des améliorations spectaculaires.

Mesures du stabilisateur de code de surface pour les atomes de Rydberg

La nature fragile de l'information quantique rend les erreurs inévitables dans tout calcul quantique effectué sur un processeur quantique réel. Pour combattre ces erreurs, le cadre de l'informatique quantique tolérante aux fautes (FTQC) a été développé. Le FTQC code un *qubit logique* en plusieurs *qubits physiques* et utilise la redondance qui en résulte pour détecter et corriger les erreurs. Tant que le taux d'erreur par opération est inférieur à un certain *seuil*, cela permet d'atteindre des taux d'erreur arbitrairement bas du qubit logique en l'encodant dans de plus en plus de qubits physiques [19, 169-172]. Récemment, plusieurs plateformes de calcul quantique ont dépassé le seuil de la FTQC en minimisant le bruit au niveau des portes à un ou deux qubits et ont démontré la FTQC dans des expériences de preuve de principe [13, 15, 16, 58-61]. Avec l'avènement de la FTQC, le *taux d'erreur logique*, c'est-à-dire le taux d'erreur du qubit logique, devient désormais une mesure plus importante que la fidélité de la porte physique. Alors que des fidélités de porte plus élevées correspondent souvent à des taux d'erreur logiques plus élevés, nous avons déjà vu dans la Sec. 5.6 que ces deux métriques peuvent parfois diverger de manière significative. L'optimisation des protocoles de portes en fonction du taux d'erreur logique qu'ils atteignent dans un protocole FTQC est donc un problème crucial.

Dans le chapitre 6, nous considérons une implémentation du code de surface [21, 168, 183], un code de correction d'erreur quantique populaire, sur un réseau stationnaire d'atomes neutres, avec des interactions entre les atomes médiées par des états de Rydberg. Dans le code de surface, un qubit logique est encodé dans un réseau

d'atomes $d \times d$ de manière à ce que les erreurs consistant en au plus $\lfloor d/2 \rfloor$ erreurs d'un seul qubit puissent toujours être corrigées. Nous nous concentrons sur la source d'erreur de la désintégration de Rydberg, qui est dominante dans de nombreuses expériences actuelles [13, 14, 105]. Il est intéressant de noter que pour des taux de désintégration suffisamment faibles γ , le protocole optimal en temps pour la mise en œuvre d'une porte CZ (voir Sec. 3.3), qui minimise essentiellement l'infidélité de la porte en présence de désintégration de Rydberg (voir Sec. 5.1) ne minimise pas le taux d'erreurs logiques. Au lieu de cela, nous trouvons une famille de nouveaux protocoles de portes qui peuvent atteindre un taux d'erreur logique significativement plus bas, bien qu'ils soient plus lents et aient une infidélité plus élevée. La raison de cet écart entre l'infidélité et les taux d'erreurs logiques réside dans les erreurs de fuite de Rydberg : De prime abord, la désintégration de Rydberg d'un atome peut en fait conduire à une population de l'état de Rydberg de l'extrémité d'une porte, soit en brisant le blocus de Rydberg et en permettant à un autre atome d'être excité à l'état de Rydberg, soit par la réexcitation de l'atome désintégré à l'état de Rydberg après l'événement de désintégration. Ces erreurs de fuite de Rydberg peuvent maintenant affecter les qubits voisins pendant les portes suivantes, un effet qui n'est pas pris en compte par l'infidélité. Plus précisément, grâce à la propagation des erreurs de fuite de Rydberg, un événement de désintégration peut entraîner des erreurs corrélées sur plusieurs qubits, ce qui permet à des événements de désintégration déjà $\lfloor d/4 \rfloor$ de conduire à une erreur logique. Les nouveaux protocoles de porte décrits dans cette section empêchent la propagation des erreurs de fuite de Rydberg et rétablissent l'échelle originale de $\lfloor d/2 \rfloor$. Ce résultat démontre l'importance d'optimiser les portes quantiques pour les erreurs logiques en plus de la fidélité des portes et ouvre la voie à la réalisation efficace de codes de surface avec des atomes neutres.

Portes multi-qubits non locales via une cavité entraînée

Les portes de haute fidélité sont essentielles pour l'informatique quantique, mais dans la perspective d'une informatique évolutive et tolérante aux pannes, il est également très souhaitable de disposer de portes quantiques non locales entre deux ou plusieurs qubits. Par exemple, la disponibilité d'une connectivité "tout-à-tout" peut réduire considérablement la profondeur des circuits quantiques typiques, par rapport à une connectivité géométriquement locale. En outre, la possibilité d'effectuer des portes multi-qubits non locales permettrait d'utiliser des codes de correction d'erreurs quantiques (QEC) avec des stabilisateurs non locaux, tels que les codes LDPC [193-196], qui ont un surcoût significativement plus faible que l'approche actuellement la plus répandue des codes de surface [168]. Dans de nombreuses plateformes physiques, cependant, ni les portes non-locales ni les portes multi-qubits ne sont disponibles de manière native, mais doivent être synthétisées de manière coûteuse à partir d'une séquence d'opérations locales à un ou deux qubits. Pour les atomes neutres interagissant via les états de Rydberg, nous avons vu dans le chapitre 3 qu'il est possible de

réaliser des portes multi-qubits. Cependant, seules des portes locales sont possibles, car la force d'interaction entre les états de Rydberg diminue rapidement avec leur distance (voir Sec. 2.5).

Une façon de réaliser des portes non locales à deux qubits est d'utiliser la navette de qubits, qui a été démontrée pour les ions piégés [179] et les atomes neutres [67, 197]. L'évaluation du coût des opérations non locales dans ce cas n'est pas triviale, car l'architecture peut effectuer certains déplacements parallèles simultanément, mais les déplacements inégaux doivent être effectués en série. Le temps de navette pour les atomes dans un réseau planaire de dimension linéaire L , pertinent pour effectuer des opérations dans certains codes LDPC, est de $O(\sqrt{L})$ [78]. Par ailleurs, des portes non locales ont déjà été proposées ou réalisées avec des atomes ou des ions neutres en assurant la médiation des interactions entre les qubits via un mode bosonique quantifié, en utilisant les modes de mouvement des ions piégés [22, 46, 198, 199] ou des modes de cavité optique pour les qubits de spin d'atomes neutres [77, 200-206]. Pour les portes déterministes, l'art antérieur trouve que l'erreur de fidélité est $O(C^{-1/2})$ où C est la coopérativité de la cavité supportant le mode [203]. En utilisant des ressources de détection supplémentaires, les portes non locales annoncées sont réalisables avec une erreur de $O(C^{-1})$ mais avec une probabilité d'échec de $O(C^{-1/2})$ [205]. Un autre schéma utilisant des transferts de photons annoncés a une meilleure probabilité de réussite mais impose des exigences strictes sur la structure de niveau des qubits afin que tous les événements de diffusion et de perte de photons soient détectables [77]. En revanche, les états intriqués non locaux peuvent être préparés comme des points fixes de cartes dissipatives avec une erreur de fidélité de $O(C^{-1})$ [207], bien qu'une relation de phase fixe doive être maintenue entre les champs s'adressant aux qubits. Bien que certaines des propositions ci-dessus puissent être étendues aux portes de Toffoli à N -qubits [205, 206], pour les simulations et les calculs quantiques numériques à grande échelle, une approche unifiée fournissant des implémentations natives de familles plus larges de portes multi-qubits serait hautement souhaitable. Il s'agit là d'un avantage considérable, qui n'est pas fourni par les schémas ci-dessus.

Dans toutes les propositions ci-dessus, les portes quantiques intriquées sont réalisées par une commande directe des qubits via un mode d'espace libre, par exemple un laser, pour activer ou désactiver l'interaction entre les qubits. Dans le chapitre 7 de cette thèse, nous explorons une approche différente basée sur le simple pilotage du mode de la cavité directement avec un champ classique qui est modulé en fonction du temps, sans nécessiter un pilotage externe des qubits. Nous constatons que cette approche permet deux nouveaux protocoles pour la mise en œuvre de grandes familles de portes quantiques déterministes non locales à qubits multiples. Appliqués à seulement deux qubits, les deux protocoles fournissent, avec les portes à qubit unique, un ensemble de portes universelles pour l'informatique quantique, avec des erreurs de portes à deux qubits s'échelonnant comme $O(C^{-1/2})$, similaires aux protocoles pilotant directement les qubits. Appliqué à plus de deux qubits, cependant, chaque protocole fournit une famille de portes déterministes non locales à qubits multiples nécessitant un contrôle minimal, montrant une combinaison unique de caractéristiques souhaitables telles que la polyvalence dans la conception des portes,

la vitesse et la robustesse.

Le premier protocole (A) fonctionne dans la limite d'un entraînement puissant de la cavité. Il met en œuvre une famille de portes de phase géométriques $U_A = \exp(i\theta\hat{n}^2)$, où \hat{n} est l'opérateur de nombre de qubits dans l'état $|1\rangle$, en déplaçant l'état de la cavité dans une boucle fermée dans l'espace de phase. N'importe quel angle θ peut être atteint en choisissant une commande appropriée de la cavité. Une application particulièrement importante du protocole A est la génération d'états GHZ multi-qubits [156, 208] en utilisant la même procédure que dans la Sec. 3.7, une tâche pour laquelle les protocoles viables pour les qubits couplés via une cavité sont rares et nécessitent un entraînement direct sur les qubits [209]. Le protocole A se distingue par sa rapidité : dans de nombreuses propositions antérieures, la cavité est fortement désaccordée par rapport à la fréquence du qubit afin d'éviter un grand nombre de photons dans la cavité et donc une grande erreur due aux pertes de photons. Cela se fait au prix d'une longue durée de porte de l'ordre de Δ/g^2 , où Δ est le désaccord de la cavité et g est le couplage entre les qubits et la cavité. Dans le protocole A, la cavité est également très désaccordée, mais une force d'entraînement de l'ordre de Δ et adaptée au taux de perte de photons permet d'obtenir des durées de porte de l'ordre de g^{-1} . Un autre avantage du protocole A est sa robustesse : Comme la porte de Mølmer-Sørensen pour les ions piégés [22], U_A est indépendant de l'état initial du mode de la cavité, ce qui est particulièrement important si le mode de la cavité se trouve dans le régime des micro-ondes et peut présenter une population thermique significative. En outre, le protocole A est intrinsèquement robuste aux imperfections de l'impulsion dans l'entraînement de la cavité, puisque seule la zone couverte et non la trajectoire exacte dans l'espace des phases détermine U_A .

Le second protocole (B) fonctionne dans la limite d'un entraînement faible et donc dans la limite opposée du protocole A. Il utilise une évolution adiabatique du système cavité-qubit conjoint pour mettre en œuvre une famille de portes de phase $U_B = \exp[ic_1/(c_2 - \hat{n})]$, où c_1 et c_2 sont des paramètres qui dépendent de l'intensité, de la durée et du désintonisme de l'entraînement appliqué. Le protocole B se distingue par sa polyvalence : Puisque U_B dépend *non linéairement* de c_2 , l'application répétée de U_B avec différentes valeurs de c_1 et c_2 peut être utilisée pour synthétiser des portes de phase *arbitraires* $\exp(i\varphi(\hat{n}))$. Cela peut par exemple être utilisé pour mettre en œuvre des portes de rotation de phase $\exp(i\alpha\sigma_z^{(1)} \otimes \dots \otimes \sigma_z^{(N)})$, qui apparaissent dans de nombreux algorithmes quantiques variationnels pour les systèmes fermioniques [210, 211]. Il peut également être utilisé pour implémenter des portes C_kZ , permettant des portes de Toffoli généralisées qui sont fréquemment utilisées comme primitives en QEC pour réaliser des circuits de vote majoritaire pour l'extraction de syndromes et pour la QEC sans mesure [212-214]. Il convient de noter que la synthèse de portes Z multicontrôlées utilisant uniquement des portes à un ou deux qubits nécessite des circuits de grande profondeur ou des qubits auxiliaires supplémentaires [215], ce qui peut être évité à l'aide du protocole B.

Les résultats de ce chapitre ont plusieurs implications principales. Alors qu'il existe des propositions pour des portes de Toffoli à N qubits sur des qubits couplés via une cavité [205, 206], nos protocoles donnent la première implémentation native pour une

grande famille d'autres portes multi-qubits. En particulier, le protocole A introduit pour la première fois un moyen d'implémenter des portes de phase géométriques pour plus de deux qubits sur ces systèmes, tandis que le protocole B permet même l'implémentation de portes de phase natives *arbitrary* sans les décomposer en portes à un ou deux qubits. Cela améliore considérablement la perspective de réaliser des stabilisateurs non locaux et des systèmes de correction d'erreurs quantiques tels que les codes LDPC avec des surcharges de qubits réduites par rapport aux principaux systèmes actuels, en particulier si nos protocoles sont parallélisés dans des architectures qui exploitent des modes multiples (par exemple la fréquence, la polarisation, les modes spatiaux pour les cavités qui se chevauchent) comme nécessaire pour les opérations parallèles afin de prendre en charge la QEC. Pour les applications à court terme, le protocole A améliore la boîte à outils pour la génération de grands états intriqués de haute fidélité tels que les états GHZ, tandis que les portes de phase arbitraires pouvant être mises en œuvre par le protocole B sont d'un intérêt significatif pour la simulation quantique. Toutes ces tâches peuvent, pour la première fois, être accomplies sans qu'il soit nécessaire de piloter les qubits de l'extérieur. En outre, les deux protocoles appliqués à seulement deux qubits forment, avec les portes à qubit unique, un ensemble de portes universel pour le calcul quantique. Ces protocoles peuvent en principe être appliqués à d'autres plates-formes de qubits de pointe pour l'informatique quantique qui exploitent des modes de bosons délocalisés, tels que des ions piégés couplés par l'intermédiaire d'un mode de mouvement.

Conclusions et perspectives

Dans cette thèse, nous avons développé plusieurs protocoles de portes nouveaux et optimisés pour des portes quantiques à deux et plusieurs qubits sur des atomes neutres interagissant soit par l'interaction de van der Waals des états de Rydberg, soit par le couplage à un mode de cavité commun. Pour les interactions médiées par les états de Rydberg, une grande famille de ces protocoles sont des protocoles *temps-optimaux*, dans lesquels une impulsion laser globale avec une phase variant doucement est appliquée sur deux ou plusieurs atomes pour mettre en œuvre une porte quantique donnée aussi rapidement que possible. Nous avons utilisé la méthode numérique de contrôle optimal quantique de GRAPE pour trouver le protocole optimal en termes de temps pour toutes les portes de phase à deux qubits et plusieurs portes de phase à plusieurs qubits, et nous avons révélé la structure mathématique des protocoles optimaux en termes de temps en utilisant le principe du maximum de Pontryagin. En raison de leur structure simple, de leur polyvalence et de leur grande fidélité, les protocoles temps-optimaux ont déjà été utilisés pour mettre en œuvre des portes CZ et pour générer des états GHZ sur un maximum de dix atomes, et devraient rester des éléments essentiels pour les ordinateurs quantiques à atomes neutres à l'avenir. L'utilisation d'impulsions optimales en fonction du temps pour remplacer certaines parties des circuits quantiques par des portes natives ou pour générer des états spéciaux autres que les états GHZ constitue une direction de recherche future intéressante. En particulier, le développement de protocoles optimaux

en temps pour générer ce que l'on appelle des *états magiques*, qui sont nécessaires pour les calculs quantiques tolérants aux fautes (FTQC), est un objectif de recherche passionnant.

Alors que la vitesse d'un protocole optimal en termes de temps réduit l'effet de nombreuses sources d'erreur, nous avons également montré dans cette thèse qu'il existe des protocoles de porte plus longs mais *robustes*, qui peuvent atteindre des fidélités plus élevées en présence de certaines sources d'erreur. Plus précisément, nous avons développé des formes d'impulsion qui mettent en œuvre une porte CZ et qui sont robustes aux déviations de l'amplitude du laser et aux désaccordages du laser dus aux décalages Doppler induits par le mouvement thermique des atomes. Pour les erreurs de désintégration de Rydberg, nous avons montré que les protocoles temporellement optimaux pour les portes CZ et C_2Z minimisent déjà essentiellement l'infidélité. Il existe plusieurs sources d'erreurs expérimentales que nous n'avons pas incluses dans notre discussion sur les portes robustes, et le développement d'approches pour les atténuer est une direction de recherche importante pour l'avenir. En particulier, nous n'avons pris en compte que les fluctuations quasi-statiques de l'amplitude et du désaccord du laser, et une extension de nos résultats à des sources de bruit dépendant du temps serait hautement souhaitable. En outre, la question de savoir s'il existe une description semi-analytique des impulsions robustes, semblable à celle des impulsions optimales en fonction du temps développée dans le chapitre 4, reste ouverte.

Malgré des protocoles de porte rapides et robustes, les erreurs sont inévitables dans tout calcul quantique. Le cadre du FTQC utilise la redondance pour atténuer les effets de ces erreurs. Dans cette thèse, nous avons montré que pour un code de surface sur les atomes de Rydberg, les protocoles qui minimisent l'infidélité des portes au niveau physique peuvent être très différents des protocoles qui minimisent le taux d'erreur *logique*. Nous avons identifié les erreurs de fuite de Rydberg comme étant la source de cette divergence et nous avons développé plusieurs protocoles dans lesquels ces erreurs sont moins préjudiciables. À l'avenir, il sera important d'intégrer nos résultats avec des approches visant à corriger d'autres erreurs spécifiques aux atomes neutres, telles que les erreurs de perte d'atomes ou les erreurs de fuite vers d'autres états hyperfins [84], dans un protocole FTQC monolithique.

Enfin, dans cette thèse, nous avons également développé deux familles de protocoles de portes qui mettent en œuvre des portes multi-qubits sur des atomes neutres interagissant via un mode de cavité commun au lieu de l'interaction de van der Waals des états de Rydberg. Cela permet une connectivité de tout à tout et des portes non locales entre les atomes. La caractéristique distinctive de nos protocoles est qu'ils peuvent être mis en œuvre en utilisant simplement une commande classique du mode de la cavité, alors qu'aucun adressage des atomes n'est nécessaire, ce qui ouvre de nouvelles possibilités expérimentales. À l'avenir, des variantes de ces protocoles pourront être utilisées pour générer de grands états intriqués non locaux, tels que les états GHZ, avec des applications en détection quantique, en cryptographie et en correction d'erreurs.

Les résultats présentés dans cette thèse ont rapproché de la réalité la vision d'un

ordinateur quantique à atomes neutres à grande échelle, capable de surpasser les ordinateurs classiques dans des tâches d'intérêt pratique. Cependant, de nombreux défis doivent encore être relevés. L'une des tâches les plus importantes est sans doute la mise en œuvre de protocoles FTQC plus importants, adaptés aux canaux d'erreur dominants rencontrés dans les atomes neutres. Il s'agit notamment de concevoir des protocoles capables de corriger simultanément les erreurs de Pauli, les erreurs de fuite de Rydberg, les erreurs de perte d'atomes et les erreurs de fuite vers d'autres états hyperfins, et d'utiliser de manière optimale les erreurs d'effacement et le bruit biaisé [14, 20]. Les protocoles de portes optimaux en temps et robustes développés dans les chapitres 3–5 ainsi que la discussion sur les erreurs de fuite de Rydberg dans le chapitre 6 constituent un bon point de départ pour la conception de tels protocoles FTQC. Une deuxième voie est l'exploration des codes de contrôle de parité à faible densité (LDPC), qui permettent d'encoder plus de qubits logiques dans le même nombre de qubits physiques que les codes de surface traditionnels [29, 78, 79]. Le développement d'approches optimisées pour l'implémentation de codes LDPC sur des atomes neutres, l'implémentation de portes logiques sur des qubits encodés dans des codes LDPC, et la compréhension et l'amélioration de la performance des codes LDPC en cas d'erreurs propres à l'architecture de l'atome neutre, sont toutes des directions de recherche futures importantes, qui peuvent être abordées avec les méthodes développées dans cette thèse.

1 Introduction

The invention of the computer in the second half of the 20th century has revolutionized all aspects of our modern world, from scientific and industrial applications to the widespread adoption of the personal computer and the rise of the internet. However, despite the existence of giant super-computers, there are still large classes of scientifically or economically relevant computational problems whose solution is impossible or impractical on current machines. These include problems in computational chemistry, material science, drug discovery, combinatorial optimization problems with applications in logistics and operations research, and problems in finance.

Quantum computers promise to solve some of these problems faster than any classical device by using algorithms that exploit quantum phenomena such as entanglement and superposition [1–4]. Additionally, other quantum technologies such as quantum sensing [5] and quantum cryptography [6] offer large improvements over their classical counterparts, and can be realized with building blocks similar to those of a quantum computer. While quantum computers have for a long time been a largely theoretical concept, the last two decades have seen a large scientific and industrial effort to develop a proof-of-principle machine. However, despite the impressive progress in recent years, the fundamentally fragile nature of quantum information makes the physical realization of quantum computing a daunting task, and all currently existing quantum computers are too small, in terms of the number of quantum bits (qubits), and too faulty, in terms of the error rate per operation, to allow a speed-up in practically relevant computational problems. It is thus necessary to develop new and improved methods of implementing quantum computations with higher quality, and on more qubits.

Several different technologies are currently explored as candidates for a quantum computing platform. Historically, two of the first platforms to demonstrate small-scale proof-of-principle quantum computations were superconducting circuits [7] and trapped ions [8]. In these platforms, quantum bits are encoded in the current in a superconducting circuit and in the electronic and nuclear state of trapped ions, respectively. However, in recent years the promising and rapidly advancing platform of trapped neutral atoms has achieved a performance which is, in metrics such as qubit number and gate error rate, comparable to that of superconducting circuits and trapped ions [9–11]. In the neutral atom platform, individual atoms are trapped in regular arrays of optical tweezers, and qubits are stored in the electronic and nuclear degrees of freedom of each atom. The state of the atoms can be manipulated with high fidelity by applying laser or microwave pulses on or close to resonance with

a transition in the atoms. Usually, to implement a quantum gate on two or more atoms, the extreme properties of so-called *Rydberg states* [12] are exploited. Rydberg states are highly excited states of an atom, in which there is a large separation between the outermost electron and the nucleus. Due to the correspondingly large polarizability of Rydberg states, there is a strong *van der Waals interaction* between adjacent atoms. This interaction is many orders of magnitude larger than for atoms in the ground state, so that quantum gates on two or more atoms can be implemented by coupling the ground states of these atoms to a Rydberg state, while spectator atoms which are not involved in the gate are not affected by the van der Waals interaction. How exactly the van der Waals interaction between Rydberg states is used to implement a given quantum gate is described by a *gate protocol*. Different gate protocols have different advantages and drawbacks in terms of the fidelity, duration and robustness of the gate, and the design of new gate protocols has been an active field of research in the recent years.

In this thesis, we propose several new gate protocols for neutral atom quantum gates on two or more qubits which are *optimal*, and explore several different notions of optimality. To find optimal gate protocols, we use a combination of analytical techniques and numerical quantum optimal control methods. The main results of this thesis can be structured by different notions of optimality:

- i) Time-Optimal protocols.* A simple notion of optimality is speed. As the adverse effects of many experimental imperfections are reduced for short gate durations, finding fast gate protocols is of large practical interest. In this thesis we use numerical and analytical quantum optimal control methods to develop a family of *time-optimal* protocols, which implement a given quantum gate as fast as possible. These protocols have a simple structure and only require a single laser pulse with a time-dependent laser phase to be applied to the atoms. The most important instance of time-optimal gate protocols is the time-optimal controlled-Z (CZ) gate, which is by now routinely employed in many experiments [13–17]. Using the time-optimal CZ protocol, gate error rates below 0.5% have been demonstrated [13], more than five times better than the previously lowest error rate of 2.6% [18]. Besides the CZ gate, in this thesis we find time-optimal protocols for general two-qubit controlled phase gates, multi-controlled gates, and for the generation of multi-qubit Greenberger-Horne-Zeilinger (GHZ) states. The latter lead to an experimental implementation of GHZ states on up to nine atoms and their use in an optical clock [17]. In this thesis we also analyze the mathematical structure of time-optimal protocols using Pontryagin’s maximum principle, and find that the laser pulse shape used to implement time-optimal protocols can be described by a simple differential equation.
- ii) Robust protocols.* If the main error sources affecting a gate are known, gate protocols can be designed to be as robust as possible against these error sources. In this thesis, we develop gate protocols for the CZ gate which minimize the gate error due to several common experimental error sources, including Rydberg decay, a finite value of the interaction strength between the atoms, amplitude

fluctuations of the Rydberg laser, and laser detunings due to a Doppler shift arising from the thermal motion of the atoms. We then analyze the trade-off between different error sources for realistic parameters of qubits stored in ^{171}Yb atoms and find that our robust protocols allow for high gate fidelities for a large range of laser amplitude fluctuations and atomic temperatures, thus significantly relaxing the technical requirements for the implementation of high-fidelity CZ gates.

iii) Protocols minimizing the logical error rate. Due to the fragile nature of quantum information, errors in a quantum computation are unavoidable. To mitigate these errors, the framework of *fault tolerant quantum computing (FTQC)* has been developed [19]. In FTQC, one *logical qubit* is encoded into several physical qubits and the resulting redundancy is used to detect and correct errors in the computation. In the context of FTQC, the error rate with which the logical qubit experiences a failure, the so-called *logical error rate*, becomes a more important metric than the physical error rate of individual gates on the physical level. In this thesis, we discover two separate mechanisms which can cause a divergence between logical and physical error rate, and demonstrate that the logical error rate can be significantly improved by using gate protocols with a sub-optimal physical error rate. The first mechanism shows that in the context of erasure conversion [20] the optimal trade-off between different error sources for robust gates changes significantly when considering the logical instead of the physical error rate. In the second, more general, mechanism, we show that Rydberg leakage errors, in which an atom erroneously remains in the Rydberg state at the end of a gate, can significantly reduce the error correction capabilities of so-called surface codes [21]. We then develop gate protocols which mitigate the effects of Rydberg leakage errors, significantly reducing the logical error rate at the expense of a small increase of the physical error rate.

Besides using the van der Waals interaction between Rydberg states, it is also possible to implement quantum gates on two or more atoms by coupling the atoms to a common mode of an optical or a microwave cavity. This has the advantage of allowing for an all-to-all connectivity and non-local gates between the qubits, but typically results in higher gate error rates. In this thesis, we propose two new families of gate protocols for atoms coupled to a cavity, using a similar mechanism than for Mølmer-Sørensen gates for trapped ions [22]. In contrast to many previous works, these protocols can be implemented simply by a classical drive of the cavity mode, while no addressing of the atoms is necessary. This opens up new experimental possibilities of implementing quantum gates via optical cavities.

This thesis is structured as follows: We start in Chapter 2 with an introduction to quantum computing with neutral atoms and discuss the encoding of a qubit in an atom, the interaction between atoms and light, the trapping of atoms in arrays of optical tweezers, and several different approaches for implementing single- and two-qubit gates, state preparation, and measurement. In Chapter 3 we then use numerical methods to identify time-optimal gate protocols for several families

of quantum gates, and discuss the mathematical structure of these protocols in Chapter 4. In Chapter 5 we discuss robust gate protocols, followed by protocols optimized for the logical error rate in Chapter 6. We turn our focus to quantum gates implemented via an optical cavity in Chapter 7. Finally, in Chapter 8 we give an outlook to applications and extensions of the results of this thesis.

The results of this thesis have been previously published in the following publications:

- S. Jandura and G. Pupillo. “Time-Optimal Two- and Three-Qubit Gates for Rydberg Atoms”. *Quantum* 6 (2022), p. 712. DOI: 10.22331/q-2022-05-13-712
- S. Jandura, J. D. Thompson, and G. Pupillo. “Optimizing Rydberg Gates for Logical-Qubit Performance”. *PRX Quantum* 4 (2023), p. 020336. DOI: 10.1103/PRXQuantum.4.020336
- S. Jandura, V. Srivastava, L. Pecorari, G. Brennen, and G. Pupillo. “Non-Local Multi-Qubit Quantum Gates via a Driven Cavity”. *arXiv:2303.13127* (2023). URL: <http://arxiv.org/abs/2303.13127>
- S. Jandura and G. Pupillo. “Surface Code Stabilizer Measurements for Rydberg Atoms”. *arXiv:2405.16621* (2024). URL: <http://arxiv.org/abs/2405.16621>
- S. Ma, G. Liu, P. Peng, B. Zhang, S. Jandura, J. Claes, A. P. Burgers, G. Pupillo, S. Puri, and J. D. Thompson. “High-Fidelity Gates and Mid-Circuit Erasure Conversion in an Atomic Qubit”. *Nature* 622 (2023), pp. 279–284. DOI: 10.1038/s41586-023-06438-1
- A. Cao, W. J. Eckner, T. L. Yelin, A. W. Young, S. Jandura, L. Yan, K. Kim, G. Pupillo, J. Ye, N. D. Oppong, and A. M. Kaufman. “Multi-Qubit Gates and ‘Schrödinger Cat’ States in an Optical Clock”. *arXiv:2402.16289* (2024). URL: <http://arxiv.org/abs/2402.16289>

The results of the following publications of the author are not included in this thesis:

- S. Jandura and E. Y.-Z. Tan. “De Finetti Theorems for Quantum Conditional Probability Distributions with Symmetry”. *Annales Henri Poincaré* (2023). DOI: 10.1007/s00023-023-01357-3
- P. J. Ollitrault, S. Jandura, A. Miessen, I. Burghardt, R. Martinazzo, F. Tacchino, and I. Tavernelli. “Quantum Algorithms for Grid-Based Variational Time Evolution”. *Quantum* 7 (2023), p. 1139. DOI: 10.22331/q-2023-10-12-1139
- L. Pecorari, S. Jandura, G. K. Brennen, and G. Pupillo. “High-Rate Quantum LDPC Codes for Long-Range-Connected Neutral Atom Registers”. *arXiv:2404.13010* (2024). URL: <http://arxiv.org/abs/2404.13010>

2 Introduction to Quantum Computing with Neutral Atoms

In the early 1980s, a fundamental connection between the two research fields of quantum physics and computer science, previously thought to be unconnected, started to emerge. In 1980, Paul Benioff was one of the first to introduce the idea of a quantum computer in form of a quantum Turing machine [30]. Soon after, Yuri Manin [31] and Richard Feynman [32] independently suggested to use a computer that exploits quantum phenomena for the simulation of quantum systems, thus overcoming the exponential overhead that is required to simulate a quantum system on a classical computer. Later, David Deutsch, Richard Jozsa, Ethan Bernstein, Umesh Vazirani, Daniel Simon and others realized that quantum computers can also outperform classical computers in solving certain oracle problems, which in themselves have no connection to quantum physics [33–36]. While these problems had no immediate practical applications, they demonstrated the computational power of quantum computers. In the mid 1990s, the first quantum algorithms with potential applications to practical problems were discovered: In his seminal work, Peter Shor proposed a quantum algorithm to factor large integers in polynomial time [37], whose realization would compromise the largely used Rivest-Shamir-Adleman (RSA) cryptosystem [38]. Later, Lov Grover developed a quantum search algorithm that can find the input to a black box function which produces a given output with just $\mathcal{O}(\sqrt{N})$ evaluations of the function, while any classical algorithm requires $\mathcal{O}(N)$ evaluations, where N is the number of possible inputs to that function. Since then, a large variety of quantum algorithms with applications to optimization problems [3, 39], finance [4], quantum chemistry [2], machine learning [40, 41], and many other fields have been developed.

Building a physical quantum computer is a daunting task. The first quantum computation was realized in 1998 with two quantum bits (qubits) encoded in the nuclear spin on a carbon nucleus and a proton in a chloroform molecule [42]. Since encoding qubits in the individual atoms of a molecule is not scalable to more than a handful of qubits, soon other quantum computing platforms became popular. Superconducting circuits [7, 43–45], trapped ions [8, 46, 47], qubits encoded in diamond vacancies [48], silicon quantum dots [49, 50], photonic qubits [51, 52], topological qubits [53, 54], and qubits encoded in neutral atoms, the subject of this thesis, are all actively researched quantum computing platforms with different advantages and drawbacks [55]. Since the first quantum computing experiments, all of these platforms have seen tremendous progress. A recent milestone is the demonstration of so-called *quantum supremacy* on superconducting qubits [56, 57], where a quantum computer

solved a problem which arguably would take several millennia to solve on a classical computer. Also the demonstration of first quantum error correction protocols on several platforms [15, 58–63], where unavoidable errors in the computation are detected and subsequently corrected, has been a crucial achievement of the recent years.

A particularly promising and rapidly advancing quantum computing platform are optically trapped neutral atoms, the subject of this thesis. Since the first proposal in 2000 [64] and the first realization of a two qubit gate 10 years later [65] there has been impressive list of experimental achievements: Two-qubit gates have been demonstrated with fidelities above 99% [13, 16, 66] and used for the execution of small quantum circuits and algorithms [67, 68]. Greenberger-Horne-Zeilinger states (GHZ), an important resource for quantum metrology, have been generated on up to 20 qubits [69] and used in optical clocks [16, 17]. Several research groups have shown quantum processors with more than 1000 qubits [70–72]. Mid-circuit measurements and non-demolition readout have been demonstrated on processors with one [73] or two [74] atomic species. The conversion of unavoidable physical errors into erasure errors, which are particularly easy to correct, has been demonstrated in proof-of-principle experiments [14, 75]. Finally, there are even first implementations of quantum error correction and logical quantum gates and circuits [15]. In the near- and mid-term future, two-qubit gate fidelities beyond 99.9% [13], processors with tens of thousands of qubits [71], interconnects between different quantum processors [76, 77], and the usage of low density parity check (LDPC) error correction codes [29, 78, 79] are all realistic goals.

This chapter gives an overview on the state of the art of quantum computing with neutral atoms. We assume that the reader is familiar with the basic concepts of platform agnostic quantum computing, such as qubits, quantum gates, and quantum circuits. An introduction to this topic can be found in Ref. [1]. The overview on neutral atom quantum computing provided in this chapter is by no means exhaustive, the interested reader is referred to the reviews [9–11, 80] for more details.

The first step in any quantum computation is, of course, deciding how qubits should be stored. We address this question in Sec. 2.1 by reviewing the level schemes of alkali and alkaline earth atoms and discussing different qubit encodings. Once we have decided on what our qubits are, we need to manipulate them. The main way of manipulating qubits stored in atoms is by applying a classically controlled electromagnetic field to the atoms, either through a laser or through a microwave antenna. In Sec. 2.2 we therefore discuss the interaction of atoms with light (and other electromagnetic radiation). Before any quantum computation can start, the atoms have to be trapped, which can be done in so-called *optical tweezers*. We briefly review this technology in Sec. 2.3. A quantum computation consists of a sequence of single- and multi-qubit operations. We discuss the implementation of the three fundamental single qubit operations of qubit initialization, single qubit gates, and measurements in Sec. 2.4. Finally, in Sec. 2.5 we discuss how the strong van der Waals interaction between atoms excited to so-called *Rydberg states* can be used to implement quantum gates on two or more qubits.

2.1 Storing Qubits in Atoms

The fundamental unit of information of every quantum computer is the quantum bit (qubit), a physical system which can be in a superposition of two *computational basis states*, conventionally called $|0\rangle$ and $|1\rangle$. In a neutral atom quantum computer qubits are stored in the electronic and nuclear degrees of freedom of individual atoms. Typically, Alkali atoms such as Potassium, Rubidium or Cesium, or alkaline earth(-like) atoms such as Strontium or Ytterbium are used for this purpose. In the following we review the level structures of these atoms and discuss different choices of the computational basis states $|0\rangle$ and $|1\rangle$.

We start by discussing the level structure of alkali atoms, the atoms in the first column of the periodic table. Qualitatively, alkali atoms are similar to Hydrogen, since their outermost shell is an *s*-shell occupied by just one electron. The level structure of alkali atoms can be understood by just considering the position operator \mathbf{r} and momentum operator \mathbf{p} of this valence electron moving in an effective potential $V(\mathbf{r})$ [81] which describes the attraction of the valence electron to the nucleus shielded by the core electrons. Additionally, the atom is described by the spin operator $\mathbf{S} = (S_x, S_y, S_z)$ of the valence electron and the spin operator $\mathbf{I} = (I_x, I_y, I_z)$ of the nucleus. The Hamiltonian of the atom is then given by

$$H = \frac{\mathbf{p}^2}{2\mu} + V(\mathbf{r}) + H_{SO} + H_{HF}. \quad (2.1)$$

Here, $\mu = 1/(1/m_e + 1/m_N)$ is the reduced mass, with m_e and m_N the mass of the electron and the nucleus, respectively. $H_{SO} \propto \mathbf{L} \cdot \mathbf{S}$ describes the spin-orbit coupling between the spin \mathbf{S} and the orbital angular momentum $\mathbf{L} = \mathbf{r} \times \mathbf{p}$ of the electron. $H_{HF} \propto \mathbf{I} \cdot \mathbf{J}$ describes the hyperfine coupling between the spin \mathbf{I} of the nucleus and the total angular momentum $\mathbf{J} = \mathbf{L} + \mathbf{S}$ of the electron [82].

H commutes with the observables $\mathbf{L}^2, \mathbf{S}^2, \mathbf{J}^2, \mathbf{I}^2, \mathbf{F}^2$ and F_z , where $\mathbf{F} = \mathbf{J} + \mathbf{I}$. Each eigenstate $|\psi\rangle$ of H can thus be associated with quantum numbers l, s, j, i, f and m_F such that $\mathbf{L}^2 |\psi\rangle = \hbar^2 l(l+1) |\psi\rangle$ with analogous expressions for $\mathbf{S}^2, \mathbf{J}^2, \mathbf{I}^2, \mathbf{F}^2$ and $F_z |\psi\rangle = \hbar m_F |\psi\rangle$ [82]. The quantum numbers l are constrained to be non-negative integers. Since the electron is a spin 1/2 particle, the quantum number s has to take the value $s = 1/2$. The quantum number i depends on the isotope of the nucleus. For example, an ^{87}Rb nucleus has a spin of $i = 3/2$. Since $\mathbf{J} = \mathbf{L} + \mathbf{S}$ and $\mathbf{F} = \mathbf{L} + \mathbf{I}$, the quantum numbers j and f are constrained to the values $|l-s|, |l-s|+1, |l-s|+2, \dots, l+s$ and $|j-i|, |j-i|+1, |j-i|+2, \dots, j+i$, respectively. The quantum number m_F can take the values $-f, -f+1, \dots, f-1, f$. Even for a given set l, s, j, i, f, m_F of quantum numbers there are still several different eigenstates of H . These eigenstates are then simply enumerated with increasing energy by the *principal quantum number* n .

Fig. 2.1 shows some of the most relevant energy levels of a ^{87}Rb atom (nuclear spin 3/2), the level structures of other alkali atoms are similar. Conventionally, the eigenstates of H are denoted as $|nl_j\rangle$, where instead of the integer l we write S for

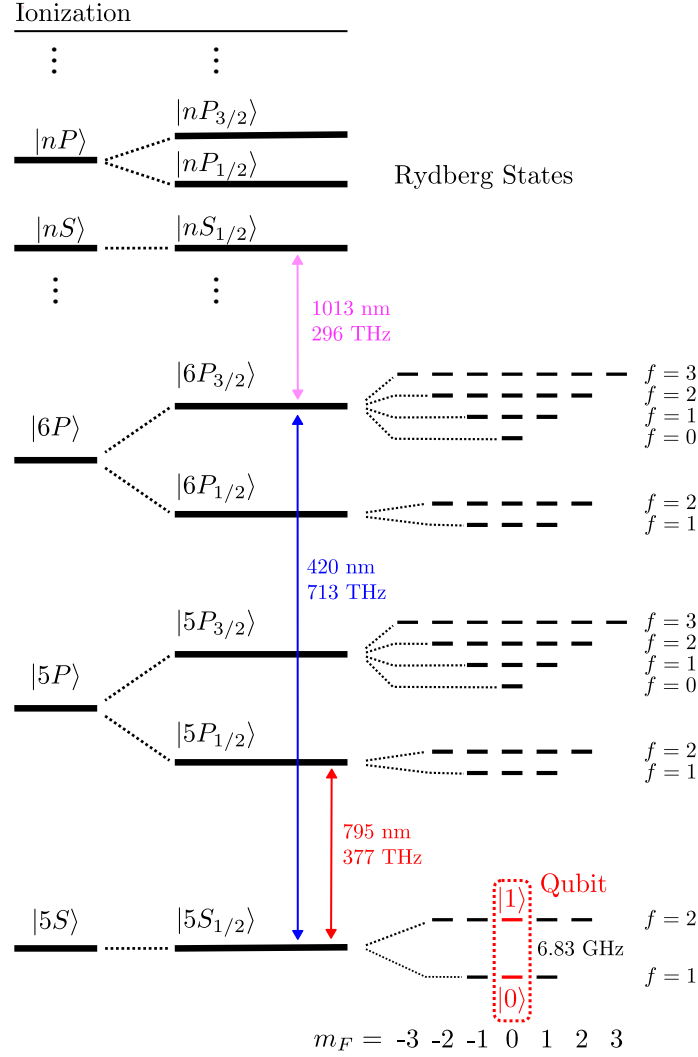


Figure 2.1: ^{87}Rb Level Structure. The energy levels of a ^{87}Rb atom under Coulomb interaction only (left column), taking spin-orbit coupling into account (middle column) and taking also the hyperfine interaction into account (right column). A qubit can be encoded in $|0\rangle = |5S_{1/2}, f = 1, m_F = 0\rangle$ and $|1\rangle = |5S_{1/2}, f = 2, m_F = 0\rangle$.

$l = 0$, P for $l = 1$, D for $l = 2$, and F for $l = 3$. The left column in Fig. 2.1 shows the eigenstates of $H_{\text{Coulomb}} = \mathbf{p}^2/2\mu + V(\mathbf{r})$, neglecting the spin of the electron and the nucleus. The middle column shows the eigenstates of $H_{\text{Coulomb}} + H_{SO}$, taking into account the spin of the valence electron, but not that of the nucleus. The splitting of the $|nl\rangle$ state into different $|nl_j\rangle$ states is called the *fine structure* of the atom. Note that the energy difference between states with the same n and l but different j is an order of α^2 smaller than the energy difference between states with different n or l , where $\alpha \approx 1/137$ is the fine structure constant.

The ground state of a ^{87}Rb atom is the $|5S_{1/2}\rangle$ state. All states energetically below this state are occupied by the core electrons and by the Pauli exclusion principle cannot be accessed by the valence electron. Two important excited states are the

$|5P\rangle$ and $|6P\rangle$ states, each of which split into a $j = 1/2$ and $j = 3/2$ state under spin-orbit coupling. The energy difference between these states and the ground state corresponds to a photon in the optical regime, allowing these states to be accessed by illuminating the atom with a laser beam (see Sec. 2.2). Finally, an important class of excited states which will play a prominent role in the rest of this thesis are so-called *Rydberg* states $|nS\rangle, |nP\rangle, |nD\rangle, \dots$, which are states with a large principal quantum number n (typically $n \gtrsim 40$). Since for Rydberg states the valence electron is far away from the nucleus and all core electrons, their energy levels are similar to the energy levels of Hydrogen and can be approximated as [83]

$$E_{n,l,j} = -\frac{1 \text{ Ry}}{(n - \delta_{l,j})^2} \quad (2.2)$$

where $1 \text{ Ry} \approx 13.6 \text{ eV}$ is the binding energy of a Hydrogen atom and the parameters $\delta_{l,j}$, called the *quantum defects*, are fitted to the experimentally obtained energy levels. The Rydberg states in ^{87}Rb are experimentally accessible from the ground state through a two-photon transition via the $|6P\rangle$ states, where the second photon from the $|6P\rangle$ states to the Rydberg states is in the infrared regime.

So far we have ignored the hyperfine coupling H_{HF} between the angular momentum J of the electron and the spin I of the nucleus. Taking H_{HF} into account splits the $|nl_j\rangle$ states into several different *hyperfine* states with different values of f and m_F . These hyperfine states are shown in the right column of Fig. 2.1. The energy splitting between hyperfine states with different f is another factor of α^2 smaller than the fine structure splitting, and typically in the microwave regime.

A qubit can be encoded in the states of an alkali atom by choosing $|0\rangle$ and $|1\rangle$ to be two hyperfine states in the $|S_{1/2}\rangle$ ground state manifold. These states are not effected by radiative decay and only couple weakly to their environment, allowing for long decoherence times (see Sec. 2.3). A popular choice is to take two states with different f and $m_F = 0$, such as $|0\rangle = |5S_{1/2}, f = 1, m_F = 0\rangle$ and $|1\rangle = |5S_{1/2}, f = 2, m_F = 0\rangle$ for ^{87}Rb [18], making the qubit frequency magnetically insensitive. However, other choices have been proposed [84]. Since both computational basis states are encoded in the ground state manifold of the atom, this type of qubit is known as ground-ground qubit. It is also possible to encode one or both computational basis states in a Rydberg state, known as ground-Rydberg and Rydberg-Rydberg qubit, respectively [11]. Due to the finite lifetime of the Rydberg state and the natural interaction between atoms in the Rydberg state (see Sec. 2.5), this approach is typically only adopted for quantum simulation [10], and rarely for quantum computation. In this thesis, we will exclusively consider ground-ground qubits.

Finally we briefly comment on possible qubit encodings in alkaline earth(-like) atoms, in which the outermost shell is an s -shell occupied by *two* electrons. These atoms, in particular Strontium and Ytterbium, have been used in several quantum computing experiments [17, 85, 86]. (Note that Ytterbium is technically not an alkaline earth atom, but its outermost shell is still a completely filled s -shell. For this reason, it is often referred to as an *alkaline earth-like* atom). The fact that now there are two electron spins \mathbf{S}_1 and \mathbf{S}_2 , which couple to a total electronic spin $\mathbf{S} = \mathbf{S}_1 + \mathbf{S}_2$

allows for an additional degree of freedom in the level structure: The two spins can either form a singlet $(|\uparrow\downarrow\rangle - |\downarrow\uparrow\rangle)/\sqrt{2}$, such that $s = 0$, or a triplet, i.e. a superposition of $|\uparrow\uparrow\rangle$, $(|\uparrow\downarrow\rangle + |\downarrow\uparrow\rangle)/\sqrt{2}$ and $|\downarrow\downarrow\rangle$, such that $s = 1$. The quantum numbers l , s and j are now often combined to a symbol $^{2s+1}l_j$, where again $l = 0, 1, 2, 3$ is replaced by S, P, D, F . Besides the quantum numbers l, s, j, i, f a state is now identified by the principal quantum numbers n_1, n_2 and the angular momentum quantum numbers l_1, l_2 of the individual electrons. The ground state of an alkaline earth atom is the $|g\rangle = |ns ns^1S_0\rangle$ state, where n is the principal quantum number of the lowest s -shell that is not occupied by the core electrons. Note that $|g\rangle$ is a singlet state. The *triplet* state with the lowest energy is the $|m\rangle = |ns np^3P_0\rangle$ state. (Note that since the total wavefunction must be antisymmetric under the exchange of both electrons there is no $|ns ns^3S_0\rangle$ state). The state $|m\rangle$ has a very long radiative lifetime (e.g. 150 s for ^{88}Sr [87]) and is therefore called *metastable* state, and effectively acts as a second ground state of the atom. There are now three possibilities to encode a qubit, called the *optical*, *metastable*, and *ground* (OMG) qubit [88]. The optical qubit consists of $|0\rangle = |g\rangle$ and $|1\rangle = |m\rangle$, and bears this name since the transition frequency between $|0\rangle$ and $|1\rangle$ is in the optical range. For the metastable and ground qubits, which are only possible for isotopes with nonzero nuclear spin, the states $|0\rangle$ and $|1\rangle$ are instead chosen to be two hyperfine states in the metastable or the ground manifold, respectively. One particular advantage of the optical and the metastable qubit is that the Rydberg states can be accessed from state $|1\rangle$ with a single-photon instead of a two-photon transition [17, 85]. Furthermore, metastable qubits allow for certain erasure conversion protocols, which simplifies the correction of errors due to Rydberg decay [14, 20]. Other advantages and drawbacks of each choice of qubit are discussed in Ref. [88].

In summary, in this section we have discussed the level schemes of alkali and alkaline earth(-like) atoms. In alkali atoms, a qubit can be encoded in two different hyperfine states in the ground state manifold, while in alkaline earth (like) atoms there is the additional possibility of an optical or a metastable qubit. Beyond the ground state, Rydberg states, i.e. states with a large principal quantum number will play a major role in this thesis. Between the ground state and Rydberg states there are several intermediate states that can be accessed optically from the ground state and that allow accessing the Rydberg state via a two photon transition.

2.2 Atom-Light Interaction

Both the internal and the motional degrees of freedoms of an atom can be controlled using light fields and electromagnetic waves at other frequencies. In the following we therefore review the interaction between an atom and a classical light field. We also briefly discuss spontaneous emission, which is a crucial process that can only be explained through a quantum mechanical treatment of light.

To understand the interaction between an atom and a light field it is sufficient to model an atom as a two level system with a ground state $|g\rangle$ and an excited state

$|e\rangle$ with energies $\hbar\omega_g$ and $\hbar\omega_e$ respectively. In the absence of light, the Hamiltonian of the atom is then just given by

$$H_0 = \hbar\omega_g |g\rangle \langle g| + \hbar\omega_e |e\rangle \langle e|. \quad (2.3)$$

An electromagnetic wave with frequency ω_l and wavevector \mathbf{k} is described by an oscillating electric field

$$\mathbf{E}(\mathbf{r}, t) = \text{Re} (\mathbf{E}_0 e^{-i(\omega_l t - \mathbf{k} \cdot \mathbf{r})}) \quad (2.4)$$

where \mathbf{E}_0 is a complex vector with $\mathbf{E}_0 \cdot \mathbf{k} = 0$. Of course the electromagnetic wave also comes with a magnetic component, whose contribution to the interaction is however much smaller than that of the electric component if the size of the atom is much smaller than the wavelength [89]. In the following we will therefore neglect the magnetic field.

The interaction of the atom at $\mathbf{r} = 0$ with the electric field can be approximated as a dipole interaction

$$\begin{aligned} H_{\text{int}} &= -\mathbf{E}(0, t) \cdot \mathbf{d} \\ &= -\mathbf{E}(0, t) \cdot (\langle g|\mathbf{d}|e\rangle |g\rangle \langle e| + \langle e|\mathbf{d}|g\rangle |e\rangle \langle g|) \\ &= -\frac{1}{2} [\mathbf{E}_0 \cdot \langle g|\mathbf{d}|e\rangle e^{i\omega_l t} + \mathbf{E}_0^* \cdot \langle g|\mathbf{d}|e\rangle e^{-i\omega_l t}] |g\rangle \langle e| + \text{h.c.} \end{aligned} \quad (2.5)$$

where \mathbf{d} is the dipole moment operator of the atom. The second equality in the above equation arises due to the spherical symmetry of the atom, which implies $\langle g|\mathbf{d}|g\rangle = \langle e|\mathbf{d}|e\rangle = 0$. In the third equality, h.c. denotes the hermitian conjugate of the previous term.

We now perform a time-dependent basis transformation with $V(t) = e^{i\omega_g t} |g\rangle \langle g| + e^{i(\omega_l + \omega_g)t} |e\rangle \langle e|$ and obtain

$$\begin{aligned} \bar{H} &= V H V^\dagger + i\hbar \dot{V} V^\dagger \\ &= \hbar\Delta |e\rangle \langle e| - \frac{1}{2} [\mathbf{E}_0 \cdot \langle g|\mathbf{d}|e\rangle e^{-2i\omega_l t} + \mathbf{E}_0^* \cdot \langle g|\mathbf{d}|e\rangle] |g\rangle \langle e| - \text{h.c.} \end{aligned} \quad (2.6)$$

where $\Delta = \omega_e - \omega_g - \omega_l$. In the so-called *rotating wave approximation* we now neglect the rapidly oscillating $\mathbf{E}_0 \cdot \langle g|\mathbf{d}|e\rangle e^{-2i\omega_l t}$ term since its time average vanishes and obtain

$$\bar{H} = \hbar\Delta |e\rangle \langle e| + \frac{\hbar\Omega}{2} |g\rangle \langle e| + \frac{\hbar\Omega^*}{2} |e\rangle \langle g| \quad (2.7)$$

where we introduced the *Rabi frequency*

$$\Omega = -\frac{1}{\hbar} \mathbf{E}_0^* \cdot \langle g|\mathbf{d}|e\rangle. \quad (2.8)$$

The amplitude of the Rabi frequency can be related to the intensity $I = c\epsilon_0 |\mathbf{E}_0|^2/2$ of the light as

$$|\Omega| = \frac{1}{\hbar} \sqrt{\frac{2I}{c\epsilon_0}} |\langle g|\mathbf{n} \cdot \mathbf{d}|e\rangle|. \quad (2.9)$$

where $\mathbf{n} = \mathbf{E}_0^*/|\mathbf{E}_0|$ and c is the speed of light and ϵ_0 the vacuum permittivity. The phase φ of the Rabi frequency is simply the phase of the electromagnetic wave.

It is useful to expand the dipole moment operator \mathbf{d} and the electric field \mathbf{E}_0 as $\mathbf{d} = \sum_{m=-1}^1 d_m \mathbf{e}_m$ and $\mathbf{E}_0 = \sum_{m=-1}^1 E_m \mathbf{e}_m$, where $\mathbf{e}_0 = (0, 0, 1)$ and $\mathbf{e}_{\pm 1} = (1, \pm i, 0)/\sqrt{2}$. Then the E_0 and $E_{\pm 1}$ describe the π and the σ^\pm polarized part of the light field, respectively, and we have

$$\Omega = -\frac{1}{\hbar} \sum_{m=-1}^m E_m^* \langle g|d_m|e\rangle. \quad (2.10)$$

Crucially, for many choices of the states $|g\rangle$ and $|e\rangle$ the transition dipole moments $\langle g|d_m|e\rangle$ vanish due to symmetry arguments. These rules are known as *selection rules* and can be summarized as follows [89]: Let l, j, f, m_f and l', j', f', m'_f be the quantum numbers of $|g\rangle$ and $|e\rangle$. Then $\langle g|d_m|e\rangle = 0$ unless all of the following hold:

- i) $|l - l'| = 1$
- ii) $|j - j'| \leq 1$
- iii) $|f - f'| \leq 1$
- iv) $m'_F = m_F + m$
- v) If $m_F = m'_F = 0$ then $f \neq f'$.

In particular, selection rule *iv)* implies a purely π polarized light field can only couple states with $m'_F = m_F$, while a purely σ^\pm polarized light field can only couple states with $m'_F = m_F \pm 1$.

Two special cases of the Hamiltonian \bar{H} [Eq. (2.7)] are of particular importance. The first case is the case of a resonant light field, i.e. $\Delta = 0$. In this case, the evolution under \bar{H} is simply given by

$$\bar{U}(t) = \exp(-i\bar{H}t/\hbar) = \cos\left(\frac{|\Omega|t}{2}\right) I - i \sin\left(\frac{|\Omega|t}{2}\right) (e^{i\varphi} |g\rangle \langle e| + e^{-i\varphi} |e\rangle \langle g|) \quad (2.11)$$

where I denotes the identity operator. In particular, for a system starting in $|g\rangle$ the probability of finding the system in state $|g\rangle$ at time t is given by

$$\langle g|\bar{U}(t)|g\rangle = \cos\left(\frac{|\Omega|t}{2}\right)^2 = \frac{1}{2} (1 + \cos(|\Omega|t)) \quad (2.12)$$

i.e. the population oscillates with frequency $|\Omega|$. These oscillations are called *Rabi oscillations*.

The second important case is a far detuned light field, $|\Delta| \gg |\Omega|$. In this case we can treat the atom-light interaction perturbatively. The Hamiltonian \bar{H} now

has dressed eigenstates $|\tilde{g}\rangle$ and $|\tilde{e}\rangle$ close to $|g\rangle$ and $|e\rangle$, respectively. The energies of these states in second order perturbation theory are given by

$$\epsilon_g/\hbar = -\frac{|\Omega|^2}{4\Delta} \quad \text{and} \quad \epsilon_e/\hbar = \Delta + \frac{|\Omega|^2}{4\Delta}. \quad (2.13)$$

In particular we see that the energy of the ground state is lowered if $\Delta > 0$ and raised if $\Delta < 0$. This phenomenon is called *light shift*. The light shift can be used to trap atoms: If we model the atom as a multi level system with ground state $|g\rangle$ and excited state $|e_1\rangle, |e_2\rangle, \dots$ the energy of the state perturbed $|\tilde{g}\rangle$ is given by

$$\epsilon_g = -\sum_i \frac{\hbar|\Omega_i|^2}{4\Delta_i} = -\frac{1}{2}\alpha(\omega_l)|\mathbf{E}_0|^2 = -\frac{\alpha(\omega_l)I}{c\epsilon_0} \quad (2.14)$$

where

$$\alpha(\omega_l) = \sum_i \frac{|\langle g|\mathbf{n} \cdot \mathbf{d}|e_i\rangle|^2}{4\hbar(\omega_{e_i} - \omega_g - \omega_l)} \quad (2.15)$$

is the polarizability of the atom at wavelength ω_l . For $\alpha(\omega_l) > 0$ the atom is thus attracted to regions with high intensity.

So far we have treated the electric field as a classical quantity. For most of this thesis, this will be a sufficient approximation. The one exception is *spontaneous emission*. If we leave the atom in the excited state $|e\rangle$ it can emit a photon and decay back to the ground state $|g\rangle$ without the presence of any external light field. This process can only be explained through a fully quantum mechanical treatment of light, which is beyond the scope of this overview. The *emission rate* can be calculated as [82]

$$\gamma = \frac{(\omega_e - \omega_g)^3 |\langle g|\mathbf{d}|e\rangle|^2}{3\pi\epsilon_0\hbar c^3} \quad (2.16)$$

and the evolution of the atom can be described through a Lindblad master equation

$$\dot{\rho} = -i[H_0, \rho] + L^\dagger \rho L - \frac{1}{2}\{L^\dagger L, \rho\} \quad (2.17)$$

where ρ is the density matrix of the atom and $L = \sqrt{\gamma}|g\rangle\langle e|$.

In summary we have derived the interaction Hamiltonian of an atom modeled as a two level system with a classical light field [Eq. (2.7)]. An extension to more than two levels is straightforward. We have also given the formula for the spontaneous emission rate of an excited state, a phenomenon that cannot be described by treating the light classically.

2.3 Trapping Atoms in Optical Tweezers

Before starting any quantum computation the atoms have to be trapped and arranged in the desired geometry. In the following we briefly describe the experimental techniques with which this can be achieved.

To trap individual atoms in a regular array or another geometry, a light field with a spatially varying intensity profile has to be produced. Atoms can then be trapped in the intensity maxima of this light field [see Eq. (2.14)]. Regular arrays of traps can be produced in an optical lattice by the interference of two counter-propagating beams [90]. A more flexible approach is to use *optical tweezers*. In this approach, spatial light modulators (SLMs) or acousto-optical deflectors (AODs) are used to create several individual laser beams, which are then tightly focused to a micron-size waist and each act as an individual trap [91–93]. Tweezers generated by SLMs can be generated by in arbitrary geometries, but are static during the experiment. In contrast, tweezers generated by AODs have to be arranged in certain regular patterns, but can be moved during the experiment [94].

To load the tweezers with atoms, first millions of atoms are trapped and laser cooled in a magneto-optical trap [95]. Then the tweezers are turned on and capture atoms in their vicinity. Due to the process of collisional blockade [96], pairs of atoms are ejected from the tweezers due to light-assisted collisions, leaving every tweezer either empty or filled with exactly one atom. To produce deterministically filled arrays of tweezers, fluorescence imaging can be used to determine which tweezers are filled. These filled tweezers can then be rearranged to produce the desired geometry. This has been demonstrated for arbitrary geometries in one [91], and two [92] dimensions, for up to 6100 atoms [71].

Trapping the atoms in tweezers is a source of decoherence for the qubits encoded in the atoms. There are two relevant error mechanisms: First, atoms can be lost from the tweezers due to collisions with the background gas. This typically limits the lifetime of the atoms in the trap to tens of seconds [91], but lifetimes up to 6000s have been observed in cryogenic setups [97]. The second error mechanism is a dephasing of the qubits. This arises because the polarizability α , and thus the trap depth, is slightly different for the states $|0\rangle$ and $|1\rangle$. Due to fluctuations in the trap depths or the motion of the atoms in the trap, this leads to fluctuations in the energy difference between $|0\rangle$ and $|1\rangle$ and thus to dephasing of the qubit. Typical values of the T_2^* time describing the time scale of this dephasing are tens of milliseconds [98], but values above one second have been reported [99]. We point out that errors due to atom loss and decoherence of the qubit are typically much smaller than the additional errors induced during two-qubit gates, and thus are not the dominant error source in a computation.

2.4 Single Qubit Operations

The three fundamental single qubit operations in a quantum computer are the initialization of a qubit in a well defined initial state, the application of single qubit gates, and the measurement of the qubit. In the following we briefly discuss techniques that can be used to realize these operations on a neutral atom quantum computer.

2.4.1 Qubit Initialization

In the beginning of a quantum computation, all atoms start in an unknown hyperfine state in the ground state manifold of the atoms. To prepare the atoms in a well defined initial state, either $|0\rangle$ or $|1\rangle$, a family of techniques collectively known as *optical pumping* is commonly used [18, 85, 95, 98, 100]. In the following we describe it for ^{87}Rb atoms (see level scheme in Fig. 2.1), but analogous schemes exist for other atoms.

Initially, all qubits start in the $5S_{1/2}$ manifold, but with different values of f and m_F . Then two π -polarized laser beams are applied, coupling $|5S_{1/2} f = 1, m_F\rangle \leftrightarrow |5P_{3/2} f = 2, m_F\rangle$ and $|5S_{1/2} f = 2, m_F\rangle \leftrightarrow |5P_{3/2} f = 2, m_F\rangle$ for all values of m_F , respectively. The only exception is that there is no coupling $|5S_{1/2} f = 2, m_F = 0\rangle \leftrightarrow |5P_{3/2} f = 2, m_F = 0\rangle$, due to a selection rule which forbids couplings with $f = f'$ if $m_F = m'_F = 0$ (see Sec. 2.2). Thus, atoms in state $|1\rangle = |5S_{1/2} f = 2, m_F = 0\rangle$ are not affected by the laser and will remain in this state, while all other atoms are excited to the $5P_{3/2}$ manifold. The states in the $5P_{3/2}$ manifold have a very short lifetime of 26 ns [101], and quickly decay back to the $S_{1/2}$ manifold. Some fraction of the atoms will decay to $|1\rangle$, where they will remain indefinitely. All other atoms will be again excited to the $5P_{3/2}$ manifold, from which a fraction of them will decay to $|1\rangle$, while for the others the cycle repeats. Asymptotically, this procedure leaves all atoms in $|1\rangle$.

In practice, state preparation errors arise due to an imperfect polarization of the laser beams, which allows the transition from $|1\rangle$ to $|5P_{3/2} f = 2, m_F = \pm 1\rangle$. These errors can be significantly reduced by an active Raman assisted optical pumping scheme [18, 95].

2.4.2 Single Qubit Gates

There are several ways of implementing single qubit gates on neutral atoms. In the simplest case, electromagnetic radiation with a frequency resonant with the transition between $|0\rangle$ and $|1\rangle$ is applied. For qubits encoded in hyperfine states with different f this radiation is in the microwave regime [98], for qubits encoded in states with the same f but different m_F it is in the radio frequency regime (RF) [85], and for optical qubits it is in the optical regime [16, 17], so a laser can be used to apply single qubit gates. In all cases, the Hamiltonian in the rotating frame is given by (see Sec. 2.2)

$$H = \frac{\Omega}{2} |0\rangle \langle 1| + \frac{\Omega^*}{2} |1\rangle \langle 0| = \frac{|\Omega|}{2} (\cos \varphi \sigma_x + \sin \varphi \sigma_y) \quad (2.18)$$

where $\sigma_{x,y}$ denote the Pauli X and Y matrices. Thus by applying H for a time $\theta/|\Omega|$ we can implement the two-parameter family of single qubit gates

$$U(\theta, \varphi) = \exp \left(-i \frac{\theta}{2} (\cos \varphi \sigma_x + \sin \varphi \sigma_y) \right). \quad (2.19)$$

The $U(\theta, \varphi)$ family of gates is sufficient to synthesize any single qubit gate [1].

Except for optical qubits, the disadvantage of this approach is that is not addressable to individual qubits, i.e. the same unitary $U(\theta, \varphi)$ is applied to all qubits. To make the gates addressable it is possible to use an additional addressable laser beam which is off-resonant from any transitions from $|0\rangle$ or $|1\rangle$. The only effect of this laser is then to induce a differential light shift $\Delta |1\rangle\langle 1|$ on the qubit. This light shift can now either be used to implement locally addressable $\exp(i\theta\sigma_z)$ gates [68], or to shift the qubits on which the microwave or RF radiation should not act out of resonance [102].

A second approach to single qubit gates which is naturally addressable is to use a *Raman transition*, i.e. two lasers coupling each of the states $|0\rangle$ and $|1\rangle$ to an intermediate state $|e\rangle$, such as a $5P_{1/2}$ in ^{87}Rb [67, 103]. Both lasers are detuned by a detuning Δ , giving the Hamiltonian

$$H = \Delta |e\rangle\langle e| + \frac{\Omega_0}{2} |0\rangle\langle e| + \frac{\Omega_1}{2} |1\rangle\langle e| + \frac{\Omega_0^*}{2} |e\rangle\langle 0| + \frac{\Omega_1^*}{2} |e\rangle\langle 1|. \quad (2.20)$$

In the limit $\Delta \gg |\Omega|$ the state $|e\rangle$ can be adiabatically eliminated [104], leading to the effective Hamiltonian

$$H_{\text{eff}} = \frac{\Omega_{\text{eff}}}{2} |0\rangle\langle 1| + \frac{\Omega_{\text{eff}}^*}{2} |1\rangle\langle 0| \quad (2.21)$$

with $\Omega_{\text{eff}} = \Omega_0\Omega_1/4\Delta$. Now any single qubit gate can be implemented just like with the Hamiltonian (2.18). Note that this approach introduces the decay of $|e\rangle$ as an additional error source, which can be mitigated by large detunings Δ , at the expense of long gate durations.

2.4.3 Qubit Readout

Qubit readout is typically done via *fluorescence imaging*. For this, typically atoms in one of the two computational basis states are first removed from the traps, for example by heating them out of the trap [18, 105] or, for alkaline earth (-like) atoms, through autoionization [14]. Let us assume without loss of generality that atoms in state $|1\rangle$ are removed, so all remaining atoms are in state $|0\rangle$. To complete the measurement we have to determine which traps are still filled with atoms. For this, one typically employs a *cycling transition*, i.e. an excited state $|e\rangle$ which has a short lifetime and only decays back to $|0\rangle$ and (almost) never to other states. Applying a laser on or close to the transition frequency between $|0\rangle$ and $|e\rangle$ then leads to the scattering of many photons, some of which are collected and detected by a camera, indicating the presence and position of the atom.

There are several improvements over this simple readout scheme. It is possible to read out only some, but not all, atoms in the array, either by shelving the qubits which are not being read out in other states [73], or by using a dual species array [100]. Furthermore, readout times can be reduced by mapping the single atom to be read out to a whole ensemble of atoms, and then using the effect of electromagnetically induced transparency [106] to read out the state of the ensemble.

2.5 Two- and Multi-Qubit Gates

The implementation of high-fidelity two-qubit gates is arguably one of the most challenging pieces of a quantum computing architecture. In this section we will discuss how Rydberg states, introduced in Sec. 2.1, can be used to implement two- and multi-qubit gates on qubits encoded in neutral atoms. We start by discussing the van der Waals interaction between two atoms in the Rydberg state in Sec. 2.5.1. We then introduce the π - 2π - π protocol for a controlled-Z (CZ) gate, the earliest proposal for a quantum gate mediated via Rydberg states, in Sec. 2.5.2. Another gate protocol, the Levine-Pichler (LP) protocol, which enables the implementation of a CZ gate without local addressability of the atoms and constitutes a large improvement over the π - 2π - π protocol, is discussed in Sec. 2.5.3. Finally, in Sec. 2.5.4 we give an overview over the many other gate protocols that have been proposed.

2.5.1 Van der Waals Interaction between Rydberg States

Let us consider two atoms located at positions 0 and $\mathbf{R} = R\mathbf{n}$. We denote by E_i and $|\psi_i\rangle$ the eigenstates and eigenenergies of the Hamiltonian of a single atom, which is given by

$$H_{\text{atom}} = \sum_i E_i |\psi_i\rangle \langle \psi_i|. \quad (2.22)$$

If R is much larger than the distance between the electrons and the nucleus in each atom, the interaction between both atoms can be approximated as a dipole-dipole interaction

$$V_{\text{dd}} = \frac{\mathbf{d}_1 \cdot \mathbf{d}_2 - 3(\mathbf{d}_1 \cdot \mathbf{n})(\mathbf{d}_2 \cdot \mathbf{n})}{4\pi\epsilon_0 R^3} \quad (2.23)$$

where \mathbf{d}_1 and \mathbf{d}_2 are the electric dipole moment operators of the two atoms. Expressed in the basis of the $|\psi_i\rangle$ the interaction reads

$$\begin{aligned} V_{\text{dd}} &= \sum_{ijkl} \langle \psi_i \psi_j | V_{\text{dd}} | \psi_k \psi_l \rangle \\ &= \frac{1}{4\pi\epsilon_0 R^3} \sum_{ijkl} [\langle \psi_i | \mathbf{d}_1 | \psi_k \rangle \cdot \langle \psi_j | \mathbf{d}_2 | \psi_l \rangle - 3 \langle \psi_i | \mathbf{d}_1 \cdot \mathbf{n} | \psi_k \rangle \langle \psi_j | \mathbf{d}_2 \cdot \mathbf{n} | \psi_l \rangle]. \end{aligned} \quad (2.24)$$

The total Hamiltonian describing the system of both atoms is given by

$$H = H_{\text{atom}} \otimes I + I \otimes H_{\text{atom}} + V_{\text{dd}}. \quad (2.25)$$

For large interatomic distances R , the interaction V_{dd} can be treated perturbatively. The first order perturbation is

$$\Delta E_{ij}^{(1)} = \langle \psi_i \psi_j | V_{\text{dd}} | \psi_i \psi_j \rangle = 0 \quad (2.26)$$

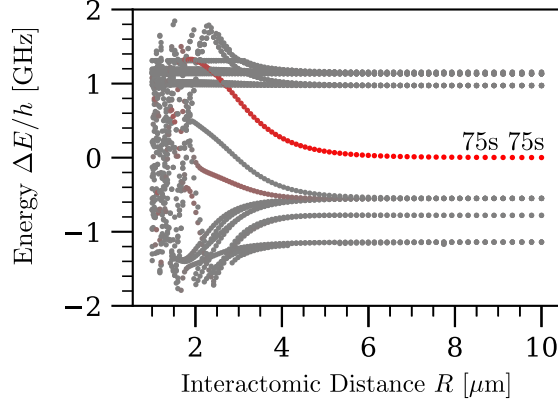


Figure 2.2: Van der Waals interaction. Eigenenergies of different eigenstates of the two-atom Hamiltonian H as a function of the interatomic distance R , relative to the energy of the $|75s, 75s\rangle$ state at $R = \infty$, for two Cesium atoms. The red color shows the overlap of the $|75s, 75s\rangle$ state with the different eigenstates. This plot was generated using the Alkali Rydberg Calculator [101].

where we used that $\langle \psi | \mathbf{d} | \psi \rangle = 0$ for every eigenstate $|\psi\rangle$ of H_{atom} . Thus, the first relevant correction is in second order perturbation theory, given by

$$\Delta E_{ij}^{(2)} = - \sum_{kl} \frac{|\langle \psi_i \psi_j | V_{\text{dd}} | \psi_k \psi_l \rangle|^2}{E_k + E_l - E_i - E_j} = - \frac{C_{ij}^{(6)}}{R^6} \quad (2.27)$$

with

$$C_{ij}^{(6)} = \frac{1}{4\pi\epsilon_0} \sum_{kl} \frac{|\langle \psi_i | \mathbf{d}_1 | \psi_k \rangle \cdot \langle \psi_j | \mathbf{d}_2 | \psi_l \rangle - 3 \langle \psi_i | \mathbf{d}_1 \cdot \mathbf{n} | \psi_k \rangle \langle \psi_j | \mathbf{d}_2 \cdot \mathbf{n} | \psi_l \rangle|^2}{E_k + E_l - E_i - E_j}. \quad (2.28)$$

Thus, two atoms in the state $|\psi_i \psi_j\rangle$ feel an attractive interaction if $C_{ij}^{(6)} > 0$ and a repulsive interaction if $C_{ij}^{(6)} < 0$. This interaction is called the *van der Waals interaction*.

In Rydberg states, i.e. states with a large principal quantum number, the van der Waals interaction is particularly strong, typically many orders of magnitude larger than in the ground state. This is because the numerator in Eq. (2.28) is large, since in Rydberg states the electron is far away from the core, leading to a large transition dipole moment. At the same time the denominator in Eq. (2.28) is small, since the energy difference between Rydberg states becomes smaller and smaller as the atom approaches ionization. Together, these effects lead to an impressive scaling $C^{(6)} \propto n^{11}$ with the principal quantum number n [12].

Fig. 2.2 visualizes the van der Waals interaction by showing the eigenenergies ΔE of some of the eigenstates of the two-atom Hamiltonian H for two Cesium atoms, relative to the energy of the $|75s, 75s\rangle$ Rydberg pair state at an interatomic distance $R = \infty$. The red color shows the overlap of the $|75s, 75s\rangle$ state with the different eigenstates. As R decreases away from ∞ , the van der Waals interaction leads to

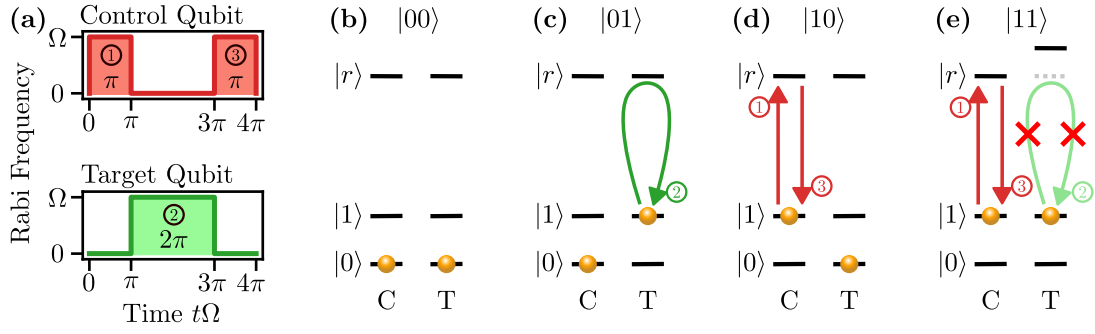


Figure 2.3: The π - 2π - π protocol. (a) Pulse sequence applied on the control and target atom. (b-e) Action of the gate on the computational basis states $|00\rangle$, $|01\rangle$, $|10\rangle$ and $|11\rangle$.

an upward shift of the energy of the $|75s, 75s\rangle$ state. For low enough distances, here around $R \approx 3 \mu\text{m}$, the perturbative approximation starts to break down, and different states start to mix. Due to the many crossing states, this is often referred to as the *spaghetti regime*, and typically avoided in a quantum computation.

An important consequence of the strong van der Waals interaction between Rydberg states is the *Rydberg blockade effect*: Suppose we use a laser (or two lasers in a two-photon transition), to excite atoms to a Rydberg state. Once one atom is excited, the energy of the Rydberg state of all other atoms is shifted by $B = -C^{(6)}/R^6$. If the interaction strength $|B|$ is much larger than the Rabi frequency of the laser, this prevents the excitation of further atoms, i.e. the excitation of these atoms is *blockaded*. As we will see in the subsequent sections, the Rydberg blockade effect plays a crucial role in the implementation of quantum gates on neutral atoms.

2.5.2 The π - 2π - π Protocol

In 2000, the first protocol for using the Rydberg blockade to implement a CZ gate was proposed [64]. This protocol, visualized in Fig. 2.3, models each atom as a three-level system with the computational basis states $|0\rangle$ and $|1\rangle$ and the Rydberg state $|r\rangle$. The states $|1\rangle$ and $|r\rangle$ can be coupled by a laser (or a two-photon transition) with Rabi frequency Ω . The protocol then works in three steps [Fig. 2.3(a)]: First, a pulse with pulse area π is applied on one of the two atoms, designated the control atom. Then, a pulse with pulse area 2π is applied on the other atom, designated the target atom. Finally, another pulse with pulse area π is applied on the control atom. In reference to the pulse durations, this protocol is often called the π - 2π - π protocol.

Let us analyze the effect of these three pulses on the different initial states $|00\rangle$, $|01\rangle$, $|10\rangle$ and $|11\rangle$ of the atoms:

- For the initial state $|00\rangle$ [Fig. 2.3(b)], none of the three pulses has any effect on the atoms, since only $|1\rangle$ is coupled to $|r\rangle$.

- For the initial state $|01\rangle$ [Fig. 2.3(c)], the pulses on the control atom have no effect, while the pulse on the target atom excites it to $|r\rangle$ and de-excites it back to $|1\rangle$, leading to $|01\rangle \mapsto -|01\rangle$.
- For the initial state $|01\rangle$ [Fig. 2.3(d)], only the pulses on the control atom have an effect. They lead to the evolution $|10\rangle \mapsto -i|r0\rangle \mapsto -|10\rangle$
- For the initial state $|11\rangle$ [Fig. 2.3(e)], the first pulse excites the control atom to $|r\rangle$, i.e. $|11\rangle \mapsto -i|r1\rangle$. Due to the Rydberg blockade effect, the second pulse is now unable to excite the target atom and instead leaves the state unchanged. Finally, the last pulses de-excites the control atom back to $|1\rangle$, leading to $|11\rangle \mapsto -|11\rangle$.

The unitary implemented by this pulse sequence is thus

$$U = |00\rangle\langle 00| - |01\rangle\langle 01| - |10\rangle\langle 10| - |11\rangle\langle 11|. \quad (2.29)$$

This is, up to a single qubit Z gate on each qubit, equivalent to a CZ gate.

A major advantage of the π - 2π - π gate is that it is independent of the exact interaction strength, and thus of the exact distance, between the atoms, as long as the interaction is large enough to guarantee the Rydberg blockade. A major disadvantage is that different pulses have to be applied to the control and the target atom. In the next section we will discuss a significant improvement, where both atoms are subjected to the same pulse.

2.5.3 The Levine-Pichler Protocol

The first protocol to implement a CZ gate with just one global pulse was proposed in 2019 [18] and is now known as the Levine-Pichler (LP) protocol. As in the π - 2π - π protocol, the LP protocol models each atom as a three level system with states $|0\rangle$, $|1\rangle$ and $|r\rangle$. Now a global laser pulse with Rabi frequency $\Omega(t)$ is applied on both atoms [Fig. 2.4(a)], leading to the level scheme shown in Fig. 2.4(b). Crucially, the Rabi frequency $\Omega(t) = |\Omega(t)|e^{i\varphi(t)}$ is not only characterized by its amplitude $|\Omega(t)|$, but also by its phase $\varphi(t)$, giving two ways to control the evolution of the atom.

To understand the LP gate, it is useful to rewrite the level scheme as shown in Fig. 2.4(c): Atoms starting in state $|00\rangle$ are completely unaffected by the global laser. The initial state $|01\rangle$ couples only to $|0r\rangle$ with Rabi frequency $\Omega(t)$, while symmetrically $|10\rangle$ couples only to $|r0\rangle$. Finally, the Hamiltonian describing the evolution of $|11\rangle$ can be written as

$$\begin{aligned} H_{11} &= \frac{\Omega(t)}{2} (|11\rangle\langle 1r| + |11\rangle\langle r1| + |1r\rangle\langle rr| + |r1\rangle\langle rr|) + \text{h.c.} + B|r\rangle\langle rr| \quad (2.30) \\ &= \frac{\sqrt{2}\Omega}{2} (|11\rangle\langle W| + |W\rangle\langle rr|) + B|r\rangle\langle rr| \end{aligned}$$

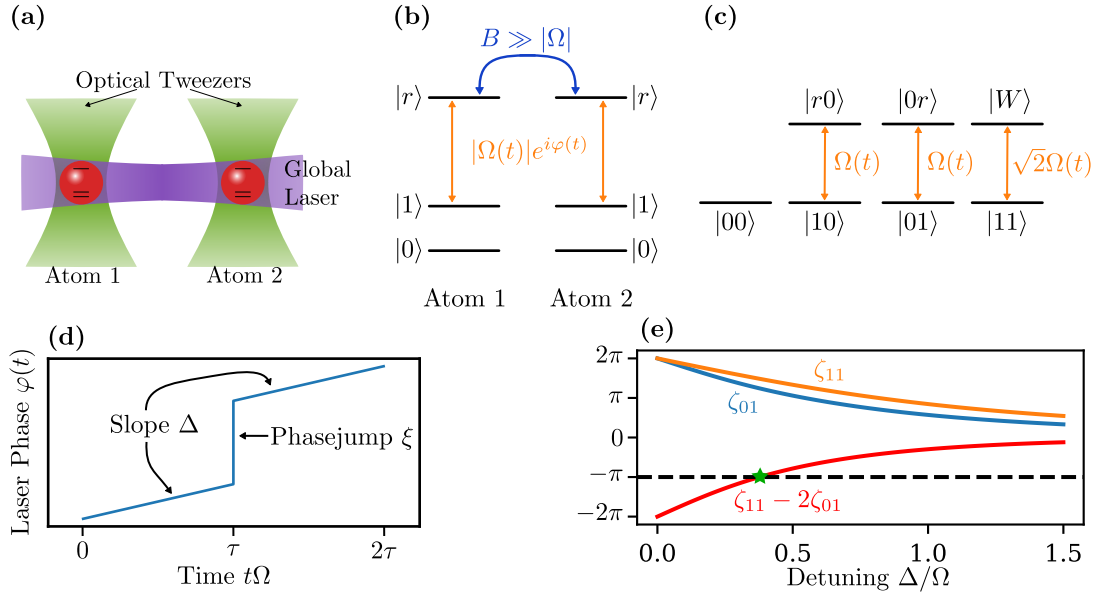


Figure 2.4: The Levine-Pichler Protocol. (a) Two atoms trapped in optical tweezers are addressed by a single global laser to implement a CZ gate. (b) Level scheme assumed by the LP gate. (c) Rewritten level scheme to show the evolution of the four computational basis states $|00\rangle$, $|01\rangle$, $|10\rangle$ and $|11\rangle$. (d) Laser phase as a function of time for the LP gate. The laser phase depends to the pulse duration τ , the detuning Δ , and the phasejump ξ . (e) Phase ζ_{01} (blue) and ζ_{11} (orange) picked up by the states $|01\rangle$ and $|11\rangle$, respectively, as the function of the detuning Δ . The red line shows $\zeta_{11} - 2\zeta_{01}$. The detuning where this quantity equals $-\pi$ (green star) is the value necessary to implement a CZ gate.

with the *bright state* $|W\rangle = (|1r\rangle + |r1\rangle)/\sqrt{2}$. In the limit $B \gg |\Omega|$ of the Rydberg blockade the $|rr\rangle$ state can even be neglected, so that also the evolution of $|11\rangle$ is described by a two level system, however with an enhanced Rabi frequency $\sqrt{2}\Omega(t)$.

As we will see in the remainder of this thesis, there exist many pulses $\Omega(t)$ that implement a CZ gate in this setup. In the LP protocol, a particularly simple pulse shape is chosen, making the analysis of the protocol analytically tractable: The amplitude is always chosen constant as $|\Omega(t)| = \Omega_0$, while the phase $\varphi(t)$ is given by the curve shown in Fig. 2.4(d), parameterized by the three parameters Δ , τ and ξ . The phase first linearly increases with a slope of Δ (equivalent to a constant laser detuning of Δ) for a duration τ . Then, the laser phase makes a discontinuous jump by ξ , followed by another linearly increasing piece with slope Δ and duration τ .

It can be shown [18] that by choosing

$$\tau = \frac{2\pi}{\sqrt{2\Omega_0^2 + \Delta^2}} \quad (2.31)$$

and

$$e^{-i\xi} = \frac{-\sqrt{\Omega_0^2 + \Delta^2} \cos \alpha + i\Delta \sin \alpha}{\sqrt{\Omega_0^2 + \Delta^2} \cos \alpha + i\Delta \sin \alpha} \quad (2.32)$$

with $\alpha = \sqrt{\Omega^2 + \Delta^2}\tau/2$, the pulse acts as

$$|01\rangle \mapsto e^{i\zeta_{01}} |01\rangle \quad (2.33)$$

$$|11\rangle \mapsto e^{i\zeta_{11}} |11\rangle. \quad (2.34)$$

The phases ζ_{01} and ζ_{11} are shown as a function of Δ in Fig. 2.4(e) as the blue and orange line, respectively. Since single qubit gates are often easy to implement, we are interested in implementing a up to single qubit gates, i.e. a gate with $\zeta_{01} = \theta$ and $\zeta_{11} = 2\theta + (2k + 1)\pi$ for some single qubit phase θ and some integer k . The condition of implementing a CZ gate up to single qubit gates is thus

$$\zeta_{11} - 2\zeta_{01} = (2k + 1)\pi. \quad (2.35)$$

The red curve in Fig. 2.4(d) shows that $\zeta_{11} - 2\zeta_{01}$ (red line) intersects $-\pi$ (black dashed line) at a crossing point (green star), which can be determined to be at $\Delta/\Omega = 0.377371$. Thus, for this value of the Δ the LP protocol implements a CZ gate.

2.5.4 Other Gate Protocols

Next to the π - 2π - π protocol and the LP protocol, many other gate protocols have been proposed, which we will briefly review in this section. An extension of the π - 2π - π protocol to multi-controlled C_kZ gates is discussed in Ref. [107]. In Ref. [108], a variant of the π - 2π - π protocol using a dark state formed by the superposition of two Rydberg states is proposed and shown to have a lower error due to Rydberg decay and effects of a finite interaction strength B . In Ref. [109] it is proposed to use shaped pulses in the π - 2π - π protocol to prevent the excitation of Rydberg states *other* than the targeted one. Similar to the LP protocol, the protocols in Refs. [110, 111] require only a global laser but, in contrast to the LP protocol, operate using adiabatic evolution of the atoms.

Instead of operating in the Rydberg blockade limit of large interaction strengths, it is also possible to operate in the opposite limit of an interaction strength much smaller than the Rabi frequency. A simple gate protocol in this regime has already been proposed in the original Ref. [64]. There are extensions of this scheme to transitions implemented via stimulated Raman adiabatic passage (STIRAP) [112] or to using an adiabatic passage through a Förster resonance [113]. In Ref. [114] a so-called ultra-fast gate with a Rabi frequency several orders of magnitude above the interaction strength between the atoms has been experimentally implemented in ^{87}Rb atoms.

Finally, there are also proposals for implementing gates on ensembles of atoms [115–117], for using Rydberg dressing [118–120], and for implementing holonomic gates [121].

3 Time-Optimal Two- and Multi-Qubit Gates on Rydberg Atoms

Quantum gates that can create entanglement between two or more qubits are a crucial component of any quantum computing architecture. For the neutral atom platform, the most popular method of implementing gates on two or more qubits is by coupling one computational basis state of each atom to one or more Rydberg states using a laser, and then using the strong van der Waals interaction between Rydberg atoms to generate entanglement. A large number of different gate protocols with different advantages and drawbacks that can be used for this purpose (see Sec. 2.5) [18, 64, 108–110, 112, 113, 115–118, 121–127]. Which of these gate protocols will achieve the highest gate fidelity in an experiment depends on the details of the experimental setup and the dominant error sources. However, two properties of a gate protocol are particularly desirable: *i)* The gate protocol should only require global control lasers addressing all atoms simultaneously. This significantly reduces the experimental complexity compared to protocols which require individual addressing of the atoms. *ii)* The gate protocol should be fast, because, independently of the exact error model, many error sources can be mitigated by short gate durations. It is thus a fundamental question to find the fastest possible, so called *time-optimal* [128–131], global gate protocol that implements a given quantum gate.

In this chapter we answer this question for the controlled-Z (CZ) gate and several of its generalizations on two or more qubits. We assume a simple level scheme in which we model each atom as a three level system consisting of the two computational basis states and one Rydberg state [64]. A laser with *time-dependent* Rabi frequency $\Omega(t)$ coupling one of the computational basis states to the Rydberg state is then used to implement the desired gate. While a variety of different pulses $\Omega(t)$ can implement the same gate, we use the quantum optimal control method of gradient ascent pulse engineering (GRAPE) [132] to select the time-optimal one.

For the CZ gate, we find that the time-optimal protocol is approximately 10% faster than the fastest previously known protocol, the Levine-Pichler protocol [18] (See Sec. 2.5.3). More importantly however, the time-optimal pulse can be implemented using a *smooth* pulse $\Omega(t)$, while the LP protocol requires a discontinuous jump in the laser phase. This significantly simplifies the experimental implementation of the time-optimal protocol compared to the LP protocol. It is this feature of the time-optimal protocol that has led to its widespread adoption in many experiments [13, 14, 16, 17], achieving fidelities up to 99.5% [13], the highest fidelity currently reported for the neutral atom platform.

While the CZ gate is the most relevant two-qubit entangling gate on the Rydberg platform, we also use our time-optimal methodology to find pulses that implement arbitrary controlled phase gates on two qubits, or phase gates on three or more qubits, such as multi-controlled Z (C_kZ) gates or gates used for the generation of GHZ states. In all cases we find smooth and easy to implement pulse shapes $\Omega(t)$. Note that for quantum gates on three and more qubits, which can be implemented natively on the Rydberg platform [18, 107, 116], the time-optimal protocols derived in this chapter are first protocols that can be implemented with a *global* pulse.

This chapter is structured as follows: Sec. 3.1 precisely formulates the problem of finding time-optimal pulses. In Sec. 3.2 we introduce the GRAPE algorithm, and use it in Sec. 3.3 to find the time-optimal protocol that implements a CZ gate under a perfect Rydberg blockade. The condition of a perfect Rydberg blockade is lifted in Sec. 3.4. Finally we turn to gates beyond the CZ gate and discuss controlled phase gates in Sec. 3.5, multi-controlled C_kZ gates in Sec. 3.6 and a protocol to generate GHZ states in Sec. 3.7.

Many results of this chapter have been published in Ref. [23], the results of Sec. 3.7 have been published in Ref. [17]. We would also like to draw the attention of the reader to Ref. [127], where a variant of the time-optimal pulse has been developed independently.

3.1 Problem Formulation

In the following we precisely define the setup that we consider (Sec. 3.1.1) and define the gate fidelity, which we will use to measure the quality of a gate (Sec. 3.1.2). Finally we provide a set of symmetry operations which map a gate protocol to other gate protocols implementing the same or a related quantum gate (Sec. 3.1.3).

3.1.1 Level Scheme and Hamiltonian

3.1.1.1 General Case

We consider N atoms and model each of them as a three level system with two computational basis states $|0\rangle$, $|1\rangle$ and the Rydberg state $|r\rangle$ [64]. We assume a time-independent interaction B_{jk} between atoms j and k which shifts the energy of states with both atoms in the Rydberg state. This is described by the diagonal interaction Hamiltonian

$$H_{\text{int}} = \sum_{j < k} B_{jk} |r_j r_k\rangle \langle r_j r_k|. \quad (3.1)$$

We furthermore assume that the states $|1_j\rangle$ and $|r_j\rangle$ are coupled by a laser pulse with a time-dependent complex Rabi frequency $\Omega_j(t) = |\Omega_j(t)|e^{i\varphi_j(t)}$ with amplitude

$|\Omega_j(t)|$ and phase $\varphi(t)$. In any experiment, the maximal achievable Rabi frequency $|\Omega_j(t)|$ is limited by the laser power and waist diameter. To include this into the model, we introduce the maximum Rabi frequency Ω_{\max} and consider only pulses with $|\Omega_j(t)| \leq \Omega_{\max}$ for the rest of this thesis. In the rotating frame and under the rotating wave approximation the action of the laser is described by the driving Hamiltonian ($\hbar = 1$)

$$H_{\text{drive}}(t) = \sum_{j=1}^N \frac{\Omega_j(t)}{2} |1_j\rangle \langle r_j| + \text{h.c.} \quad (3.2)$$

The total Hamiltonian is then given by

$$H(t) = H_{\text{int}} + H_{\text{drive}}(t). \quad (3.3)$$

Note that the states $|1\rangle$ and $|r\rangle$ can also be coupled by a two-photon transition, in which case $\Omega_j(t)$ denotes the effective Rabi frequency.

Our goal is now to find a pulse $\Omega_1(t), \dots, \Omega_N(t)$ that implements a desired quantum gate. For this it is necessary to calculate the evolution of all computational basis states $|q\rangle$ ($q \in \{0, 1\}^N$) under the time dependent Schrödinger equation (TDSE) $|\dot{\psi}\rangle = -iH|\psi\rangle$. An important property of our setup is that the state $|0\rangle$ of any atom is not coupled to any other state. To formalize this, we consider the family $(P_q)_q$ of projectors, where for $q \in \{0, 1\}^N$ the operator P_q denotes the projector onto the space \mathcal{H}_q spanned by all states in which atom j is in state $|0\rangle$ if $q_j = 0$ and in state $|1\rangle$ or $|r\rangle$ if $q_j = 1$. For example, for $N = 2$ atoms we obtain $P_{00} = |00\rangle \langle 00|$, $P_{01} = |01\rangle \langle 01| + |0r\rangle \langle 0r|$, $P_{10} = |10\rangle \langle 10| + |r0\rangle \langle r0|$ and $P_{11} = |11\rangle \langle 11| + |1r\rangle \langle 1r| + |r1\rangle \langle r1| + |rr\rangle \langle rr|$. Crucially, H is block diagonal with respect to the P_q , i.e.

$$H = \sum_q H_q \quad \text{with } H_q = P_q H P_q. \quad (3.4)$$

To calculate the evolution of a computational basis state $|q\rangle$, it is thus sufficient to only consider H_q and not the whole Hamiltonian H . Hence, for each of the 2^N different values of q we have to solve the TDSE for the 2^{n_q} dimensional Hamiltonian H_q , where $n_q = \sum_j q_j$ is the number of atoms that start in state $|1\rangle$. In Secs. 3.1.1.2 and 3.1.1.3 below we will see that both the number of TDSEs and the dimension of each TDSE can be reduced if we consider certain symmetries.

Note that Eq. (3.2) does not explicitly consider a detuning of the laser, since such a detuning can already be described by a time-dependent phase. To see this, assume that on a single atom the drive Hamiltonian would be given by

$$H'_{\text{drive}} = -\Delta(t) |r\rangle \langle r| + \frac{\Omega(t)}{2} |1\rangle \langle r| + \text{h.c.} \quad (3.5)$$

for a laser detuning $\Delta(t)$. We can switch into a time-dependent frame given by the basis transformation

$$V(t) = |0\rangle \langle 0| + |1\rangle \langle 1| + \exp\left(-i \int_0^t dt' \Delta(t')\right) |r\rangle \langle r|. \quad (3.6)$$

In this new frame, the Hamiltonian is given by

$$H_{\text{drive}} = V H'_{\text{drive}} V^\dagger + i\dot{V}V^\dagger = \frac{1}{2}\Omega(t) \exp\left(i \int_0^t dt' \Delta(t')\right) |1\rangle \langle r| + \text{h.c.} \quad (3.7)$$

Thus, a detuning $\Delta(t)$ can be accounted for by modifying the laser phase as $\varphi(t) \mapsto \varphi(t) + \int_0^t dt' \Delta(t')$. Reversely, we can always switch into a frame with a constant laser phase by modifying the detuning as $\Delta(t) \mapsto \Delta(t) + d\varphi(t)/dt$. For $N > 1$ atoms the same argument applies analogously, since H_{int} commutes with U . Furthermore, since V acts like the identity on the computational subspace spanned by $|0\rangle$ and $|1\rangle$, the Hamiltonians H_{drive} and H'_{drive} implement exactly the same quantum gates.

3.1.1.2 Permutation Symmetric Case

A particularly important case is obtained if all Rabi frequencies and all interaction strengths are equal, i.e. if $\Omega_1(t) = \dots = \Omega_N(t) =: \Omega(t)$ and $B_{12} = \dots = B_{N-1,N} := B$. Equal Rabi frequencies are naturally obtained if all atoms are addressed with a single global laser, which is experimentally significantly simpler than individual addressing of the atoms. Note that a constant phase difference between the Rabi frequency of any two atoms j and k , i.e. $\Omega_j(t) = e^{i\alpha} \Omega_k(t)$ for a constant phase α , can be compensated by the basis transformation $|r_j\rangle \mapsto e^{-i\alpha} |r_j\rangle$ and is thus still captured by the case of equal Rabi frequencies. The condition of equal interaction strength is trivially satisfied for $N = 2$ atoms, and can be achieved for $N = 3$ or $N = 4$ atoms by aligning the atoms in the shape of an equilateral triangle or a regular tetrahedron, respectively.

To understand the evolution of an initial computational basis state $|q\rangle$ ($q \in \{0, 1\}^N$) we consider the Dicke states $|D_{q,m}\rangle$ [133], defined as equal superposition of all basis states in \mathcal{H}_q with exactly m atoms in state $|r\rangle$, for $0 \leq m \leq n_q = \sum_j q_j$. Formally, $|D_{q,m}\rangle$ is given by

$$|D_{q,m}\rangle = \frac{1}{\sqrt{|\mathcal{S}_{q,m}|}} \sum_{s \in \mathcal{S}_{q,m}} |s\rangle \quad (3.8)$$

with

$$\mathcal{S}_{q,m} = \left\{ s \in \{0, 1, r\}^N \mid s_j = r \text{ exactly } m \text{ times and } \forall j s_j = 0 \Leftrightarrow q_j = 0 \right\}. \quad (3.9)$$

If the atoms start in the initial state $|q\rangle$, the state at any later time can be written as a superposition of the $|D_{q,m}\rangle$. Hence it is useful to express the Hamiltonian H_q in this basis.

The interaction Hamiltonian acts on $|D_{q,m}\rangle$ as $H_{\text{int}} |D_{q,m}\rangle = \binom{m}{2} B |D_{q,m}\rangle$, where for $m \geq 2$ $\binom{m}{2} = m!/[2(m-2)!]$ denotes the binomial coefficient and we use the convention $\binom{m}{2} = 0$ if $m < 2$. To calculate the matrix elements of H_{drive} we note that an application of H_{drive} changes the number of atoms in $|r\rangle$ by ± 1 , so

$\langle D_{q,m} | H_{\text{drive}} | D_{q,m'} \rangle = 0$ unless $m' = m \pm 1$. For the remaining matrix elements we obtain

$$\langle D_{q,m+1} | H_{\text{drive}} | D_{q,m} \rangle = \frac{\Omega^*(t)}{2} \frac{|S_{q,m}|(n_q - m)}{\sqrt{|S_{q,m}||S_{q,m+1}|}} = \sqrt{(m+1)(n_q - m)} \frac{\Omega^*(t)}{2} \quad (3.10)$$

where the first equality follows because each of the $|S_{q,m}|$ terms in $|D_{q,m}\rangle$ can be excited to a term in $|D_{q,m+1}\rangle$ by $n_q - m$ terms in H_{drive} , and the second equality follows from $|S_{q,m}| = \binom{n_q}{m} = n_q!/[m!(n_q - m)!]$.

Thus, the Hamiltonian H_q in the permutation symmetric case can be simplified to an $n_q + 1$ dimensional Hamiltonian

$$H_q = B \sum_{m=0}^{n_q} \binom{m}{2} |D_{q,m}\rangle \langle D_{q,m}| + \frac{\Omega(t)}{2} \sum_{m=0}^{n_q-1} \sqrt{(m+1)(n_q - m)} |D_{q,m}\rangle \langle D_{q,m+1}| + \text{h.c.} \quad (3.11)$$

Note that even so q can take 2^N different values there are, up to relabeling the basis states, only $N + 1$ different Hamiltonian H_q , one for each value of n_q . Thus we can find the evolution of each computational basis state $|q\rangle$ by only solving $N + 1$ TDSEs with dimensions $1, 2, \dots, N + 1$ respectively. For example, for $N = 2$ atoms the three Hamiltonians are given by

$$H_{00} = 0 \quad (3.12)$$

$$H_{01} = \frac{\Omega(t)}{2} |D_{01,0}\rangle \langle D_{01,1}| + \text{h.c.} \quad (3.13)$$

$$H_{11} = B |D_{11,2}\rangle \langle D_{11,2}| + \frac{\sqrt{2}\Omega(t)}{2} [|D_{11,0}\rangle \langle D_{11,1}| + |D_{11,1}\rangle \langle D_{11,2}|] + \text{h.c.} \quad (3.14)$$

with $|D_{01,0}\rangle = |01\rangle$, $|D_{01,1}\rangle = |0r\rangle$, $|D_{11,0}\rangle = |11\rangle$, $|D_{11,1}\rangle = (|1r\rangle + |r1\rangle)/\sqrt{2}$ and $|D_{11,2}\rangle = |rr\rangle$.

3.1.1.3 The Rydberg Blockade Limit

A second particularly important case is that of equal Rabi frequencies $\Omega_1(t) = \dots = \Omega_N(t) =: \Omega(t)$ and interaction strengths $B_{jk} \gg |\Omega(t)|$ for all j, k . Note that in contrast to Sec. 3.1.1.2 here we do not require that all B_{jk} are equal, making this case easily experimentally accessible. In the $B_{jk} \gg |\Omega(t)|$ case only states with zero or one atoms in the Rydberg state $|r\rangle$ can be accessed when starting in a computational basis state (Rydberg blockade). Thus Eq. (3.11) can be reduced to the states $|D_{q,0}\rangle = |q\rangle$ and $|D_{q,1}\rangle =: |W_q\rangle$ and we obtain

$$H_q = \frac{\sqrt{n_q}\Omega(t)}{2} |q\rangle \langle W_q| + \text{h.c.} \quad (3.15)$$

To find the evolution of each computational basis state we thus only have to solve N TDSEs of dimension 2 each (note that the $n_q = 0$ case of dimension 1 is trivial).

In summary, we have defined the Hamiltonian H_q [Eq. (3.4)] that governs the evolution of an initial basis state $|q\rangle$ under a laser pulse $\Omega_1(t), \dots, \Omega_N(t)$, and discussed simplifications for the case of a global laser pulse [Eq. (3.11)] and in the Rydberg blockade limit [Eq. (3.15)].

3.1.2 Time-Optimal Problem and Gate Fidelity

With the Hamiltonian $H(t)$ defined in the previous section [(Eq. (3.3))] we can now precisely state the problem that we will solve in this chapter:

Time-Optimal Problem: Given a target unitary U_{target} on the computational subspace, find the minimal T such that there exists a pulse $\Omega_1, \Omega_2, \dots, \Omega_N : [0, T] \rightarrow \mathbb{C}$ with $|\Omega_j(t)| \leq \Omega_{\text{max}}$ for all t such that $\Pi U \Pi = U_{\text{target}}$ up to a global phase, where

$$U = \tau \exp \left(-i \int_0^T H(t) dt \right) \quad (3.16)$$

is the unitary implemented by the pulse $\Omega_1, \dots, \Omega_N$ and $\Pi = \sum_{q \in \{0,1\}^N} |q\rangle \langle q|$ is the projector onto the computational subspace. Here and in the following $\tau \exp$ denotes the time ordered exponential.

Note that since H does not couple the state $|0\rangle$, it is only possible to solve the time-optimal problem for diagonal *phase gates*, i.e. gates of the form

$$U_{\text{target}} = \sum_{q \in \{0,1\}^N} e^{i\zeta_q} |q\rangle \langle q| \quad (3.17)$$

for phases $(\zeta_q)_{q \in \{0,1\}^N}$.

To solve the time-optimal problem it is useful to have a measure of how much U and U_{target} differ. The average gate fidelity, which we introduce in the remainder of this section, will serve as such a measure. It is defined as

$$F = \int_{\mathcal{C}} d|\psi\rangle \left| \langle \psi | U_{\text{target}}^\dagger U |\psi\rangle \right|^2 \quad (3.18)$$

where \mathcal{C} denotes the manifold of all normalized computational states and $d|\psi\rangle$ denotes the normalized Haar measure on \mathcal{C} . A fidelity $F = 1$ corresponds to an exact implementation of U up to a physically unimportant global phase, i.e. $U = e^{i\alpha} U_{\text{target}}$ for some α .

The integral in Eq. (3.18) can be evaluated to [134]

$$F = \frac{1}{2^N(2^N + 1)} \left[\left| \text{tr} \left(U_{\text{target}}^\dagger \Pi U \Pi \right) \right|^2 + \text{tr} \left(U_{\text{target}}^\dagger \Pi U \Pi \right) \right]. \quad (3.19)$$

In the following we denote by $|\psi_q(t)\rangle$ the solution of the TDSE $|\dot{\psi}_q\rangle = -iH_q|\psi_q\rangle$ with $|\psi_q(0)\rangle = |q\rangle$. Since $|\psi_q(t)\rangle$ is in \mathcal{H}_q for all t and $|q\rangle$ is the only computational basis state in $|q\rangle$ it follows that

$$\Pi U \Pi = \sum_{q \in \{0,1\}^N} \langle q | \psi_q(T) \rangle |q\rangle \langle q| \quad (3.20)$$

so that

$$F = \frac{1}{2^N(2^N + 1)} \left[\left| \sum_{q \in \{0,1\}^N} e^{-i\bar{\zeta}_q} \langle q | \psi_q(T) \rangle \right|^2 + \sum_{q \in \{0,1\}^N} |\langle q | \psi_q(T) \rangle|^2 \right] \quad (3.21)$$

For the permutation symmetric cases discussed in Secs. 3.1.1.2 and 3.1.1.3 it is sufficient to consider the initial states $|q^{(m)}\rangle = |0\dots 0, 1\dots 1\rangle$ with m atoms in state $|1\rangle$. In this case, only permutation symmetric phase gates with $\zeta_q =: \bar{\zeta}_{n_q}$ are possible, and we obtain the fidelity

$$F = \frac{1}{2^N(2^N + 1)} \left[\left| \sum_{m=0}^N \binom{N}{m} e^{-i\bar{\zeta}_m} \langle q^{(m)} | \psi_{q^{(m)}}(T) \rangle \right|^2 + \sum_{m=0}^N \binom{N}{m} |\langle q^{(m)} | \psi_{q^{(m)}}(T) \rangle|^2 \right] \quad (3.22)$$

As an alternative to the average gate fidelity, the Bell state fidelity defined as

$$F_{\text{Bell}} = \frac{1}{4^N} \left| \sum_{q \in \{0,1\}^N} e^{-i\bar{\zeta}_q} \langle q | \psi_q(T) \rangle \right|^2 = \left| \langle \psi | U_{\text{target}}^\dagger U | \psi \rangle \right|^2 \quad (3.23)$$

with $|\psi\rangle = 2^{-N/2} \sum_q |q\rangle$ is often considered. Its name arises because for $N = 2$ it measures the fidelity with which a two atom Bell state $(|00\rangle + |11\rangle)/\sqrt{2}$ can be prepared using for a CZ gate ($\bar{\zeta}_0 = \bar{\zeta}_1 = 0, \bar{\zeta}_2 = \pi$) and single qubit gates applied to an initial product state. In this thesis we use, unless otherwise notes, the average gate fidelity F , but very similar results are expected with the Bell state fidelity F_{Bell} instead. In particular, a gate has an average gate fidelity of 1 if and only if it has a Bell state fidelity of 1.

In summary, we have defined the average gate fidelity $1 - F$ and provided explicit formulas for evaluating it for the general [Eq. (3.21)] and the permutation symmetric [Eq. (3.22)] case.

3.1.3 Symmetry Operations

Given a pulse that implements a certain phase gate, we can find a related pulse that implements the same or a related phase gate by a combination of several symmetry operations. Thus, the time-optimal pulses found later in this chapter are only unique

up to these symmetries. In this section we consider the symmetry operations of phase shifts, time reversal, and complex conjugation.

Let $\Omega_1(t), \dots, \Omega_N(t)$ be a pulse of duration T that for interaction strengths B_{jk} implements a $(\zeta_q)_q$ phase gate. We will construct several pulses $\bar{\Omega}_1(t), \dots, \bar{\Omega}_N(t)$ that for interaction strengths \bar{B}_{jk} implement a $(\bar{\zeta}_q)_q$ phase gate. We denote by $\bar{H}(t)$ the Hamiltonian from Eq. (3.3) with $\bar{\Omega}_1(t), \dots, \bar{\Omega}_N(t)$ and \bar{B}_{jk} and by $|\bar{\psi}_q(t)\rangle$ the solution of the TDSE given by \bar{H} with initial state $|q\rangle$.

The three symmetry operations act as follows:

- i) Phase shifts:* Consider $\bar{\Omega}_j(t) = e^{i\alpha_j}\Omega_j(t)$ for constants $\alpha_1, \dots, \alpha_N$ and $\bar{B}_{jk} = B_{jk}$. This implements a $\bar{\zeta}_q = \zeta_q$ phase gate. To see this, note that $|\bar{\psi}_q(t)\rangle = V|\psi_q(t)\rangle$ with

$$V = \bigotimes_{j=1}^N (|0\rangle\langle 0| + |1\rangle\langle 1| + e^{-i\alpha_j}|r\rangle\langle r|). \quad (3.24)$$

Since $|\psi_q(T)\rangle = e^{i\zeta_q}|q\rangle$ it follows that also $|\bar{\psi}_q(T)\rangle = e^{i\zeta_q}|q\rangle$, so \bar{H} implements a $(\zeta_q)_q$ phase gate.

- ii) Time reversal:* Consider $\bar{\Omega}_j(t) = \Omega_j(T-t)$ and $\bar{B}_{jk} = -B_{jk}$. This implements a $\bar{\zeta}_q = -\zeta_q$ phase gate. To see this, first consider $\bar{\Omega}_j(t) = -\Omega_j(T-t)$ and $\bar{B}_{jk} = -B_{jk}$, so that we obtain $\bar{H}(t) = -H(T-t)$. The solution of the TDSE under \bar{H} is given by

$$|\bar{\psi}_q(t)\rangle = e^{-i\zeta_q}|\psi_q(T-t)\rangle \quad (3.25)$$

since $|\bar{\psi}_q(0)\rangle = |q\rangle$ and

$$|\dot{\bar{\psi}}_q(t)\rangle = ie^{-i\zeta_q}H(T-t)|\psi_q(T-t)\rangle = -i\bar{H}(t)|\bar{\psi}_q(t)\rangle \quad (3.26)$$

Thus we have $|\bar{\psi}_q(T)\rangle = e^{-i\zeta_q}|q\rangle$, so the pulse $\bar{\Omega}_j(t) = -\Omega_j(T-t)$ implements a $\bar{\zeta}_q = -\zeta_q$ phase gate. By the symmetry under phase shifts it follows that also the pulse $\bar{\Omega}_j(t) = \Omega_j(T-t)$ implements a $\bar{\zeta}_q = -\zeta_q$ phase gate.

- iii) Complex conjugation:* Consider $\bar{\Omega}_j(t) = \Omega_j(t)^*$ and $\bar{B}_{jk} = -B_{jk}$. This implements a $\bar{\zeta}_q = -\zeta_q$ phase gate. To see this, we first consider the joint complex conjugation and time reversal symmetry $\bar{\Omega}_j(t) = \Omega_j(T-t)^*$ and $\bar{B}_{jk} = B_{jk}$, so that $\bar{H}(t) = H(T-t)^*$. The solution of the TDSE under \bar{H} is given by

$$|\bar{\psi}_q(t)\rangle = e^{i\zeta_q}|\psi_q(T-t)\rangle^* \quad (3.27)$$

since $|\bar{\psi}_q(0)\rangle = |q\rangle$ and

$$|\dot{\bar{\psi}}_q(t)\rangle = e^{-i\zeta_q}[iH(T-t)|\psi_q(T-t)\rangle]^* = -i\bar{H}(t)|\bar{\psi}_q(t)\rangle \quad (3.28)$$

Thus we have $|\bar{\psi}_q(T)\rangle = e^{i\zeta_q}|q\rangle$, so the pulse $\bar{\Omega}_j(t) = \Omega_j(T-t)^*$ implements a $\bar{\zeta}_q = \zeta_q$ phase gate. Together with time reversal symmetry it follows that the $\bar{\Omega}_j(t) = \Omega_j(t)^*$ implements a $\bar{\zeta}_q = -\zeta_q$ phase gate.

These three symmetry operations show that when using numerical methods to find the time-optimal pulse for a gate, several solutions are to be expected. Firstly, two time-optimal pulses can differ by an arbitrary constant phase. This degree of freedom can be eliminated by restricting the discussion to pulses where $\Omega_j(0)$ is real and positive, as we will do from now on. Even with this restriction there are in general two different time-optimal pulses for a given phases $(\zeta_q)_q$, related by joint complex conjugation and time reversal. In the special case of $B \gg |\Omega_j(t)|$ and for phase gates where $\zeta_q \in \{0, \pi\}$ for all q , there are in general even four different time-optimal pulses, because also individual time reversal or complex conjugation give pulses implementing the same gate. As will be apparent in Secs. 3.3–3.7, sometimes, but not always, time-optimal pulses are invariant under joint time-reversal and complex conjugation, reducing the number of distinct time-optimal pulses to two.

3.2 Gradient Ascent Pulse Engineering (GRAPE)

Quantum optimal control methods [135, 136] are a large family of numerical or analytical techniques to find the, in some sense, optimal way of steering a quantum system whose Hamiltonian depends on a set of classical controls. They have been successfully used on a variety of quantum computing platforms such as superconducting qubits [137–141], trapped ions [142, 143] and neutral atoms [69, 144–150]. In this section, we introduce the numerical quantum optimal control method of gradient ascent pulse engineering (GRAPE). GRAPE was originally developed to design pulse sequences for NMR spectroscopy [132] and has since been used on a large variety of quantum optimal control problems [131, 135–137, 151, 152]. We discuss one of the simplest possible versions of GRAPE in Sec. 3.2.1 and its application to quantum gates implemented via Rydberg states in Sec. 3.2.2. An analytical quantum optimal control method based on Pontryagin’s maximum principle (PMP) will be discussed in Chapter 4.

3.2.1 General Algorithm

In the following we describe one of the simplest versions of the GRAPE algorithm. Let us consider the following quantum optimal control problem: Let \mathcal{H} be a Hilbert space and $H(u(t))$ a Hamiltonian depending on N time-dependent *controls* $u = (u_1, \dots, u_N) : [0, T] \rightarrow \mathcal{U} \subseteq \mathbb{R}^K$. Here and in the following we consider the pulse duration T as fixed, i.e. it is not part of the optimization. We are given an initial state $|\psi_i\rangle \in \mathcal{H}$ and a target state $|\psi_f\rangle \in \mathcal{H}$. Our goal is now to find a control $u(t)$ that minimizes the cost functional

$$J[u] = |\langle \psi_f | \psi(T) \rangle|^2 \quad (3.29)$$

where $|\psi(t)\rangle$ is the solution to the TDSE

$$i\dot{|\psi(t)\rangle} = -iH(u(t))|\psi(t)\rangle \quad |\psi(0)\rangle = |\psi_i\rangle. \quad (3.30)$$

To solve this problem, we employ the GRAPE algorithm. In GRAPE, we make a piecewise constant Ansatz and describe $u(t)$ by $M \gg 1$ values $u^{(0)}, \dots, u^{(M-1)} \in \mathcal{U}$ such that $u(t) = u^{(m)}$ if $m\Delta t \leq t < (m+1)\Delta t$, with $\Delta t = T/M$. In this way, any reasonable control function $u(t)$ can be arbitrarily well approximated as $M \rightarrow \infty$. With the piecewise constant Ansatz, the cost functional $J[u]$ becomes a function $J(u^{(0)}, \dots, u^{(M-1)})$ given by

$$J(u^{(0)}, \dots, u^{(M-1)}) = |\langle \psi_f | U_{M-1} U_{M-2} \dots U_1 U_0 | \psi_i \rangle|^2 \quad (3.31)$$

where $U_m = \exp(-iH(u^{(m)})\Delta t)$. To minimize J , we can now use a gradient based minimization algorithm such as gradient descent or the Broyden-Fletcher-Goldfarb-Shanno (BFGS) method [153]. For this, we do not only need to calculate J , but also its derivatives $\partial J / \partial u_j^{(m)}$. Calculating J requires $\mathcal{O}(M)$ matrix-vector multiplications. If we would estimate all MK derivatives $\partial J / \partial u_j^{(m)}$ using a finite difference method, we would need $\mathcal{O}(M^2K)$ matrix-vector multiplications. GRAPE instead provides an efficient way to calculate all derivatives in just $\mathcal{O}(MK)$ matrix-vector multiplications, significantly speeding up the calculation of the gradient for $M \gg 1$. To calculate the derivatives $\partial J / \partial u_j^{(m)}$ using GRAPE, we first calculate

$$|\psi_0\rangle = |\psi_i\rangle \quad (3.32)$$

$$|\psi_1\rangle = U_0 |\psi_i\rangle \quad (3.33)$$

$$|\psi_2\rangle = U_1 U_0 |\psi_i\rangle \quad (3.34)$$

⋮

$$|\psi_M\rangle = U_{M-1} U_{M-2} \dots U_1 U_0 |\psi_i\rangle \quad (3.35)$$

by M matrix-vector multiplications. Then we calculate

$$|\chi_M\rangle = |\psi_f\rangle \quad (3.36)$$

$$|\chi_{M-1}\rangle = U_{M-1}^\dagger |\psi_f\rangle \quad (3.37)$$

$$|\chi_{M-2}\rangle = U_{M-2}^\dagger U_{M-1}^\dagger |\psi_f\rangle \quad (3.38)$$

⋮

$$|\chi_0\rangle = U_0^\dagger U_1^\dagger \dots U_{M-2}^\dagger U_{M-1}^\dagger |\psi_f\rangle \quad (3.39)$$

again by M matrix-vector multiplications. Note that these calculations have to be done only once for a given set of controls $u^{(0)}, \dots, u^{(M-1)}$, and do not have to be repeated for every derivative $\partial J / \partial u_j^{(m)}$. Now we have

$$J = |\langle \chi_0 | \psi_0 \rangle|^2 = |\langle \chi_1 | \psi_1 \rangle|^2 = \dots = |\langle \chi_M | \psi_M \rangle|^2 \quad (3.40)$$

$$= |\langle \chi_1 | U_0 | \psi_0 \rangle|^2 = |\langle \chi_2 | U_1 | \psi_1 \rangle|^2 = \dots = |\langle \chi_M | U_{M-1} | \psi_{M-1} \rangle|^2 \quad (3.41)$$

To calculate a given derivative $\partial J / \partial u_j^{(m)}$ we use that neither $|\psi_m\rangle$ nor $|\chi_{m+1}\rangle$ depend on $u_j^{(m)}$. Thus we obtain

$$\frac{\partial J}{\partial u_j^{(m)}} = \frac{\partial |\langle \chi_{m+1} | U_m | \psi_m \rangle|^2}{\partial u_j^{(m)}} = 2\text{Re} \left(\langle \chi_{m+1} | U_m | \psi_m \rangle^* \left\langle \chi_{m+1} \left| \frac{\partial U_m}{\partial u_j^{(m)}} \right| \psi_m \right\rangle \right) \quad (3.42)$$

which can be calculated in $\mathcal{O}(1)$ matrix-vector multiplications. Since there are MK derivatives to be calculated, this requires a total of $\mathcal{O}(MK)$ matrix-vector multiplications. The required derivative $\partial U_m / \partial u_j^{(m)}$ can either be calculated using a finite difference method or using analytical approaches (see Sec. 3.2.2).

3.2.2 Application to Rydberg Atoms

Now we will adapt the simple version of GRAPE presented in the previous section to maximize the fidelity F (see Eq. (3.21)) of a neutral atom phase gate. The system is described by the Hamiltonians H_q (see Eqs. (3.4), (3.11), (3.15)), which depend on the laser amplitudes $|\Omega_1|, \dots, |\Omega_N|$ and phases $\varphi_1, \dots, \varphi_N$. Despite aiming to eventually find the time-optimal pulse, in this section we will assume a fixed pulse duration T and describe how GRAPE can be used to find pulses $\Omega_j(t)$ and $\varphi_j(t)$ of duration T that maximize F . Later we will then vary the pulse duration T to find time-optimal pulse.

We start as in the previous section by making a piecewise constant Ansatz of M pieces and assuming $\Omega_j(t) = |\Omega_j^{(m)}| \exp(i\varphi_j^{(m)})$ if $m\Delta t \leq t < (m+1)\Delta t$, so that the fidelity now depends on the parameters $|\Omega_j^{(m)}|$ and $\varphi_j^{(m)}$. To maximize F using a gradient based algorithm we need to calculate the derivatives $\partial F / \partial |\Omega_j^{(m)}|$ and $\partial F / \partial \varphi_j^{(m)}$. For this, we proceed as follows: For each of the Hamiltonians H_q we calculate $|\psi_{0,q}\rangle, \dots, |\psi_{M,q}\rangle$ and $|\chi_{M,q}\rangle, \dots, |\chi_{0,q}\rangle$ according to Eq. (3.32)–(3.39), with $|\psi_{0,q}\rangle = |q\rangle$ and $|\chi_{M,q}\rangle = e^{i\zeta_q} |q\rangle$. We then calculate the derivatives

$$\frac{\partial \langle \chi_{M,q} | \psi_{M,q} \rangle}{\partial |\Omega_j^{(m)}|} = \left\langle \chi_{m+1,q} \left| \frac{\partial U_{m,q}}{\partial |\Omega_j^{(m)}|} \right| \psi_{m,q} \right\rangle \quad (3.43)$$

$$\frac{\partial \langle \chi_{M,q} | \psi_{M,q} \rangle}{\partial \varphi_j^{(m)}} = \left\langle \chi_{m+1,q} \left| \frac{\partial U_{m,q}}{\partial \varphi_j^{(m)}} \right| \psi_{m,q} \right\rangle \quad (3.44)$$

with $U_{m,q} = \exp(-iH_q(\Omega_1^{(m)}, \dots, \Omega_N^{(m)})\Delta t)$.

The fidelity is given by

$$F = \frac{1}{2^N(2^N + 1)} \left[\left| \sum_q \langle \chi_{M,q} | \psi_{M,q} \rangle \right|^2 + \sum_q |\langle \chi_{M,q} | \psi_{M,q} \rangle|^2 \right] \quad (3.45)$$

(see Eq. (3.21)) so that

$$\begin{aligned} \frac{\partial F}{\partial |\Omega_j^{(m)}|} = \frac{1}{2^N(2^N + 1)} 2\text{Re} & \left[\left(\sum_q \langle \chi_{M,q} | \psi_{M,q} \rangle \right)^* \left(\sum_q \frac{\partial \langle \chi_{M,q} | \psi_{M,q} \rangle}{\partial |\Omega_j^{(m)}|} \right) \right. \\ & \left. + \sum_q \langle \chi_{M,q} | \psi_{M,q} \rangle^* \frac{\partial \langle \chi_{M,q} | \psi_{M,q} \rangle}{\partial |\Omega_j^{(m)}|} \right] \end{aligned} \quad (3.46)$$

and

$$\begin{aligned} \frac{\partial F}{\partial \varphi_j^{(m)}} = \frac{1}{2^N(2^N + 1)} 2\text{Re} \left[\left(\sum_q \langle \chi_{M,q} | \psi_{M,q} \rangle \right)^* \left(\sum_q \frac{\partial \langle \chi_{M,q} | \psi_{M,q} \rangle}{\partial \varphi_j^{(m)}} \right) \right. \\ \left. + \sum_q \langle \chi_{M,q} | \psi_{M,q} \rangle^* \frac{\langle \chi_{M,q} | \psi_{M,q} \rangle}{\partial \varphi_j^{(m)}} \right]. \end{aligned} \quad (3.47)$$

Inserting Eqs. (3.43) and (3.44) into Eq. (3.46) and Eq. (3.46) now allows us to calculate the derivatives $\partial F / \partial |\Omega_j^{(m)}|$ and $\partial F / \partial \varphi_j^{(m)}$.

It remains to calculate the derivatives $\partial U_{m,q} / \partial |\Omega_j^{(m)}|$ and $\partial U_{m,q} / \partial \varphi_j^{(m)}$ required in Eqs. (3.43) and (3.44). In general we obtain these by approximating $U_{m,q}$ with its Taylor approximation $U_{m,q} \approx \sum_{l=0}^L (-iH_q \Delta t)^l / l!$, so that

$$\frac{\partial U_{m,q}}{\partial |\Omega_j|} = \sum_{\substack{l,l' \geq 0 \\ l+l' < L}} \frac{(-i\Delta t)^{l+l'+1}}{(l+l'+1)!} H_q^l \frac{\partial H_q}{\partial |\Omega_j|} H_q^{l'} \quad (3.48)$$

with an analogous expression for $\partial U_{m,q} / \partial \varphi_j^{(m)}$. The order L is chosen large enough to ensure convergence to machine precision, typically $L \approx 10$.

There are two cases in which the expansion in a Taylor series can be avoided: The first case is that of a global drive $\Omega_1 = \dots = \Omega_N = \Omega$ in the limit $B \gg |\Omega|$, where the Hamiltonian H_q is just a 2×2 matrix (see Sec. 3.1.1.3), so that $U_{m,q}$ as well as its derivatives can be calculated analytically. The second case is if we only want to calculate the $\partial U_{m,q} / \partial \varphi_j^{(m)}$ but not the $\partial U_{m,q} / \partial |\Omega_j^{(m)}|$, e.g. because we fix the value of the $|\Omega_j^{(m)}|$ and only optimize over the $\varphi_j^{(m)}$. In this case we can use that $H_q(\Omega_1, \dots, \Omega_N) = V H_q(|\Omega_1|, \dots, |\Omega_N|) V^\dagger$ with

$$V = \bigotimes_{j=1}^N \left(|0\rangle \langle 0| + |1\rangle \langle 1| + e^{-i\varphi_j^{(m)}} |r\rangle \langle r| \right) \quad (3.49)$$

so that $U_{m,q} = V \bar{U}_{m,q} V^\dagger$ with $\bar{U}_{m,q} = \exp[-iH_q(|\Omega_1|, \dots, |\Omega_N|)\Delta t]$. Then we get

$$\frac{\partial U_{m,q}}{\partial \varphi_j^{(m)}} = \frac{\partial V}{\partial \varphi_j^{(m)}} \bar{U}_{m,q} V^\dagger + V \bar{U}_{m,q} \frac{\partial V^\dagger}{\partial \varphi_j^{(m)}}. \quad (3.50)$$

Now we use that $\partial V / \partial \varphi_j^{(m)} = -iV |r_j\rangle \langle r_j|$ to obtain

$$\frac{\partial U_{m,q}}{\partial \varphi_j^{(m)}} = -iV [|r_j\rangle \langle r_j|, \bar{U}_{m,q}] V^\dagger. \quad (3.51)$$

Together with $\bar{U}_{m,q}$, which only needs to be calculated once since it does not depend on the $\varphi_j^{(m)}$, this allows us to calculate $\partial U_{m,q} / \partial \varphi_j^{(m)}$.

In summary, we have introduced the GRAPE algorithm and shown how it can be used to calculate the derivative of the gate fidelity F with respect to the laser amplitude and phase at any time. Using a gradient based optimizer, a pulse shape $\Omega_1(t), \dots, \Omega_N(t)$ that achieves a (local) minimum of the infidelity $1 - F$ can then be found. In the next sections we will use GRAPE to find the minimal infidelity $1 - F$ for different pulse durations and identify the time-optimal duration as the smallest duration in which $1 - F = 0$ can be achieved.

3.3 Time-Optimal CZ Gate for a Perfect Rydberg Blockade

In this section we apply the theory developed in Secs. 3.1 and 3.2 to the simplest time-optimal problem: Finding the shortest possible global laser pulse $\Omega(t) = \Omega_1(t) = \Omega_2(t)$ that in the $B \gg \Omega_{\max}$ limit implements a CZ gate on $N = 2$ atoms. The dynamics of this system is described by two two-level systems

$$H_{01} = \frac{\Omega(t)}{2} |01\rangle \langle 0r| + \text{h.c.} \quad (3.52)$$

$$H_{11} = \frac{\sqrt{2}\Omega(t)}{2} |11\rangle \langle W_{11}| + \text{h.c.} \quad (3.53)$$

which have to be controlled simultaneously. Since single qubit gates are typically performed with a much larger fidelity than two qubit gates we slightly weaken our goal and only require that $\Omega(t)$ implements a CZ gate *up to single qubit gates*, i.e. $\Omega(t)$ implements a phase gate with $\zeta_{00} = 0$, $\zeta_{01} = \zeta_{10} = \theta$ and $\zeta_{11} = 2\theta + \pi$ for some phase θ . The additional parameter θ can easily be included in the optimization, the derivative $\partial F / \partial \theta$ is given by

$$\frac{\partial F}{\partial \theta} = \frac{1}{20} \text{Re} \left[(1 + 2 \langle \chi_{M,01} | \psi_{M,01} \rangle + \langle \chi_{M,11} | \psi_{M,11} \rangle) \right. \quad (3.54) \\ \left. (-2i \langle \chi_{M,01} | \psi_{M,01} \rangle - 2i \langle \chi_{M,11} | \psi_{M,11} \rangle) \right].$$

Since H_{01} and H_{11} are proportional to $\Omega(t)$, the time-optimal pulse must satisfy $|\Omega(t)| = \Omega_{\max}$ for all t . To see this, consider a pulse $\Omega(t) = |\Omega(t)| \exp(i\varphi(t))$ of duration T with $|\Omega(t)| < \Omega_{\max}$ for some times t . We can define a rescaled pulse $\bar{\Omega}(t) = \Omega_{\max} \exp(i\varphi(\tau^{-1}(t)))$ where

$$\tau(t) = \int_0^t dt' \frac{|\Omega(t')|}{\Omega_{\max}}. \quad (3.55)$$

This rescaled pulse implements the same gate as the original pulse and has a duration $\tau(T) < T$. Hence, the time-optimal pulse must satisfy $|\Omega(t)| = \Omega_{\max}$ for all t .

With this insight we now use GRAPE together with the BFGS minimization algorithm [153] to find the laser phase $\varphi(t)$ and the single qubit phase θ that minimize

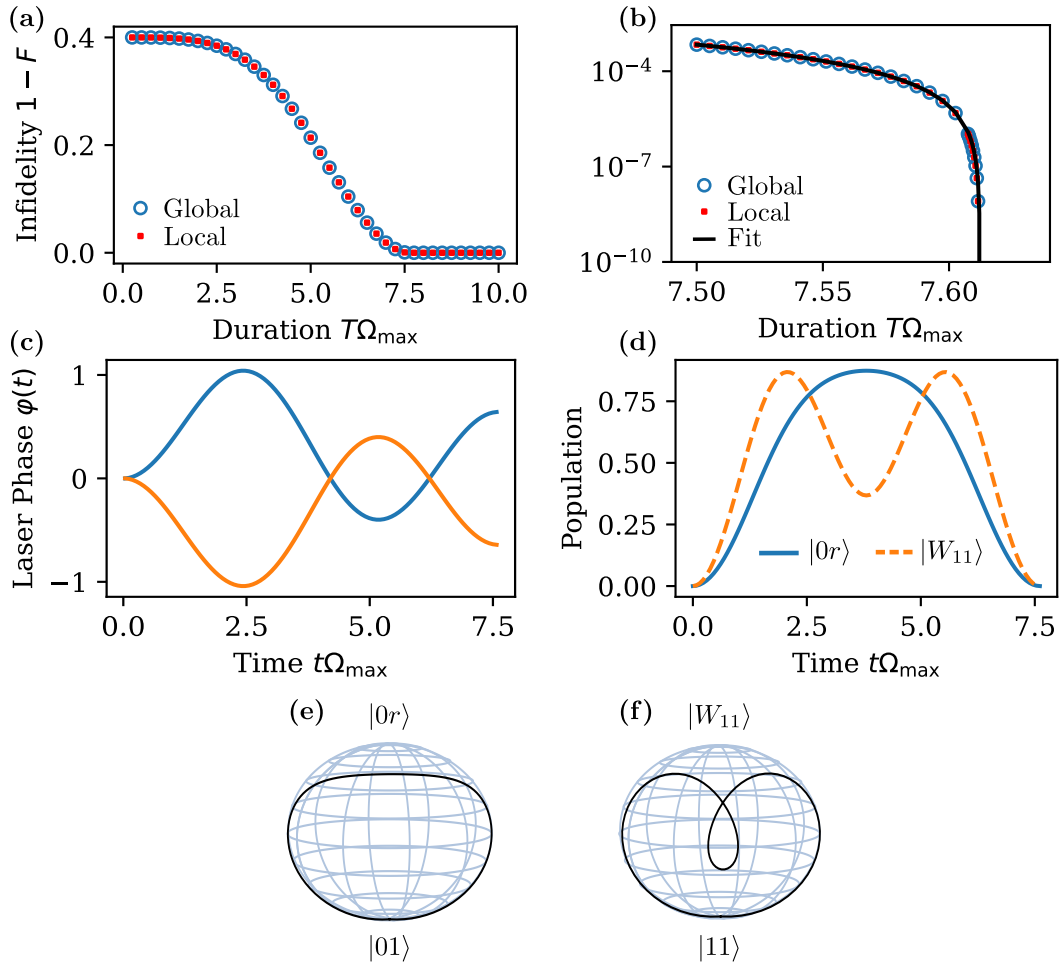


Figure 3.1: Time-Optimal CZ gate. (a) Minimal infidelity $1 - F$ of a CZ gate as found by GRAPE for pulse durations $0 \leq T\Omega_{\max} \leq 10$. Blue circles (red squares) show infidelity for a global(local) pulse. (b) Zoom-in and fit of the infidelity near the time-optimal time $T_*\Omega_{\max} = 7.612$. (c) Two different pulses $\varphi(t)$ (related by complex conjugation or time reversal) found by GRAPE at the time-optimal duration T_* . (d) Population of the states $|0r\rangle$ and $|W_{11}\rangle$ under the time-optimal pulse when starting in $|01\rangle$ and $|11\rangle$ respectively. (e/f) Trajectories of $|\psi_{01}\rangle$ and $|\psi_{11}\rangle$ on the Bloch sphere during the time-optimal pulse.

the infidelity $1 - F$ for different pulse durations T . We use $M = 100$ steps and start the optimization with $\varphi^{(1)}, \dots, \varphi^{(M)}$ and θ chosen independently and uniformly random from $[0, 2\pi)$. We verify that the minimal infidelity does not depend on this initial guess.

Fig. 3.1(a) shows the minimal infidelity $1 - F$ as a function of the pulse duration T in units of $1/\Omega_{\max}$ (blue circles). In the limit of $T \rightarrow 0$ the infidelity approaches $1 - F = 0.4$, corresponding to the implementation of the identity instead of the CZ gate. With increasing T the infidelity drops and finally reaches $1 - F = 0$ at $T = T_* \approx 7.6$. For $T > T_*$ the infidelity is zero. Note that the LP protocol (Sec. 2.5.3) demonstrates that there exists an $\Omega(t)$ with $1 - F = 0$, so we know that for $T > T_*$ the infidelity is exactly 0, and does not only approach 0 as $T \rightarrow \infty$.

To determine T_* more precisely we again use GRAPE to find the infidelity for $7.5 \leq T\Omega_{\max} \leq 7.65$, shown in Fig. 3.1(b) with the infidelity in log-scale. We fit the infidelity for T close to T_* as

$$1 - F(T) = \begin{cases} c(T_* - T)^2 & \text{if } T < T_* \\ 0 & \text{if } T > T_* \end{cases} \quad (3.56)$$

and obtain $T_*\Omega_{\max} = 7.612$ and $c = 5.45 \times 10^{-2}$ [black line in Fig. 3.1(b)]. Eq. (3.56) is found empirically and excellently fits the observed infidelities.

Fig. 3.1(c) shows the two different pulses $\varphi(t)$ that we obtain at $T = T_*$. Which pulse is obtained depends on the random starting point of the optimization. The two pulses can be transformed into each other either by time reversal [$\bar{\varphi}(t) = \varphi(T-t)$] or complex conjugation [$\bar{\varphi}(t) = -\varphi(t)$] (see Sec. 3.1.3), so that up to symmetry operations the time-optimal pulse is unique. Note that interestingly the pulse is invariant under joint time reversal and complex conjugation, so that there are only two and not four distinct time-optimal pulses. In contrast to the LP gate the laser phase of the time-optimal is a continuous function of time without any phase jumps. Its time dependency is similar to that of a cosine, a fact which we will explore in detail in Chapter 4.

To understand how the pulse acts on the initial states $|01\rangle$ and $|0r\rangle$ we consider the population $|\langle 0r|\psi_{01}(t)\rangle|^2$ and $|\langle W_{11}|\psi_{11}(t)\rangle|^2$ of the states $|0r\rangle$ and $|W_{11}\rangle$, respectively, in Fig. 3.1(d). The population of $|0r\rangle$ increases until $t = T/2$ and then decreases to 0 until $t = T$, while the population of $|W_{11}\rangle$ increases until $t \approx T/4$, but then decreases again until $t = T/2$, followed by a symmetric increase until $t \approx 3T/4$ and a drop to 0 at $t = T$. Figs. 3.1(e) and (f) show the evolution of $|\psi_{01}\rangle$ and $|\psi_{11}\rangle$ on the Bloch sphere spanned by $|01\rangle$ and $|0r\rangle$ as well as $|11\rangle$ and $|W_{11}\rangle$, respectively. Interestingly, $|\psi_{11}\rangle$ shows a self-intersecting path.

Finally we consider what happens when we lift the constraint of a global pulse and allow for different pulses $\Omega_1(t) \neq \Omega_2(t)$ on the two atoms. Analogously to the global case we calculate the minimal infidelity as a function of T using GRAPE (red squares in Figs. 3.1(a/b)). Interestingly, the minimal infidelity exactly coincides with that for a global pulse, showing that individual addressability of the atoms brings no speedup for a CZ gate. We also find the pulses $\Omega_1(t)$ and $\Omega_2(t)$ to agree with the global pulse $\Omega(t)$ up to a constant phase (not shown).

In conclusion we have identified the time-optimal pulse shape $\Omega(t)$ that implements a CZ gate in the $B \gg \Omega_{\max}$ limit. It consists of a constant amplitude Ω_{\max} and a time-dependent phase $\varphi(t)$ which is a smooth and simple function of time [Fig. 3.1]. The time-optimal pulse duration $T_* = 7.612/\Omega_{\max}$ is approximately 10% faster than the duration of the LP protocol, showing that also the LP protocol is close to time-optimal. Finally we have demonstrated that the constraint to global pulses isn't a constraint at all: Even when allowing individual addressability of the atoms, the time-optimal pulse is the global pulse found before.

3.4 Time-Optimal CZ Gate for Finite Interaction Strengths

In Sec. 3.3 we found the time-optimal pulse to implement a CZ gate in the limit $B/\Omega_{\max} \rightarrow \infty$, in which it is impossible to excite both atoms simultaneously to the Rydberg state. However, in a real experiment, B/Ω_{\max} is always finite, so that a residual population of the state $|rr\rangle$ cannot be completely avoided. In this section we solve this problem and identify time-optimal pulses that implement a CZ gate for finite interaction strengths B . We demonstrate that it is possible to implement a CZ gate for all values of B from the $B \gg \Omega_{\max}$ limit, where the pulses are similar to those of Sec. 3.3, to the $B \ll \Omega_{\max}$ limit. We note that this is not only useful for Rydberg blockade gates in the regime of a finite blockade, where typically still $B \gg \Omega_{\max}$, but also for spin-flip blockade gates using dressed Rydberg states [154], in which interaction strengths are typically of the order of Ω_{\max} .

For a finite B , the Hamiltonian H_{11} [see Eq. (3.53)] is modified to a three level system as

$$H_{11} = B |rr\rangle \langle rr| + \frac{\sqrt{2}\Omega(t)}{2} (|11\rangle \langle W_{11}| + |W_{11}\rangle \langle rr|) + \text{h.c.} \quad (3.57)$$

while H_{01} remains unchanged [see Eq. (3.52)]. Note that since H_{11} is not proportional to $\Omega(t)$ anymore, it is now possible that the time-optimal pulse satisfied $|\Omega(t)| < \Omega_{\max}$.

We use GRAPE to find the time-optimal pulse duration as a function of the interaction strength B by proceeding analogously to Sec. 3.3. However, in contrast to Sec. 3.3 we now find that the optimized pulse depends on the the initial guess of the pulse. Thus we find several *locally* time-optimal pulses, out of which the shortest one is the *globally* time-optimal pulse.

Fig. 3.2 shows the locally time-optimal pulse durations as a function of B for the regime of small [Fig. 3.2(a)], intermediate [Fig. 3.2(b)] and large [Fig. 3.2(c)] interaction strengths B . By observing how the pulse shape changes with B we identify three distinct types of pulses (types 1–3, marked by different markers in Fig 3.2), such that for pulses of the same type the pulse shape changes continuously with B . Figs. 3.3,3.4 and 3.5 show the laser amplitude $|\Omega(t)|$ and phase $\varphi(t)$ at selected values of B for pulses of type 1,2 and 3, respectively.

For large $B > 4\Omega_{\max}$ [Fig. 3.2(c)] we find that there are only two locally time-optimal solutions (type 1 and type 2). Pulses of type 1 always have a slightly longer duration than pulses of type 2, but for both types the durations are in the range $7.5 \leq T\Omega_{\max} \leq 7.65$, within 1.5% of the duration of the time-optimal pulse at $B/\Omega_{\max} \rightarrow \infty$. Qualitatively, the two types of pulses correspond to the two time-optimal pulses that in the $B/\Omega_{\max} \rightarrow \infty$ limit are related by complex conjugation (see Sec. 3.3). Pulses of type 1(2) qualitatively resemble the blue(orange) pulse in

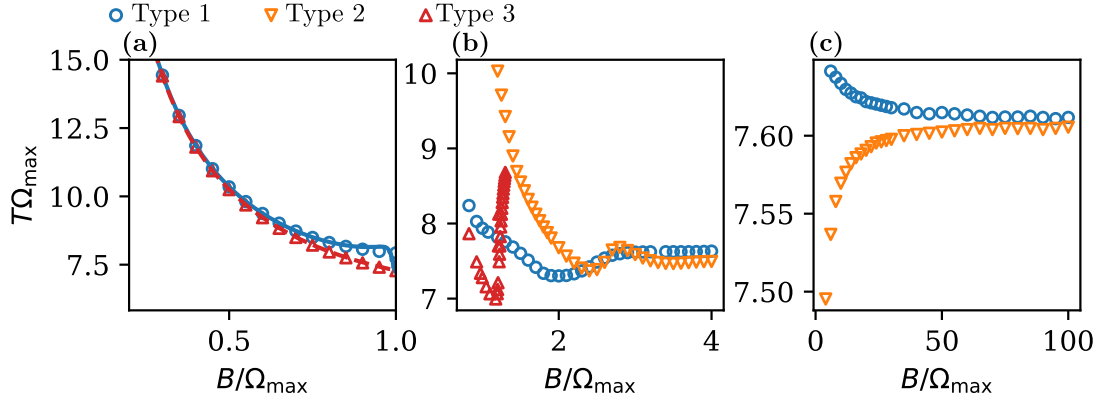


Figure 3.2: Pulse durations T (in units of $1/\Omega_{\max}$) of locally time-optimal pulses as a function of the interaction strength B . We identify three types of pulse shapes such that pulse shapes of the same type change continuously with B (see main text). (a) For small interaction strength $B < \Omega_{\max}$. Solid lines show fits assuming a simple protocol of two rectangular pulses with an idle time in between (see main text). (b) For intermediate interaction strengths $\Omega_{\max} \leq B \leq 4\Omega_{\max}$. (c) For large interaction strengths $4\Omega_{\max} \leq B \leq 100\Omega_{\max}$.

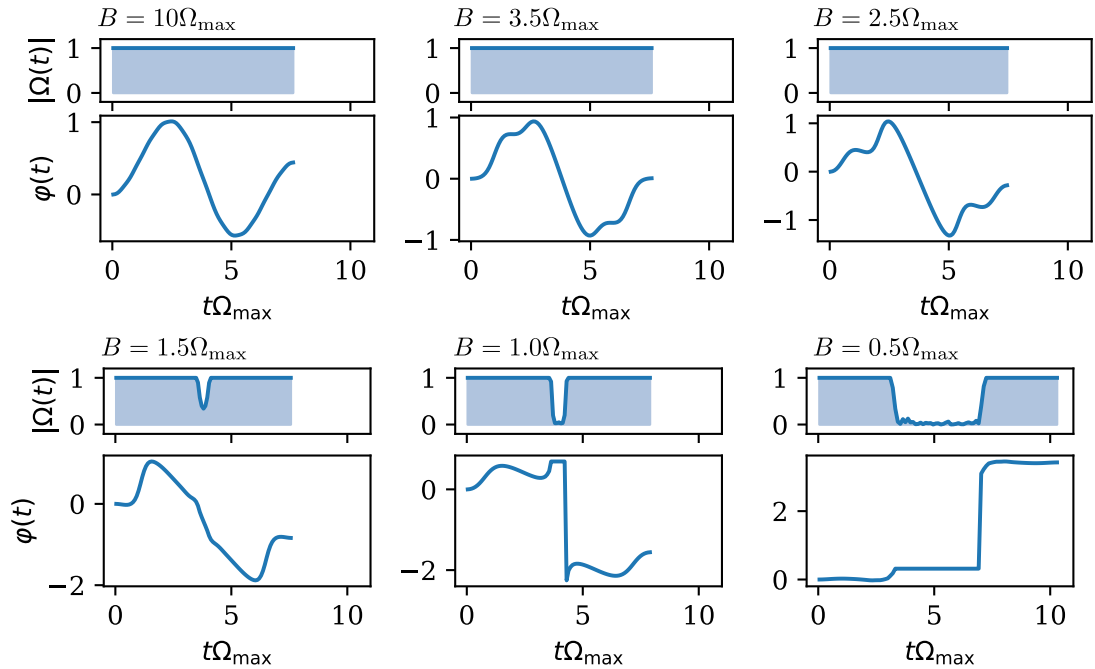


Figure 3.3: Type 1 Pulses. Pulse shapes $|\Omega(t)|$ and $\varphi(t)$ at selected interaction strengths B for pulses of type 1.

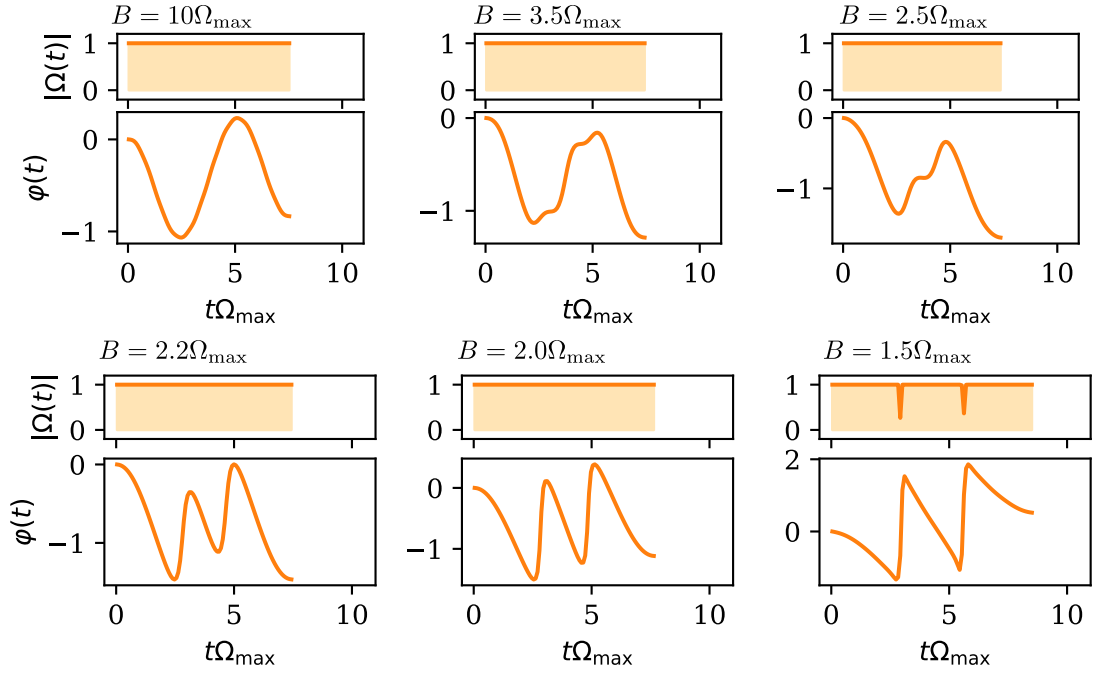


Figure 3.4: Type 2 Pulses. Pulse shapes $|\Omega(t)|$ and $\varphi(t)$ at selected interaction strengths B for pulses of type 2.

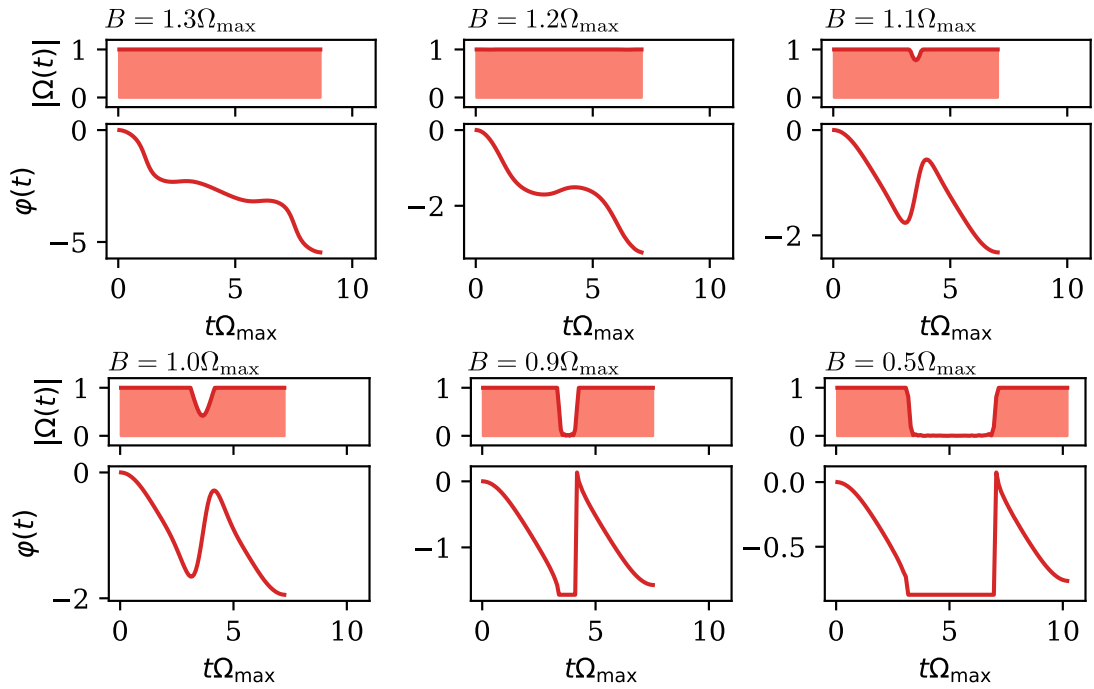


Figure 3.5: Type 3 Pulses. Pulse shapes $|\Omega(t)|$ and $\varphi(t)$ at selected interaction strengths B for pulses of type 3.

Fig. 3.1(c). For $B > 4\Omega_{\max}$ we find that, as in the $B \rightarrow \infty$ limit, the pulse amplitude is always maximal $|\Omega(t)| = \Omega_{\max}$.

For the regime of intermediate B ($\Omega_{\max} \leq B \leq 4\Omega_{\max}$) we observe a more complex behavior of the pulse duration [see Fig. 3.2(b)]. Around $B = 2.8\Omega_{\max}$ the duration of type 2 pulses increases over that of type 1 pulses, only to drop below it again at $B = 2.6\Omega_{\max}$. At $B = 2.4\Omega_{\max}$ the duration of type 2 pulses then increases rapidly and reaches $10/\Omega_{\max}$ at $B = 1.2\Omega_{\max}$. The duration of type 1 pulses instead decreases, reaching its minimum of $T = 7.3/\Omega_{\max}$ at $B = 2.0\Omega_{\max}$, after which it starts to increase again. Pulses of type 2 always show $|\Omega(t)| = \Omega_{\max}$ [Fig. 3.4], while for pulses of type 1 a dip in $|\Omega(t)|$ at $t = T/2$ starts to appear around $B = 1.5\Omega_{\max}$ [Fig. 3.3].

At $B = 1.3\Omega_{\max}$ pulse shapes of a new type, type 3, start to appear. Their pulse duration drops rapidly, reaching its minimum of $T = 6.9/\Omega_{\max}$ at $B = 1.15\Omega_{\max}$, before rapidly increasing again. Like pulses of type 1, pulses of type 3 show a dip in $|\Omega(t)|$ at $t = T/2$ which appears around $B = 1.1\Omega_{\max}$ [Fig. 3.5].

In the regime of small $B \leq \Omega_{\max}$ we only find pulses of type 1 and type 3, with type 3 always having the shorter pulse duration [Fig. 3.2(a)]. The pulse duration of both types increases rapidly with decreasing B . The pulses for type 1 and type 3 show a similar structure (see Fig. 3.3 and 3.5): They consist of two pulses with a maximum laser amplitude $|\Omega(t)| = \Omega_{\max}$ and an idle time with $\Omega(t) = 0$ in between them. However, for type 1 the laser phase is constant during each of the two pulses, while for type 3 the phase changes approximately linearly with time, corresponding to a laser with a constant detuning.

Based on this observation we now make the Ansatz

$$\Omega(t) = \begin{cases} \Omega_{\max} e^{-i\delta t} & \text{if } 0 < t < \tau \\ 0 & \text{if } \tau < t < T - \tau \\ \Omega_{\max} e^{-i[\delta(t+\tau-T)+\alpha]} & \text{if } T - \tau < t < T \end{cases} \quad (3.58)$$

which depends on the laser detuning δ , the phase difference α between the two pulses, the total pulse duration T and the length τ of the two individual pulses. In the limit $B \rightarrow 0$ this implements a CZ gate for $\delta = 0$, $\alpha = \pi$, $\tau = \pi/\Omega_{\max}$ and $T = \pi/B$. This gate works by simply exciting $|1\rangle$ to $|r\rangle$ on both atoms simultaneously and letting the $|rr\rangle$ state acquire a phase of π by waiting for a duration of π/B . This has been described as *Model A* in Ref. [64].

For different values of $B \leq \Omega_{\max}$ we now numerically minimize the gate fidelity using the Ansatz (3.58) over the parameters T, τ, δ, α and the single qubit phase θ by which the implemented gate differs from a CZ gate. For each value of B we find *two* sets of parameters which achieve $1 - F = 0$. The pulse durations T for these two solutions are shown as a function of B by the solid blue and red lines in Fig. 3.2(a). We observe a very good agreement with the pulse durations found by GRAPE, showing that for $B \leq \Omega_{\max}$ the Ansatz (3.58) indeed captures the time-optimal pulse. For type 1 we find that in the $B \rightarrow 0$ limit the detuning satisfies

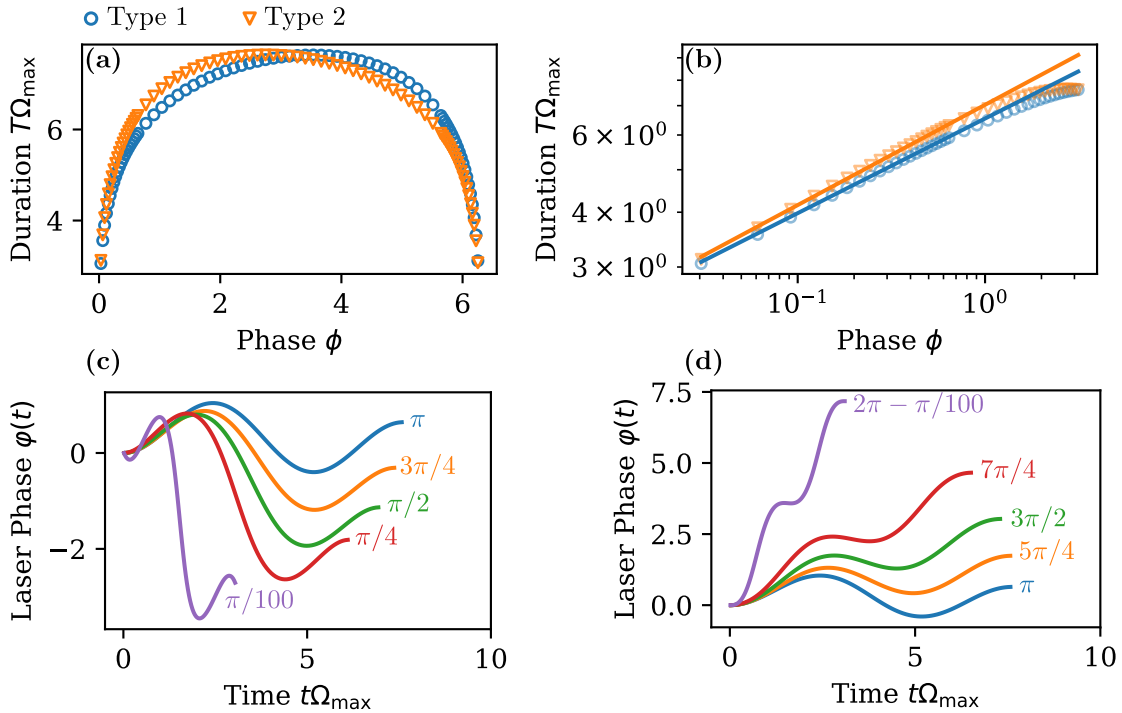


Figure 3.6: Time-Optimal C-Phase Gate. (a) Pulse durations for pulses of type 1 (blue circles) and type 2 (orange triangles) as a function of the two qubit phase ϕ . (b) Same as subfigure (a) but in log-log scale. Solid lines show fits $T = \phi^\nu$. (c)/(d) Pulses of type 1 for selected values of ϕ below/above π . Pulses of type 2 are complex conjugated or time reversed versions of type 1 pulses, and implement a controlled $2\pi - \phi$ phase gate.

$\delta/B \rightarrow 0$, while for type 3 we find $\delta/B \rightarrow 1/2$. This shows that for type 1 pulses the laser is resonant with the $|11\rangle \leftrightarrow |W_{11}\rangle$ transition, but slightly detuned from the $|W_{11}\rangle \leftrightarrow |rr\rangle$ transition, while for type 3 pulses the laser is resonant with the two photon $|11\rangle \leftrightarrow |rr\rangle$ transition but slightly detuned from the $|11\rangle \leftrightarrow |W_{11}\rangle$ and $|W_{11}\rangle \leftrightarrow |rr\rangle$ transitions.

In conclusion, we have identified the locally time-optimal pulses implementing a CZ gate at various interaction strengths B . We found three qualitatively different types of pulses, each of which changes continuously with B . For large B two of those pulse types correspond to the two time-optimal pulses in the $B \rightarrow \infty$ limit, for small B the time-optimal pulses are described by the simple Ansatz (3.58).

3.5 Time-Optimal C-Phase Gates

In the following we identify the time-optimal pulses $\varphi(t)$ that implement a controlled-phase (C-Phase) gate on two atoms, i.e a phase gate with $\zeta_{00} = 0$, $\zeta_{01} = \zeta_{10} = \theta$ and $\zeta_{11} = 2\theta + \phi$ for some so called *two-qubit phase* ϕ . C-Phase gates are particularly useful in quantum simulations, but also appear in quantum algorithms such as the

quantum Fourier transform [1]. Note that the CZ gate is a special case of a C-Phase gate with $\phi = \pi$. We note that results similar to those in this section have been independently obtained in Ref. [13].

For C-Phase gates we only consider the case of a perfect Rydberg blockade and proceed analogously to the time-optimal CZ gate (Sec. 3.3). For different phases ϕ we identify the time-optimal pulse duration T and the corresponding laser phase $\varphi(t)$. For all values of ϕ we find two different locally time-optimal pulses, which we label type 1 and type 2 [Fig. 3.6(a)]. At $\phi = \pi$, both pulses have the same duration and correspond to one of the two time-optimal pulses that are related by complex conjugation [Type 1(2) is the blue(orange) pulse in Fig. 3.1(c)]. For phases $\phi < \pi$ we find that type 1 pulses always have the shorter duration, while for $\phi > \pi$ type 2 pulses are shorter. Note that by the complex conjugation or time reversal symmetry (Sec. 3.1.3), type 2 pulses at a given two-qubit phase ϕ are identical to the complex conjugated or time reversed version of the type 1 pulses at $\phi' = 2\pi - \phi$, and vice versa.

Fig. 3.6(a) shows that the minimal pulse duration approaches 0 only very slowly as ϕ approaches 0 or 2π . Fig. 3.6(b) shows the same data as Fig. 3.6(a) with both axis on a log scale. We fit the pulse duration for low ϕ as a polynomial

$$T\Omega_{\max} = c\phi^\nu \quad (3.59)$$

and find an excellent agreement between the data and the fit. We obtain the coefficients $\nu = 0.22$ for type 1 and $\nu = 0.23$ for type 2. This shows that implementing a C-Phase gate for low ϕ on Rydberg atoms requires a very long pulse duration, scaling approximately as $T \propto \phi^{1/4}$.

Fig. 3.6(c/d) shows the pulse shapes $\varphi(t)$ for selected values of ϕ for pulses of type 1. The pulses qualitatively resemble the time-optimal pulse of the CZ gate, but require a larger range of the laser phase as ϕ approaches 0 or 2π . A semianalytical description of these pulse shapes will be given in Chapter 4.

In summary we have identified the time-optimal global pulses to implement C-Phase gates for the whole range $0 < \phi < 2\pi$ of possible two qubit phases ϕ . For each ϕ there are two distinct locally time-optimal pulses. For both pulse types the pulse duration only drops slowly as $T \propto \phi^{1/4}$ as $\phi \rightarrow 0$.

3.6 Time-Optimal Multi-Controlled C_kZ Gates

In the following we turn to the extension of the time-optimal CZ gate to multi-controlled C_kZ gates on three or more atoms. These gates are phase gates on $k + 1$ atoms with $\zeta_{1\dots 1} = \pi$ and $\zeta_q = 0$ for $q \neq 1\dots 1$ and can be seen as applying a Z gate on one of the qubits conditioned on all other qubits being in state $|1\rangle$. C_kZ gates, in particular the C_2Z gate which is up to single qubit gates is equivalent to a Toffoli gate, are a useful resource in many quantum algorithms [1]. We again only aim to

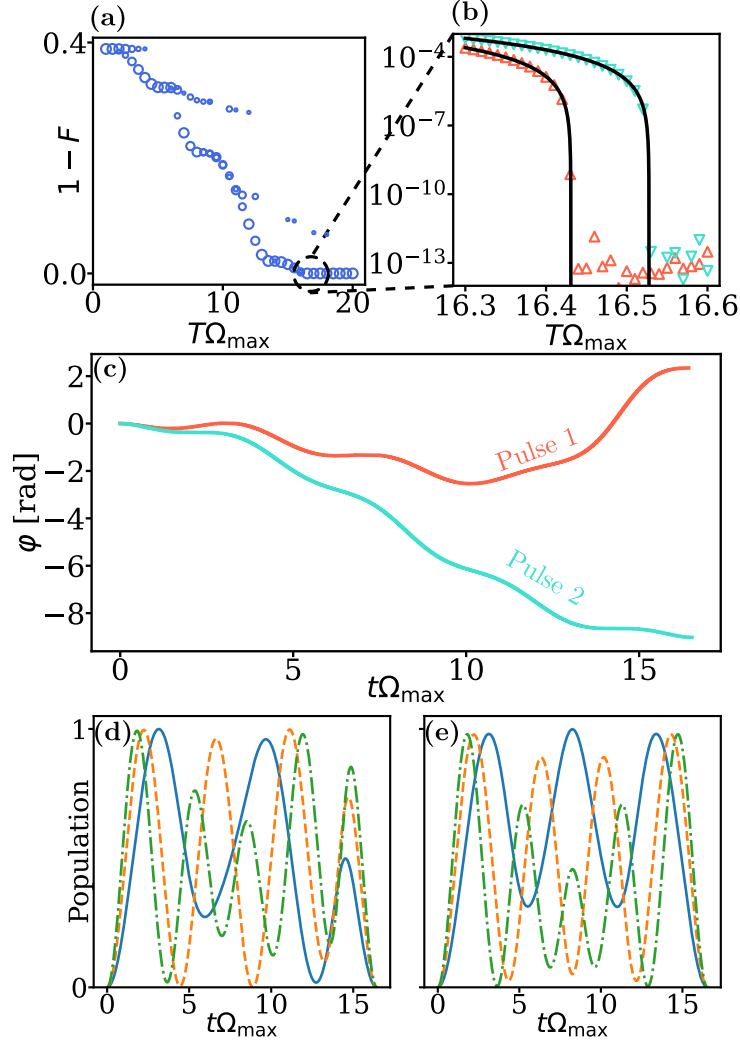


Figure 3.7: Time-Optimal C_2Z gate. (a) Infidelity as $1 - F$ as a function of pulse duration T measured in units of Ω_{\max} . Depending on the random starting point of the optimization, the algorithm converges to one of several local minima. The diameter of the marker is proportional to how often each minima was found. (b) Zoom-in onto the region $16.3 \leq T\Omega_{\max} \leq 16.6$. We identify two distinct pulses (red upward pointing and turquoise downward pointing triangles), whose time-optimal pulse duration ($16.43/\Omega_{\max}$ and $16.53/\Omega_{\max}$, respectively), we obtain by a fit of the form of Eq. (3.56). (c) Laser phase $\varphi(t)$ for Pulse 1 and Pulse 2 as a function of time. (d/e) Population of $|00r\rangle$ (blue, solid line) when starting in $|001\rangle$, of $|W_{011}\rangle$ when starting in $|011\rangle$ (orange, dashed line), and of $|W_{111}\rangle$ when starting in $|111\rangle$ (green, dash-dotted line) for Pulse 1/2.

implement a C_kZ gate up to a single qubit phase θ , i.e. a gate with $\zeta_q = \theta \sum_j q_j$ for $q \neq 1\dots 1$ and $\zeta_{1\dots 1} = (k+1)\theta + \pi$ for some θ .

We start by identifying the time-optimal pulse for a C_2Z gate the case of an infinite blockade strength in Sec. 3.6.1, followed by an adaptation to a finite blockade strength $B = 10\Omega_{\max}$ in Sec. 3.6.2. In Sec. 3.6.3 we discuss a variant of the C_kZ gate for $2 \leq k \leq 6$ which allows for significantly shorter gate durations, first proposed in

Ref. [13].

3.6.1 Rydberg Blockade Limit

For a C_2Z gate under infinite strengths we have to consider the three two-level Hamiltonians

$$H_{001} = \frac{\Omega(t)}{2} |001\rangle \langle 00r| + \text{h.c} \quad (3.60)$$

$$H_{011} = \frac{\sqrt{2}\Omega(t)}{2} |011\rangle \langle W_{011}| + \text{h.c} \quad (3.61)$$

$$H_{111} = \frac{\sqrt{3}\Omega(t)}{2} |111\rangle \langle W_{111}| + \text{h.c} \quad (3.62)$$

where $|W_{011}\rangle = (|01r\rangle + |0r1\rangle)/\sqrt{2}$ and $|W_{111}\rangle = (|11r\rangle + |1r1\rangle + |r11\rangle)/\sqrt{3}$. We now find the time-optimal C_2Z by proceeding analogously to the time-optimal CZ gate in Sec. 3.3. Fig. 3.7(a) shows the minimal infidelity $1 - F$ found by GRAPE as a function of the pulse duration T . We start by minimizing the fidelity for the largest considered value of T and then use this pulse as the starting point of the optimization for the subsequent value of T . In contrast to the CZ gate, we observe that the final fidelity depends on the randomly chosen starting point of the optimization, and determine several distinct local minima. The radius of the markers in Fig. 3.7(a) is proportional to how often each local minimum was found. Despite the existence of several local minima we still observe the emergence of clear continuous curve describing the lowest infidelity as a function of T . We approximate that the shortest possible pulse duration is given by $T_*\Omega_{\max} \approx 16.5$.

Fig. 3.7(b) shows the infidelity $1 - F$ in the regime $16.3 \leq T_*\Omega_{\max} \leq 16.6$. We observe that there are actually two locally time-optimal pulses: Pulse 1, indicated by the red upward pointing triangles, is also the globally time-optimal pulse and has a duration $T_*\Omega_{\max} = 16.43$. Pulse 2, indicated by the turquoise downward pointing triangles, and has a duration of $T_*\Omega_{\max} = 16.53$ and is less than 1% slower than Pulse 1. Fig. 3.7(c) shows the laser phases $\varphi(t)$ for both Pulse 1 and Pulse 2 (the amplitude for both pulses is given by $|\Omega(t)| = \Omega_{\max}$). The laser phase for Pulse 1 first decreases and then increases again, while the laser phase for Pulse 2 continuously decreases. Interestingly, Pulse 2 is invariant under joint time-reversal and complex conjugation, so that there is only other pulse related to it by complex conjugation and/or time reversal (see Sec. 3.1.3). In contrast, there are three other pulses related to Pulse 1 by these symmetry operations.

To gain a better understanding of the action of the two pulse shapes, Fig. 3.7(d) shows the population of $|00r\rangle$ when starting in $|001\rangle$ (solid blue line), the population of $|W_{011}\rangle$ when starting in $|011\rangle$ (dashed orange line) and the population of $|W_{111}\rangle$ when starting in $|111\rangle$ (dash-dotted green line), all under the evolution given by Pulse 1. Fig. 3.7(e) shows the same populations for the evolution under Pulse 2. For both cases we see that the populations oscillate with time, with the populations

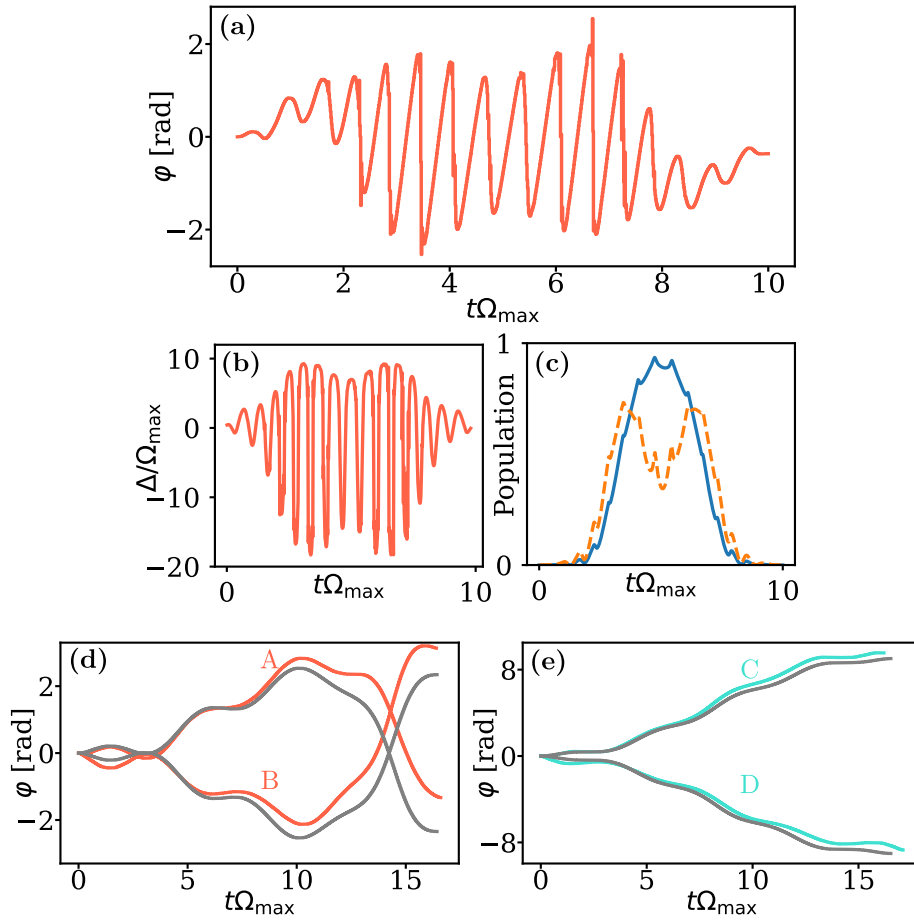


Figure 3.8: C_2Z gate at finite interaction strengths. (a) Laser phase $\varphi(t)$ of the time-optimal pulse at $B_{12} = B_{23} = B_{13} = 10\Omega_{\max}$. (b) Detuning $\Delta = d\varphi/dt$ for the pulse from (a). (c) Population of the states $|0rr\rangle$ (blue, solid line) and $|D_{111,2}\rangle$ (orange, dashed line) during the pulse from (a). (d) Pulses at $B = 10\Omega_{\max}$ (red) that qualitatively resemble Pulse 1 from the $B \rightarrow \infty$ limit (gray). (e) Analogous to (d) for Pulse 2.

involving more atoms in state $|1\rangle$ oscillating faster. This is consistent with the simple case of a constant laser phase, where the population of the state $|W_q\rangle$ would oscillate with frequency $\sqrt{n_q}\Omega_{\max}$, where $n_q = \sum_j q_j$ is the number of atoms starting in state $|1\rangle$. For Pulse 1 and Pulse 2 the laser phase is not constant, but the qualitative behavior is kept and adapted such that the populations of $|00r\rangle$, $|W_{011}\rangle$ and $|W_{111}\rangle$ are all zero at the end of the pulse.

In summary we have shown that there are two smooth and simple pulse shapes that implement a C_2Z gate in a time-optimal or almost time-optimal manner. These pulses constitute the first gate protocol for a C_2Z that only requires a global laser pulse instead of individual addressing of the atoms.

3.6.2 Finite Interaction Strengths

In a real experiment, the limit of an infinite interaction strength can never be exactly satisfied. In the following we thus consider the more realistic case of a finite blockade strength. For simplicity, we restrict ourselves to the case of $B_{12} = B_{23} = B_{13} = 10\Omega_{\max}$. The case of equal interaction strength can be experimentally realized by aligning the atoms in the shape of an equilateral triangle.

The Hamiltonian H_{001} from Eq. (3.60) stays unmodified in the case of finite B , while H_{011} and H_{111} from Eqs. (3.61) and (3.62) are modified as

$$H_{011} = B |0rr\rangle \langle 0rr| + \frac{\sqrt{2}\Omega(t)}{2} (|011\rangle \langle W_{011}| + |W_{011}\rangle \langle 0rr|) + \text{h.c.} \quad (3.63)$$

$$H_{111} = 3B |rrr\rangle \langle rrr| + B |D_{111,2}\rangle \langle D_{111,2}| \quad (3.64)$$

$$+ \frac{\sqrt{3}\Omega(t)}{2} |111\rangle \langle W_{111}| + \Omega(t) |W_{111}\rangle \langle D_{111,2}| + \frac{\sqrt{3}\Omega(t)}{2} |D_{111,2}\rangle \langle rrr| + \text{h.c.}$$

where $|D_{111,2}\rangle = (|1rr\rangle + |r1r\rangle + |rr1\rangle)/\sqrt{3}$.

We start by finding the time-optimal pulse for a C_2Z gate using GRAPE starting the optimization with a randomly chosen pulse. Interestingly, we are able to achieve a pulse duration of $T\Omega_{\max} = 10.0$, significantly shorter than in the $B \rightarrow \infty$ case. Fig. 3.8(a) shows the laser phase $\varphi(t)$ as a function of time, while the laser amplitude is again always maximal ($|\Omega(t)| = \Omega_{\max}$). The laser phase shows rapid oscillations as a function of time. To better understand the mechanism of this pulse, we plot the detuning $\Delta = d\varphi/dt$ in Fig. 3.8(c). We observe that Δ is frequently of the order of $-B$, showing that the laser is not always strongly detuned from the $|W_{011}\rangle \leftrightarrow |0rr\rangle$ and the $|W_{111}\rangle \leftrightarrow |D_{111,2}\rangle$ transitions. Fig. 3.8(c) confirms this by showing the populations of $|W_{011}\rangle$ (solid blue line) and $|D_{111,2}\rangle$ (orange dashed line). For both states we find a significant population during the pulse. Together, this shows that the pulse from Fig. 3.8(a) works fundamentally different than the pulses at $B \rightarrow \infty$ by significantly populating the states $|0rr\rangle$ and $|D_{111,2}\rangle$.

While being faster than the pulse in the $B \rightarrow \infty$ limit, the disadvantage of the pulse found above is that it is very sensitive to fluctuations in B . For example, decreasing B by just 10% increases the infidelity to $1 - F = 0.59$. This renders the pulse impractical for experimental implementations, where there is often a considerable uncertainty in B due to an uncertainty of the interatomic distance arising from the thermal motion of the atoms.

To mitigate this problem we now aim to find pulses at the finite value of B which are perturbations of pulses at $B \rightarrow \infty$. For this, we use that for far detuned pulses (i.e. $|\Delta| \ll B$), the effect of the finite value of B is in first order of B^{-1} given by an AC stark shift as

$$\bar{H}_{011} = -\frac{|\Omega(t)|^2}{2B} |W_{011}\rangle \langle W_{011}| + \frac{\sqrt{2}\Omega(t)}{2} |011\rangle \langle W_{011}| \quad (3.65)$$

$$\bar{H}_{111} = -\frac{|\Omega(t)|^2}{B} |W_{111}\rangle \langle W_{111}| + \frac{\sqrt{3}\Omega(t)}{2} |111\rangle \langle W_{111}| \quad (3.66)$$

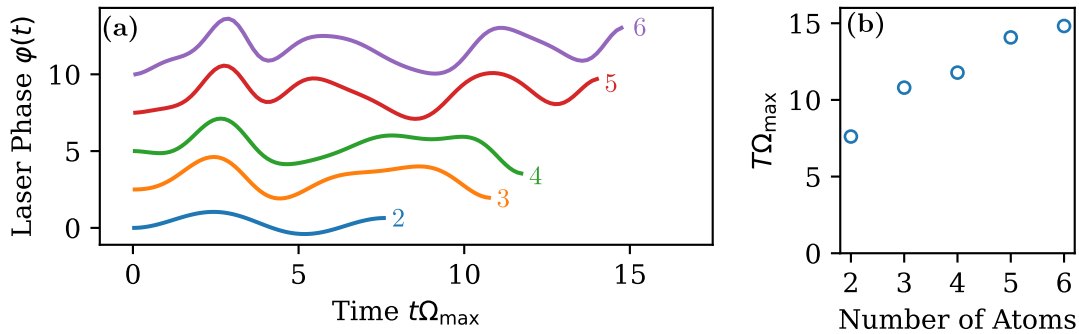


Figure 3.9: Variant of the C_kZ gate.(a) Laser phase $\varphi(t)$ for the variant of a C_kZ gate discussed in Sec. 3.6.3 for $1 \leq k \leq 5$. The number next to each gate indicates $k + 1$, the total number of atoms. (b) Pulse duration as the function of $k + 1$, the total number of atoms in the gate.

We now use GRAPE to find the time-optimal pulses under the approximate Hamiltonians H_{001} , \bar{H}_{011} and \bar{H}_{111} . We then use these pulses as an initial guess for the evolution under the exact Hamiltonians H_{001} , \bar{H}_{011} and \bar{H}_{111} . Since H_{001} , \bar{H}_{011} and \bar{H}_{111} don't contain states with two or more atoms in the Rydberg states, this procedure inhibits pulses with a significant population of these states.

The resulting pulses are shown in Fig. 3.8(d) in red [similar to Pulse 1 in Sec. 3.6.1(c)] and in Fig. 3.8(e) in turquoise [similar to Pulse 2 in Sec. 3.6.1(c)]. They resemble the pulses in the $B \rightarrow \infty$ limit, shown as the grey curves. Since at finite B only joint complex conjugation and time reversal gives a pulse implementing the same gate, while individual complex conjugation or time reversal would also require a switch of the sign of B (see Sec. 3.1.3), we find two different pulses at finite B for both Pulse 1 and Pulse 2. The pulse durations are given by $T_A\Omega_{\max} = 16.4$, $T_B\Omega_{\max} = 16.6$, $T_C\Omega_{\max} = 17.1$ and $T_D\Omega_{\max} = 16.2$ for the pulses marked as A,B,C and D in Fig. 3.8(d/e) respectively, similar to those found in the $B \rightarrow \infty$ limit. The pulses in Fig. 3.8(d/e) are also significantly more robust against fluctuations in B than the pulse in Fig. 3.8(a). For all of them, the infidelity stays below 4×10^{-4} when reducing B by 10%.

In summary, we identified two kinds of pulses at finite values of B : A pulse much shorter than the time-optimal pulse in the $B \rightarrow \infty$ limit which significantly populates states with more than one atom in the Rydberg state and is thus very sensitive to fluctuations in B , and a family of pulses qualitatively resembling those from the $B \rightarrow \infty$ limit which are much more robust against fluctuations in B .

3.6.3 Phase on $|0\dots 0\rangle$ instead of $|1\dots 1\rangle$

In Secs. 3.6.1 and 3.6.2 we considered a permutation symmetric phase gate with $\zeta_{000} = \zeta_{001} = \zeta_{011} = 0$ and $\zeta_{111} = \pi$. In Ref. [13] it was discovered that faster pulses are possible for phase gates with $\zeta_{000} = 0$ and $\zeta_{001} = \zeta_{011} = \zeta_{111} = \pi$. These gates can be converted into C_2Z gates by applying an X gate on each qubit before and

after the gate. For completeness we also include a short discussion of these results, which should not be attributed to the author, in this thesis.

Fig. 3.9(a) shows the time-optimal pulses for this variant of a C_kZ gate for $1 \leq k \leq 5$ as found by GRAPE in the $B/\Omega_{\max} \rightarrow \infty$ limit. Interestingly the pulse shapes for $k = 3$ and $k = 4$ resemble each other, as do the pulse shapes for $k = 5$ and $k = 6$. Fig. 3.9(b) shows the pulse duration as a function of k and reveals an approximately linear dependency of T on k . Crucially, the pulse for $k = 3$ has a duration of just $T\Omega_{\max} = 10.81$, about 34% faster than the pulses from Sec. 3.6.1.

3.7 A Protocol to Generate GHZ States

Greenberger-Horne-Zeiling (GHZ) states are N qubit quantum states of the form

$$|\text{GHZ}\rangle = \frac{1}{\sqrt{2}} \left(|0\rangle^{\otimes N} + |1\rangle^{\otimes N} \right). \quad (3.67)$$

They are of particular importance for quantum metrology, where they can be used for sensing beyond the standard quantum limit (SQL) and are able to achieve the Heisenberg quantum limit [155].

In the following we will show how N -qubit GHZ states can be implemented on neutral atoms by global single qubit gates and a single permutation symmetric phase gate which can be implemented using a global laser pulse. We assume that all N atoms are within a Rydberg blockade radius of each other, such that at most one of them can be in the Rydberg state at any given time. Our GHZ state preparation protocol has been experimentally implemented in Ref. [17], achieving a fidelity $F > 0.7$ for a 9 qubit GHZ state and demonstrating an optical clock with a fractional frequency instability below the SQL.

To generate a GHZ state, we initialize the qubits in the state $|+\rangle^{\otimes N}$ where $|+\rangle = (|0\rangle + |1\rangle)/2$. Then we apply a global laser pulse $\Omega(t)$ to implement the N -qubit permutation symmetric phase gate

$$U = \exp \left(i\pi \sum_{j < k} \hat{n}_j \hat{n}_k \right) \quad (3.68)$$

where $\hat{n}_j = |1_j\rangle \langle 1_j|$. Note that U corresponds to applying a CZ gate between every pair of qubits. The state $U |+\rangle^{\otimes N}$ is thus the graph state of the fully connected graph [156]. In the following we show that, up to a global phase,

$$U |+\rangle^{\otimes N} = \frac{1}{\sqrt{2}} \left(|+\rangle^{\otimes N} + i |-\rangle^{\otimes N} \right) \quad (3.69)$$

where $|\pm i\rangle = (|0\rangle \pm i|1\rangle)/\sqrt{2}$ are the eigenstates of the Pauli Y operator with eigenvalue ± 1 . Thus a GHZ state can be generated from $U |+\rangle^{\otimes N}$ by applying global single qubit gates.

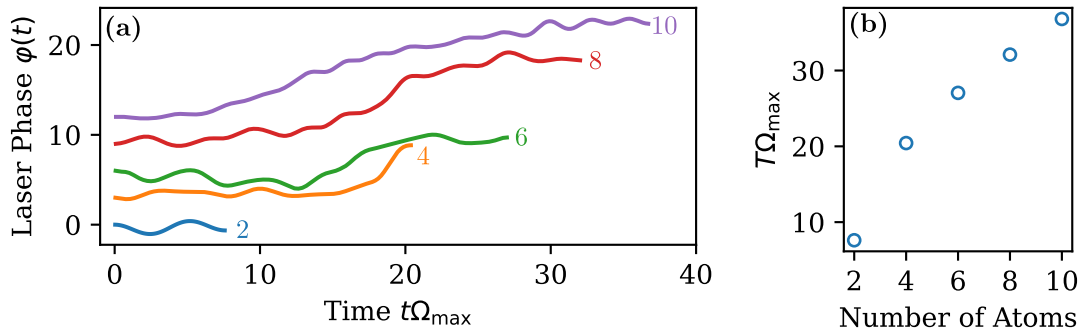


Figure 3.10: Pulses to generate a GHZ state. (a) Laser phase $\varphi(t)$ to implement U for 2,4,6,8 and 10 atoms. (b) Pulse duration as a function of the number of atoms.

To show Eq. (3.69) we use that, since $U|+\rangle^{\otimes N}$ is the graph state of the fully connected graph, it holds for all j that $S_j U|+\rangle^{\otimes N} = U|+\rangle^{\otimes N}$, where the stabilizer S_j is given by $S_j = Z_1 \dots Z_{j-1} X_j Z_{j+1} \dots Z_N$ and X_k or Z_k denote the Pauli X - or Z -operator applied on qubit k , respectively. Since for all j, k we have $S_j S_k = Y_j Y_k$ it follows that also $Y_j Y_k U|+\rangle^{\otimes N} = U|+\rangle^{\otimes N}$. Thus we can already conclude that $U|+\rangle^{\otimes N}$ is of the form

$$U|+\rangle^{\otimes N} = \alpha |+\rangle^{\otimes N} + \beta |-\rangle^{\otimes N} \quad (3.70)$$

for some coefficients α and β . Since $S_j |+\rangle^{\otimes N} = i |-\rangle^{\otimes N}$ and $S_j |-\rangle^{\otimes N} = -i |+\rangle^{\otimes N}$ it follows $\alpha = -i\beta$, showing Eq. (3.69).

It remains to find pulses $\Omega(t)$ that implement the unitary U . Using the methods laid out in Secs. 3.1–3.3 we find the time-optimal pulse that implements U up to single qubit phase θ . The pulses for 2,4,6,8 and 10 atoms are shown in Fig. 3.10(a). We observe that the complexity of the pulses increases with increasing N . Fig. 3.10(b) shows the time-optimal pulse duration, which also increases with N .

Finally we point out an interesting feature of our implementation of U : Since atoms in state $|0\rangle$ act just like missing atoms, a laser pulse $\Omega(t)$ that implements U on N atoms will also implement U on any number $N' < N$ atoms, albeit not in a time-optimal manner. In Ref. [17] this was used to prepare GHZ states of different sizes by preparing atom ensembles of different sizes and then applying the *same* pulse $\Omega(t)$ simultaneously on all ensembles. This collection of GHZ states of different sizes was then used to implement a cascaded quantum phase estimation protocol [157], increasing the dynamic range for sensing compared to a single GHZ state.

In summary we have demonstrated how the multi-qubit gate U can be used together with global single qubit gates to generate GHZ states, and how U can be implemented using simple and smooth laser pulses.

3.8 Conclusion

In this chapter we have used the numerical quantum optimal control technique of GRAPE to find time-optimal protocols for the implementation of several two- and multi-qubit quantum gates. Specifically, we have explored CZ gates for both an infinite and a finite interaction strength between the atoms, and C-Phase gates, multi-controlled C_kZ gates, and gates to generate GHZ states, for an infinite interaction strength. The time-optimal protocols only require a global laser without individual addressability of the atoms, and implement a gate simply by modulating the laser phase as a function of time. Due to their high fidelity, simplicity, and versatility, time-optimal gates have already been experimentally realized to implement CZ gates [13–16] and to generate GHZ states [17]. In this chapter we have assumed the simplest possible level scheme and modeled each atom as a three level system. As demonstrated in Ref. [14], the optimal control methods used in this chapter could also be used on more complicated level schemes, e.g. including two different Rydberg states and a dipole-dipole interaction between them [108, 114].

4 Mathematical Structure of Time-Optimal Pulses

In Chapter 3 we found the time-optimal laser pulse that implements a CZ gate on Rydberg atoms using the numerical quantum optimal control method of GRAPE. Notably, this pulse has a rather simple structure, the laser phase $\varphi(t)$ approximately resembles the shape of a sinus. The simple structure of the time-optimal pulse is not surprising, since also the underlying optimal control problem is rather simple: It just consists of steering two different two-level systems whose Hamiltonian depends on a single control parameter, the laser phase φ .

The simple nature of the optimal control problem allows us to approach it with analytical methods. In this chapter, we will use Pontryagin's maximum principle (PMP) [158, 159] to obtain a semi-analytical form of the time-optimal laser phase $\varphi(t)$. Specifically, we will prove that for any time-optimal C-Phase gate on two atoms in the Rydberg blockade limit the laser detuning $\Delta = d\varphi/dt$ is given by a solution of

$$\frac{1}{2}\dot{\Delta}^2 + V(\Delta) = 0 \quad \Delta(0) = 0 \quad (4.1)$$

with

$$V(\Delta) = \frac{1}{8}\Delta^4 + c_2\Delta^2 + c_1\Delta + c_0 \quad (4.2)$$

for some coefficients c_2, c_1, c_0 . In other words, the detuning Δ has the same functional dependence on time as the position of a classical particle with mass 1 and energy 0 oscillating in the quartic potential $V(\Delta)$. Furthermore, we show that at the final time T the time-optimal pulse satisfies $\Delta(T) = 0$, corresponding to the return of the particle to its initial position.

Our analytical result makes no statement on the parameters c_2, c_1, c_0 , which still have to be determined numerically. Hence, instead of the $M \gg 1$ parameters that are required in GRAPE by making a piecewise constant Ansatz of $\varphi(t)$ with M pieces, this semi-analytical approach characterizes time-optimal pulses by only three parameters. Analogously, we demonstrate that for three qubit C_2Z gates, as discussed in Sec. 3.6.1, time-optimal pulses can be described by only seven parameters.

This chapter is structured as follows: We start by stating the PMP, which is originally a classical optimal control method, in Sec. 4.1. While a complete proof of the PMP is out of the scope of this thesis, we give an intuitive proof sketch in Sec. 4.2. In Sec. 4.3 adapt the PMP to quantum optimal control problems. In Sec. 4.4 we then apply the PMP to describe time-optimal pulses on Rydberg atoms obtain a

set of coupled ordinary differential equations, which we then use to derive Eq. (4.1). We also numerically determine the parameters c_2, c_1, c_0 for a C-Phase gate as the function of the two-qubit phase ϕ and demonstrate the agreement between the semi-analytical results of this section with the numerical results of Sec. 3.5. Finally in Sec. 4.6 we discuss the extension of our semi-analytical approach to three qubit C_2Z gates.

Sections 4.1–4.3 of this chapter are based on the reviews [159, 160], while Secs. 4.4–4.6 constitute original work.

4.1 General formulation of the PMP

We start this section with an analogy of the PMP in classical mechanics. In spirit, the PMP makes a statement similar to the Euler-Lagrange equation in classical mechanics, but applied to an optimal control problem. In classical mechanics, we know that a particle that moves from an initial point (t_i, x_i) to a final point (t_f, x_f) in spacetime takes a trajectory $x(t)$ that minimizes the action

$$S[x] = \int_{t_i}^{t_f} L(x(t), \dot{x}(t)) dt \quad (4.3)$$

where L is the Lagrangian of the system. To find the trajectory $x(t)$, we could thus try to numerically minimize $S[x]$ over all possible trajectories $x(t)$ with $x(t_i) = x_i$ and $x(t_f) = x_f$, similar to optimizing the gate fidelity $1 - F$ over all laser phases $\varphi(t)$. However, we could also use that the optimal trajectory obeys the Euler-Lagrange equation

$$\frac{d}{dt} \left(\frac{\partial L}{\partial \dot{x}} \right) + \frac{\partial L}{\partial x} = 0. \quad (4.4)$$

Instead of optimizing over *all* trajectories, we can restrict ourselves to optimizing over all trajectories that satisfy Eq. (4.4). Since we know the initial position $x(t_i) = x_i$, these trajectories can be parameterized by their initial velocity $\dot{x}(t_i)$. To find the trajectory $x(t)$ we now have to find the initial velocity $\dot{x}(t_i)$ which satisfies the terminal condition $x(t_f) = x_f$. The GRAPE algorithm of Chapter 3 is analogous to minimizing $S[x]$ directly over all possible trajectories $x(t)$, while the PMP approach explored in this chapter is analogous to using the Euler-Lagrange equation.

We now give an exact statement of the PMP based on Ref. [159, 160]. Consider a real n -dimensional manifold M describing the space of all possible states of a system. For simplicity we here assume that M is embedded in $\mathbb{R}^{n'}$ for some $n' \geq n$. We are given a set $\mathcal{U} \subseteq \mathbb{R}^K$ of admissible controls and a *steering function* $f(x, u)$ which takes a point $x \in M$ and a control $u \in \mathcal{U}$ to a tangent vector $f(x, u) \in T_x M$ in the tangent space of M at x . We are also given an initial point $x_i \in M$ and a target submanifold $\mathcal{T} \subseteq M$. A particularly interesting case is $\mathcal{T} = \{x_f\}$ where the target submanifold collapses to a single point $x_f \in M$.

A *controlled trajectory* of duration $T > 0$ is now defined as a pair (x, u) of two functions $x : [0, T] \rightarrow M$ and $u : [0, T] \rightarrow \mathcal{U}$ such that $x(0) = x_i$, $x(T) \in \mathcal{T}$ and $\dot{x}(t) = f(x(t), u(t))$ for all $t \in [0, T]$. The duration T can either be fixed, in which case we only consider controlled trajectories of duration T , or free, in which case we take T as a property of the trajectory and consider trajectories of all $T > 0$.

We are now given a *Lagrangian* $L : M \times \mathcal{U} \rightarrow \mathbb{R}$ and a *terminal cost function* $\Phi : \mathcal{T} \rightarrow \mathbb{R}$. The *cost* of a controlled trajectory (x, u) is defined as

$$J[x, u] = \int_0^T L(x(t), u(t)) dt + \Phi(x(T)). \quad (4.5)$$

We say that (x, u) is an optimal trajectory if $J[x, u] \leq J[x', u']$ for all controlled trajectories (x', u') . The time-optimal optimization problem is a special case of this optimization problem with a free duration T as well as $L = 1$ and $\Phi = 0$.

To state the PMP we define a *Hamiltonian* depending on a tangent vector $p \in T_x M$ and a real number $p^0 \in \mathbb{R}$ as

$$\mathcal{H}(x, p, p^0, u) = \langle p, f(x, u) \rangle + p^0 L(x, u) \quad (4.6)$$

where $\langle \cdot, \cdot \rangle$ denotes the inner product. This Hamiltonian is not to be confused with the Hamiltonian describing the evolution of a quantum system. We therefore denote it as \mathcal{H} instead of H . Note that with this definition of \mathcal{H} we obtain

$$\dot{x} = \frac{\partial \mathcal{H}}{\partial p} \quad (4.7)$$

in analogy to Hamilton's equation in classical mechanics. (For $n > 1$ we take $\partial/\partial x$ to mean the gradient with respect to x .)

The PMP now states that for every optimal trajectory (x, u) there exist so-called *costates* $p(t) \in T_{x(t)} M$ and a number $p^0 \in \{-1, 0\}$ such that all of the following statements hold

i) The pair $(p^0, p(t))$ never vanishes, i.e. if $p^0 = 0$ then $p(t) \neq 0$ for all t .

ii) The costates satisfy

$$\dot{p} = -\frac{\partial \mathcal{H}}{\partial x}. \quad (4.8)$$

Again, this is in analogy to Hamilton's equation in classical mechanics.

iii) For all times t it holds that

$$H(x(t), p(t), p^0, u(t)) = \max_{u'} H(x(t), p(t), p^0, u') \quad (4.9)$$

where \max denotes the maximum.

iv) The Hamiltonian along the optimal trajectory, i.e. $H(x(t), p(t), p^0, u(t))$, is constant. If T is free, we even have $H(x(t), p(t), p^0, u(t)) = 0$ for all t .

v) Denote by Π the projector onto the tangent space $T_{x(T)}\mathcal{T}$ of \mathcal{T} at $x(T)$. (If \mathcal{T} collapses to a single point we take $\Pi = 0$). Then

$$\Pi(p(T)) = p^0 \Pi \left(\frac{\partial \Phi(x(T))}{\partial x} \right) \quad (4.10)$$

In other words, Eq. (4.10) tells us the final value of the costates $p(T)$, but only along the directions of the tangent space of \mathcal{T} at the final point $x(T)$.

For our application of the PMP we will mostly work with statements *ii*) and *iii*). They allow to find optimal trajectories as follows: If the maximum in Eq. (4.9) is achieved by a unique value u , Eq. (4.9) can be used to obtain a relationship $u(x, p)$. (Later we will prove that for time-optimal pulses on Rydberg atoms, this maximizer $u(x, p)$ is indeed always unique.) Then, given the initial state $x(0) = x_i$ and the initial costate $p(0)$, the differential equations Eq. (4.7) and (4.8) can be solved to obtain $x(t), p(t)$ and $u(t)$ for the whole trajectory. Unfortunately, the initial costate $p(0)$ of the optimal trajectory is generally unknown and has to be determined by other means, for example by numerically finding all initial costates $p(0)$ that lead to a trajectory with $x(T) \in \mathcal{T}$ and then selecting the trajectory with the minimal cost out of all of these candidates. Nevertheless this reduces the search space from the space of all controlled trajectories to the space of all initial costates, i.e. from an infinite dimensional space to a finite dimensional space.

4.2 Proof Sketch

An exact proof of the PMP is beyond the scope of this thesis, the interested reader is referred to Ref. [160]. In the following we sketch proof of the PMP based on the Lagrange multiplier theorem, adapted from Ref. [159].

The Lagrange multiplier theorem states the following: Suppose we want to minimize a differentiable function $f : \mathbb{R}^n \rightarrow \mathbb{R}$ under m equality constraints $g_1(x) = g_2(x) = \dots = g_m(x) = 0$, where the $g : \mathbb{R}^n \rightarrow \mathbb{R}$ are differentiable. Let x be the minimum of f under these constraints. If the gradients $\nabla g_1(x), \dots, \nabla g_m(x)$ are linearly independent then there exists a so-called *Lagrange multiplier* $\lambda \in \mathbb{R}^m$ such that

$$\nabla f(x) = \sum_{j=1}^m \lambda_j \nabla g_j(x). \quad (4.11)$$

The requirement that the $\nabla g_1(x), \dots, \nabla g_m(x)$ have to be linearly independent can be elegantly incorporated by stating that there exists a $\lambda_0 \in \{-1, 0\}$ and a $\lambda \in \mathbb{R}^m$ such that the pair (λ_0, λ) does not vanish and such that

$$\lambda_0 \nabla f(x) + \sum_{j=1}^m \lambda_j \nabla g_j(x) = 0. \quad (4.12)$$

If the $\nabla g_1(x), \dots, \nabla g_m(x)$ are linearly independent then by the Lagrange multiplier theorem there exists a solution to Eq. (4.12) with $\lambda_0 = -1$. If the $\nabla g_1(x), \dots, \nabla g_m(x)$ are instead linearly dependent, then by the definition of linear dependence there exists a solution to Eq. (4.12) with $\lambda_0 = 0$ and $\lambda \neq 0$.

We now apply the Lagrange multiplier theorem to the minimization of the cost function $J[x, u]$. We want to minimize J over all trajectories $x : [0, T] \rightarrow M$ with $x(0) = x_i$ and $x(T) \in \mathcal{T}$, all controls $u : [0, T] \rightarrow M$, and, if T is free, over all durations T , under the constraint that for all t we have $\dot{x}(t) = f(x(t), u(t))$. By the Lagrange multiplier theorem there exist $p^0 \in \{-1, 0\}$ and time dependent costates $p(t)$ such that for

$$S = p^0 \Phi(x(T)) + \int_0^T [p^0 L(x(t), u(t)) + \langle p(t), f(x(t), u(t)) - \dot{x}(t) \rangle] dt \quad (4.13)$$

the variations δS with respect to δx and δu vanish. For the case of a free final time we additionally obtain $\partial S / \partial T = 0$.

Using integration by parts and the definition of the Hamiltonian \mathcal{H} [Eq. (4.6)], S can be conveniently rewritten as

$$S = p^0 \Phi(x(T)) - \langle p(T), x(T) \rangle + \langle p(0), x(0) \rangle + \int_0^T [\mathcal{H}(x(t), p(t), p^0, u(t)) + \langle \dot{p}(t), x(t) \rangle] dt. \quad (4.14)$$

The variation of S is then given by

$$\delta S = \left\langle p^0 \frac{\partial \Phi(x(T))}{\partial x} - p(T), \delta x(T) \right\rangle + \int_0^T \left[\left\langle \frac{\partial \mathcal{H}}{\partial x} + \dot{p}, \delta x(t) \right\rangle + \left\langle \frac{\partial \mathcal{H}}{\partial u}, \delta u(t) \right\rangle \right] dt. \quad (4.15)$$

From $\delta S = 0$ for all variations δx with $\delta x(T) \in T_{x(T)}\mathcal{T}$ it follows that $\partial \mathcal{H} / \partial x + \dot{p} = 0$ [statement *ii*] and that

$$p^0 \Pi \left(\frac{\partial \Phi(x(T))}{\partial x} \right) - \Pi(p(T)) = 0 \quad (4.16)$$

[statement *v*]. From $\delta S = 0$ for all variations δu it follows that $\partial \mathcal{H} / \partial u = 0$. This is a weaker version of statement *iii*), since it only assesses that the optimal control u is an extremum or a saddle point of \mathcal{H} . The proof that u is indeed a maximum of \mathcal{H} , as stated by statement *iii*), is beyond the scope of this proof sketch.

Now only statement *iv*) is missing. To prove that \mathcal{H} is constant along the optimal trajectory we simply calculate

$$\frac{d\mathcal{H}}{dt} = \underbrace{\frac{\partial \mathcal{H}}{\partial x}}_{=-\dot{p}} \dot{x} + \underbrace{\frac{\partial \mathcal{H}}{\partial p}}_{=\dot{x}} \dot{p} + \underbrace{\frac{\partial \mathcal{H}}{\partial u}}_{=0} \dot{u} = 0. \quad (4.17)$$

To show that for free T we even have $\mathcal{H} = 0$ along the optimal trajectory we use that $\partial S/\partial T = 0$ and calculate

$$\begin{aligned}
0 &= \frac{\partial S}{\partial T} = \frac{\partial}{\partial T} (p^0 \Phi(x(T)) - \langle p(T), x(T) \rangle) + \mathcal{H}(x(T), p(T), p^0, u(T)) + \langle \dot{p}(T), x(T) \rangle \\
&= \left\langle p^0 \frac{\partial \Phi(x(T))}{\partial x} - p(T), \dot{x}(T) \right\rangle + \mathcal{H}(x(T), p(T), p^0, u(T)) \\
&= \mathcal{H}(x(T), p(T), p^0, u(T))
\end{aligned} \tag{4.18}$$

where the last equality follows from statement v). Since \mathcal{H} vanishes at the final time and is constant along the optimal trajectory it must also vanish everywhere along the optimal trajectory. This completes our proof of the PMP.

4.3 Formulation of the PMP for Quantum Optimal Control Problems

In this section we adapt the formulation of the PMP from Sec. 4.1 to the specific case of controlling a quantum system. For this, we consider the following problem: Given a Hamiltonian $H(u)$ depending on a set of controls $u \in \mathcal{U} \subseteq \mathbb{R}^m$, an initial state $|\psi_i\rangle$, a manifold of possible final states \mathcal{T} , a Lagrangian $L(|\psi\rangle, u)$ depending on a quantum state and a control, and a terminal cost function $\Phi(|\psi\rangle)$ for quantum states in \mathcal{T} , we want to minimize

$$J = \int_0^T L(|\psi(t)\rangle, u(t)) dt + \Phi(|\psi(T)\rangle) \tag{4.19}$$

over all trajectories $|\psi(t)\rangle$ and controls $u(t)$ of duration T with $|\psi(0)\rangle = |\psi_i\rangle$, $|\psi(T)\rangle \in \mathcal{T}$ and $|\dot{\psi}(t)\rangle = -iH(u(t))|\psi(t)\rangle$.

This is exactly the setting of the PMP as discussed in Sec. 4.1, with the manifold M being the set of all normalized quantum states, and the steering function f given by $f(|\psi\rangle, u) = -iH(u)|\psi\rangle$. The fact that our state space is now a complex vector space requires two adaptations of the PMP: First, all inner products $\langle x, y \rangle$ in the formulation of the PMP have to be replaced by the *real part* of the inner product between quantum states $\text{Re}(\langle \phi | \psi \rangle) = \langle \text{Re}(|\psi\rangle), \text{Re}(|\phi\rangle) \rangle + \langle \text{Im}(|\psi\rangle), \text{Im}(|\phi\rangle) \rangle$. Second, the gradients of Φ and \mathcal{H} with respect to x and p have to be replaced by Wirtinger derivatives. The Wirtinger derivative of a real function $f(|\psi\rangle)$ depending on a complex state $|\psi\rangle$ is defined as

$$\frac{\partial f}{\partial |\psi\rangle} = \frac{\partial f}{\partial \text{Re}(|\psi\rangle)} - i \frac{\partial f}{\partial \text{Im}(|\psi\rangle)} \tag{4.20}$$

where on the right hand side we treat $\text{Re}(|\psi\rangle)$ and $\text{Im}(|\psi\rangle)$ as independent variables. The Wirtinger derivative is the natural extension of the derivative to functions with

complex inputs and real outputs, as it satisfies

$$f(|\psi\rangle + \varepsilon|\phi\rangle) = f(|\psi\rangle) + \varepsilon \operatorname{Re} \left(\left\langle \frac{\partial f}{\partial |\psi\rangle} \middle| \phi \right\rangle \right) + \mathcal{O}(\varepsilon^2). \quad (4.21)$$

as $\varepsilon \rightarrow 0$. With these modifications we can now state the PMP. The costates $p^0, p(t)$ from the real formulation are now replaced by $\chi^0 \in \{-1, 0\}$ and quantum costates $|\chi(t)\rangle$. The PMP Hamiltonian \mathcal{H} (different from the Hamiltonian H of the quantum system), is defined as

$$\begin{aligned} \mathcal{H}(|\psi\rangle, |\chi\rangle, \chi^0, u) &= \operatorname{Re} \langle \chi | -iH(u)|\psi\rangle + \chi^0 L(|\psi\rangle, u) \\ &= \operatorname{Im} \langle \chi | H(u)|\psi\rangle + \chi^0 L(|\psi\rangle, u). \end{aligned} \quad (4.22)$$

Since the states $|\psi(t)\rangle$ that we consider are confined to the manifold defined by $\langle \psi(t)|\psi(t)\rangle = 1$, the costates are confined to the tangent space of this manifold and must satisfy $\operatorname{Re} \langle \chi(t)|\psi(t)\rangle = 0$ for all times t .

The PMP now states that for the optimal trajectory $(|\psi(t)\rangle, u(t))$ there exist $\chi^0 \in \{-1, 0\}$ and costates $|\chi(t)\rangle$ with $\operatorname{Re} \langle \chi(t)|\psi(t)\rangle = 0$ such that all of the following statements hold:

i) The pair $(\chi^0, |\chi(t)\rangle)$ vanishes at no time t .

ii) The costates satisfy

$$|\dot{\chi}\rangle = -\frac{\partial \mathcal{H}}{\partial |\psi\rangle} = -iH|\chi\rangle + \chi^0 \frac{\partial L}{\partial |\psi\rangle}. \quad (4.23)$$

iii) For all times t it holds that

$$\mathcal{H}(|\psi(t)\rangle, |\chi(t)\rangle, \chi^0, u(t)) = \max_{u'} \mathcal{H}(|\psi(t)\rangle, |\chi(t)\rangle, \chi^0, u') \quad (4.24)$$

iv) \mathcal{H} is constant along the optimal trajectory. If the final time T is free, we even have $\mathcal{H}(|\psi(t)\rangle, |\chi(t)\rangle, \chi^0, u(t)) = 0$ for all t .

v) Let Π be the projector onto the tangent space of \mathcal{T} at $|\psi(T)\rangle$. Then

$$\Pi |\chi(T)\rangle = \chi^0 \Pi \frac{\partial \Phi(|\psi(T)\rangle)}{\partial |\psi\rangle}. \quad (4.25)$$

4.4 Application of the PMP to Time-Optimal Gates on Rydberg Atoms

We now apply the PMP to the problem of simultaneously controlling N quantum systems with the Hamiltonians

$$H_n = \frac{\sqrt{n}\Omega_{\max}e^{i\varphi}}{2} |0\rangle \langle 1| + \text{h.c.} = \frac{\sqrt{n}\Omega_{\max}}{2} (\cos \varphi \sigma_x - \sin \varphi \sigma_y) \quad (4.26)$$

with $n = 1, 2, \dots, N$, where σ_x and σ_y denote the Pauli X and Y operators, respectively. For simplicity we will set $\Omega_{\max} = 1$ for the remainder of this chapter.

The Hamiltonians H_1, \dots, H_N describe, up to relabeling of the states, the evolution of N atoms under a perfect Rydberg blockade and a global pulse with Rabi frequency $\Omega_{\max} e^{i\varphi(t)}$ as described in Sec. 3.1. We start with N systems in the initial state $|\psi_n(0)\rangle = |0\rangle$ and evolve them under the TDSE $|\dot{\psi}_n\rangle = -iH_n |\psi_n\rangle$. To implement a phase gate with phases $\bar{\zeta}_1, \dots, \bar{\zeta}_N$ in a time-optimal fashion, our goal is to find the shortest possible pulse $\varphi : [0, T] \rightarrow \mathbb{R}$ such that there is a θ with $|\psi_n(T)\rangle = e^{i(n\theta + \bar{\zeta}_n)} |0\rangle$ for all n .

The PMP can be applied to this problem with the Hamiltonian $H = H_1 \oplus \dots \oplus H_N$, the target manifold

$$\mathcal{T} = \left\{ e^{i(\theta + \bar{\zeta}_1)} |0\rangle \oplus e^{i(2\theta + \bar{\zeta}_2)} |0\rangle \oplus \dots \oplus e^{i(N\theta + \bar{\zeta}_N)} |0\rangle \mid \theta \in [0, 2\pi] \right\} \quad (4.27)$$

the Lagrangian $L = 1$, and the terminal cost function $\Phi = 0$. The pulse duration T is of course taken to be free. The PMP states that for the optimal trajectory $|\psi_1(t)\rangle, \dots, |\psi_N(t)\rangle, \varphi(t)$ there are costates $\chi^0 \in \{-1, 0\}$ and $|\chi_1(t)\rangle, \dots, |\chi_N(t)\rangle$ with $\text{Re} \langle \chi_n(t) | \psi_n(t) \rangle = 0$ such that the following conditions hold:

- i)* The tuple $(\chi^0, |\chi_1(t)\rangle, \dots, |\chi_N(t)\rangle)$ never vanishes.
- ii)* The costates satisfy the TDSE

$$|\dot{\chi}_n\rangle = -iH_n |\chi_n\rangle. \quad (4.28)$$

- iii)* For all times t the optimal phase $\varphi(t)$ is a maximizer of

$$\begin{aligned} \mathcal{H} &= \sum_n \text{Im} \langle \chi_n | H_n | \psi_n \rangle + \chi^0 \\ &= \frac{1}{2} \cos \varphi \left(\sum_n \sqrt{n} \text{Im} \langle \chi_n | \sigma_x | \psi_n \rangle \right) - \frac{1}{2} \sin \varphi \left(\sum_n \sqrt{n} \text{Im} \langle \chi_n | \sigma_y | \psi_n \rangle \right) + \chi^0 \end{aligned} \quad (4.29)$$

This maximum is unique and can be calculated analytically. It is given by φ such that

$$\cos \varphi = \frac{\sum_n \sqrt{n} \text{Im} \langle \chi_n | \sigma_x | \psi_n \rangle}{\sqrt{(\sum_n \sqrt{n} \text{Im} \langle \chi_n | \sigma_x | \psi_n \rangle)^2 + (\sum_n \sqrt{n} \text{Im} \langle \chi_n | \sigma_y | \psi_n \rangle)^2}} \quad (4.30)$$

and

$$\sin \varphi = -\frac{\sum_n \sqrt{n} \text{Im} \langle \chi_n | \sigma_y | \psi_n \rangle}{\sqrt{(\sum_n \sqrt{n} \text{Im} \langle \chi_n | \sigma_x | \psi_n \rangle)^2 + (\sum_n \sqrt{n} \text{Im} \langle \chi_n | \sigma_y | \psi_n \rangle)^2}} \quad (4.31)$$

[See statement *iv)* below and Appendix 4.A on why the denominator cannot vanish] The value of \mathcal{H} along the optimal trajectory is then given by

$$\mathcal{H} = \frac{1}{2} \left[\left(\sum_n \sqrt{n} \text{Im} \langle \chi_n | \sigma_x | \psi_n \rangle \right)^2 + \left(\sum_n \sqrt{n} \text{Im} \langle \chi_n | \sigma_y | \psi_n \rangle \right)^2 \right]^{1/2} + \chi^0. \quad (4.32)$$

iv) Along the optimal trajectory we have $\mathcal{H} = 0$. For now, we will assume $\chi^0 = -1$. We consider so-called *abnormal* solutions with $\chi^0 = 0$ [159] separately in Appendix 4.A and show that no abnormal solution can implement a C-Phase gate faster than the fastest normal solution.

With $\chi^0 = -1$ we obtain that

$$\left(\sum_n \sqrt{n} \text{Im} \langle \chi_n | \sigma_x | \psi_n \rangle \right)^2 + \left(\sum_n \sqrt{n} \text{Im} \langle \chi_n | \sigma_y | \psi_n \rangle \right)^2 = 4. \quad (4.33)$$

This also simplifies Eq. (4.30) and (4.31) to

$$\cos \varphi = \frac{1}{2} \sum_n \sqrt{n} \text{Im} \langle \chi_n | \sigma_x | \psi_n \rangle \quad (4.34)$$

and

$$\sin \varphi = -\frac{1}{2} \sum_n \sqrt{n} \text{Im} \langle \chi_n | \sigma_y | \psi_n \rangle. \quad (4.35)$$

v) The derivative of the final state $|\psi_n(T)\rangle$ with respect to the single qubit phase θ is given by $d|\psi_n(T)\rangle/d\theta = in|\psi_n(T)\rangle$. The tangent space of \mathcal{T} at $|\psi_1(T)\rangle \oplus \dots \oplus |\psi_N(T)\rangle$ is thus a one dimensional vector space spanned by $i|\psi_1(T)\rangle \oplus 2i|\psi_2(T)\rangle \oplus \dots \oplus Ni|\psi_N(T)\rangle$. Thus, statement *v)* of the PMP becomes

$$0 = \sum_n \text{Re}(in \langle \chi_n(T) | \psi_n(T) \rangle) = - \sum_n n \text{Im} \langle \chi_n(T) | \psi_n(T) \rangle. \quad (4.36)$$

Since $|\psi_n\rangle$ and $|\chi_n\rangle$ both evolve under the TDSE given by H_n , their scalar product $\langle \chi_n | \psi_n \rangle$ is constant in time. Thus, we can conclude that at all times

$$\sum_n n \text{Im} \langle \chi_n | \psi_n \rangle = 0. \quad (4.37)$$

Given initial costates $|\chi_1(0)\rangle, \dots, |\chi_N(0)\rangle$, the TDSEs $|\dot{\psi}_n\rangle = -iH_n|\psi_n\rangle$ and $|\dot{\chi}_n\rangle = -iH_n|\chi_n\rangle$ together with Eq. (4.34) and (4.35) allow us to calculate $|\psi(t)\rangle, |\chi(t)\rangle$ and $\varphi(t)$ along the whole trajectory. Our goal is now to find initial costates as well as a pulse duration T such that the final states are of the form $|\psi_n(T)\rangle = e^{i(n\theta + \zeta_n)}|0\rangle$ for some θ . The PMP further states that we can limit our search to initial costates which satisfy $\text{Re} \langle \chi_n | \psi_n \rangle = 0$ as well as Eq. (4.33) and Eq. (4.37).

A particularly elegant formulation can be obtained by introducing N 3-dimensional vectors $v_n = (v_n^{(x)}, v_n^{(y)}, v_n^{(z)})$ given by $v_n^{(\alpha)} = \text{Im} \langle \chi_n | \sigma_\alpha | \psi_n \rangle$ for $\alpha \in \{x, y, z\}$. Then

$$\dot{v}_n^{(\alpha)} = \text{Im}(i \langle \chi_n | [H_n, \sigma_\alpha] | \psi_n \rangle) \quad (4.38)$$

which leads to

$$\dot{v}_n = \sqrt{n} \begin{pmatrix} \cos \varphi \\ -\sin \varphi \\ 0 \end{pmatrix} \times v_n = \sqrt{n} \begin{pmatrix} -\sin \varphi v_n^{(z)} \\ -\cos \varphi v_n^{(z)} \\ \cos \varphi v_n^{(y)} + \sin \varphi v_n^{(x)} \end{pmatrix} \quad (4.39)$$

with

$$\cos \varphi = \frac{1}{2} \sum_n \sqrt{n} v_n^{(x)} \quad \sin \varphi = -\frac{1}{2} \sum_n \sqrt{n} v_n^{(y)}. \quad (4.40)$$

We thus obtain $3N$ coupled quadratic differential equations for the v_n .

Solving this system of differential equations can be simplified by the presence of conserved quantities. From Eq. (4.39) we immediately obtain N conserved quantities

$$r_n = \|v_n\| = \sqrt{v_n^{(x)2} + v_n^{(y)2} + v_n^{(z)2}}. \quad (4.41)$$

Additionally, Eq. (4.33) gives

$$\left(\sum_n \sqrt{n} v_n^{(x)} \right)^2 + \left(\sum_n \sqrt{n} v_n^{(y)} \right)^2 = 4. \quad (4.42)$$

Finally,

$$C = \sum_n v_n^z \quad (4.43)$$

is a conserved quantity. To see this, we calculate

$$\begin{aligned} \frac{dC}{dt} &= \frac{1}{2} \sum_n \sqrt{n} (\cos \varphi v_n^{(y)} + \sin \varphi v_n^{(x)}) \quad (4.44) \\ &= \frac{1}{2} \underbrace{\left(\sum_n \sqrt{n} v_n^{(y)} \right)}_{=-\sin \varphi} \cos \varphi + \frac{1}{2} \underbrace{\left(\sum_n \sqrt{n} v_n^{(x)} \right)}_{=\cos \varphi} \sin \varphi \\ &= 0. \end{aligned}$$

Solving this system of $3N$ differential equations with $N + 2$ conserved quantities for an arbitrary N is still a daunting task. However, in Sec. 4.5 we will provide an analytical solution in the $N = 2$ case.

We end this section with an interesting observation: From statement $v)$ of the PMP we know that $\sum_n n \text{Im} \langle \chi_n | \psi_n \rangle = 0$ at all times (see Eq. (4.37)). At $t = 0$ and $t = T$ all $|\psi_n\rangle$ are proportional to $|0\rangle$, so that $|\psi_n\rangle = \sigma_z |\psi_n\rangle$. Hence we obtain

$$\sum_n n v_n^{(z)}(t) = 0 \quad (4.45)$$

at $t = 0$ and $t = T$. Now we introduce the detuning $\Delta = d\varphi/dt$ and find that

$$\Delta \cos \varphi = \frac{d}{dt} \sin \varphi = -\frac{1}{2} \sum_n \sqrt{n} \dot{v}_n^y = \frac{1}{2} \sum_n n \cos \varphi v_n^{(z)} \quad (4.46)$$

Dividing by $\cos \varphi$ gives

$$\Delta = \frac{1}{2} \sum_n n v_n^{(z)}. \quad (4.47)$$

In particular, we obtain $\Delta(0) = \Delta(T) = 0$, showing that for any time-optimal pulse the laser detuning must vanish at the beginning and at the end of the pulse.

In summary, in this section we have shown that the time-optimal laser phase $\varphi(t)$ for a phase gate on N atoms can be obtained by a solution of $3N$ coupled quadratic differential equations. Unfortunately the initial condition of this system of differential equations are not known, so that each possible initial condition gives a different candidate pulse $\varphi(t)$, out of which the time-optimal one still has to be selected. We have also shown that the detuning Δ of the time-optimal pulse must vanish in the beginning and in the end of the pulse.

4.5 Semi-Analytical Pulses for Two-Qubit Gates

In this section we continue the discussion of Sec. 4.4 for the special case of $N = 2$ atoms. For this we use that the r_n are conserved quantities and introduce the parameterization

$$v_n = \begin{pmatrix} \sqrt{r_n^2 - z_n^2} \cos \xi_n \\ \sqrt{r_n^2 - z_n^2} \sin \xi_n \\ z_n \end{pmatrix} \quad (4.48)$$

with the new variables ξ_1, ξ_2, z_1, z_2 . Expressing Eq. (4.42) in this new parameterization gives

$$\begin{aligned} 4 &= \left(\sqrt{r_1^2 - z_1^2} \cos \xi_1 + \sqrt{2} \sqrt{r_2^2 - z_2^2} \cos \xi_2 \right)^2 + \left(\sqrt{r_1^2 - z_1^2} \sin \xi_1 + \sqrt{2} \sqrt{r_2^2 - z_2^2} \sin \xi_2 \right)^2 \\ &= r_1^2 - z_1^2 + 2(r_2^2 - z_2^2) + \sqrt{8} \sqrt{r_1^2 - z_1^2} \sqrt{r_2^2 - z_2^2} \cos(\xi_1 - \xi_2). \end{aligned} \quad (4.49)$$

so that

$$\sqrt{8} \sqrt{r_1^2 - z_1^2} \sqrt{r_2^2 - z_2^2} \cos(\xi_1 - \xi_2) = 4 - (r_1^2 - z_1^2) - 2(r_2^2 - z_2^2). \quad (4.50)$$

Calculating \dot{z}_1 gives

$$\begin{aligned} \dot{z}_1 &= \cos \varphi v_1^{(y)} + \sin \varphi v_1^{(x)} \\ &= \sqrt{r_1^2 - z_1^2} (\cos \varphi \sin \xi_1 + \sin \varphi \cos \xi_1) \\ &= \frac{1}{2} \sqrt{r_1^2 - z_1^2} \left(\sqrt{r_1^2 - z_1^2} \cos \xi_1 + \sqrt{2} \sqrt{r_2^2 - z_2^2} \cos \xi_2 \right) \sin \xi_1 \\ &\quad - \frac{1}{2} \sqrt{r_1^2 - z_1^2} \left(\sqrt{r_1^2 - z_1^2} \sin \xi_1 + \sqrt{2} \sqrt{r_2^2 - z_2^2} \sin \xi_2 \right) \cos \xi_1 \\ &= \frac{1}{\sqrt{2}} \sqrt{r_1^2 - z_1^2} \sqrt{r_2^2 - z_2^2} \sin(\xi_1 - \xi_2) \end{aligned} \quad (4.51)$$

so that

$$\sqrt{8}\sqrt{r_1^2 - z_1^2}\sqrt{r_2^2 - z_2^2}\sin(\xi_1 - \xi_2) = 4\dot{z}_1. \quad (4.52)$$

By adding the squares of Eq. (4.50) and (4.52) we obtain

$$8(r_1^2 - z_1^2)(r_2^2 - z_2^2) = 16\dot{z}_1^2 + [4 - (r_1^2 - z_1^2) - 2(r_2^2 - z_1^2)]^2. \quad (4.53)$$

From Eq. (4.47) and Eq. (4.43) we obtain $z_1 + 2z_2 = 2\Delta$ and $z_1 + z_2 = C$ so that

$$z_1 = -2\Delta + 2C \quad (4.54)$$

$$z_2 = 2\Delta - C. \quad (4.55)$$

Substituting this into Eq. (4.53) and using that $\dot{C} = 0$ gives

$$\frac{1}{2}\dot{\Delta}^2 + V(\Delta) = 0 \quad (4.56)$$

were

$$V(\Delta) = c_4\Delta^4 + c_3\Delta^3 + c_2\Delta^2 + c_1\Delta + c_0 \quad (4.57)$$

with

$$c_4 = 1/8 \quad (4.58)$$

$$c_3 = 0 \quad (4.59)$$

$$c_2 = (-2C^2 + r_1^2 - 2r_2^2 + 12) / 16 \quad (4.60)$$

$$c_1 = -C \quad (4.61)$$

$$c_0 = \left[(6C^2 - r_1^2 - 2r_2^2 + 4)^2 - 8(4C^2 - r_1^2)(C^2 - r_2^2) \right] / 128. \quad (4.62)$$

This completes our proof of Eq. (4.1), the main result of this chapter, and shows that the laser detuning for a time-optimal C-Phase gate on two qubits has the same functional dependency as the oscillation of a classical particle in a quartic potential.

It remains to numerically determine the coefficients c_2, c_1, c_0 such that the resulting pulse $\Delta(t)$ implements a C-Phase gate with a given two qubit have ϕ , and to compare this pulse with the results obtained by GRAPE in Sec. 3.5. For this, it is useful to use a slightly different parameterization of V : Since $V(0) < 0$, but $V(\Delta) \rightarrow \infty$ as $\Delta \rightarrow \pm\infty$, V must have at least one negative and at least one positive root. (As we will see, there are in fact the only roots of V .) We denote by $\Delta_- < 0$ the largest negative and by $\Delta_+ > 0$ the smallest positive root. V can then be parameterized as

$$V(\Delta) = (\Delta - \Delta_-)(\Delta - \Delta_+) \left(\frac{1}{8}\Delta^2 + \frac{\Delta_+ + \Delta_-}{8}\Delta + \frac{V_0}{\Delta_+\Delta_-} \right) \quad (4.63)$$

where $V_0 = V(0) < 0$. The last factor of V has the roots

$$\frac{\Delta_+ + \Delta_-}{2} \pm \sqrt{\frac{(\Delta_+ + \Delta_-)^2}{4} - \frac{8V_0}{\Delta_+\Delta_-}}. \quad (4.64)$$

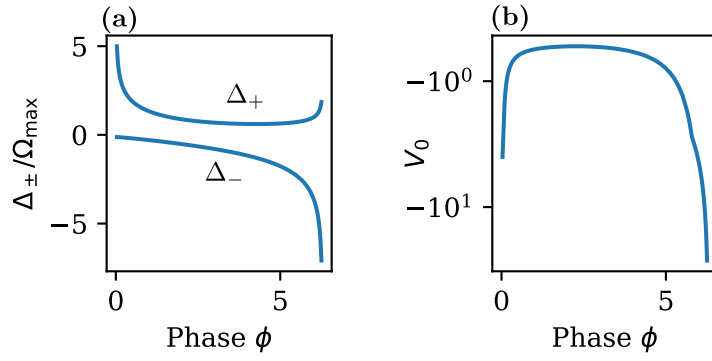


Figure 4.1: Optimal parameters of $V(\Delta)$. Parameters (a) Δ_{\pm} and (b) V_0 to implement a time-optimal C-Phase gate as a function of the two-qubit phase ϕ .

If $0 > V_0 > \Delta_+ \Delta_- (\Delta_+ + \Delta_-)^2 / 32$, these roots are real but always in the interval $[\Delta_-, \Delta_+]$, contradicting the fact that Δ_- is the largest negative and Δ_+ is the smallest positive root of V . Thus we obtain the additional constraint

$$V_0 < \frac{1}{32} \Delta_+ \Delta_- (\Delta_+ + \Delta_-)^2 \quad (4.65)$$

and can conclude that Δ_+ and Δ_- are in fact the only roots of V .

To find the parameters Δ_+, Δ_- and V_0 that correspond to a C-Phase gate with a two-qubit phase ϕ we now proceed as follows: We first assume without loss of generality that $\dot{\Delta}(0) > 0$ (This corresponds to the pulses of type 1 in Sec. 3.5. The pulses with $\dot{\Delta}(0) < 0$ correspond to pulses of type 2 and are related to pulses of type 1 by the transformation $\Delta \mapsto -\Delta, \phi \mapsto 2\pi - \phi$). For a given set of parameters Δ_-, Δ_+, V_0 we now numerically integrate the second order differential equation

$$\ddot{\Delta}(t) = -\frac{dV(\Delta)}{d\Delta} \quad (4.66)$$

with the initial conditions $\Delta(0) = 0$ and $\dot{\Delta} = \sqrt{-2V_0}$. From inspecting the C-Phase pulses found by GRAPE [Fig. 3.6(c/d)] we see that the time-optimal pulses have a detuning $\Delta(t) = 0$ at exactly two times $0 < t < T$. This means that the pulse duration T has to be chosen such that $\Delta(T) = 0$ for the fourth time in the pulse (counting the initial time $t = 0$). Having found $\Delta(t)$, we now solve the TDSE given by the H_1, H_2 [Eq. (4.26)] to obtain the final states $|\psi_1(t)\rangle, |\psi_2(t)\rangle$. Now we evaluate the Bell state fidelity (see Sec. 3.1.2) as

$$F = \min_{\theta} \frac{1}{16} \left| 1 + 2e^{-i\theta} \langle 0 | \psi_1(T) \rangle + e^{-i(2\theta+\phi)} \langle 0 | \psi_2(T) \rangle \right|^2. \quad (4.67)$$

Finally, we numerically minimize the infidelity $1 - F$ over Δ_-, Δ_+, V_0 using the BFGS algorithm with gradients estimated by a finite difference method [161]. We choose the starting point of the optimization by estimating Δ_{\pm} from the maximum/minimum value of Δ and V_0 from $\dot{\Delta}(0)$ of the pulses found by GRAPE. The optimal parameters Δ_{\pm} and V_0 are shown in Fig. 4.1(a) and (b), respectively. Interestingly V_0 , and thus the initial slope of Δ , diverges as $\phi \rightarrow 0, 2\pi$. We note that the

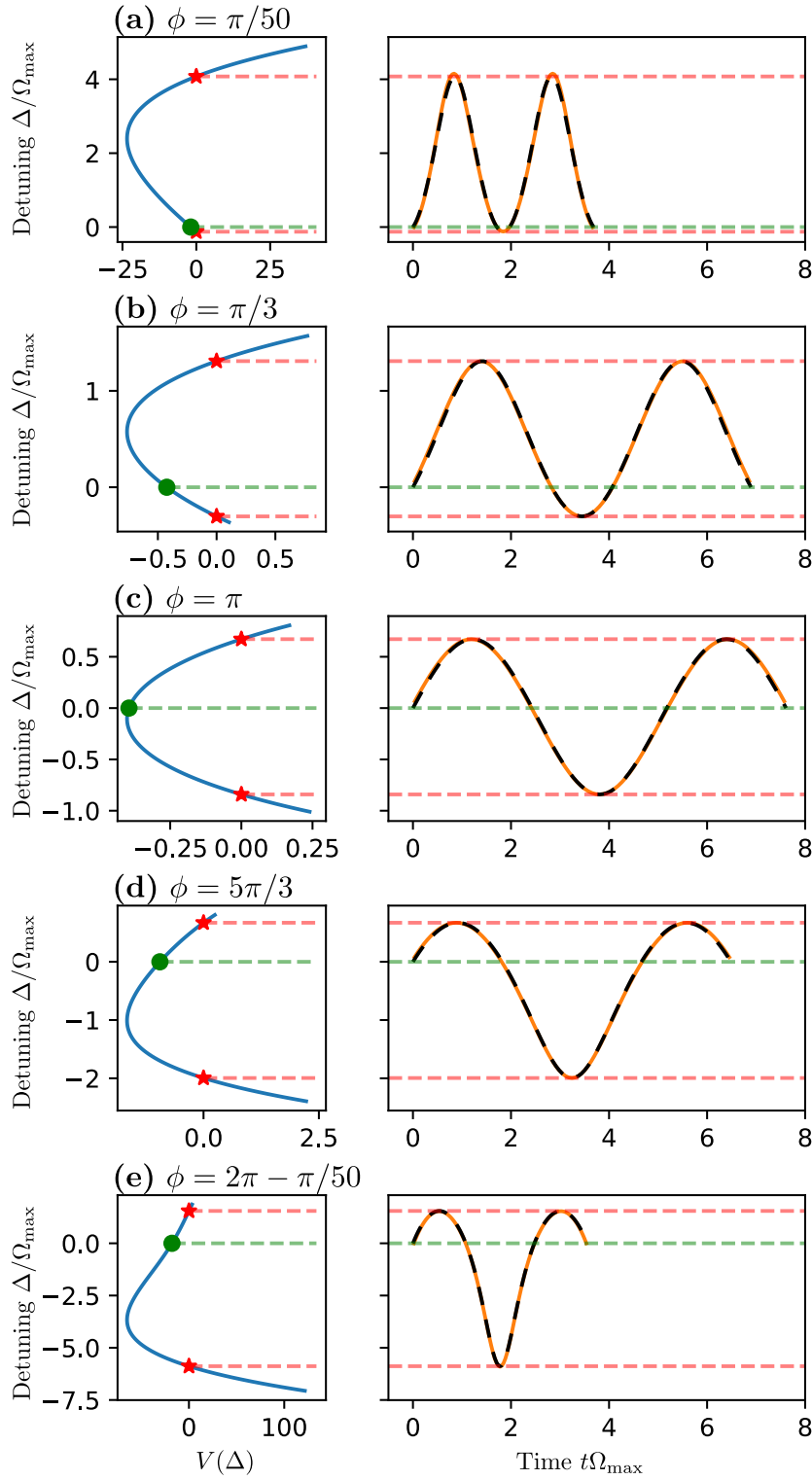


Figure 4.2: Pulse shapes found using the PMP. Left column: Potential $V(\Delta)$ for a C-Phase gate with two qubit phase ϕ . Red stars show the turning points with $V(\Delta) = 0$, green circle shows the starting point $\Delta = 0$. Right column: Detuning $\Delta(t)$ of the time-optimal pulse. The orange pulse is obtained by GRAPE, the black pulse is obtained by the PMP. Dashed red and green lines show the turning points and the start/end point of Δ , respectively.

minimal infidelity $1 - F$ is always below 10^{-8} , showing that a C-Phase gate can be achieved exactly using the pulses found by the PMP.

To show that these pulses are also the same as the pulses found by GRAPE, and thus the time-optimal pulses, we compare the detunings $\Delta(t)$ for both methods in Fig. 4.2 for different values of ϕ . The left column shows the potential $V(\Delta)$ with the turning points Δ_{\pm} of the detuning marked by red stars, and the initial detuning $\Delta = 0$ marked by a green circle. The pulses obtained by the PMP are shown as the black dashed curves in the right column of Fig. 4.2. They correspond to an oscillation of a particle with position Δ and energy 0 in the potential $V(\Delta)$. The turning points at Δ_{\pm} as well as the initial and final detuning $\Delta(0) = \Delta(T) = 0$ are indicated by the red and green dashed lines, respectively. The orange curve shows the pulses found by GRAPE in Sec. 3.5. We observe an excellent agreement between the pulses found by GRAPE and by the PMP for all values of ϕ , showing that the semi-analytical pulses found in this chapter indeed capture the time-optimal pulses.

In summary, we have demonstrated that time-optimal pulses for C-Phase gates can be described by just three parameters (Δ_{\pm} and V_0) and are given by the solution of the differential equation (4.56). The detuning $\Delta(t)$ of time-optimal pulses is thus given by the position of a particle oscillating in a quartic potential $V(\Delta)$. The PMP makes no statement on the values of Δ_{\pm} and V_0 that are required for a given phase ϕ . Instead we determined Δ_{\pm} and V_0 numerically by matching the final state $|\psi_1(T)\rangle, |\psi_2(T)\rangle$ with the desired target state.

4.6 Extension to Three-Qubit C_2Z Gates

In the following we discuss the extension of our semi-analytical approach based on the PMP to the three-qubit C_2Z gates found in Sec. 3.6.1. Here, in contrast to the two-qubit case, we are not able to obtain a single one-dimensional differential equation that describes the time-optimal pulses. Instead, we directly optimize over the initial costates $|\chi_1(0)\rangle, |\chi_2(0)\rangle, |\chi_3(0)\rangle$ and the pulse duration T to minimize the gate infidelity.

To obtain a guess for the initial costates we consider the pulses found by GRAPE in Sec.3.6.1. GRAPE provides us with M laser phases $\varphi^{(0)}, \dots, \varphi^{(M-1)}$ such that the states at time $t_m = mT/M$ are given by

$$|\psi_n(t_m)\rangle = U_n^{(m-1)} \dots U_n^{(0)} |\psi_n(0)\rangle \quad (4.68)$$

with $U_n^{(m)} = \exp(-iH_n(\varphi^{(m)})T/M)$. Correspondingly, the costates are given by

$$|\chi_n(t_m)\rangle = U_n^{(m-1)} \dots U_n^{(0)} |\chi_n(0)\rangle. \quad (4.69)$$

According to statement *iii*) of the PMP (Eq. (4.24)), we have for all m that

$$0 = \sum_n \text{Im} \left\langle \chi_n(t_m) \left| \frac{\partial H_n}{\partial \varphi} \right| \psi_n(t_m) \right\rangle = \sum_n \text{Im} \langle \chi_n(0) | \alpha_m \rangle \quad (4.70)$$

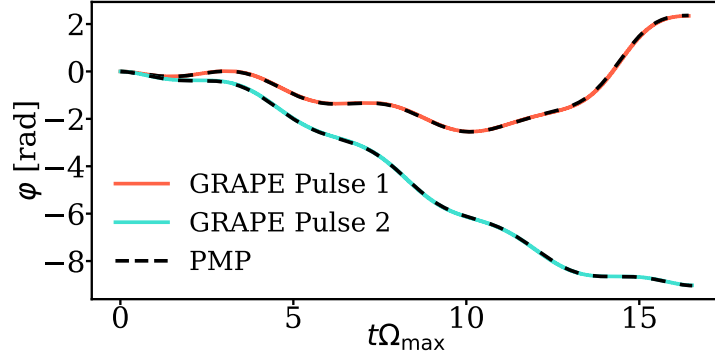


Figure 4.3: Semianalytic description of C_2Z pulses. Laser phase $\varphi(t)$ for a time-optimal C_2Z gate as obtained by GRAPE (red line: Pulse 1, turquoise line: Pulse 2) and by the PMP (dashed black line).

with

$$|\alpha_{n,m}\rangle = (U_n^{(0)})^\dagger \dots (U_n^{(m-1)})^\dagger \frac{\partial H_n}{\partial \varphi} U_n^{(m-1)} \dots U_n^{(0)} |\psi_n(0)\rangle. \quad (4.71)$$

Note that the $|\alpha_{n,m}\rangle$ can be calculated just from the laser phases $\varphi^{(0)}, \dots, \varphi^{(M-1)}$ obtained by GRAPE.

Eq. (4.70) is an overdetermined system of linear equations of the $|\chi_n(0)\rangle$. If $\varphi(t)$ is the time-optimal pulse, the PMP guarantees that this system has a solution. Since the pulse found by GRAPE is only a piecewise constant approximation of the true time-optimal pulse, Eq. (4.70) does not have an exact solution. However, by minimizing

$$\sum_m \left| \sum_n \text{Im} \langle \chi_n(0) | \alpha_{n,m} \rangle \right|^2 \quad (4.72)$$

under the constraint

$$\left(\sum_n \sqrt{n} \text{Im} \langle \chi_n(0) | 0 \rangle \right)^2 + \left(\sum_n \sqrt{n} \text{Re} \langle \chi_n(0) | 0 \rangle \right)^2 = 4 \quad (4.73)$$

[Eq. (4.33)] we can obtain a guess for the initial costates $|\chi_n(0)\rangle$.

We now use this guess as a starting point and minimize the infidelity $1 - F$ over the initial costates and the pulse duration using the BFGS algorithm [161]. For the time-optimal pulse (Pulse 1 in Sec. 3.6.1) we find

$$|\chi_1(0)\rangle = -0.82374869i |0\rangle + (-0.22639913 - 1.53071651i) |1\rangle \quad (4.74)$$

$$|\chi_2(0)\rangle = +1.98173098i |0\rangle + (-0.67792116 + 0.14076179i) |1\rangle \quad (4.75)$$

$$|\chi_3(0)\rangle = -1.05129372i |0\rangle + (+0.68595665 + 1.92352732i) |1\rangle \quad (4.76)$$

Since Pulse 2 is also locally, albeit not globally, time-optimal, the PMP also applies and we find

$$|\chi_1(0)\rangle = -0.71519316i |0\rangle + (-0.45059305 - 1.82739933i) |1\rangle \quad (4.77)$$

$$|\chi_2(0)\rangle = +2.12637520i |0\rangle + (-0.57394979 + 0.17718447i) |1\rangle \quad (4.78)$$

$$|\chi_3(0)\rangle = -1.19933851i |0\rangle + (+0.73078560 + 2.06507777i) |1\rangle \quad (4.79)$$

Fig. 4.3 compares the pulses found using GRAPE and using the PMP, and finds an excellent agreement between both pulses. The three initial costates $|\chi_1(0)\rangle$, $|\chi_2(0)\rangle$ and $|\chi_3(0)\rangle$ are jointly described by seven independent real parameters, since they are characterized by the nine real numbers $\text{Im}\langle 0|\chi_n\rangle$, $\text{Re}\langle 1|\chi_n\rangle$ and $\text{Im}\langle 1|\chi_n\rangle$ with the two constraints $\text{Im}\langle 0|\chi_1\rangle + 2\text{Im}\langle 0|\chi_2\rangle + 3\text{Im}\langle 0|\chi_3\rangle = 0$ and Eq. (4.73). This established that the time-optimal pulses for a C_2Z gate can be described by just 7 real parameters for each pulse.

4.7 Conclusion

In this section we have used the PMP to derive a simple differential equation for the laser detuning of time-optimal pulses for C-Phase gates. We have shown that the detuning follows the same dynamics as the oscillation of a particle in a quartic potential. We found the optimal pulses obtained with the PMP to be in excellent agreement with the pulses found numerically in Chapter 3, while only requiring three real parameters to fully specify the pulse. We have also demonstrated that the PMP can in principle also be applied to C_kZ gates, where however the resulting differential equation is significantly more complex. There are several remaining open questions: First, it is unclear whether the coefficients c_0, c_1, c_2 or Δ_{\pm} and V_0 describing the quartic potential can be analytically related to the phase ϕ of the C-Phase gate. A second interesting research question is whether the differential equation describing time-optimal gates on three qubits can be simplified to a form similar to that for two-qubit gates. Finally, the PMP approach could be extended to gates with a finite interaction strength, or to gates with individual addressability of the atoms. The latter might result in an analytical proof of the numerical result that for the CZ gate no speed-up can be obtained using local addressability (see Sec. 3.3). We remark that all of these open questions appear rather challenging.

4.A Discussion of Abnormal Solutions

In this appendix we discuss case of abnormal solutions of the PMP with $\chi^0 = 0$. We restrict ourselves to the case of $N = 2$ atoms. In this case, statement *iv)* of the PMP implies

$$v_1^{(x)} + \sqrt{2}v_2^{(x)} = v_1^{(y)} + \sqrt{2}v_2^{(y)} = 0 \quad (4.80)$$

at all times t . Taking the time derivative and using Eq. (4.39) leads to

$$(v_1^{(z)} + 2v_2^{(z)}) \sin \varphi = (v_1^{(z)} + 2v_2^{(z)}) \cos \varphi = 0 \quad (4.81)$$

which implies $v_1^{(z)} + 2v_2^{(z)} = 0$. Taking the time derivative again gives

$$(v_1^{(y)} + 2\sqrt{2}v_2^{(y)}) \cos \varphi + (v_1^{(x)} + 2\sqrt{2}v_2^{(x)}) \sin \varphi = 0. \quad (4.82)$$

By inserting Eq. (4.80) we obtain

$$v_1^{(y)} \cos \varphi + v_1^{(x)} \sin \varphi = 0. \quad (4.83)$$

which by Eq. (4.39) implies $\dot{v}_1^{(z)} = 0$. Thus, already $v_1^{(x)^2} + v_1^{(y)^2}$ is a conserved quantity, and Eq. (4.83) implies

$$v_1^{(x)} = a \cos \varphi \quad v_1^{(y)} = -a \sin \varphi \quad (4.84)$$

for some constant a . Taking the time derivative one more time gives

$$-v_1^{(z)} \sin \varphi = -a\dot{\varphi} \sin \varphi \quad -v_1^{(z)} \cos \varphi = -a\dot{\varphi} \cos \varphi. \quad (4.85)$$

This implies $\Delta = \dot{\varphi} = v_1^{(z)}/a = \text{const}$. Thus, all abnormal solutions must have a constant detuning.

In the following we will show that while it is possible to implement certain C-Phase gates with a constant detuning, such a C-Phase gate will always have a longer duration than the normal solutions found in Sec. 4.5. For a constant detuning Δ we have to consider the two constant Hamiltonians

$$H_{01} = \Delta |1\rangle \langle 1| + \frac{\Omega_{\max}}{2} \sigma_x \quad (4.86)$$

$$H_{11} = \Delta |1\rangle \langle 1| + \frac{\sqrt{2}\Omega_{\max}}{2} \sigma_x. \quad (4.87)$$

The evolution operators for a duration T are given by

$$\begin{aligned} \exp(-iH_{01}T) = e^{-i\Delta T/2} & \left[\cos \left(\frac{1}{2} \sqrt{\Omega_{\max}^2 + \Delta^2 T} \right) I \right. \\ & \left. -i \sin \left(\frac{1}{2} \sqrt{\Omega_{\max}^2 + \Delta^2 T} \right) \frac{\Delta \sigma_z + \Omega_{\max} \sigma_x}{\sqrt{\Omega_{\max}^2 + \Delta^2}} \right] \end{aligned} \quad (4.88)$$

and

$$\begin{aligned} \exp(-iH_{11}T) = e^{-i\Delta T/2} & \left[\cos \left(\frac{1}{2} \sqrt{2\Omega_{\max}^2 + \Delta^2 T} \right) I \right. \\ & \left. -i \sin \left(\frac{1}{2} \sqrt{2\Omega_{\max}^2 + \Delta^2 T} \right) \frac{\Delta \sigma_z + \sqrt{2}\Omega_{\max} \sigma_x}{\sqrt{2\Omega_{\max}^2 + \Delta^2}} \right] \end{aligned} \quad (4.89)$$

We see that an initial state $|0\rangle$ will only return to $|0\rangle$, up to some phase, at the end of the gate if

$$T = \frac{2\pi k}{\sqrt{\Omega_{\max}^2 + \Delta^2}} = \frac{2\pi k'}{\sqrt{2\Omega_{\max}^2 + \Delta^2}} \quad (4.90)$$

for some integers $k, k' \geq 1$. In this case, a C-Phase gate with two-qubit phase $\phi = k'\pi + \frac{\Delta T}{2}$ is implemented.

From Eq. (4.90) it follows that

$$\Delta = \pm \sqrt{\frac{2k^2 - k'^2}{k'^2 - k^2}} \Omega_{\max} \quad (4.91)$$

$$T = \frac{2\pi}{\Omega_{\max}} \sqrt{k'^2 - k^2} \quad (4.92)$$

Since the minimal difference between two square numbers is $3 = 2^2 - 1^2$, it follows that $T \geq 2\sqrt{3}\pi/\Omega_{\max} \approx 10.88/\Omega_{\max}$. Hence, while there exist C-Phase gates which can be implemented with a constant Δ , they are always slower than the normal solutions found in Sec. 4.5, which had a maximum duration of $T = 7.612/\Omega_{\max}$.

5 Robust Gate Protocols

One of the most important directions for the continued development of neutral atom quantum processors is improving the fidelity of two- and multi-qubit gates. In Chapters 3 and 4 we tackled this challenge by finding the fastest possible, time-optimal, gate protocols. Since many error sources are less detrimental for shorter pulse durations, this approach offers a gate protocol with a high fidelity independent of the exact error model. For quantum gates based on the Rydberg blockade effect however, the leading error sources are often well understood and account for a large fraction of the experimentally observed infidelity [13, 14, 105]. It is thus possible to develop gate protocols that are robust against these specific error sources, at the expense of obtaining protocols that are longer than the time-optimal protocol.

In this chapter we consider several practically relevant error sources, and use a combination of analytical reasoning and optimal control methods to find gate protocols with increased robustness against them. We consider the same level scheme as in Chapters 3 and 4, with two or three atoms, each of which is modeled as a three level system with computational basis states $|0\rangle$ and $|1\rangle$ and an auxiliary Rydberg state $|r\rangle$, a symmetric van der Waals interaction $B \sum_{j < k} |r_j r_k\rangle \langle r_j r_k|$, and a global laser with a time-dependent (complex) Rabi frequency $\Omega(t)$ coupling the states $|1\rangle$ and $|r\rangle$. Throughout this chapter we assume that, at least in the absence of imperfections, we have $B = \infty$, so that the simultaneous excitation of more than two atoms to the Rydberg state is impossible. We consider four different error sources in this chapter: a finite lifetime of the Rydberg state, an uncertain finite interaction strength B , and uncertainties in the amplitude and detuning of the global laser. The level scheme and the error sources are visualized in Fig. 5.1.

The results of this chapter for the robustness of gate protocols against these error sources can be summarized as follows:

- i) Rydberg decay.* Rydberg states have a finite lifetime γ limited by spontaneous emission to low lying states and the coupling to other Rydberg states due to black body radiation. The decay of the Rydberg state during a gate leads to an error. We identify the pulses which minimize the error due to Rydberg decay, and show that the infidelity can only be reduced by less than 1% for the CZ gate and less than 10% for the C_2Z gate compared to the time-optimal pulses. Hence, for both the CZ and the C_2Z gate the time-optimal pulses are almost optimal at mitigating this error source.

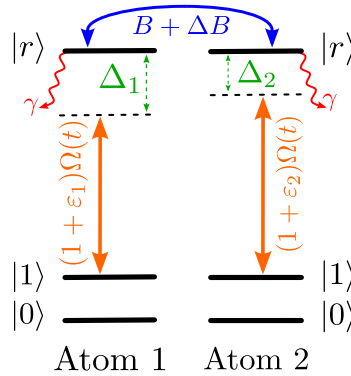


Figure 5.1: Level scheme and error sources considered in this chapter.

Each atom is modeled as a three-level system with states $|0\rangle$, $|1\rangle$ and $|r\rangle$. There is a van der Waals interaction shifting the energy of the state of both atoms in $|r\rangle$, and a global laser coupling $|1\rangle$ and $|r\rangle$ with Rabi frequency $\Omega(t)$. The error sources considered in this chapter are marked in different colors: The decay of the Rydberg state (red), uncertainties in the interaction strength (blue), deviations of the expected laser amplitude (orange), and laser detunings (green).

- ii) *Uncertainties in the interaction strengths.* The interaction strength B is often finite and not known exactly, since it depends on the interatomic distance between the atoms, which fluctuates with the motion of the atoms in the optical tweezer. While we have shown in Sec. 3.4 that it is possible to implement a CZ and a C_2Z gate exactly at finite interaction strengths, these protocols are only designed to work at a specific interaction strength B . Here we instead find gate protocols which implement a CZ and C_2Z exactly only at $B = \infty$, but whose infidelity increases as slowly as possible with $1/B$. This makes these gates advantageous if the interaction strength is large but unknown.
- iii) *Laser amplitude deviations.* Instead of the expected Rabi frequency $\Omega(t)$, the atoms can experience a Rabi frequency $(1 + \varepsilon_i)\Omega(t)$, with different ε_i for different atoms. These shot-to-shot fluctuations can either arise due to fluctuations of the laser intensity, or due to fluctuations of the atomic position with respect to the center of the laser beam, for example due to the motion of the atom in the trap. We use quantum optimal control techniques to find a pulse shape $\Omega(t)$ for a CZ gate which reduces the effect of amplitude fluctuations by more than two orders of magnitude, at the expense of a longer pulse duration.
- iv) *Laser detuning.* Various error sources can lead to detunings Δ_i of the laser and the $|1\rangle \leftrightarrow |r\rangle$ transition. The most important sources of detuning include stray electric fields, which shift the energy of the Rydberg state, Doppler shifts of the laser frequency due to the thermal motion of the atoms in the trap, and fluctuations in the amplitude of the global laser (see *iii*), which due to the Stark shift arising from the coupling to other, off-resonant, states, also affect the energies of the states $|1\rangle$ and $|r\rangle$. We find that for arbitrary detunings Δ_i , only a small improvement of the robustness over the time-optimal pulse can be achieved. For detunings arising from Doppler shifts, we however find that by reversing the sign of the Doppler shift in the middle of the pulse it

is possible to improve the robustness against this error by several orders of magnitude. Similarly, for detunings arising due to a Stark shift induced by the global laser, we can use the correlation between amplitude deviations and laser detuning to design robust pulses.

We first consider the four error sources above separately. However, in a real experiment all four error sources are present at the same time, and the ideal gate protocol strikes a compromise between the robustness against all of them. To better understand this compromise, we consider realistic parameters of a ^{171}Yb experiment [85], and find that for medium or large laser amplitude deviations or Doppler detunings the robust pulses against amplitude deviations or Doppler detunings outperform the time-optimal pulse, while for small laser amplitude deviations or Doppler detunings the time-optimal pulse, which essentially minimizes the errors due to Rydberg decay, becomes the better choice. However, recently it has been proposed [20, 162] and experimentally demonstrated [14] that in metastable qubits Rydberg decay errors can be converted into so-called *erasure errors*, which are significantly simpler to correct in an error correction code than other errors. Taking this into account, we surprisingly find a large range of imperfections where using pulses robust against amplitude deviations or detunings increases the gate infidelity, but decreases the logical error rate, compared to the time-optimal pulse. This demonstrates that gate fidelity and logical error rate can differ significantly, and that optimizing gates specifically for logical-level optimization can yield dramatic improvements.

This chapter is structured as follows: In Sec. 5.1 and Sec. 5.2 we discuss CZ and C_2Z gates which are as robust as possible against Rydberg decay and variations in the blockade strength, respectively. In Sec. 5.3 we then design pulses for a CZ gates that are particularly robust against amplitude deviations, and show that pulses with similar properties for laser detunings do not exist. In Sec. 5.4 we propose a workaround for detunings arising from Doppler shifts based on inverting the sign of the Doppler shift in the middle of the pulse. Finally, in Secs. 5.5 and 5.6 we consider the trade-off between Rydberg decay, laser amplitude deviations, and Doppler detunings for a CZ gate under realistic parameters in terms of the gate fidelity and the logical error rate, respectively.

The results of Secs. 5.1 and 5.2 have previously been published in Ref. [23]. Sections. 5.3–5.6 have previously been published in Ref. [24]. Similar results have been independently obtained in Ref. [163].

5.1 Minimizing Rydberg Decay

We start by considering a finite lifetime $1/\gamma$ of the Rydberg state. We include this error source as a non-hermitian term $H_{nh} = -i\frac{\gamma}{2}\Pi_R$, where $\Pi_R = \sum_j |r_j\rangle\langle r_j|$ denotes the projector onto the states with one atom in the Rydberg state. (Since there can never be two or more atoms in the Rydberg state, Π_R is indeed a projector.) The

treatment as a non-hermitian term is exact if all of the Rydberg decay goes outside of the computational subspace, and otherwise slightly overestimates the error, since the Rydberg state could decay back to $|0\rangle$ and $|1\rangle$, leading to a non-zero fidelity even after a decay event[108].

We can expand the state $|\psi_q(t)\rangle$ when starting in the computational basis state $|q\rangle$ as $|\psi_q(t)\rangle = |\psi_q^{(0)}(t)\rangle + \gamma |\psi_q^{(1)}(t)\rangle + \mathcal{O}(\gamma^2)$, with the first order contribution at the final time T given by

$$|\psi_q^{(1)}(T)\rangle = -\frac{\gamma}{2} \int_0^T U_q(t, T) \Pi_R U_q(0, t) |q\rangle dt \quad (5.1)$$

where $U_q(t_1, t_2)$ denotes the evolution from time t_1 to time t_2 under the Hamiltonian H_q that describes the decay-free case (see Sec. 3.1.1). Now suppose we have a global pulse $\Omega(t)$ which in the decay-free case implements a $(\zeta_q)_q$ phase gate, i.e. satisfies $|\psi_q^{(0)}(T)\rangle = \exp(i\zeta_q) |q\rangle$. The fidelity (see Sec. 3.1.2) of this pulse in the presence of decay is now to first order in γ given by

$$\begin{aligned} F &= \frac{1}{2^N(2^N + 1)} \left(\left| \sum_q 1 - \frac{\gamma}{2} \int_0^T dt \langle \psi_q^{(0)}(t) | \Pi_R | \psi_q^{(0)}(t) \rangle \right|^2 \right. \\ &\quad \left. + \sum_q \left| 1 - \frac{\gamma}{2} \int_0^T dt \langle \psi_q^{(0)}(t) | \Pi_R | \psi_q^{(0)}(t) \rangle \right|^2 \right) \\ &= \frac{1}{2^n(2^n + 1)} \left(2^{2N} - 2^N \sum_q \gamma \int_0^T dt \langle \psi_q^{(0)}(t) | \Pi_R | \psi_q^{(0)}(t) \rangle \right. \\ &\quad \left. + 2^N - \sum_q \gamma \int_0^T dt \langle \psi_q^{(0)}(t) | \Pi_R | \psi_q^{(0)}(t) \rangle \right) \\ &= 1 - \gamma 2^{-N} \sum_q \int_0^T dt \langle \psi_q^{(0)}(t) | \Pi_R | \psi_q^{(0)}(t) \rangle \\ &= 1 - \gamma T_R \end{aligned} \quad (5.2)$$

where we introduced the averaged Rydberg time

$$T_R = 2^{-N} \sum_q \int_0^T dt \langle \psi_q^{(0)}(t) | \Pi_R | \psi_q^{(0)}(t) \rangle. \quad (5.3)$$

Our goal is now to find the pulse $\Omega(t)$ that implements an exact CZ or a C_2Z gate at $\gamma = 0$ and minimizes T_R , and thus also the infidelity due to Rydberg decay.

To find this pulse $\Omega(t)$ we use GRAPE (see Sec. 3.2) with the Hamiltonians H_q including the non-hermitian $-i\frac{\gamma}{2}\Pi_R$ term and minimize the gate infidelity. For the two qubit case, the H_q are given by

$$H_{01} = \frac{\Omega(t)}{2} |01\rangle \langle 0r| + \text{h.c.} - i\frac{\gamma}{2} |0r\rangle \langle 0r| \quad (5.4)$$

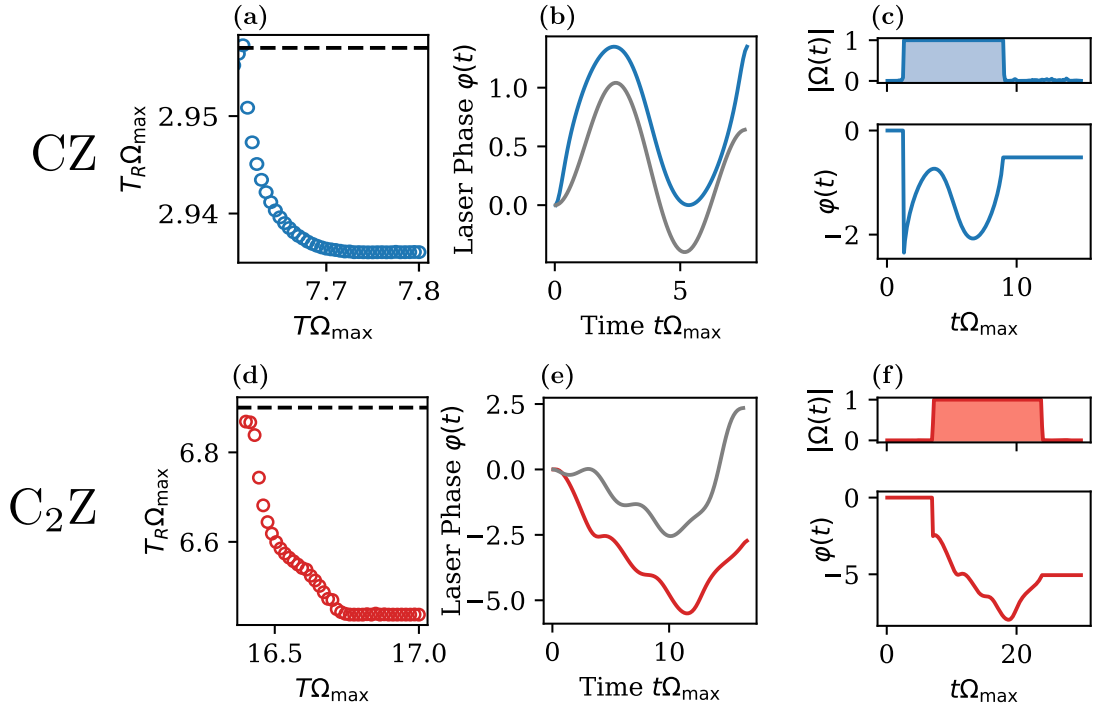


Figure 5.2: Minimizing errors due to Rydberg decay. (a) Minimal Rydberg time T_R for pulses implementing a CZ gate found by GRAPE at different pulse durations T . Black dashed line shows the value of T_R for the time-optimal pulse. (b) Laser phase $\varphi(t)$ for the pulse that minimizes T_R at $T = 7.72/\Omega_{\max}$ (blue) and the time-optimal pulse (gray). For both pulses, the laser amplitude is always maximal. (c) Laser amplitude and phase of the pulse found by GRAPE minimizing T_R at a pulse duration $T = 15/\Omega_{\max}$. (d-f) Analogous to (a-c) with the C_2Z gate instead of the CZ gate. In (e) and (f) the pulse durations are $16.74/\Omega_{\max}$ and $30/\Omega_{\max}$, respectively.

$$H_{11} = \frac{\sqrt{2}\Omega(t)}{2} |11\rangle \langle W_{11}| + \text{h.c.} - i\frac{\gamma}{2} |W_{11}\rangle \langle W_{11}| \quad (5.5)$$

with straightforward generalizations to the three qubit case. We choose a small value $\gamma = 10^{-4}\Omega_{\max}$, which ensures that the pulse that minimizes $1 - F$ still approximately implements a CZ or C_2Z gate in the absence of decay. However, we stress that the resulting pulse will also minimize the infidelity for all other values of γ , as long as $\gamma T_R \ll 1$.

Fig. 5.2(a) shows the value of T_R of the optimal pulse for a CZ gate found by GRAPE as a function of the pulse duration T . We verified that the infidelity of all optimal pulses in the absence of decay is always below 10^{-9} , and that the minimal value of T_R does not change when changing γ . Both results confirm that our choice of $\gamma = 10^{-4}\Omega_{\max}$ is small enough only minimize T_R over pulses which implement an exact CZ gate at $\gamma = 0$, and there is no trade-off between the infidelity at $\gamma = 0$ and T_R . For the pulse duration $T = 7.612/\Omega_{\max}$, the duration of the time-optimal pulse, Fig. 5.2(a) shows that as expected the minimal value of T_R is also that of the time-optimal pulse, $T_R = 2.957/\Omega_{\max}$ [black dashed line in Fig. 5.2(a)]. As the pulse duration T increases, the minimal value of T_R decreases slightly, reaching a plateau of $T_R = 2.936/\Omega_{\max}$ around $T \approx 7.72/\Omega_{\max}$. Fig. 5.2(b) shows that this pulse (blue)

is a distorted version of the time-optimal pulse (gray). We verify that even for a very large pulse duration $T = 15/\Omega_{\max}$ no further reduction of T_R is obtained. Fig. 5.2(c) shows the pulse found by GRAPE at this duration. As expected, this pulse has a laser amplitude of 0, except for a window of duration $\sim 7.72/\Omega_{\max}$, where the pulse that minimizes T_R is executed. Thus, the infidelity of the CZ gate due to Rydberg decay can only be reduced by approximately 0.8% compared to the time-optimal gate, by increasing the gate duration by 1.4%. We conclude that the time-optimal pulse is also essentially optimal at minimizing the infidelity due to Rydberg decay.

Similar results are obtained for the three-qubit C_2Z gate. Analogously to Fig. 5.2(a), Fig. 5.2(d) shows the minimal value of T_R for a pulse implementing a C_2Z gate as a function of the pulse duration. T_R drops by 7% from $T_R = 6.90/\Omega_{\max}$ (value of the time-optimal pulse) to $T_R = 6.43/\Omega_{\max}$ when increasing the pulse duration by 1.8% from $16.43/\Omega_{\max}$ to $16.74/\Omega_{\max}$. Fig. 5.2(e) shows the pulse minimizing T_R is again a distorted version of the time-optimal pulse, and Fig. 5.2(f) demonstrates that even at the much larger pulse duration $T = 30/\Omega_{\max}$ the pulse minimizing T_R is identical to the pulse at duration $16.74/\Omega_{\max}$.

In conclusion we have shown that the pulses minimizing T_R , and thus the error due to Rydberg decay, for the CZ and C_2Z gate are approximately, but not exactly, identical to the time-optimal pulses. We note that a parameterization of the pulses minimizing T_R using the PMP as in Chapter 4 is in principle possible by taking the Lagrangian in the PMP to be $L = 2^{-N} \sum_q dt \langle \psi_q | \Pi_R | \psi_q \rangle$, the expected population of the Rydberg state.

5.2 Robustness to Interaction Strength Variations

In this section we consider errors due to finite interaction strength B . However, instead of designing pulses that work at a specific blockade strength B , we consider only pulses that implement a CZ or C_2Z gate exactly at $B = \infty$. Within the set of these pulses, we then identify the pulses that are affected the least by a finite B . This results in gate protocols which are as robust as possible against variations against B , at least when $B \gg |\Omega|$. Throughout this chapter we assume that B is unknown but constant. Since B depends only on the interatomic distance, and the oscillation period of the atoms in the tweezers is typically much shorter than the pulse duration [105], this assumption is typically justified.

In the limit of large B , all effects of the finiteness of B can to first order in $1/B$ be described by a Stark shift of the energy of the states with one atom in the Rydberg state. For $N = 2$ atoms this means modifying H_{11} to

$$H_{11} = \underbrace{\frac{\sqrt{2}\Omega(t)}{2} |11\rangle \langle W_{11}| + \text{h.c.}}_{H_{11}^{(0)}} - \underbrace{\frac{|\Omega|^2}{2B} |W_{11}\rangle \langle W_{11}|}_{H_{11}^{(1)}/B} + \mathcal{O}(B^{-2}) \quad (5.6)$$

where we split $H_{11} = H_{11}^{(0)} + \frac{1}{B}H_{11}^{(1)}$. The quantum state when starting in $|11\rangle$ can be equivalently expanded as $|\psi_{11}(t)\rangle = |\psi_{11}^{(0)}\rangle + B^{-1}|\psi_{11}^{(1)}\rangle + B^{-2}|\psi_{11}^{(2)}\rangle + \mathcal{O}(B^{-3})$, while $|\psi_{01}\rangle$ stays unmodified. For the three qubit case, H_{011} and H_{111} are modified analogously to Eq. (5.6).

Now let us consider a pulse $\Omega(t)$ which at $B = \infty$ implements a CZ gate with fidelity $F = 1$, i.e. satisfies $|\psi_{01}^{(0)}(T)\rangle = e^{i\theta}|01\rangle$ and $|\psi_{11}^{(0)}(T)\rangle = -e^{2i\theta}|11\rangle$ for some single qubit phase θ . In Appendix 5.A we show that the infidelity of such a pulse is given by

$$(1 - F)B^2 = \frac{1}{4} \langle \psi_{11}^{(1)}(T) | \psi_{11}^{(1)}(T) \rangle - \frac{1}{10} \left| \langle 11 | \psi_{11}^{(1)}(T) \rangle \right|^2 + \mathcal{O}(B^{-1}). \quad (5.7)$$

In Appendix 5.A we also derive a similar formula for the C_2Z gate. To lowest order, the gate error thus increases quadratically with $1/B$.

Our goal is now to use GRAPE to minimize the second derivative $d^2(1 - F)/d(1/B)^2$ at $B = \infty$, as given by the right hand side of Eq. (5.7). Note that this minimizes the gate error simultaneously for all values of B for which contributions of order B^{-3} and higher can be neglected. To apply GRAPE, $|\psi_{11}^{(0)}\rangle$ and $|\psi_{11}^{(1)}\rangle$ are treated as independent states satisfying

$$\frac{d}{dt} \begin{pmatrix} |\psi_{11}^{(0)}\rangle \\ |\psi_{11}^{(1)}\rangle \end{pmatrix} = -i \begin{pmatrix} H_{11}^{(0)} & 0 \\ H_{11}^{(1)} & H_{11}^{(0)} \end{pmatrix} \begin{pmatrix} |\psi_{11}^{(0)}\rangle \\ |\psi_{11}^{(1)}\rangle \end{pmatrix}. \quad (5.8)$$

Eq. (5.8) now replaces the Schrödinger Equation for $|\psi_{11}\rangle$ in the formulation of GRAPE. For the three qubit case, we proceed analogously for the states $|\psi_{011}\rangle$ and $|\psi_{111}\rangle$.

To minimize $d^2(1 - F)/d(1/B)^2$ over all states with fidelity $F = 1$ in the $B = \infty$ case, the objective function for GRAPE is taken as

$$J = C(1 - F) + \frac{1}{2} \frac{d^2(1 - F)}{d(1/B)^2} \Big|_{B=\infty}. \quad (5.9)$$

Here, C is a large constant ensuring that only pulses with fidelity close to 1 in the $B = \infty$ case can minimize J . We take $C = 10^4$ and verify that indeed the gate errors at $B = \infty$ are always below $3 \cdot 10^{-6}$.

Given a pulse $\Omega(t)$ with duration T that implements a CZ gate at $B = \infty$, the gate error at finite B can be reduced by an arbitrary factor β^2 , for $0 < \beta < 1$, by simply stretching the pulse to duration T/β and taking $\tilde{\Omega}(t) = \beta\Omega(\beta t)$. To see this, note that $H_{11}^{(1)}$ is decreased by β^2 , while the pulse duration is increased by $1/\beta$. Hence $|\psi_{11}^{(1)}\rangle$ is decreased by β , and $1 - F$ according to Eq. (5.7) by β^2 . To compare different pulses beyond a stretch, the dimensionless quantity $\alpha = (1 - F)B^2T^2$ is from now on taken as a metric for pulse robustness.

Using Eq. (5.7), the time-optimal pulse for the CZ gate is found to have $\alpha = 35.9$. To improve upon this, GRAPE is now used to minimize α over both the amplitude

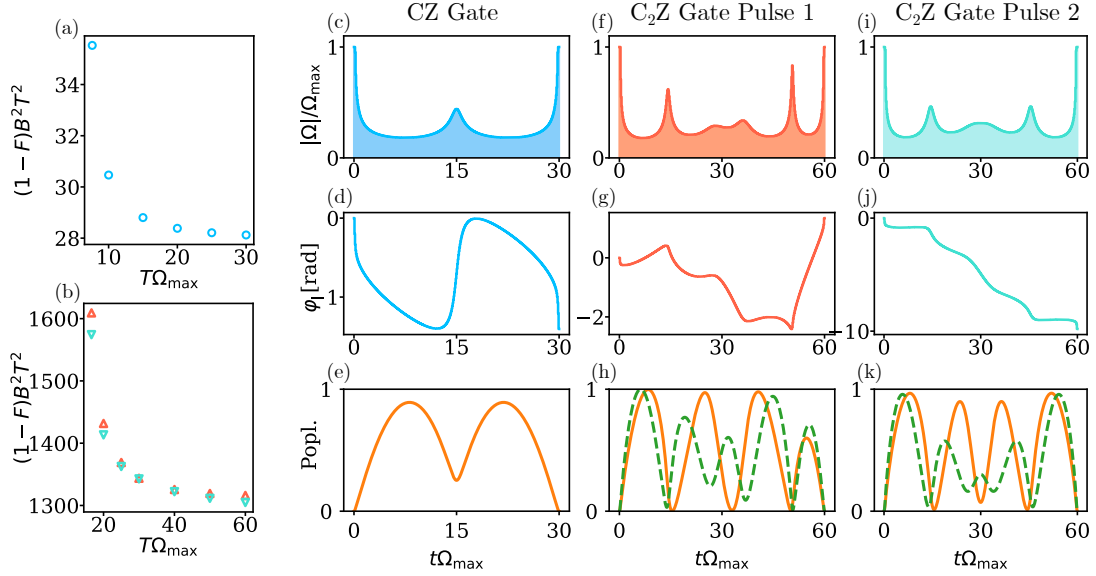


Figure 5.3: Pulses for the CZ and the C_2Z gate that are as robust as possible against variations of the blockade strength. (a) Rescaled gate errors $(1 - F)B^2T^2$ for different values of the dimensionless gate duration $T\Omega_{\max}$ for the CZ gate. (b) Rescaled gate errors $(1 - F)B^2T^2$ for the C_2Z gate. Red upward pointing triangles show optimization results when initializing GRAPE with the time-optimal Pulse 1, turquoise downward pointing triangles when initializing with Pulse 2. (c) [(d)] Laser amplitude [phase] minimizing $(1 - F)B^2T^2$ for the CZ gate at $T\Omega_{\max} = 30$. (e) Population of $|W_{11}\rangle$ during the pulse from (c)/(d) as a function of time. The laser amplitude is large when the population of $|W_{11}\rangle$ is small. (f) [(g)] Laser amplitude(phase) minimizing $(1 - F)B^2T^2$ for the C_2Z gate when initializing GRAPE with Pulse 1 at $T\Omega_{\max} = 60$. (h) Population of $|W_{011}\rangle$ (orange solid line) and $|W_{111}\rangle$ (green dashed line) during Pulse 1 as a function of time. The laser amplitude is large when the populations of $|W_{011}\rangle$ and $|W_{111}\rangle$ are small. (i),(j),(k) Analogous to (f),(g),(h) for Pulse 2 instead of Pulse 1.

and the phase of the laser pulse at a fixed T , using the time-optimal pulse stretched to duration T as initial guess. The minimal values of α for values of $T\Omega_{\max}$ between 7.61 and 30 are shown in Fig. 5.3(a). α decreases as the pulse duration increases, but asymptotically approaches a non-zero value around $\alpha \approx 28$ as $T \rightarrow \infty$, which is an improvement of over 20% compared to the time-optimal pulse. The amplitude and the phase of $\Omega(t)$ at $T\Omega_{\max} = 30$ are shown in Figs. 5.3(c) and (d) respectively. The amplitude starts maximal, then drops to about 25% after a quarter of the pulse duration. Towards the middle of the pulse the amplitude increases again to around 50%, then it decreases again to 25% at three quarters of the pulse duration and finally increases to the maximal amplitude at the end of the pulse. This behavior can be understood by considering the population of $|W_{11}\rangle$, the only state affected by the Stark shift due to the finite B . The population of $|W_{11}\rangle$, shown in Fig. 5.3(e), starts at 0 and increases to 0.9 at $t \approx 0.25T$. It then decreases to 0.25 at $t = 0.5T$ and increases again to 0.9 at $t \approx 0.75T$, before dropping to 0 at the end of the pulse. Notably, the laser amplitude is inversely correlated to the population $|W_{11}\rangle$. Through this, whenever the population of $|W_{11}\rangle$ is large, the laser amplitude, and thus also the Stark shift of $|W_{11}\rangle$, is reduced.

For the C_2Z gate we find that the time-optimal Pulse 1 has $\alpha = 1850$, the slightly slower Pulse 2 has $\alpha = 1660$. GRAPE is applied with either Pulse 1 or Pulse 2 as initial guess to minimize α for $T\Omega_{\max}$ between 16.6 and 60, shown in Fig. 5.3(b) with red upward pointing triangles for Pulse 1 as initial guess and turquoise downward pointing triangles for Pulse 2 as initial guess. For both cases α decreases when T is increased and asymptotically approaches $\alpha \approx 1300$ for both pulses, an improvement of 30% over the time-optimal Pulse 1 and of 20% over Pulse 2. The amplitude and phase for the pulse minimizing α at $T\Omega_{\max} = 60$ when initializing GRAPE with pulse 1 are shown in Figs. 5.3(f) and (g) respectively, the amplitude and phase when initializing GRAPE with Pulse 2 in Figs. 5.3(i) and (j) respectively. The laser amplitude is again inversely correlated to the populations $|W_{011}\rangle$ and $|W_{111}\rangle$, shown in Fig. 5.3(h) and (k) as orange solid line and green dashed line respectively, and displays several peaks at times where the population of these states is small.

The results in this section show that both for the CZ and for the C_2Z gate the time-optimal pulses can be improved to decrease the effect of a finite interaction strength at the cost of a longer pulse duration. The improvement of the gate error goes beyond simply stretching the pulses and is based on a modulation of the laser amplitude to reduce the Stark shift when the states affected by it are populated most.

5.3 Amplitude- and Detuning-Robust Pulses

In this section we identify global pulses $\Omega(t)$ that implement a CZ gate and are robust against unknown but constant deviations of the laser amplitude and detuning. The

Hamiltonians H_q in the presence of these imperfections are given by

$$H_{10} = \frac{(1 + \varepsilon_1)\Omega(t)}{2} |10\rangle \langle r0| + \text{h.c.} + \Delta_1 |r0\rangle \langle r0| \quad (5.10)$$

$$H_{01} = \frac{(1 + \varepsilon_2)\Omega(t)}{2} |01\rangle \langle 0r| + \text{h.c.} + \Delta_2 |0r\rangle \langle 0r| \quad (5.11)$$

$$H_{11} = \frac{(1 + \varepsilon_1)\Omega(t)}{2} |11\rangle \langle r1| + \text{h.c.} + \Delta_1 |r1\rangle \langle r1| \quad (5.12)$$

$$+ \frac{(1 + \varepsilon_2)\Omega(t)}{2} |11\rangle \langle 1r| + \text{h.c.} + \Delta_2 |1r\rangle \langle 1r|$$

Eq. (5.12) can be simplified to

$$H_{11} = \frac{\sqrt{2}(1 + \varepsilon_+)\Omega(t)}{2} |11\rangle \langle W_+| + \text{h.c.} \quad (5.13)$$

$$+ \Delta_- |W_+\rangle \langle W_-| + \text{h.c.}$$

$$+ \Delta_+ (|W_+\rangle \langle W_+| + |W_-\rangle \langle W_-|).$$

Here, $|W_\pm\rangle = [(1 + \varepsilon_1)|r1\rangle \pm (1 + \varepsilon_2)|1r\rangle]/\beta$, with $\beta = \sqrt{(1 + \varepsilon_1)^2 + (1 + \varepsilon_2)^2}$, while $\Delta_\pm = (\Delta_1 \pm \Delta_2)/2$ and $\varepsilon_+ = (\varepsilon_1 + \varepsilon_2)/2$. Note that Eq. (5.12) and Eq. (5.13) only agree up to terms in second order in ε and Δ . Since ε and Δ are typically small deviations, this suffices for the rest of our analysis.

5.3.1 Amplitude Robust pulses

We start by finding a pulse $\Omega(t)$ which is robust against amplitude deviations $\varepsilon_i \neq 0$, while taking $\Delta_i = 0$. We expand the Hamiltonians in ε as $H_{10} = H_{10}^{(0)} + \varepsilon_1 H_{10}^{(1)}$, $H_{01} = H_{01}^{(0)} + \varepsilon_2 H_{01}^{(1)}$ and $H_{11} = H_{11}^{(0)} + \varepsilon_+ H_{11}^{(1)}$ and the quantum state when starting in $|01\rangle$ as $|\psi_{10}\rangle = |\psi_{10}^{(0)}\rangle + \varepsilon_1 |\psi_{10}^{(1)}\rangle + \mathcal{O}(\varepsilon_1^2)$, with analogous expansions for $|\psi_{10}\rangle$ and $|\psi_{11}\rangle$. A pulse $\Omega(t)$ of duration τ implements a CZ gate, up to single-qubit rotations, in the deviation-free case if for all $q \in \{10, 01, 11\}$ it holds that $|\psi_q^{(0)}(\tau)\rangle = e^{i\zeta_q} |q\rangle$ with $\zeta_{01} = \zeta_{10} = \theta$ and $\zeta_{11} = 2\theta + \pi$ for some single qubit phase θ that does not depend on the ε_i (Note that in this section we use τ instead of T to denote the duration of a pulse, and use T instead to denote the temperature of the atoms). In this chapter we use the Bell state fidelity instead of the average gate fidelity (see sec. 3.1.2). It is commonly used fidelity measure on the Rydberg platform [18, 105, 109, 111] and for a CZ gate given by

$$F = \frac{1}{16} \left| 1 + \sum_{q \in \{10, 01, 11\}} e^{-i\zeta_q} \langle q | \psi_q^{(0)} \rangle \right|^2. \quad (5.14)$$

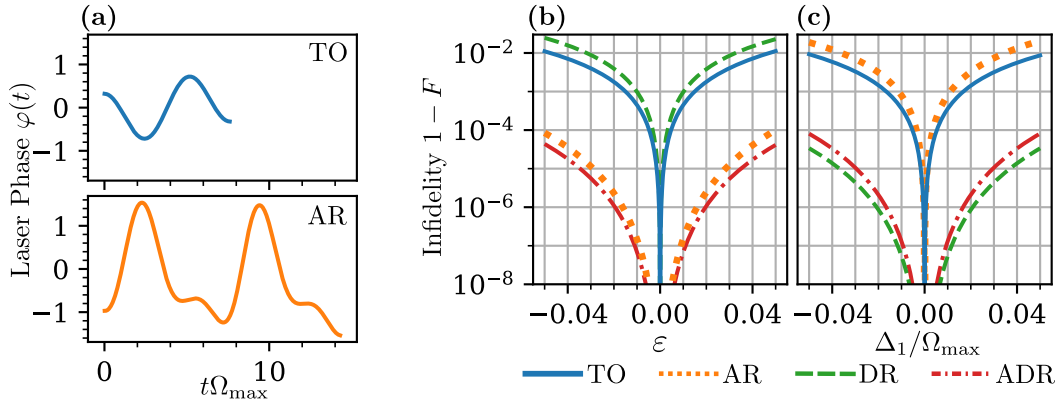


Figure 5.4: Comparison between robust pulses. (a) The laser phase as a function of time for the time-optimal (TO) and amplitude-robust (AR) pulse implementing the CZ gate. The amplitude of the pulses is always given by $|\Omega(t)| = \Omega_{\max}$. (b) Infidelity of the time-optimal (TO), amplitude-robust (AR), Doppler-robust (DR) and amplitude- and Doppler-robust (ADR) pulses as a function of $\varepsilon := \varepsilon_1 = \varepsilon_2$, with $\Delta_1 = \Delta_2 = 0$. (c) Infidelity of the same pulses as a function of Δ_1 , with $\varepsilon = 0$ and $\Delta_2 = 0$.

We say that the pulse is robust against amplitude deviations if $|\psi_q^{(1)}\rangle = 0$ for all q , such that the leading term of the deviation of $|\psi_q\rangle$ from $e^{i\theta_q}|q\rangle$ is quadratic in ε_i . To find the robust pulse we minimize the cost function

$$J = 1 - F + \sum_q \langle \psi_q^{(1)} | \psi_q^{(1)} \rangle \quad (5.15)$$

using GRAPE. Here we use that, as in Sec. 5.2, the $|\psi_q\rangle$ satisfy

$$\frac{d}{dt} \begin{pmatrix} |\psi_q^{(0)}\rangle \\ |\psi_q^{(1)}\rangle \end{pmatrix} = -i \begin{pmatrix} H_q^{(0)} & 0 \\ H_q^{(1)} & H_q^{(0)} \end{pmatrix} \begin{pmatrix} |\psi_q^{(0)}\rangle \\ |\psi_q^{(1)}\rangle \end{pmatrix}. \quad (5.16)$$

Eq. (5.16) can now be used in GRAPE as the Schrödinger equation for the joint state $(|\psi_q^{(0)}\rangle, |\psi_q^{(1)}\rangle)$.

We find that for *any* pulse duration τ longer than a certain critical $\tau_* \approx 14.32/\Omega_{\max}$ there exists a pulse with $J = 0$, i.e. a pulse that implements a CZ gate with fidelity $F = 1$ which is simultaneously robust to first order against amplitude deviations. We refer to the shortest possible pulse with $\tau = \tau_*$ as the “amplitude-robust” (AR) pulse. The AR pulse is of the form $\Omega(t) = \Omega_{\max} \exp[i\varphi(t)]$, i.e. it has always maximal amplitude. The laser phase $\varphi(t)$ of the AR pulse as a function of the dimensionless time $t\Omega_{\max}$ is shown in Fig. 5.4(a), together with the time-optimal (TO) pulse (without any robustness) found in Sec. 3.3. We emphasize that the laser phase of the AR pulse is a smooth function of time, which may be easier to implement experimentally than a pulse with discontinuities in the amplitude or phase. The average time spent in the Rydberg state during the AR pulse is $\tau_R = 4.74/\Omega_{\max}$, roughly 60% longer than the TO pulse, which achieves $\tau_R = 2.96/\Omega_{\max}$.

To demonstrate the robustness of the AR pulse we first calculate the infidelity $1 - F$ in the absence of Rydberg decay ($\gamma = 0$), as a function of the amplitude error $\varepsilon_1 = \varepsilon_2 =: \varepsilon$. The infidelities are displayed in Fig. 5.4(b) by the orange dotted (AR pulse) and blue solid (TO pulse) lines. The AR pulse achieves an infidelity $1 - F < 10^{-4}$ even for very large values of $|\varepsilon|$ up to 0.05, improving on the TO pulse by several orders of magnitude. A similar robustness is obtained for $\varepsilon_1 \neq \varepsilon_2$ (not shown).

5.3.2 Detuning Robust Pulses

Now we turn to pulses which are robust against a detuning of the laser, but not against deviations of the laser amplitude, i.e. we assume $\varepsilon_1 = \varepsilon_2 = 0$. For this setting, we demonstrate analytically that no pulse exists for which the implemented gate is first-order insensitive to Δ_1 and Δ_2 . Analogously to the amplitude robust pulse, we expand the Hamiltonians and quantum states as $H_q = H_q^{(0)} + \Delta_1 H_q^{(1,1)} + \Delta_2 H_q^{(1,2)}$ and $|\psi_q(t)\rangle = |\psi_q^{(0)}\rangle + \Delta_1 |\psi_q^{(1,1)}\rangle + \Delta_2 |\psi_q^{(1,2)}\rangle + \mathcal{O}(\Delta^2)$. Through perturbation theory we find that for any pulse with $|\psi_q^{(0)}\rangle = e^{i\zeta_q} |q\rangle$ the first order correction satisfies

$$\langle q | \psi_q^{(1,j)}(\tau) \rangle = -i e^{i\zeta_q} \int_0^\tau \langle \psi_q^{(0)}(t) | H_q^{(1,j)} | \psi_q^{(0)}(t) \rangle dt. \quad (5.17)$$

By using that $\sum_j H_q^{(1,j)}$ is the projector onto the states with one atom in the Rydberg state we see that $\sum_j \langle q | \psi_q^{(1,j)}(\tau) \rangle = -i \exp(i\zeta_q) \tau_q^R$, where $\tau_q^R = \int_0^\tau dt (1 - |\langle q | \psi_q^{(0)} \rangle|^2)$ is the average time spent in the Rydberg state when starting in state $|q\rangle$. Since $\tau_q^R > 0$ for all pulses which implement a CZ gate, we see that there is no pulse with $|\psi_q^{(1,1)}(\tau)\rangle = |\psi_q^{(1,2)}(\tau)\rangle = 0$. Hence there is no pulse such that the implemented gate is to first order insensitive to Δ_1 and Δ_2 . This motivates the search for different solutions to dominant detuning errors in experiments in Sec. 5.4 below. Note that the same argument applies even if we restrict the discussion to equal detunings $\Delta_1 = \Delta_2 = \Delta$.

We note that while no robust pulse exists, it is still possible to minimize the sensitivity to finite Δ . In Appendix 5.B we use a combination of GRAPE and analytical techniques to find the pulse that minimizes $1 - F$ at small but finite values of Δ , while still achieving $F = 1$ at $\Delta = 0$. This optimal pulse improves the infidelity by only 17% compared to the TO pulse, an improvement much less relevant than the several orders of magnitude achieved by, e.g., the AR pulse against amplitude deviations or the pulses described below.

5.3.3 Stark Shift Robust Pulses

One important source of detuning are uncompensated AC-Stark shifts arising due to the off-resonant coupling of the global laser to other states. For an uncertain Rabi frequency $(1 + \varepsilon_i)\Omega$, these Stark shifts are of the form $\chi(1 + \varepsilon_i)^2\Omega^2$. The known

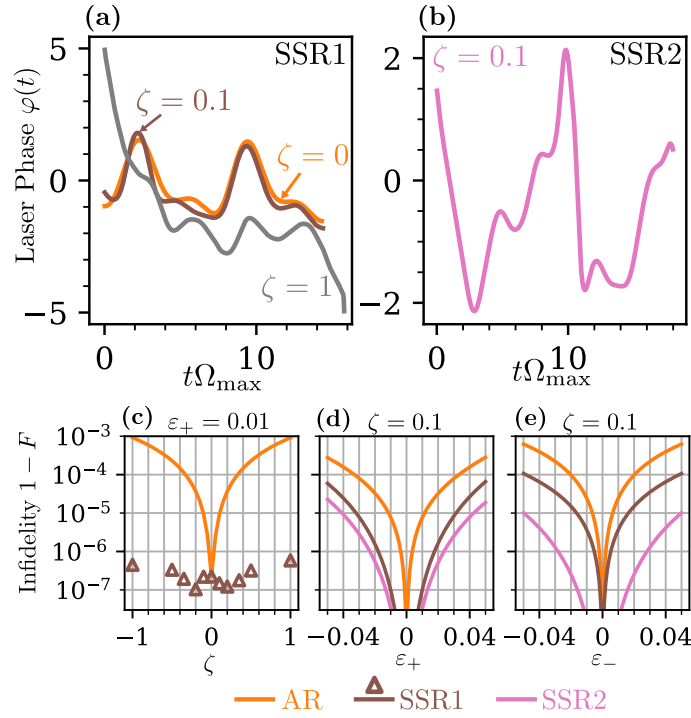


Figure 5.5: Stark shift robust pulses. (a) The Stark shift robust pulses at identical errors $\varepsilon_1 = \varepsilon_2$ (SSR1) for $\zeta = 0.0$ (identical to AR pulse), $\zeta = 0.1$ and $\zeta = 1$ (b) The Stark shift robust pulses at independent errors $\varepsilon_1 \neq \varepsilon_2$ (SSR2) for $\zeta = 0.1$ (c) The infidelity $1 - F$ for the AR pulse (solid lines) and the SSR1 pulses (triangles) as a function of ζ at $\varepsilon_1 = \varepsilon_2 = 0.01$ (d)[(e)] The infidelity as a function of $\varepsilon_+[\varepsilon_-]$ for the AR, SSR1 and SSR2 pulse at $\zeta = 0.1$

part $\chi\Omega^2$ of the Stark shift can be compensated by adjusting the laser frequency accordingly, leaving an unknown detuning $\Delta_i = \zeta\varepsilon_i\Omega + \mathcal{O}(\varepsilon^2)$, where $\zeta = 2\chi\Omega$ is a dimensionless quantity measuring the strength of the Stark shift.

Crucially, the detuning Δ induced by a Stark shift and the amplitude deviation ε are *correlated*. This allows, in contrast to Sec. 5.3.2, for the existence of pulses which are to first order robust against Stark shifts, so called Stark shift robust (SSR) pulses. For SSR pulses we distinguish between the case of identical errors on both atoms ($\varepsilon_1 = \varepsilon_2$), and the case of independent errors ($\varepsilon_1 \neq \varepsilon_2$). For the case of identical errors, the SSR pulse (termed SSR1) can be found analogously to the AR pulse (Sec. 5.3.1) by changing the first order contribution $H_q^{(1)}$ of the Hamiltonian to include the Stark shift (e.g. $H_{01} = \Omega/2 |10\rangle\langle r0| + \text{h.c.} + \zeta\Omega |r0\rangle\langle r0|$). The SSR1 pulses for $\zeta = 0.1$ and $\zeta = 1$ are shown in Fig. 5.5(a) together with the AR pulse ($\zeta = 0$). The shape of the SSR1 pulse is a small perturbation of the AR pulse for small ζ (see $\zeta = 0.1$), while for large ζ its shape is qualitatively different from the AR pulse (see $\zeta = 1$). The SSR1 pulse for $\zeta = 0.1$ ($\zeta = 1$) spends an average time of $\tau_R = 4.76/\Omega_{\max}$ ($\tau_R = 4.22/\Omega_{\max}$) in the Rydberg state, comparable to the AR pulse. For $\zeta \gtrsim 2$, the optimization procedure fails to find an SSR1 pulse, which is consistent with the fact that for a pure detuning error ($\zeta \rightarrow \infty$), no robust pulse exists (Sec. 5.3.2).

To quantify the performance of the SSR1 pulse compared to the AR pulse, Fig. 5.5(c) shows the infidelity $1 - F$ at $\varepsilon_1 = \varepsilon_2 = 0.01$ for different values of ζ for the AR pulse (orange line) and the SSR1 pulses (brown triangles). While the infidelity of the AR pulse strongly increases with increasing ζ , the infidelity of the SSR pulses stays constant and outperforms the AR pulse at $|\zeta| = 1$ by more than three orders of magnitude.

For the case of independent errors, it has to be ensured that the final state $|\psi_{11}\rangle$ is also robust against amplitude deviations if $\varepsilon_- = (\varepsilon_1 - \varepsilon_2)/2 \neq 0$. This is achieved by expanding $H_{11} = H_{11}^{(0)} + \varepsilon_+ H_{11}^{(1)} + \varepsilon_- H_{11}^{(1)}$, where $H_{11}^{(1)} = \zeta \Omega_{\max} |W_+\rangle \langle W_-| + \text{h.c.}$ contains only Stark shift terms, and including the corresponding $\langle \psi_{11}^{(1)} | \psi_{11}^{(1)} \rangle$ term in the cost function (5.15). The resulting SSR pulse (termed SSR2) is displayed in Fig. 5.5(b) for $\zeta = 0.1$. In contrast to the SSR1 pulse it is qualitatively different from the ADR pulse, due to the additional requirement that $|\psi_{11}^{(1)}\rangle = 0$. The SSR2 pulse for $\zeta = 0.1$ spends an average time of $\tau_R = 5.87/\Omega_{\max}$ in the Rydberg state, roughly 25% more than the SSR1 pulse.

The performance difference between the SSR1 and SSR2 pulse is demonstrated in Fig. 5.5(d,e). Panel (d) shows the infidelity of the AR (orange), SSR1 (brown) and SSR2 (pink) pulse at $\zeta = 0.1$ as a function of ε_+ , while $\varepsilon_- = (\varepsilon_1 - \varepsilon_2)/2 = 0$. Here, the SSR1 and SSR2 pulses show a similar infidelity, and both significantly outperform the AR pulse. In contrast, panel (e) shows the infidelity of the same pulses as a function of ε_- , while $\varepsilon_+ = 0$. As expected, the SSR2 pulse now significantly outperforms both the AR and the SSR1 pulse.

5.4 Doppler Robust Pulses

A second practically relevant source of detuning error is the Doppler shift $\Delta_j = kv_j$ where k is the wavevector of the global laser and v_j is the velocity of atom j along the direction of the laser. In contrast to a fixed detuning discussed in Sec. 5.3.2, the sign of the Doppler shift can be flipped by changing the sign of k or v . In the following we will argue that a robust gate can be achieved by splitting the gate into two identical halves applied sequentially, with the sign of Δ_j reversed between the two halves, as illustrated in Fig. 5.6(a). We start in Sec. 5.4.1 by showing how this reversal of Δ_j allows for pulses robust against Doppler shifts. In Sec. 5.4.2 we then discuss two potential experimental methods for reversing Δ_j .

5.4.1 Design of Doppler Robust Pulses

In order to be robust against Doppler errors, we use GRAPE to search for a pulse $\Omega(t)$ of duration τ that satisfies two conditions. First, implementing a C-Phase gate with two qubit phase $\pi/2$ when $\Delta = 0$ (i.e., satisfying $|\psi_q^{(0)}(\tau)\rangle = e^{i\zeta_q} |q\rangle$ with $\zeta_{01} = \zeta_{10} = \theta$ and $\zeta_{11} = \pi/2 + 2\theta$ for some single qubit phase θ). Second,

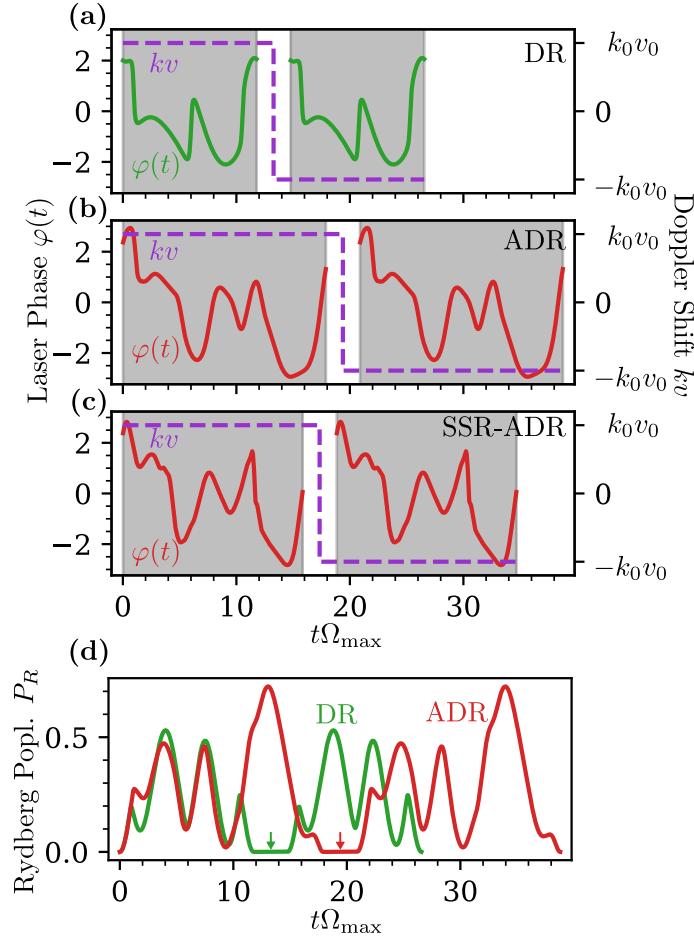


Figure 5.6: Doppler-robust and amplitude- and Doppler-robust pulses. Laser phase for (a) the Doppler-robust (DR, green), (b) the amplitude- and Doppler-robust (ADR, red), and (c) the Stark-shift robust (SSR) ADR pulse. Each pulse consists of two identical halves, shown by the grey areas, applied with opposite Doppler shifts $\Delta = kv$ (purple dashed lines), achieved as described in the text. In each of the halves the laser amplitude is maximal ($|\Omega(t)| = \Omega_{\max}$), while $\Omega(t) = 0$ outside of the gray areas. (d) The population P_R of the Rydberg state (averaged over the four computational basis states as initial states) for the DR and ADR pulse as a function of time. Note that between the two halves of the pulses (shown by the arrows) the population of the Rydberg state is zero.

achieving a first order error $|\psi_q^{(1,j)}\rangle$ which is entirely along the direction of $|q\rangle$, i.e. $(I - |q\rangle\langle q|)|\psi_q^{(1,j)}(\tau)\rangle = 0$. The state after applying this pulse once is then

$$|\psi_q(\tau)\rangle = \left(e^{i\zeta_q} + \sum_j \Delta_j \langle q|\psi_q^{(1,j)}(\tau)\rangle \right) |q\rangle + \mathcal{O}(\Delta^2). \quad (5.18)$$

When applying the pulse $\Omega(t)$ a second time, the sign of Δ_j is reversed. This implies $|\psi_q(2\tau)\rangle = e^{2i\zeta_q} |q\rangle + \mathcal{O}(\Delta^2)$, and thus the combined pulse is robust against Doppler errors. Crucially, the Rydberg population after the first pulse is of order $\mathcal{O}(\Delta^2)$, which makes the gate insensitive to the relative phase of the lasers between the two pulses and also allows an arbitrary waiting time between the pulses without incurring errors from Rydberg state decay.

GRAPE can be applied to this problem analogously to the amplitude robust case, with the cost function

$$J = 1 - F + \sum_{j,q} \langle \psi_q^{(1,j)}(\tau)|(I - |q\rangle\langle q|)|\psi_q^{(1,j)}(\tau)\rangle. \quad (5.19)$$

The shortest possible pulse which is robust against Doppler errors, called the ‘‘Doppler-robust’’ (DR) pulse, is shown in Fig. 5.6(a). The population of the Rydberg state (averaged over the four computational basis states as initial states) is shown in Fig. 5.6(d). As mentioned above, the population of the Rydberg state vanishes between the two pulses. The average time that the DR pulse spends in the Rydberg state (over the entire gate) is given by $\tau_R = 5.56/\Omega_{\max}$.

By simply adding the cost functions for the AR and the DR cases, we can identify the shortest possible pulse which is robust against both imperfections, which we call the ‘‘amplitude- and Doppler-robust’’ (ADR) pulse. The laser phase of the ADR pulse is displayed in Fig. 5.6(b), the population of the Rydberg state in Fig. 5.6(d). The ADR pulse spends an average time $\tau_R = 10.37$ in the Rydberg state, and is thus significantly more affected by its decay than the other three pulses. We remark that the ADR pulse is also robust against amplitude deviations ε_i that are different in the two halves of the pulse, since each half is individually robust against amplitude deviations.

The infidelity of all four pulses (TO, AR, DR and ADR) as a function of the detuning Δ_1 of the first atom is shown in Fig. 5.4(b). For the TO and AR pulse the detuning is kept constant, while for the DR and ADR pulse its sign is switched after the first half of the pulse. The DR and ADR pulse achieve $1 - F < 10^{-4}$ for $|\Delta_1|/\Omega_{\max} < 0.05$, two to three orders of magnitude better than the TO and AR pulses. We also compare the performance of the DR and ADR pulses to the TO and AR pulses when varying the amplitude deviation ϵ in Fig. 5.4(a). As expected, the DR pulse does not show any robustness to amplitude deviations and behaves similar to the TO pulse, while the ADR pulse outperforms not only the TO pulse, but also the AR pulse.

Analogously to the AR pulse, a Stark shift robust version exists also for the ADR pulse, shown for $\zeta = 0.1$ in Fig. 5.6(d). As for the AR pulse, the Stark shift robust

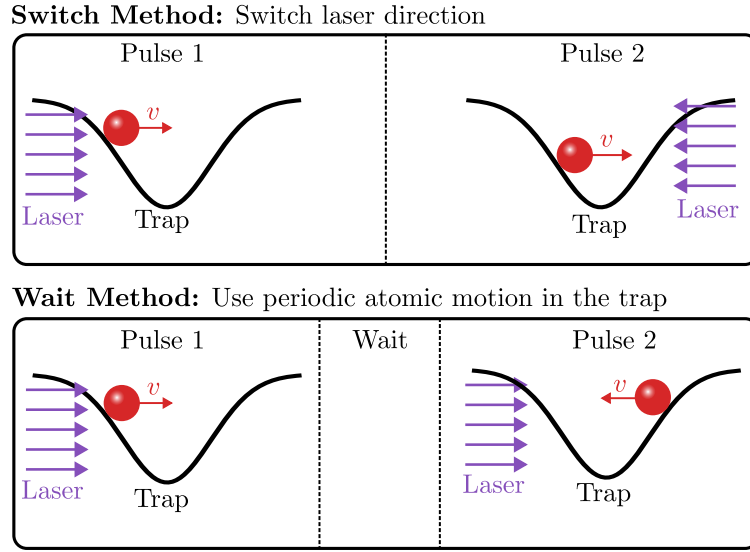


Figure 5.7: Switch and wait method. Illustration of the switch and the wait method for reversing the sign of the Doppler shift. In the switch method, the direction of the laser, and thus the sign of k , is switched after the first pulse. In the wait method instead we propose to wait for half an oscillation of the atom in the trap, switching the sign of v and thus the sign of the Doppler shift.

ADR pulse is qualitatively similar to the ADR pulse in the absence of a Stark shift. It spends an average time of $\tau_R = 10.66/\Omega_{\max}$ in the Rydberg state. Note that the ADR pulses is inherently robust against Stark shift errors with $\varepsilon_1 = -\varepsilon_2$, so that in contrast to the AR pulse no distinction between identical and independent errors is necessary. To see this, first note that for the states $|\psi_{10}\rangle$ and $|\psi_{10}\rangle$ the distinction between identical and independent errors is irrelevant, because only one of the two atoms is affected by the error. The remaining state $|\psi_{\overline{11}}\rangle$ (describing the state of the atoms *after the first pulse half* when starting in $|11\rangle$) is intrinsically robust against Stark shift errors with $\varepsilon_1 = -\varepsilon_2$, because these errors only result in a nonzero detuning $\Delta_- = \zeta\varepsilon_1|\Omega_{\max}|$ and a corresponding perturbation $H_{\overline{11}}^{(1)} = \zeta\Omega_{\max}|W_+\rangle\langle W_-| + \text{h.c.}$. By the Doppler robustness of the ADR pulse, it holds that $\langle W_{\pm}|\psi_{\overline{11}}^{(1)}\rangle = 0$. But because $H_{\overline{11}}^{(1)}$ only leads to the population of $|W_-\rangle$ and otherwise leaves the evolution unchanged, it also holds that $\langle 11|\psi_{\overline{11}}^{(1)}\rangle = 0$, so that $|\psi_{\overline{11}}^{(1)}\rangle = 0$. Hence each of the two pulse halves of the ADR pulse are robust against Stark shift errors with $\varepsilon_1 = -\varepsilon_2$, so also the whole ADR pulse is robust against those errors. Note that this even holds if the ε_i are different in each of the pulse halves.

5.4.2 Reversing the Doppler Shift

The DR and ADR pulse require that Δ_j is reversed after the first half of the pulse. Here we propose two methods for switching the sign of Δ_j , called the *switch* method and the *wait* method.

In the switch method, the direction of the laser (i.e. the sign of k) is reversed between

the two pulses. Note that the switch method works regardless of the relative phase between the two laser beams, because the Rydberg population in between the two pulse halves vanishes [see Fig. 5.6(b)].

The wait method instead makes use of the fact that the atom is confined in a potential that is approximately harmonic, and therefore the velocity in the direction of the laser propagation is periodic with trap frequency ω_{tr} . By waiting for a time π/ω_{tr} between the two pulses, the sign of v , and thus the sign of Δ_j , is reversed. Since the Rydberg state is not populated between the two pulse halves, no additional decay error arises during this wait time even if $\omega_{\text{tr}} \ll \gamma$.

The wait method makes several implicit assumptions on the motion of the atoms. First, we assume that the propagation direction of the laser is along one of the normal modes of the trap. Second, we assume that the coherence of the atomic motion is much longer than one motional period [164]. Finally, we assume that the atomic temperature is low enough for the trap anharmonicity to be negligible. In Appendix 5.D.1 we estimate the impact of a finite trap anharmonicity and show that for achievable experimental parameters it does not significantly affect the gate performance.

Both the switch and the wait method require that the velocity of the atoms is approximately constant during each pulse. The acceleration of the atoms during the pulses is thus a source of error. For the switch method this error can be avoided by abruptly turning off the trapping potential during the pulses, which is already common practice in many experiments to avoid differential light shifts and anti-trapping of the Rydberg state [165]. However, this approach is unsuitable for the wait method, since it affects the velocity reversal, and is also undesirable because it heats the atom and may prevent the execution of deep circuits with many gates. To mitigate these disadvantages, we propose to modulate the trapping potential sinusoidally in time, and to apply the pulses at times where the potential is zero (Appendix 5.C). This gives rise to an approximately constant velocity of the atoms during the pulses while also eliminating the differential light shift and heating from square-wave modulation [166]. For the wait method, we show that it is possible to apply the two pulse halves at two different times of vanishing potential such that the velocity is reversed between the two pulses. Note that fast sinusoidal trap modulation was experimentally demonstrated in an optical tweezer for the purpose of eliminating light shifts in a cavity QED experiment [166]. For the remainder of this chapter we assume that the trap modulation is applied for both the switch and the wait method, in Appendix 5.D.2 we discuss the two methods *without* the trap modulation.

In conclusion, we have shown how the reversal of the Doppler shift in the middle of the gate allows for a pulse which is robust against errors arising from Doppler shifts, and a pulse which is robust against both amplitude deviations and Doppler shifts. We demonstrated that the infidelity arising due to Doppler shifts is reduced by several orders of magnitude by the robust pulses, and provided two methods to switch the sign of the Doppler shift.

5.5 Infidelities in a Realistic Error Model

To assess the performance of the TO, AR, DR and ADR pulses in a realistic experiment, we now include the decay of the Rydberg state and atomic motion in a harmonic trap. For this we assume random and uncorrelated initial velocities and positions for both atoms, drawn from a normal distribution with standard deviation $\sqrt{k_B T/m}$ and $\sqrt{k_B T/m\omega_{\text{tr}}^2}$, respectively, where T is the temperature and m is the mass of the atoms. We then assume that the atoms follow classical trajectories in the harmonic trap, which we incorporate as a modified Rabi frequency $\tilde{\Omega}(t) = e^{-ikx(t)}\Omega(t)$. In the case of the DR and ADR pulses, we simulate both the switch and wait method of reversing the detuning between the two pulse halves, applying the modulation of the trapping potential as described in Appendix 5.C for both methods. We sample the laser amplitude error ε from a normal distribution with standard deviation σ_ε . For simplicity, we set $\varepsilon_1 = \varepsilon_2 = \varepsilon$, but note that the same robustness is achieved if $\varepsilon_1 \neq \varepsilon_2$ since the AR and ADR pulses are robust against ε_1 and ε_2 independently.

For the Rydberg excitation, we consider parameters recently proposed for metastable ^{171}Yb qubits using a single-photon excitation to the $|75\ ^3S_1\ F = 3/2\rangle$ Rydberg state [20], although we note that these are broadly similar to proposed or achieved values for other alkaline earth atoms such as Sr [66, 127] and ground-state ^{171}Yb qubits [85, 167]. The specific numerical values considered here are: $\Omega_{\text{max}} = 2\pi \times 5.5$ MHz, $2\pi/k = 302$ nm, $1/\gamma = 100\ \mu\text{s}$, $\omega_{\text{tr}} = 2\pi \times 50$ kHz and $m = 171$ u. The interaction strength is $B \sim 5$ THz $\mu\text{m}^6/R^6$, so that $B \gg \Omega_{\text{max}}$ for realistic values of the interatomic distance R in the range of 3-6 μm [85]. In the following calculations we assume a perfect Rydberg blockade. Similar parameters can be obtained for alkali atoms, but we note that two-photon excitation typically reduces the wavevector associated with Doppler shifts, at the expense of an additional decay error from the decay of the intermediate state. As the Stark shift strength in metastable ^{171}Yb qubits is unknown, we assume the value measured in ^{88}Sr qubits, given by $2\pi\chi \approx 10\text{kHz}/\text{MHz}^2$ [66]. For the Rabi frequency Ω_{max} this corresponds to $\zeta \approx 0.1$. In the following we always use the Stark shift robust variants of the AR and ADR pulse. Since we restrict ourselves to the $\varepsilon_1 = \varepsilon_2$ case, we use the SSR1 pulse as the Stark shift robust variant of the AR pulse.

Our results are summarized in Fig. 5.8. We first consider the performance with only amplitude or Doppler errors. The infidelity as a function of σ_ε with $T = 0$ is shown in Fig. 5.8(a). For small values of σ_ε the decay of the Rydberg state is the dominant error, so the fidelities depend only on the time spent in the Rydberg state. The order of the pulses by increasing time spent in the Rydberg state (in our case identical to increasing pulse duration) is TO, AR, DR, ADR. In contrast, as σ_ε increases, the infidelity of the AR and ADR pulses stays almost constant, while the infidelity of the TO and DR pulses increases quadratically. At $\sigma_\varepsilon \gtrsim 0.010$ the AR pulse becomes favourable compared to the TO pulse, at $\sigma_\varepsilon \gtrsim 0.026$ the ADR pulse becomes favorable compared to the TO pulse. The AR pulse outperforms the ADR pulse, because while both pulses are robust to deviations of the laser amplitude, the AR pulse spends less time in the Rydberg state.

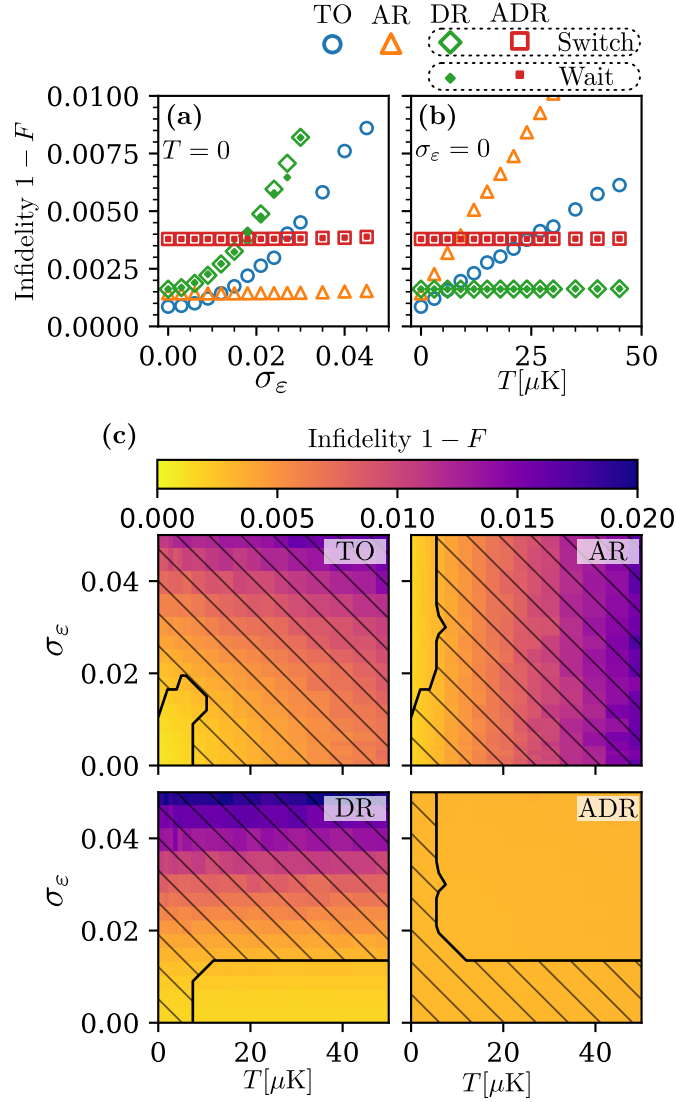


Figure 5.8: Infidelities in a realistic error model. The infidelity $1 - F$ of the TO, AR, DR and ADR pulse at different values of the amplitude uncertainty σ_ε and the atomic temperature T . (a) $1 - F$ as a function of σ_ε at $T = 0$. For the DR and ADR pulse, open symbols show the infidelity with the switch method, while filled symbols show the infidelity with the wait method. Sinusoidal modulation of the trap is applied in all cases. (b) $1 - F$ as a function of T at $\sigma_\varepsilon = 0$. (c) Color plot of $1 - F$ as a function of both σ_ε and T . For the DR and ADR pulse we use the wait method including the sinusoidal modulation of the trap. The encircled regions show the range of imperfections where each pulse performs the best.

Next we consider the performance as a function of T , in the absence of amplitude errors ($\sigma_\varepsilon = 0$) [Fig. 5.8(b)]. At low temperatures the pulses are again ordered by the time they spent in the Rydberg state. With increasing temperature, however, the infidelity of the DR and ADR pulses stays almost constant, while the infidelity of the TO and AR pulses increases linearly with T (quadratically with Δ). For $T \gtrsim 6\mu\text{K}$ the DR pulse outperforms the TO pulse, for $T \gtrsim 28\mu\text{K}$ the ADR pulse outperforms the TO pulse. These results do not depend on whether the switch or the wait method is used. We note that the infidelity of the TO pulse at elevated temperatures is roughly consistent with previous estimates for various non-robust blockade gates [127, 165]. We remark that with increasing temperature, other imperfections not considered here, such as the anharmonicity of the trap may become increasingly relevant (see Appendix 5.D.1 for a discussion).

Finally, we consider the infidelity in the presence of both amplitude and Doppler errors. Fig. 5.8(c) shows the infidelity of all four pulses over a range of imperfections. Additionally, the region in which each pulse has the lowest infidelity out of the four considered pulses is marked. The results are shown for the wait method, we verified that for the switch method identical results are obtained. As expected, the TO pulse performs best when all imperfections are small, while ADR pulse is the best pulse for large amplitude uncertainties and large temperatures. The AR and DR pulses are the best choice when either the amplitude uncertainty is large or the temperature is large, while the other imperfection is small.

5.6 Conditional Infidelity and Logical Error Rate

In the previous section we saw that, even with the use of robust pulses, gate errors of the order 10^{-3} are unavoidable, making it impossible to perform a quantum computation with more than 10^3 operations. However, for many useful quantum algorithms, a significantly larger operations is necessary [168]. The problem that the reasonably achievable gate error rates are orders of magnitude below what is required for longer quantum computations is not unique to neutral atom quantum processors, but in fact occurs in almost all quantum computing platforms.

To allow quantum computing even with faulty gates, the framework of fault tolerant quantum computation (FTQC) has been developed [19, 169–172] (see also Chapter 6). FTQC uses redundancy to encode one *logical* qubit in several *physical* qubit, where in a neutral atom quantum computer each physical qubit can be encoded in a single atom. As long as the error of each physical gate is below a certain *threshold*, it is possible to use FTQC to achieve an arbitrarily low *logical error rate* in the logical qubit by using more and more physical qubits.

In the context of FTQC, both the error probability and the type of error are important. Recently, it was proposed [20, 162] and experimentally demonstrated [14] that using the metastable state in ^{171}Yb to encode qubits ensures that the vast majority of Rydberg decay errors result in transitions out of the computational subspace that

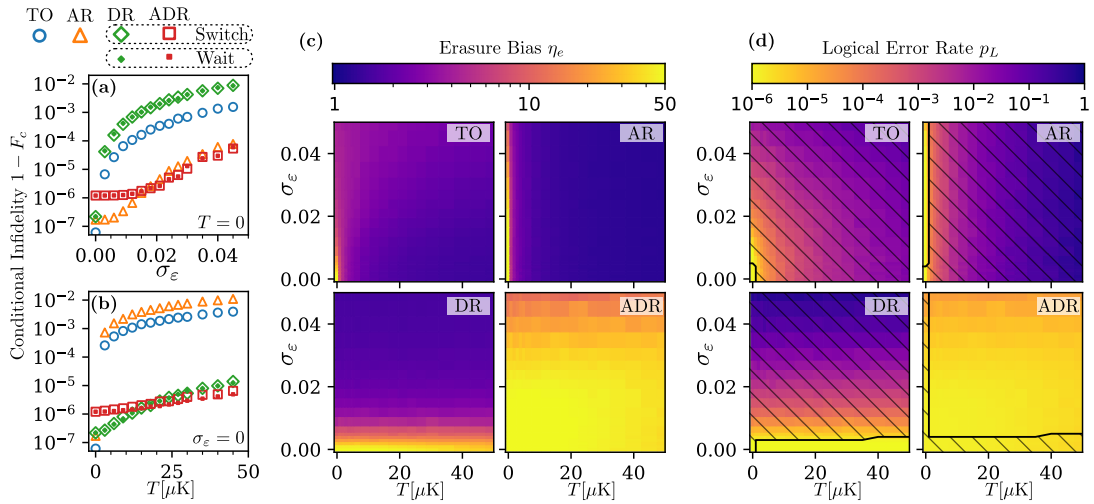


Figure 5.9: Conditional infidelity, erasure bias, logical error rate. (a) Conditional fidelity $1 - F_c$ of the four pulses as a function of the amplitude uncertainty σ_ϵ at $T = 0$. For the DR and ADR pulse, open symbols show results with the switch method, while filled symbols show the results with the wait method. For both methods the sinusoidal modulation of the trap is applied. (b) $1 - F_c$ as function of T at $\sigma_\epsilon = 0$. (c) The erasure bias η_e as a function of T and σ_ϵ (using the wait method including the trap modulation for the DR and ADR pulse), assuming $\eta_e = 50$ in the absence of imperfections. (d) The logical error rate p_L as a function of T and σ_ϵ . The encircled regions show the range of imperfections where each pulse performs the best.

can be efficiently detected [20]. This converts decay errors into so-called *erasure errors*, for which the FTQC threshold is much higher.

Maintaining this advantage in the presence of experimental imperfections requires that the fraction of errors converted into erasures, R_e , is close to unity. From the fact that a small fraction of decays of the Rydberg state does lead back to the computational subspace, Ref. [20] estimated that $R_e = 0.98$ for the case of spontaneous decays from the Rydberg state, which is the only fundamental limitation to the fidelity of multi-qubit Rydberg gates. In this case, the estimated XZZX surface code threshold can be as high as $p_{th} = 4.15\%$, compared to $p_{th} = 0.93\%$ for a comparable Pauli error model [20]. Similar estimates have been made for other erasure-biased qubits [173].

To understand the error decomposition of our robust pulses, we start by assuming that *all* Rydberg decay errors lead to transitions outside of the computational subspace and compute the *conditional fidelity* F_c , i.e. the fidelity conditioned on the final state being in the computational subspace. The conditional infidelity $1 - F_c$ is shown as a function of the amplitude uncertainty σ_ϵ at $T = 0$ in Fig. 5.9(a) and as a function of T at $\sigma_\epsilon = 0$ in Fig. 5.9(b), assuming the same experimental parameters as in Sec. 5.5. The robust pulses always outperform the non-robust pulses by several orders of magnitude and satisfy $1 - F_c \ll 1 - F$ [see Fig. 5.8(a),(b) and Fig. 5.9(a),(b)], showing that errors are dominated by transitions out of the com-

putational subspace. This is expected because the robust pulses effectively trade sensitivity to imperfections for Rydberg decay. Note that again the switch and the wait method give identical results in Figs. 5.9(a)(b). For the rest of this work we show the results from the wait method, but have verified that they do not change significantly when using the switch method instead.

To quantify the logical error rate achievable for the robust pulses for metastable ^{171}Yb qubits, we now include that not all, but only a fraction of $r = 0.98$ of the decay errors are converted into erasures [20]. To calculate the logical error rate we assume, analogously to Ref. [20], a Pauli error channel, in which an erasure error occurs with probability p_e and a random Pauli error occurs with probability p_p . We identify p_e and p_p from the probability p_d of a decay error and the conditional infidelity $1 - F_c$ in the exact error model as $p_e = rp_d$ and $p_p \approx (1 - r)p_d + (1 - p_d)(1 - F_c)$. Then a fraction $R_e = p_e/(p_e + p_d)$ of all errors are converted into erasures. For the pulse proposed here, we compute a quantity related to R_e , the erasure bias $\eta_e = 1/(1 - R_e)$. A larger erasure bias implies a larger fraction of erasure errors, and thus a higher threshold error probability. In the $\varepsilon = \Delta = 0$ case the erasure bias is then given by $\eta_e = 50$, the predicted maximum value for ^{171}Yb [20]. Inspecting Fig. 5.9(c), it is clear that the TO pulse only achieves a large value of η_e for very small temperatures and amplitude uncertainties and that η_e drops rapidly to ~ 1 in the presence of significant amplitude or Doppler errors. The ADR pulse instead maintains $\eta_e \approx 50$ over the whole range of considered parameters of σ_ε up to 0.05 and T up to $50\mu\text{K}$. The DR pulse achieves $\eta_e \approx 50$ as long as σ_ε is small, but η_e drops rapidly as σ_ε increases, while the AR pulse shows the opposite behavior.

Using the total infidelity and η_e , we can estimate the logical error rate for a given error correcting code. For concreteness, we consider the $d = 5$ XZZX surface code, where the logical error rate after a single round of fault-tolerant error correction, p_L , is presented in Ref. [20] for a range of physical error rates $p = 1 - F$ and erasure biases η_e . The estimated value of p_L is shown in Fig. 5.9(d) for the four pulses studied here. Remarkably, the ADR pulses outperforms the other three pulses by many orders of magnitude unless either σ_ε or T is very small. This is in contrast to Fig. 5.8(c), which shows that the total infidelity of the ADR pulse is larger than that of the other three pulses until σ_ε or T reach modest values. This illustrates a fundamental tradeoff that is one of the central results of this chapter: the larger infidelity associated with the longer ADR sequence is more than compensated by the increased η_e .

5.7 Conclusion

In this chapter we have presented several new laser pulses that implement a CZ or C_2Z gate and maximize the robustness against Rydberg decay, uncertainties in the interaction strength, deviations in the laser amplitude, and a detuning of the laser. We found that the time-optimal gates found in Chapter 3 are essentially as robust as possible against Rydberg decay errors, and can be modified by modulating the

laser amplitude to increase their robustness against uncertainties in the interaction strengths.

Using a combination of optimal control methods and analytical reasoning we also found pulses robust against amplitude deviations of the laser and Doppler shifts, where the latter is achieved by reversing the sign of the Doppler shift between two halves of the pulse. These robust pulses strongly suppress errors from amplitude deviations and Doppler shifts, at the cost of a slightly larger error due to decay of the Rydberg state. Additionally we estimated the logical qubit performance in the context of the erasure-biased metastable ¹⁷¹Yb qubit, found that one of the new pulses (the ADR pulse) outperforms all other pulses unless the imperfections are very small, because they maintain the erasure bias even in the presence of imperfections. Robust pulses enable significant gains from quantum error correction even for significantly elevated temperatures and amplitude deviations.

The results of this chapter significantly relax the technical requirements for FTQC with neutral atoms [165] by extending the erasure conversion concept to amplitude and Doppler shift errors [20]. The most important of these is the constraint to have near-ground-state atomic temperatures: while this level of cooling has been achieved for a number of neutral atom qubit species [167, 174–177], it is a fundamental challenge to maintain these temperatures over long sequences of gates or atom transport operations. We note that re-cooling after transport is a significant overhead in trapped ion CCD architectures [178, 179], and that sympathetic cooling is not straightforward in neutral atoms [180].

Besides laser amplitude inhomogeneities, Doppler shifts, decay of the Rydberg state, and uncertainties in the interaction strength, an experimental realization of the proposed gates will be affected by error sources not included in our analysis, including time dependent parameter fluctuations, such as laser phase noise, and uncertainties in the applied pulse shape. While our pulses are not explicitly robust to those errors, there is no indication that they are significantly more susceptible to them, compared to previous approaches such as the TO pulse. Including additional error sources in the design of robust pulses will be the subject of further investigation. The work of this chapter allows experimental efforts to be concentrated on error sources against which our protocols are not robust, at the expense of error sources against which our protocols are robust.

5.A Gate Error for a CZ and C₂Z Error in Second Order in 1/B

In this appendix we derive perturbative expressions for the infidelity at finite B for pulses that implement a CZ or C₂Z with fidelity $F = 1$ in the $B = \infty$ case. For this, we expand $|\psi_q\rangle = |\psi_q^{(0)}\rangle + \frac{1}{B} |\psi_q^{(1)}\rangle + \frac{1}{B^2} |\psi_q^{(2)}\rangle + \mathcal{O}(B^{-3})$ and show that for the

CZ gate it holds that

$$F = 1 - \frac{1}{B^2} \left(\frac{1}{4} \langle \psi_{11}^{(1)} | \psi_{11}^{(1)} \rangle - \frac{1}{10} \left| \langle 11 | \psi_{11}^{(1)} \rangle \right|^2 \right) + \mathcal{O}(B^{-3}) \quad (5.20)$$

while for the C_2Z gate we obtain

$$F = 1 - \frac{1}{72B^2} \left(27 \langle \psi_{011}^{(1)} | \psi_{011}^{(1)} \rangle + 9 \langle \psi_{111}^{(1)} | \psi_{111}^{(1)} \rangle - \left| 3 \langle 011 | \psi_{011}^{(1)} \rangle - e^{-i\theta} \langle 111 | \psi_{111}^{(1)} \rangle \right|^2 \right. \\ \left. - 3 \left| \langle 011 | \psi_{011}^{(1)} \rangle \right|^2 - \left| \langle 111 | \psi_{111}^{(1)} \rangle \right|^2 \right) \quad (5.21)$$

where θ is the single qubit phase.

To show Eq. (5.20), we use two ingredients: Firstly any quantity $x = x^{(0)} + \frac{1}{B}x^{(1)} + \frac{1}{B^2}x^{(2)} + \dots$ depending on B satisfies

$$|x|^2 = |x^{(0)}|^2 + \frac{2}{B} \text{Re}((x^{(0)})^* x^{(1)}) + \frac{1}{B^2} \left(|x^{(1)}|^2 + 2 \text{Re}((x^{(0)})^* x^{(2)}) \right) + \mathcal{O}(B^{-3}). \quad (5.22)$$

Secondly, for any normalized vector $|\phi_q\rangle$ depending on B and with $|\phi_q^{(0)}\rangle = |q\rangle$ it holds that

$$1 = \langle \phi_q | \phi_q \rangle = 1 + \frac{1}{B} \text{Re}(\langle q | \phi_q^{(1)} \rangle) + \frac{1}{B^2} (\langle \phi_q^{(1)} | \phi_q^{(1)} \rangle + 2 \text{Re}(\langle q | \phi_q^{(2)} \rangle)) + \mathcal{O}(B^{-3}) \quad (5.23)$$

so that

$$\text{Re}(\langle q | \phi_q^{(1)} \rangle) = 0 \quad (5.24)$$

and

$$\text{Re}(\langle q | \phi_q^{(2)} \rangle) = -\frac{1}{2} \langle \phi_q^{(1)} | \phi_q^{(1)} \rangle. \quad (5.25)$$

For the fidelity of a CZ gate we obtain from Eq. (3.22) with $|\phi_{01}\rangle = e^{-i\theta} |\psi_{01}(T)\rangle$ and $|\phi_{11}\rangle = -e^{-2i\theta} |\psi_{11}(T)\rangle$ that

$$F = \frac{1}{20} (|1 + 2 \langle 01 | \phi_{01} \rangle + \langle 11 | \phi_{11} \rangle|^2 + |1 + 2 \langle 01 | \phi_{01} \rangle + \langle 11 | \phi_{11} \rangle|^2) \quad (5.26)$$

Now we apply Eq. (5.22). Because the pulse has fidelity 1 in the $B = \infty$ case we have $|\phi_{01}\rangle = |01\rangle$ and $|\phi_{11}^{(0)}\rangle = |11\rangle$, so that

$$F = \frac{1}{20} (|3 + \langle 0 | \phi_{11} \rangle|^2 + |3 + \langle 0 | \phi_{11} \rangle|^2) \\ = \frac{1}{20} \left(20 + \frac{10}{B} \text{Re}(\langle 0 | \phi_{11}^{(1)} \rangle) + \frac{1}{B^2} \left(2 \left| \langle 0 | \phi_{11}^{(1)} \rangle \right|^2 + 10 \text{Re}(\langle 0 | \phi_{11}^{(2)} \rangle) \right) \right) + \mathcal{O}(B^{-3}) \quad (5.27)$$

By inserting Eqs. (5.24) and (5.25) into Eq. (5.27) we obtain Eq. (5.20).

For the C_2Z gate we obtain from Eq. (3.22) with $|\phi_{001}\rangle = e^{-i\theta} |\psi_{001}\rangle$, $|\phi_{011}\rangle = e^{-2i\theta} |\psi_{011}\rangle$ and $|\phi_{111}\rangle = -e^{-3i\theta} |\psi_{011}\rangle$ that

$$F = \frac{1}{72} \left(|1 + 3 \langle 001 | \phi_{001} \rangle + 3 \langle 011 | \phi_{011} \rangle + \langle 111 | \phi_{111} \rangle|^2 \right. \\ \left. + |1 + 3 \langle 001 | \phi_{001} \rangle + 3 \langle 011 | \phi_{011} \rangle + \langle 111 | \phi_{111} \rangle|^2 \right) \quad (5.28)$$

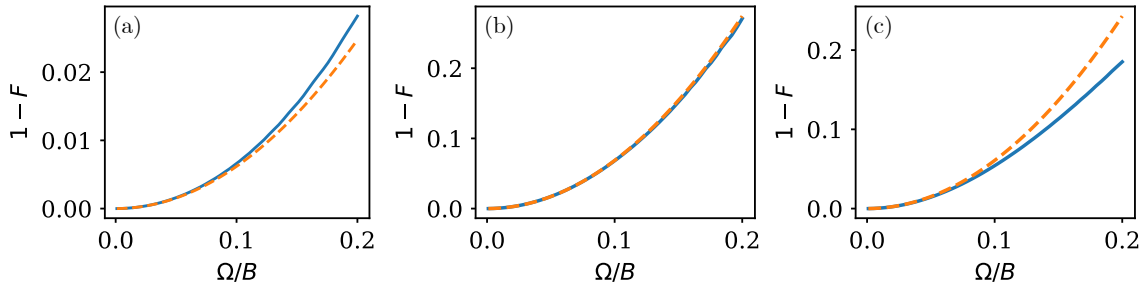


Figure 5.10: Comparison between exact and approximate infidelity. Comparison between the exact gate error at finite B (blue, solid line) and the gate error calculated from Eqs. (5.20) and (5.21) together with approximating the effects of a finite B through an Stark shift (orange, dashed line). (a) For the time-optimal pulse for the CZ gate. (b)[(c)] For Pulse 1[2] for the C_2Z gate. For all three pulses there is an excellent agreement between the exact gate error and the approximation for large enough B .

We apply Eq.(5.22) and use that $|\phi_{001}\rangle = |001\rangle$, $|\phi_{011}^{(0)}\rangle = |011\rangle$ and $|\phi_{111}^{(0)}\rangle = |111\rangle$ to obtain

$$F = \frac{1}{72} \left[72 + \frac{1}{B} \text{Re} \left(54 \langle 011 | \phi_{011}^{(1)} \rangle + 18 \langle 111 | \phi_{111}^{(1)} \rangle \right) + \frac{1}{B^2} \left(\left| 3 \langle 011 | \phi_{011}^{(1)} \rangle + \langle 111 | \phi_{111}^{(1)} \rangle \right|^2 \right. \right. \\ \left. \left. + 3 \left| \langle 011 | \phi_{011}^{(1)} \rangle \right|^2 + \left| \langle 111 | \phi_{111}^{(1)} \rangle \right|^2 + \text{Re} \left(54 \langle 011 | \phi_{011}^{(2)} \rangle + 18 \langle 111 | \phi_{111}^{(2)} \rangle \right) \right) \right] \quad (5.29)$$

By inserting Eqs. (5.24) and (5.25) into Eq. (5.29) we obtain Eq. (5.21).

We numerically confirm Eqs. (5.20) and (5.21) as well as the fact that to first order in $1/B$ it is sufficient to account for the finiteness of B through a Stark shift. For this, we consider the time-optimal pulse for the CZ gate and Pulse 1 and Pulse 2 for the C_2Z gate (see Secs. 3.3 and 3.6) and calculate the gate error once using the exact Hamiltonian and once from Eqs. (5.20) and (5.21). In the latter case, the $|\psi_q^{(1)}\rangle$ are found through Eq. (5.8). The exact and the approximate gate error are shown in Fig. 5.10 as blue solid line and orange dotted line, respectively. For all three considered pulses the exact and the approximate gate error are in excellent agreement for large B .

5.B Pulse Most Robust against Detuning Errors

In Sec. 5.3.2 we showed that there exists no pulse $\Omega(t)$ such that the quantum state after the pulse is to first order insensitive to the detunings Δ_1 and Δ_2 . In this appendix we derive a pulse which is nevertheless as robust as possible. For this we assume $\Delta_1 = \Delta_2 = \Delta$, which is the case when the detuning error arises from frequency noise of the laser and not from Doppler shifts.

The fidelity of the pulse can be expanded as $F = F^{(0)} + \Delta F^{(1)} + \Delta^2 F^{(2)} + \mathcal{O}(\Delta^3)$ with $F^{(0)}$ given by Eq. (5.14) and

$$F^{(1)} = \frac{1}{2} \sqrt{F^{(0)}} \sum_{q \in \{10,01,11\}} \operatorname{Re} (e^{-i\zeta_q} \langle q | \psi_q^{(1)} \rangle) \quad (5.30)$$

$$F^{(2)} = \frac{1}{16} \left| \sum_{q \in \{10,01,11\}} e^{-i\zeta_q} \langle q | \psi_q^{(1)} \rangle \right|^2 + \frac{1}{2} \sqrt{F^{(0)}} \sum_{q \in \{10,01,11\}} \operatorname{Re} (e^{-i\zeta_q} \langle q | \psi_q^{(2)} \rangle). \quad (5.31)$$

We now consider a pulse with $F^{(0)} = 1$, i.e. $|\psi_q^{(0)}\rangle = e^{i\zeta_q} |q\rangle$. By normalization of $|\psi_q\rangle$ it must hold that $\operatorname{Re}(e^{-i\zeta_q} \langle q | \psi_q^{(1)} \rangle) = \operatorname{Re}(\langle \psi_q^{(0)} | \psi_q^{(1)} \rangle) = 0$ and that $\langle \psi_q^{(1)} | \psi_q^{(1)} \rangle + 2\operatorname{Re}(e^{-i\theta_q} \langle q | \psi_q^{(2)} \rangle) = 0$. Inserting this into Eqs. (5.30) and (5.31) we obtain $F^{(1)} = 0$ and

$$F^{(2)} = \frac{1}{16} \left| \sum_q e^{-i\zeta_q} \langle q | \psi_q^{(1)} \rangle \right|^2 - \frac{1}{4} \sum_q \langle \psi_q^{(1)} | \psi_q^{(1)} \rangle \quad (5.32)$$

Our goal is now to find the pulse which minimizes $-F^{(2)}$ while satisfying $F^{(0)} = 1$. As a reference we calculate for the time-optimal pulse $-F^{(2)} = 3.45/\Omega_{\max}^2$.

We now insert the relation $e^{-i\zeta_q} \langle q | \psi_q^{(1)} \rangle = -i\tau_q^R$ (see Eq. (5.17) into Eq. (5.32) and use the fact that, because $\Delta_1 = \Delta_2$, $|\psi_{10}\rangle$ and $|\psi_{01}\rangle$ are identical up to relabeling the states. We obtain $-F^{(2)} = -F_c^{(2)} - F_r^{(2)}$ with

$$-F_c^{(2)} = \frac{1}{16} (4(\tau_{10}^R)^2 + 3(\tau_{11}^R)^2 - 2\tau_{10}^R \tau_{11}^R) \quad (5.33)$$

$$-F_r^{(2)} = \frac{1}{2} |\langle r0 | \psi_{10}^{(1)} \rangle|^2 + \frac{1}{4} |\langle W_+ | \psi_{11}^{(1)} \rangle|^2 \quad (5.34)$$

Here, $-F_c^{(2)}$ is the *conditional fidelity* and measures the infidelity arising from deviations of the final state in the computational subspace while $-F_r^{(2)}$ measures the infidelity arising from population of the Rydberg state. Since $\tau_q^R > 0$ we see that also $-F_c^{(2)} > 0$ and thus $-F^{(2)} > 0$.

A lower bound on the minimal possible $-F^{(2)}$ is obtained by minimizing $-F_c^{(2)}$ over all pulses with $F^{(0)} = 1$. We do so using the GRAPE algorithm with the cost function $J = C(1 - F^{(0)}) - F_c^{(2)}$ for a large $C = 10^4$. The large value of C ensures that the pulse minimizing J will have $F^{(0)} \approx 1$, while the second term in J ensures that the pulse minimizes $-F_c^{(2)}$. We find that the minimal value is $-F_c^{(2)} = 2.87/\Omega_{\max}^2$, for a pulse Ω_* with duration $\tau_* = 7.70/\Omega_{\max}$. The pulse Ω_* is shown in the shaded area in Fig. 5.11. Through the pulse Ω_* , the value of $-F_c^{(2)}$ decreases by 17% compared to the TO pulse.

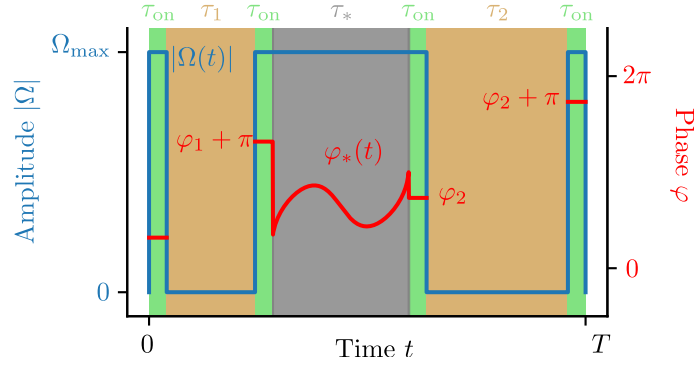


Figure 5.11: Most robust pulse against detunings. Schematic shape of the amplitude (blue, left vertical axis) and phase (red, right vertical axis) of the pulse achieving the highest robustness against the detuning of the laser. As explained in Appendix 5.B the pulse consists of 7 pieces of durations $\tau_{\text{on}}, \tau_1, \tau_{\text{on}}, \tau_*, \tau_{\text{on}}, \tau_2$ and τ_{on} , respectively. The gray area shows the pulse minimizing $-F_c^{(2)}$, while the rest of the pulse compensates the errors in the Rydberg state.

Now we show the following: Using the pulse Ω_* as a building block we can construct a new pulse $\Omega(t)$ with $-F_r^{(2)} = 0$, while still satisfying $-F_c^{(2)} = 2.87/\Omega_{\text{max}}^2$, the same value as for Ω_* . The amplitude and phase of $\Omega(t)$ are shown schematically in Fig. 5.11. The pulse is described by 5 parameters $\tau_{\text{on}}, \tau_1, \tau_2, \varphi_1$ and φ_2 and consists of seven parts:

$$\Omega(t) = \begin{cases} \Omega_{\text{max}} e^{i\varphi_1} & \text{if } t \in [0, t_1] \\ 0 & \text{if } t \in (t_1, t_2] \\ \Omega_{\text{max}} e^{i(\varphi_1 + \pi)} & \text{if } t \in (t_2, t_3] \\ \Omega_*(t) & \text{if } t \in (t_3, t_4] \\ \Omega_{\text{max}} e^{i\varphi_2} & \text{if } t \in (t_4, t_5] \\ 0 & \text{if } t \in (t_5, t_6] \\ \Omega_{\text{max}} e^{i(\varphi_2 + \pi)} & \text{if } t \in (t_6, t_7] \end{cases} \quad (5.35)$$

with $t_1 = \tau_{\text{on}}, t_2 - t_1 = \tau_1, t_3 - t_2 = \tau_{\text{on}}, t_4 - t_3 = \tau_*, t_5 - t_4 = \tau_{\text{on}}, t_6 - t_5 = \tau_2$ and $t_7 - t_6 = \tau_{\text{on}}$. The pulse $\Omega(t)$ starts by turning on the laser for a time τ_{on} with phase φ_1 (green area in Fig. 5.11), followed by an idle time of τ_1 (orange area in Fig. 5.11) and another pulse of duration τ_{on} , but this time with opposite sign of Ω , i.e. with phase $\varphi_1 + \pi$. After these first three parts the pulse Ω_* is applied (gray area in Fig. 5.11), followed by the last three parts which have the same structure as the first three parts, but with laser phase φ_2 and idle time τ_2 . The pulse $\Omega(t)$ is designed such that for $\Delta = 0$ it implements the same gate as $\Omega_*(t)$, because the second and the sixth part of $\Omega(t)$ have no effect and the first and third part as well as the fourth and seventh part cancel each other.

In the following we consider the limit $\tau_{\text{on}} \rightarrow 0$, while keeping $\tau_{\text{on}}\tau_j$ constant (for $j = 1, 2$). We calculate how the pulse $\Omega(t)$ acts on the relevant computational basis states $|10\rangle, |01\rangle$ and $|11\rangle$, starting with $|10\rangle$. We start by calculating the zeroth order contribution of the state, $|\psi_{10}^{(0)}\rangle$. Outside of the short parts of the pulse with

duration τ_{on} it is given by

$$|\psi_{10}^{(0)}(t)\rangle = \begin{cases} |10\rangle - ie^{-i\varphi_1}\Omega_{\text{max}}\tau_{\text{on}}/2|r0\rangle & \text{if } t \in [t_1, t_2] \\ |\psi_{10,*}^{(0)}(t-t_3)\rangle & \text{if } t \in [t_3, t_4] \\ e^{i\zeta_{10}}(|10\rangle - ie^{-i\varphi_2}\Omega_{\text{max}}\tau_{\text{on}}/2|r0\rangle) & \text{if } t \in [t_5, t_6] \end{cases} \quad (5.36)$$

where $|\psi_{10,*}\rangle$ denotes the state when executing the pulse $\Omega_*(t)$. Note that because we work in the limit $\tau_{\text{on}} \rightarrow 0$ there is no population in the Rydberg state except when the pulse Ω_* is executed, so that $\langle 10|\psi_{10}^{(1)}(t_7)\rangle = \langle 10|\psi_{10,*}^{(1)}(\tau_*)\rangle$ and thus $-F_c^{(2)} = 2.87/\Omega_{\text{max}}^2$.

To calculate the error along $|r0\rangle$, $\langle r0|\psi_{10}^{(1)}(t_7)\rangle$, we note that the pulse Ω_* maps the state $|r0\rangle$ to $e^{-i\zeta_{10}}|r0\rangle$ in the $\Delta = 0$ case. This is due to the symmetry between $|10\rangle$ and $|r0\rangle$ in the Hamiltonian (5.10). This fact together with Eq. (5.36) gives

$$\begin{aligned} \langle r0|\psi_{10}^{(1)}(t_7)\rangle = & - e^{i(-\zeta_{10}-\varphi_1)}\tau_1\tau_{\text{on}}\Omega_{\text{max}}/2 \\ & + \langle r0|\psi_{10,*}^{(1)}(\tau_*)\rangle \\ & - e^{i(\zeta_{10}-\varphi_2)}\tau_2\tau_{\text{on}}\Omega_{\text{max}}/2 \end{aligned} \quad (5.37)$$

Analogously we find when starting in $|11\rangle$ that

$$\begin{aligned} \langle W_+|\psi_{11}^{(1)}(t_7)\rangle = & - \sqrt{2}e^{i(-\zeta_{11}-\varphi_1)}\tau_1\tau_{\text{on}}\Omega_{\text{max}}/2 \\ & + \langle W_+|\psi_{11,*}^{(1)}(\tau_*)\rangle \\ & - \sqrt{2}e^{i(\zeta_{11}-\varphi_2)}\tau_2\tau_{\text{on}}\Omega_{\text{max}}/2 \end{aligned} \quad (5.38)$$

The pulse $\Omega(t)$ thus satisfies $-F_r^{(2)} = 0$ if

$$\frac{1}{2} \begin{pmatrix} e^{-i\zeta_{10}} & e^{i\zeta_{10}} \\ \sqrt{2}e^{-i\zeta_{11}} & \sqrt{2}e^{i\zeta_{11}} \end{pmatrix} \begin{pmatrix} \xi_1 \\ \xi_2 \end{pmatrix} = \begin{pmatrix} \langle r0|\psi_{10,*}^{(1)}(\tau_*)\rangle \\ \langle W_+|\psi_{11,*}^{(1)}(\tau_*)\rangle \end{pmatrix} \quad (5.39)$$

with $\xi_j = e^{-i\phi_j}\tau_j\tau_{\text{on}}\Omega_{\text{max}}$. Now the ξ_j and thus the τ_j and φ_j can be found by simply solving the linear system of equations (5.39). We find the solutions $\varphi_1 = 2.21$, $\varphi_2 = -0.05$, $\tau_1 = \tau_2 = 1.01/(\tau_{\text{on}}\Omega_{\text{max}}^2)$. We numerically verified that in the limit $\tau_{\text{on}} \rightarrow 0$ the pulse $\Omega(t)$ indeed achieves $-F^{(2)} = 2.87/\Omega_{\text{max}}^2$.

5.C Modulation of the Trapping Potential

The wait method proposed in Sec. 5.4.2 requires a periodic motion of the atoms in the optical tweezer trap. While this can be in principle achieved simply by keeping the trapping potential constant in time, this approach induces differential light shifts between ground and Rydberg states, and can also lead to the anti-trapping of the Rydberg state. In the following we provide a method to achieve a periodic motion of the atoms through a trapping potential which is sinusoidally modulated in time.

The pulse halves can then be executed at times where the trap intensity vanishes and there is no differential light shift and no anti-trapping of the Rydberg state. Additionally, this method ensures that the velocity of the atoms, and thus the Doppler shift, is constant during each of the pulse halves. This is an improvement because the Doppler robust pulses are only designed to be robust against a Doppler shift which is constant during each pulse half.

We propose to modulate the potential V induced by the optical tweezers trapping the atoms sinusoidally in time with frequency ν , so that it is given by

$$V(t, x) = V_0(1 - \cos(\nu t))x^2 \quad (5.40)$$

The evolution of the atoms in the trap is thus governed by $\ddot{x} = -\frac{2V_0}{m}(1 - \cos(\nu t))x$, which is a rescaled version of the Mathieu differential equation [181]. According to Floquet's theorem, the solutions are of the form $x(t) = e^{i\omega_{\text{tr}}t}y(t) + \text{c.c.}$ where y is a $2\pi/\nu$ -periodic function and $2\omega_{\text{tr}}/\nu$ is called the Mathieu characteristic exponent. While ω_{tr} can in general be complex, it has been shown that $\omega_{\text{tr}} \in \mathbb{R}$ for sufficiently large ν [182]. For example, in the limit $\nu \rightarrow \infty$ the potential $V(t)$ can be replaced by its time average and we obtain simply $\omega_{\text{tr}} = \sqrt{2V_0/m}$.

We now apply the two pulse halves that make up the DR and ADR pulse centered at times $t_1 = 2\pi n_1/\nu$ and $t_2 = 2\pi n_2/\nu$, where n_1 and n_2 are integers. In this way $V(t_1) = V(t_2) = 0$, so the atoms move with a constant velocity and differential light shifts vanish. Now our goal is to find a modulation frequency ν such that a velocity reversal is achieved between t_1 and t_2 . Since we require $v(t_1) = -v(t_2)$ the relation $(t_2 - t_1)\omega_{\text{tr}} = \pi$ has to be satisfied, so $\nu = 2(n_2 - n_1)\omega_{\text{tr}}$. For a given value of V_0 and $(n_2 - n_1)$ we can now numerically find ν by first finding the Mathieu characteristic exponent ω_{tr} . To ensure that the duration of the time slots with almost constant velocity is as long as possible we take $n_2 - n_1 = 2$ and find $\nu = 4.079\sqrt{2V_0/m}$. In our numerical calculations of the infidelity we took V_0 such that $\omega_{\text{tr}} = \nu/4$ stays at the value of 50 kHz that we assumed before the trap modulation. The maximum potential $2V_0$ has to be roughly twice as much as the potential needed for an oscillation of the atoms at the same frequency without the trap modulation.

The potential $V(t)$ and the exemplary velocity v of an atom moving in this potential are shown in Fig. 5.12. The two pulse halves making up the Doppler robust pulse are to be applied in two adjacent time slots marked by the vertical green bars. As can be observed from the figure, the velocity is flat at these time slots, and changes sign between any two adjacent time slots. Furthermore, the differential light shift is strongly suppressed over the duration of the pulse.

5.D Comparing Switch and Wait Method of Doppler Shift Reversal

In Secs. 5.5 and 5.6 we saw that the switch and the wait methods give identical fidelities and logical error rates. In this appendix, we discuss two aspects in which

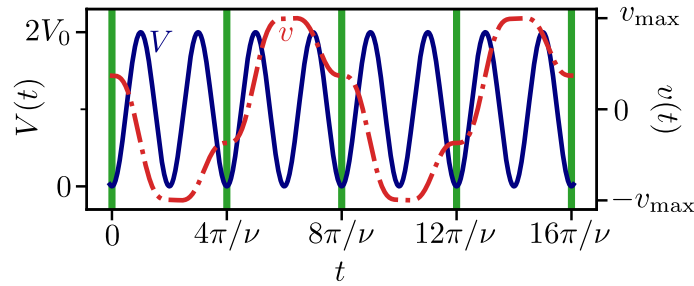


Figure 5.12: Sinusoidal modulation of trapping potential. We propose a sinusoidal modulation of the trapping potential V (blue, solid line) with frequency ν . The exemplary velocity of an atom moving in this potential is shown by the red, dash-dotted line. The two halves of the DR and ARD pulse are executed in adjacent time-slots marked by the green, vertical lines. During the time-slots the potential is zero, and the velocity is thus constant. The velocity switches sign between adjacent time-slots.

the performance of the two methods differ. We start in Sec. 5.D.1 by discussing the effects of trap inhomogeneities and anharmonicities, which only affect the wait method. In Sec. 5.D.2 by we then show that *without* the trap modulation the performance of the wait method is unaffected, while the performance of the switch method decreases significantly. We conclude with a comparison between the switch and the wait method in Sec. 5.D.3.

5.D.1 Robustness to Trap Inhomogeneities and Anharmonicity

The wait method is sensitive to several non-ideal characteristics that can arise in practice. The first is an imprecise knowledge of the trap frequency, or a difference in frequency across multiple traps. This gives a contribution to the infidelity scaling as $T\sigma_\omega^2$, where σ_ω is the standard deviation of the trap frequency ω_{tr} . We find that the induced errors are almost completely in the computational subspace, so that the contribution to the conditional infidelity is the same as to the infidelity. In order to keep a relative impact below 10% on the infidelity at $T = 50 \mu\text{K}$, we require $\sigma_\omega/\omega_{\text{tr}} < 0.06$ (0.04) for the DR (ADR) pulse. However, to maintain an erasure bias above 45 [90% of the value shown in Fig. 5.9(c)], the trap frequencies must be stabilized to $\sigma_\omega/\omega < 0.01$ (0.005). We note that achieving a 1% frequency uniformity requires only 2% intensity uniformity (assuming equal beam sizes), a number which has been experimentally demonstrated in large-scale tweezer arrays [86].

The wait method is also sensitive to the anharmonicity of the trap, which naturally arises from the Gaussian shape of the optical tweezer, and gives rise to a temperature-dependent trap frequency. As before, there is a similar contribution to the infidelity and conditional infidelity, which scales as T^3/U_0^2 , where U_0 is the tweezer depth. Considering an optical tweezer with a $1/e^2$ intensity radius $w_0 = 500$ nm, the trap frequency $\omega_{\text{tr}} = 2\pi \times 50$ kHz assumed in Secs. 5.5 and 5.6 is consistent

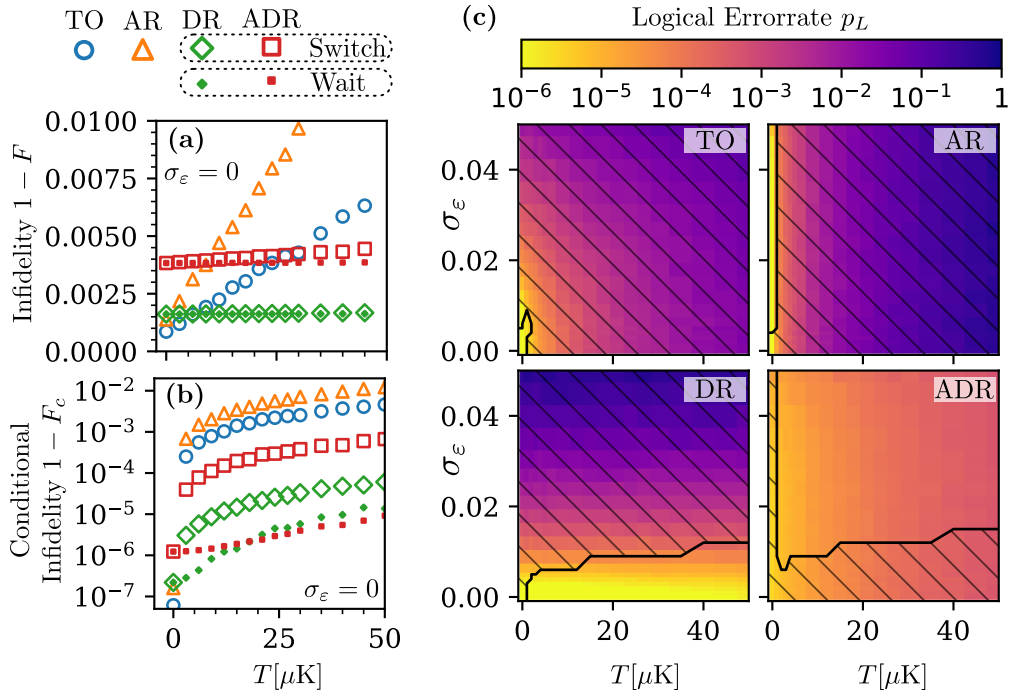


Figure 5.13: Performance of the switch and the wait method *without* the trap modulation. (a) Infidelity at $\sigma_\epsilon = 0$, (b) Conditional infidelity at $\sigma_\epsilon = 0$ (c) The logical error rate switch method. For the ADR pulse a decrease of the logical error rate by approximately one order of magnitude is observed compared to the use of the trap modulation (Fig. 5.9d)

with a tweezer depth of $U_0 = 127 \mu\text{K}$, for which the anharmonicity will affect the erasure bias in Fig. 5.9(c) significantly, reducing it to approximately $\eta_e = 27(17)$ at $T = 10 \mu\text{K}$ and $\eta_e = 3.0(1.8)$ at $T = 30 \mu\text{K}$ for the DR(ADR) pulse. However, the conditional infidelity improves as $1/U_0^2$, allowing for rapid improvement in deeper traps. For example, setting $U_0 = 2 \text{ mK}$ can recover $\eta_e \approx 40$ for the ADR pulse at temperatures up to $30 \mu\text{K}$. At fixed w_0 , this will increase the trap frequency to $\omega_{\text{tr}} = 2\pi \times 200 \text{ kHz}$, which we have verified does not significantly affect the other results presented. The effect is even smaller for lighter atoms or larger w_0 .

Note that trap inhomogeneities and anharmonicity affect the wait method regardless of the use of the trap modulation, while the switch method is unaffected by these imperfections.

5.D.2 Performance without Trap Modulation

In Fig. 5.13(a),(b) we show the infidelity and the conditional infidelity without the trap modulation. We observe that for the wait method the infidelity and conditional infidelity are essentially identical to the results including the trap modulation [see Figs. 5.8(b) and 5.8(c)]. In contrast, for the switch method without the trap modulation the ADR pulse has a slightly worse fidelity, and the conditional infidelity for

the DR and ADR pulse increases by one to two orders of magnitude. We conclude that the switch method is significantly more sensitive to changes in the velocity during each pulse than the wait method. We attribute this to the fact that for a time dependent velocity, the wait method gives a more exact reversal of the Doppler shift than the switch method. This is because in the switch method only the Doppler shift at the end of first pulse is the negative of the Doppler shift at the beginning of the second pulse, while for the wait method the Doppler shift at each point in the first half is the negative of the Doppler shift of the same point in the second half.

In Fig. 5.13(c) the logical error rate of the switch method without the trap modulation is shown. The error rate achievable at $50 \mu\text{K}$ using the ADR pulse increases by approximately one order of magnitude to 10^{-4} compared to the use of the trap modulation. Again the wait method performs identically regardless of whether the trap modulation is applied (not shown).

Note that it is still favorable to apply the trap modulation for the wait method, because it mitigates differential light shifts and the anti-trapping of the Rydberg state, which are not considered above.

5.D.3 Comparison between Switch and Wait Method

Combining the results from Secs. 5.D.1 and 5.D.2 we can summarize the advantages and disadvantages of both methods: The switch method requires a more elaborate experimental setup than the wait method, because the laser direction has to be switched. Additionally, its performance is worse than the wait method if the trap modulation is not applied. However, the switch method is more robust to trap inhomogenities and anharmonicity. On the other hand, the wait method can be implemented with just a single laser beam, and achieves the same performance regardless of whether the trap modulation is applied (neglecting errors from differential light shifts). However, it is affected by trap inhomogenities and anharmonicity, whose effect can be mitigated by increasing the trap frequency and depth.

6 Surface Code Stabilizer Measurements for Rydberg Atoms

The fragile nature of quantum information makes errors unavoidable in any quantum computation performed on a real quantum processor. To combat these errors, the framework of fault tolerant quantum computation (FTQC) has been developed. FTQC encodes a *logical qubit* into several *physical qubits* and uses the resulting redundancy to detect and correct errors. As long as the error rate per operation is below a certain *threshold*, this allows for arbitrarily low error rates of the logical qubit by encoding it in more and more physical qubits [19, 169–172]. Recently, several quantum computing platforms have surpassed the threshold for FTQC by minimizing noise at the level of single- and two-qubit gates and demonstrated FTQC in proof-of-principle experiments [13, 15, 16, 58–61]. With the advent of FTQC, the *logical error rate*, i.e. the error rate of the logical qubit, now becomes a more important metric than the physical gate fidelity. While higher gate fidelities often correspond to higher logical error rates, we have already seen in Sec. 5.6 that these two metrics can sometimes diverge significantly. It is thus a crucial problem to optimize gate protocols for the logical error rate that they achieve in an FTQC protocol.

In this chapter we consider an implementation of the surface code [21, 168, 183], a popular quantum error correction code, on a stationary array of neutral atoms, with interactions between the atoms mediated via Rydberg states. In the surface code, one logical qubit is encoded in a $d \times d$ array of atoms in a way such that errors consisting of at most $\lfloor d/2 \rfloor$ single qubit errors can always be corrected. We focus on the error source of Rydberg decay, which is dominant in many current experiments [13, 14, 105]. Interestingly, we find that for low enough decay rates γ , the time-optimal protocol for the implementation of a CZ gate (see Sec. 3.3), which essentially minimizes the gate infidelity in the presence of Rydberg decay (see Sec. 5.1) does not minimize the logical error rate. Instead we find a family of new gate protocols that can achieve a significantly lower logical error rate, despite being slower and having a higher infidelity. The reason for this discrepancy between infidelity and logical error rates are Rydberg leakage errors: At first counter-intuitive, Rydberg decay of an atom can actually lead to a population of the Rydberg state of the end of a gate, either by breaking the Rydberg blockade and allowing another atom to get excited to the Rydberg state, or by the re-excitation of the decayed atom to the Rydberg state after the decay event. These Rydberg leakage errors can now affect neighboring qubits during subsequent gates, an effect which is not captured by the infidelity. Specifically, through the propagation of Rydberg leakage errors, one decay event

can lead to correlated errors on several qubits, allowing already $\lceil d/4 \rceil$ decay events to lead to a logical error. The new gate protocols presented in this chapter prevent the propagation of Rydberg leakage errors, and restore the original $\lceil d/2 \rceil$ scaling. This result demonstrates the importance of optimizing quantum gates for logical errors in addition to gate fidelities and opens the way to the efficient realization of surface codes with neutral atoms.

This chapter is structured as follows: We start in Sec. 6.1 by giving a brief introduction to quantum error correction with surface codes. In Sec. 6.2 we then discuss how these codes can be realized on neutral atom arrays, and how we calculate the logical error rate for different gate protocols. In Sec. 6.3 we consider a model with two different atomic species, and a Rydberg blockade only between atoms of different species, and show why the time-optimal protocol can only correct for $\lceil d/4 \rceil$ decay events in this settings. Given this insight we construct a gate protocol which can correct $\lceil d/2 \rceil$ decay events, and compare it with the time-optimal protocol. Finally in Sec. 6.4 we extend this model to just a single atomic species with a Rydberg blockade between all neighboring atoms.

This chapter has been previously published in Ref. [26].

6.1 Introduction to Quantum Error Correction with Surface Codes

In this section we give a brief introduction to the surface code [21, 183]. An in-depth review of this topic can be found in Ref. [168].

The surface code is one of the most popular quantum error correction code, due to the combination of its high threshold and the possibility to implement it using only geometrically local gates. In the surface code, one logical qubit is encoded in an $d \times d$ array of physical qubits called *data qubits*, shown as solid circles in Fig. 6.1(a). The linear size d of the array is called the distance, and has to be an odd integer. The surface code is an example of a *stabilizer code* [170] and as such, it is specified by $d^2 - 1$ stabilizers $S \in \{I, X, Y, Z\}^{\otimes d^2}$, where X, Y, Z are the Pauli operators. These stabilizers must commute with each other and have to be independent, meaning that no stabilizer can be written of the product of the other stabilizers. The *code space* of a stabilizer code is then given by the joint $+1$ eigenspace of all stabilizers, i.e.

$$\mathcal{H}_c = \{|\psi\rangle \mid S|\psi\rangle = |\psi\rangle \text{ for every stabilizer } S\}. \quad (6.1)$$

It can be shown that $\dim(\mathcal{H}_c) = 2$ [1], so that we can encode one qubit in \mathcal{H}_c .

On the surface code, the stabilizers take the form $S = X_{j_1} X_{j_2} X_{j_3} X_{j_4}$ (X -stabilizers) or $S = Z_{j_1} Z_{j_2} Z_{j_3} Z_{j_4}$ (Z -stabilizers), where X_j and Z_j denote the Pauli X and Z operators on qubit j , respectively. The four qubits in each stabilizer are taken to be the corners of a plaquette of the lattice of data qubits, with X and Z -stabilizers

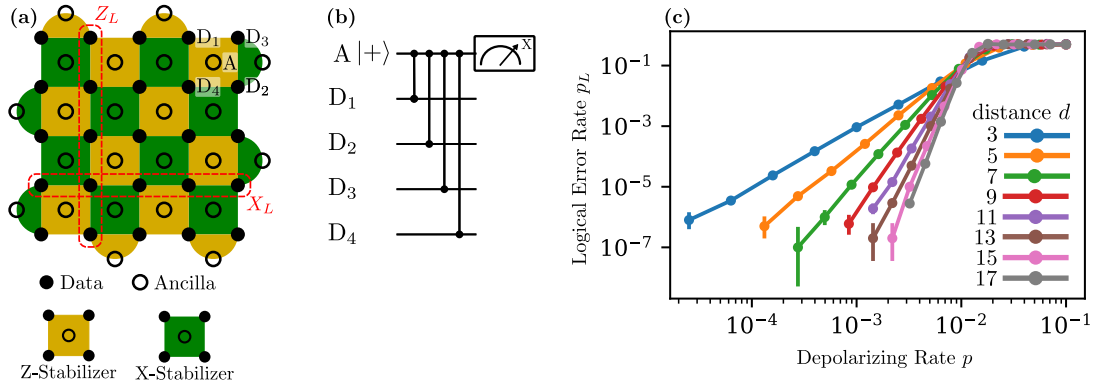


Figure 6.1: Introduction to the surface code. (a) The surface code consists of a $d \times d$ lattice of data qubits (filled black circles). The code space is defined by $d^2 - 1$ stabilizers of Z - or X -type (yellow or green squares, respectively), which tile the plaquettes of the lattice of data atoms in a checkerboard pattern. Logical Z and X operators can be applied by applying X and Z operators along a column and row of the lattice, respectively. To read out stabilizers, an ancilla qubit (open circles) is placed onto each plaquette of the lattice. (b) Circuit to read out a Z -stabilizer. (c) Logical error rate p_L as a function of the depolarizing rate p for different distanced d , assuming a two-qubit depolarizing channel after each CZ gate of the circuit in (b).

alternating in a checkerboard pattern as shown in Fig. 6.1(a). (Note that stabilizers at the boundary of the lattice only contain two qubits.) All X -stabilizers clearly commute with each other, as do all Z -stabilizers. To see that also every X -stabilizer commutes with every Z -stabilizer, note that any X and Z -stabilizer have either zero or two qubits in common. If they have zero qubits in common, they clearly commute, while if they have two qubits in common, they commute because the X and Z operators on each of these two qubits anticommute.

We can define the logical Z operator $Z_L = Z_{j_1} \dots Z_{j_d}$, where the qubits j_1, \dots, j_d are aligned along a column of the surface code [see Fig. 6.1(a)]. Note that the choice of column does not matter, since a logical operator defined along a different column can always be written as a product of Z_L and Z -stabilizers. Z_L commutes with all stabilizers, since it has either zero or two qubits in common with every X -stabilizer, and naturally commutes with all Z -stabilizers. Furthermore, Z_L is independent of all stabilizers, i.e. cannot be written as a product of them. We can now define the logical computational basis states $|0\rangle_L$ and $|1\rangle_L$ as the (up to a global phase) unique $+1$ and -1 eigenstates of Z_L in \mathcal{H}_c . Analogously, we can define the logical X operator $X_L = X_{j_1} \dots X_{j_d}$, where the qubits j_1, \dots, j_d are aligned along a row of the surface code, and the states $|+\rangle_L$ and $|-\rangle_L$ as the ± 1 eigenstates of X_L . Note that, as desired, Z_L and X_L anticommute because they have exactly one qubit in common. With the definition of \mathcal{H}_c and the operators Z_L and X_L we have now completely defined the logical qubit.

To understand how errors in the surface code can be corrected, assume that we start in a state $|\psi\rangle \in \mathcal{H}_c$, and an X -error occurs on qubit j , leaving us is $|\psi'\rangle = X_j |\psi\rangle$.

Since X_j commutes with all X -stabilizers, we clearly still have $S|\psi'\rangle = |\psi'\rangle$ for all X -stabilizers S . For the Z -stabilizers, we note that there are exactly two Z -stabilizers S that contain the qubit j and thus anticommute with X_j . These two Z -stabilizers satisfy $S|\psi'\rangle = -|\psi'\rangle$, while for all other Z -stabilizers we have $S|\psi'\rangle = |\psi'\rangle$. Thus, by measuring the stabilizers we can determine which two Z -stabilizers contain the qubit with the error, and hence determine the location of the error. Analogously, single Z -errors can be detected by the corresponding X -stabilizers, and single Y errors can be detected because they are equivalent to an X and a Z -error on the same qubit.

Now assume the error $E = P_{j_1} \dots P_{j_n}$ with $P_j \in \{X, Y, Z\}$ occurs on the qubits j_1, \dots, j_n . As long as not too many qubits are affected by this error, it is still possible to use the measured eigenvalues of the stabilizers to infer a correction operation E' such that EE' is a product of stabilizers, so that we obtain $E'E|\psi\rangle = |\psi\rangle$ and the error can be corrected. There are several algorithms, called *decoders*, for finding E' from the values of the stabilizers, such as minimum weight perfect matching [184], union find [185] or believe propagation with ordered statistics post-processing [186]. However, when too many error occur simultaneously, any decoder will fail. The minimum example of such an intractable error are $\lceil d/2 \rceil$ Z -errors on qubits aligned vertically along a column of the lattice. This error leads to exactly the same stabilizer measurement outcomes as a Z -error on all $\lfloor d/2 \rfloor$ other qubits of the column. Assuming independent errors, the latter case is more probable and will be chosen as the correction operation. However, now the original error and the correction operation together form exactly the operator Z_L and the attempt to correct the errors has actually lead to a logical error. Thus, only errors with less than $\lceil d/2 \rceil$ affected qubits can be corrected with certainty.

It remains to discuss how the stabilizers of the surface code can be measured. For this, we can insert one *ancilla qubit* for each stabilizer into the array of data qubits [shown by the open circles in Fig. 6.1(a)]. To measure a Z -stabilizer, the circuit in Fig. 6.1(b) is then executed: First the ancilla qubit is prepared in $|+\rangle = (|0\rangle + |1\rangle)/\sqrt{2}$, followed by CZ gates between the ancilla and each data qubit, and the measurement of the ancilla qubit in the X -basis. X -stabilizers can be measured analogously, with Hadamard gates inserted on all data qubits before and after the measurement. Of course the CZ gates used to measure the stabilizers introduce errors themselves, as do the the Hadamard gates and state preparation and qubit measurement. However, it is possible to correct for these errors by performing the stabilizer measurement $\mathcal{O}(d)$ times, and using a modified version of the decoders mentioned above [168].

An important metric of a surface code is its logical error rate p_L , which measures the probability of a introducing a logical error per round of stabilizer measurement. The logical error rate depends on the error model describing the physical errors. A simple error model is that every CZ gate is followed by a two-qubit depolarizing noise channel with depolarizing rate p , i.e. each two-qubit error $E \in \{I, X, Y, Z\}^{\otimes 2} \setminus \{I \otimes I\}$ is inserted with probability $p/15$. (More complicated error models are explored in the remainder of this chapter.) Fig. 6.1(c) shows the logical error rate as a function

of the depolarizing rate p , calculated using the Clifford simulator STIM [187] and a minimum weight perfect matching decoder [184]. We observe that asymptotically the logical error rate decreases polynomially with the depolarizing rate, and that the exponent of this polynomial matches $\lceil d/2 \rceil$. This is consistent with the above discussed fact that a surface code of distance d can correct all errors of weight $\lfloor d/2 \rfloor$, but that there are uncorrectable error of weight $\lceil d/2 \rceil$.

6.2 Stabilizer Measurement Schemes for Rydberg Atoms

In the following we discuss how the abstract, hardware-agnostic, surface code discussed in Sec. 6.1 can be implemented on a stationary array of Rydberg atoms. We consider a rotated surface code of distance d made of $2d^2 - 1$ stationary atoms arranged in a square lattice [Fig. 6.1(a)]. Stabilizers are given by products of Pauli X or Z operators on four data atoms on the corner of a plaquette, and read out using one ancilla qubit in the center of the plaquette. We assume that all stabilizers are measured independently, and stabilizer measurements are only performed simultaneously if they involve disjoint sets of atoms. Let us consider a single Z -stabilizer measurement (X -stabilizer measurements are performed in the same way, with Hadamard gates inserted on all data atoms before/after the measurement): Each one of the five atoms on the plaquette is modeled as a three level system, with computational basis states $|0\rangle$, $|1\rangle$ and Rydberg state $|r\rangle$ [Fig. 6.2(b)]. Their dynamics is governed by a Lindblad master equation $\dot{\rho} = -i[H, \rho] + \sum_{i,q} L_i^{(q)} \rho L_i^{(q)\dagger} - \{L_i^{(q)\dagger} L_i^{(q)}, \rho\}/2$ with Hamiltonian ($\hbar = 1$)

$$H = \sum_{ij=0}^4 B_{ij} |r_i r_j\rangle \langle r_i r_j| + \sum_{i=0}^4 \frac{\Omega_i(t)}{2} |r_i\rangle \langle 1_i| + \text{h.c.} \quad (6.2)$$

and $L_i^{(q)} = \sqrt{\gamma/2} |q_i\rangle \langle r_i|$ for $i \in \{0, \dots, 4\}$ and $q \in \{0, 1\}$. Here, B_{ij} is the interaction strength between atoms i and j prepared in the Rydberg state $|r\rangle$, $\Omega_i(t)$ is the (complex) time-dependent Rabi frequency of a laser incident on atom i coupling $|1\rangle$ and $|r\rangle$ and γ is the decay rate of the Rydberg state, which we assume to decay to $|0\rangle$ and $|1\rangle$ with a branching ratio of 1:1. We consider either $B_{ij} = 0$ or $B_{ij} = \infty$, corresponding, respectively, to the absence of interactions or a perfect *Rydberg blockade* between atoms i and j , where simultaneous occupation of Rydberg states for atoms i and j is impossible.

To measure a stabilizer, we follow the circuit shown in Fig. 6.2(a): First, the ancilla atom is prepared in $|+\rangle = (|0\rangle + |1\rangle)/\sqrt{2}$. Then, laser pulses Ω_0 and $\Omega_1(t), \dots, \Omega_4(t)$ are applied on the ancilla and the four data atoms, respectively, where we assume that for all pulses $|\Omega_j(t)| \leq \Omega_{\max}$, with Ω_{\max} the maximal achievable Rabi frequency. The pulses are chosen such that in the decay free case ($\gamma = 0$) a unitary U is implemented which, up to single qubit gates $R_Z(\theta_a) = \exp(i\theta_a |1\rangle \langle 1|)$ and $R_Z(\theta_d)$

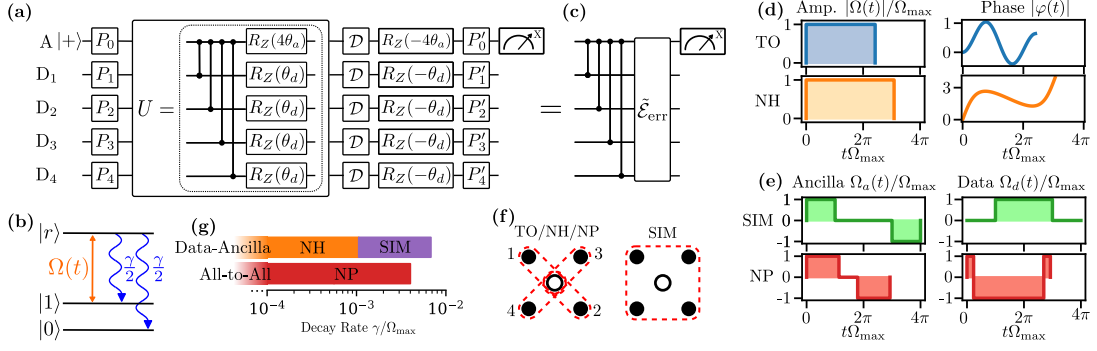


Figure 6.2: Implementing a surface code on Rydberg atoms. (a) Circuit to measure a Z -stabilizer (see main text). (b) Each atom is modeled as a three level system with states $|0\rangle, |1\rangle, |r\rangle$, a time-dependent drive $\Omega(t)$ with phase $\varphi(t)$ and amplitude $|\Omega(t)| \leq \Omega_{\max}$ coupling $|1\rangle$ and $|r\rangle$, and a decay from $|r\rangle$ to $|0\rangle$ and $|1\rangle$ with decay rate $\gamma/2$ each. (c) The realistic stabilizer measurement is equivalent to four CZ gates followed by an error channel $\tilde{\mathcal{E}}_{\text{err}}$. (d) Amplitude and phase of Ω for the symmetric time-optimal (TO), no-hopping (NH) protocols (e) Laser pulse $\Omega_a(t)$ and $\Omega_d(t)$ applied on the ancilla- and data atom, respectively, for the simultaneous (SIM) and no-phase (NP) protocols. (f) For the TO/NH/NP protocols four CZ gates are applied subsequently in the indicated order. For the SIM protocol only one global gate is applied on all 5 atoms simultaneously. (g) Summary of which protocol has the lowest logical error rate as a function of γ in the $d \rightarrow \infty$ limit.

on ancilla and data atoms, respectively, corresponds to four controlled- Z (CZ) gates, one between each data atom and the ancilla atom (however, see discussion for the SIM protocol below). For simplicity we assume that all population remaining in the Rydberg state at the end of the pulses is then removed by applying the channel $\mathcal{D}(\rho) = \Pi\rho\Pi + \langle r|\rho|r\rangle\Pi/2$ on each atom, with $\Pi = |0\rangle\langle 0| + |1\rangle\langle 1|$. This could be realized either by simply waiting long enough for the Rydberg state to decay with high probability, or by coupling the Rydberg state to a short lived intermediate state which decays to $|0\rangle$ and $|1\rangle$. Thus, our model captures the effect of Rydberg leakage errors during one stabilizer measurement, but not between different stabilizer measurements. Finally, single qubit gates $R_Z(-4\theta_a)$ and $R_Z(-\theta_d)$ are applied on the ancilla and data atoms, respectively, to compensate for the single qubit rotation induced by U , and the ancilla qubit is measured in the X -basis. The noisy stabilizer measurement can now be seen as four ideal CZ gates between the ancilla and the data qubits, followed by a 5-qubit error channel $\tilde{\mathcal{E}}_{\text{err}}$ and the measurement of the ancilla qubit [Fig. 6.2(c)]. To simulate $\tilde{\mathcal{E}}_{\text{err}}$ using a Clifford simulator we apply randomized compiling [188] and assume that random Pauli gates P and the Clifford conjugate gates P' are inserted before and after the measurement, respectively. This ensures that $\tilde{\mathcal{E}}_{\text{err}}$ is a Pauli channel, i.e. of the form

$$\tilde{\mathcal{E}}_{\text{err}}(\rho) = \sum_Q \lambda_Q Q\rho Q \quad (6.3)$$

where Q is summed over all 5-qubit Pauli strings and λ_Q is the probability of Pauli error Q . We note that omitting P and P' from the measurement circuit while

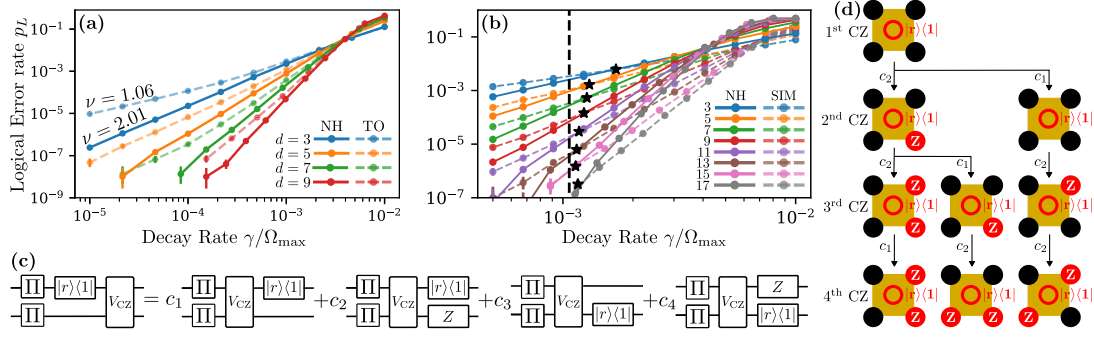


Figure 6.3: Data-ancilla blockade. (a) Logical error rate p_L as a function of the decay rate γ (in units of Ω_{\max}) for the NH (solid lines) and TO (dashed lines) protocols. (b) Logical error rate for the NH (solid lines) and SIM (dashed lines) protocol. Black stars show the crossover points between these two protocols. The gray dashed line shows the asymptotic crossing point $\gamma_{\times} = 1.1 \times 10^{-3} \Omega_{\max}$ in the limit $d \rightarrow \infty$ (see Appendix 6.D). (c) Four different ways how a $|r\rangle\langle 1|$ error can propagate through a V_{CZ} gate. Coefficients c_1, \dots, c_4 are calculated in the main text. The projectors Π restrict the state before the $|r\rangle\langle 1|$ error to the computational subspace. (d) Three possible ways how a $|r\rangle\langle 1|$ error on the ancilla qubit after the first gate (first row) can spread. The n -th row shows error after n V_{CZ} gates.

still assuming that $\tilde{\mathcal{E}}_{\text{err}}$ is of the form of Eq. 6.3 corresponds to the Pauli twirling approximation [189].

The logical error probability p_L of this scheme depends on the pulses $\Omega_0(t), \dots, \Omega_4(t)$. To compute p_L , we first compute the error probabilities λ_Q by solving the Lindblad master equation given by H and $L_i^{(q)}$ (see Appendix 6.A). We then use the stabilizer circuit simulator STIM [187] together with a minimum weight perfect matching decoder [184] to calculate the logical error rate p_L of d rounds of stabilizer measurements using the computed λ_Q .

We have now established our model for implementing a stabilizer measurement on a stationary array of Rydberg atoms, and shown how to numerically calculate the logical error rate p_L as a function of the pulses $\Omega_0(t), \dots, \Omega_4(t)$. In the next sections we will use this to compare different pulses.

6.3 The Data-Ancilla Blockade Model

In order to exemplify the role of Rydberg leakage errors in stabilizer measurements, we now discuss a so-called *data-ancilla* blockade model, where we assume that for atoms on the same plaquette there is only a Rydberg blockade between the ancilla and all data atoms, but not between two data atoms. This model can be approximately realized in dual species arrays [74, 190, 191]. In Sec. 6.4 we then discuss the *all-to-all* blockade model, where we assume a Rydberg blockade between all atoms

on a plaquette. This model can be approximately realized in single-species arrays [68, 105].

In both blockade models, the stabilizer measurement can be realized by applying four subsequent CZ gates, each with the same pulse $\Omega_a(t)$ on the ancilla atom and $\Omega_d(t)$ on the data atom. The gate infidelity under Rydberg decay is minimized if each CZ gate is implemented using the time-optimal (TO) gate (Sec. 3.3), in which the same laser pulse $\Omega(t) = \Omega_a(t) = \Omega_d(t)$ with constant amplitude Ω_{\max} and time dependent phase $\varphi(t)$ is applied *symmetrically* on both atoms [Fig. 6.2(d)]. This implements a $V_{CZ} := \text{CZ}[R_Z(\theta_a) \otimes R_Z(\theta_d)]$ gate [where $R_Z(\theta_a)$ acts on the ancilla and $R_Z(\theta_d)$ acts on the data atom, respectively], with $\theta_a = \theta_d = 2.17$ [23].

Figure 6.3(a) shows the logical error rate p_L for the TO protocol (dashed lines) for distances between $d = 3$ and $d = 9$ in the data-ancilla blockade model. In particular, for $d = 3$ we find that for small enough decay rates γ the logical error rate scales as $p_L \sim \gamma^\nu$ with $\nu \approx 1$, meaning that already a single decay event can cause a logical error. This contradicts the expectation that a $d = 3$ surface code should be able to correct a single decay event.

To understand why the TO protocol performs worse than expected, it is sufficient to consider a single decay event during the first of the four V_{CZ} gates: Due to the fraction of the laser pulse that is applied after the decay event, it is possible that the ancilla qubit is found in $|r\rangle$ at the end of the gate. Instead of a Pauli X , Y or Z -error this corresponds to a $|r\rangle\langle 1|$ error which occurs right after the first V_{CZ} gate on the ancilla qubit. (Note that no $|r\rangle\langle 0|$ error can occur, since a atom starting in $|0\rangle$ can never be excited to $|r\rangle$). This latter type of Rydberg error can be detrimental, as V_{CZ} only acts as a CZ gate on the computational subspace, but its action on states outside of the computational subspace depends on the gate protocol. In particular, a $|r\rangle\langle 1| \otimes I$ error followed by a V_{CZ} gate is equivalent to a V_{CZ} gate followed by a linear combination of $|r\rangle\langle 1| \otimes I$, $|r\rangle\langle 1| \otimes Z$, $I \otimes |r\rangle\langle 1|$ and $Z \otimes |r\rangle\langle 1|$ errors, with coefficients c_1, c_2, c_3 and c_4 , respectively [Fig 6.3(c)].

In the Appendix 6.C, the coefficients c_1 to c_4 for a symmetric protocol with $\theta_a = \theta_d =: \theta$ in which the same pulse $\Omega(t)$ is applied to both atoms are calculated as

$$c_{1/2} = (e^{-2i\theta} \mp ie^{-3i\theta} \sin \theta) / 2 \quad (6.4)$$

$$c_{3/4} = \pm (e^{-3i\theta} \cos \theta) / 2 \quad (6.5)$$

where the $-$ sign is used for c_1 and c_4 and the $+$ sign is used for c_2 and c_3 . In particular, for the TO protocol we find that all c_i are nonzero and thus all four propagation channels occur with a nonzero amplitude. Hence, a single $|r\rangle\langle 1|$ error after the first V_{CZ} gate can propagate in 3^4 different ways. Three of those error propagation paths are shown in Fig. 6.3(d), where each of the four rows shows possible errors after each of the four V_{CZ} gates. We see that a single $|1\rangle\langle r|$ error on the ancilla qubit can lead to pairs of Z -errors on the data qubits that are aligned horizontally, vertically, or diagonally. The pair of vertically aligned Z -errors is particularly detrimental, since the logical Z operator is oriented vertically [Fig. 6.1(a)] and thus only $\lceil d/4 \rceil$

of those errors suffice to make a logical Z -error. This is in contrast to independent single qubit errors, where $\lceil d/2 \rceil$ errors are necessary for a logical error. Note that, since also horizontally or diagonally aligned errors can occur, this behavior cannot be fixed by changing the order in which the V_{CZ} gates are applied to the data qubits.

Equations (6.4) and (6.5) show however a way in which the spreading of the $|1\rangle\langle r|$ error can be prevented: For $\theta = \pi/2$ we obtain $c_1 = -1, c_2 = c_3 = c_4 = 0$, so that the $|1\rangle\langle r|$ error commutes with the V_{CZ} gate, up to a global phase. Using quantum optimal control methods [132] and the methodology developed in Chapter 3 we determine the shortest possible pulse $\Omega_1(t) = \Omega_2(t)$ that implements a V_{CZ} gate with $\theta = \pi/2$ [see Fig. 6.2(d)]. Similar to the TO pulse, this pulse requires a continuous variation of the laser phase with time only, while the amplitude is kept fixed at Ω_{max} , which is expected to be experimentally advantageous [13]. When applied to the whole plaquette, this continuous pulse forms the basis of the *No-Hopping (NH)* protocol for stabilizer measurements. Note that in the NH protocol, the time spent in the Rydberg state is increased by less than 10% compared to the TO protocol. The solid lines in Fig. 6.3(a) show the logical error rate for the NH protocol: For large decay rates $\gamma \gtrsim 10^{-3}\Omega_{\text{max}}$ the NH protocol yields essentially the same logical error rates as the TO protocol since both protocols spend a similar time in the Rydberg state. However, for small decay rates $\gamma \lesssim 10^{-3}\Omega_{\text{max}}$, the NH protocol significantly reduces the logical error rate compared to the TO protocol for all distances d , demonstrating that in this regime the propagation of Rydberg leakage errors becomes the dominant error source. For $d = 3$, ν takes the expected value $\nu = 2.01 \approx 2$, showing that two decay events are necessary to produce one logical error in the NH protocol. We expect that in the currently experimentally accessible region $10^{-4}\Omega_{\text{max}} \lesssim \gamma \lesssim 10^{-3}\Omega_{\text{max}}$ [13, 14, 17, 74, 75] the logical error rate can then be improved by more than one order of magnitude. Since the exponent ν scales linearly with the distance d , even larger improvements are expected for larger distances.

The data-ancilla blockade also allows for a stabilizer measurement protocol in which the four CZ gates are not applied subsequently, but *simultaneously*, by applying a π -pulse on the ancilla qubit, followed by a 2π -pulse applied on all data qubits, and a final π -pulse on the ancilla qubit [Fig. 6.2(e)]. This is similar to $\pi - 2\pi - \pi$ protocol [64] (see Sec. 2.5.2, though here the 2π -pulse is applied to all qubits. By acting on all qubits simultaneously, this protocol (called SIM protocol from now on) reduces the time spent in the Rydberg state by $\sim 40\%$ compared to the NH protocol. Fig. 6.3(b) shows that for a decay rate $\gamma > \gamma_{\times} = 1.1 \times 10^{-3}\Omega_{\text{max}}$ the SIM protocol also reduces the logical error rate compared to the NH protocol. However, in the SIM protocol a single decay event of the ancilla qubit during the 2π pulse on the data qubits can lead to *any* 5-qubit error Q , so that again only $\lceil d/4 \rceil$ decay events are necessary for a logical error (see Appendix 6.D). We thus find that for $\gamma < \gamma_{\times}$ the NH protocol achieves the lower logical error rate [see Fig. 6.2(g)].

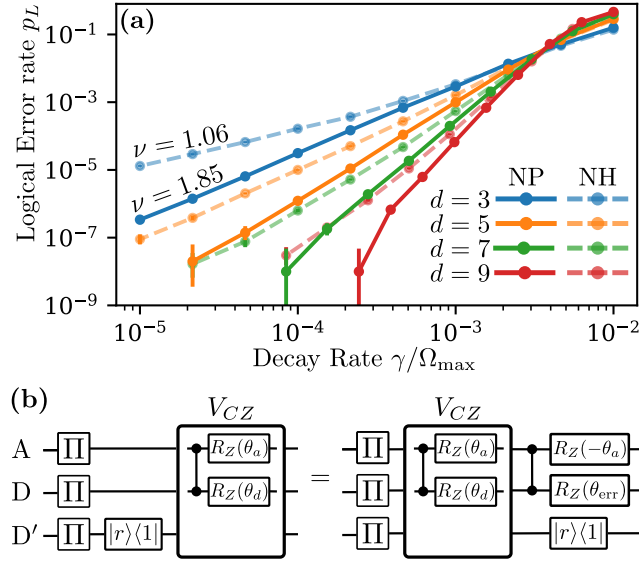


Figure 6.4: All-to-all blockade. (a) Logical error rate p_L as a function of the decay rate γ (in units of Ω_{\max}) for the NP (solid lines) and NH (dashed lines) protocols. (b) Propagation of $|r\rangle\langle 1|$ qubit on a spectator qubit by a V_{CZ} gate. $\theta_{\text{err}} = -\theta_d$ for the all-to-all blockade and $\theta_{\text{err}} = 0$ for the data-ancilla blockade (see main text).

6.4 The All-to-All Blockade Model

Now we turn our discussion to the all-to-all blockade model, in which there is also a Rydberg blockade between data qubits on the same plaquette. Fig. 6.4(a) shows the logical error rate of the NH protocol in this blockade model (dashed lines). Similar to the TO protocol under the data-ancilla blockade, we find that in a $d = 3$ surface code with the NH protocol a single decay event can already cause a logical error ($\nu = 1.06 \approx 1$). To understand this phenomenon we consider how a $|r\rangle\langle 1|$ error on a *spectator* data qubit D' , i.e. a qubit not involved in a V_{CZ} gate between the ancilla qubit A and a data qubit D , is propagated by this V_{CZ} gate [Fig. 6.4(b)]. Under the all-to-all blockade model, the $|r\rangle\langle 1|$ error on D' completely prevents the execution of the V_{CZ} gate, leading to a $V_{CZ}^\dagger = \text{CZ}[R_Z(-\theta_a) \otimes R_Z(\theta_{\text{err}})]$ error with $\theta_{\text{err}} = -\theta_d$. We note that this is different from the data-ancilla blockade, where a Rydberg excitation of D' still allows D to be excited to the Rydberg state, so that V_{CZ} acts like a single qubit $R_Z(\theta_d)$ gate on D , corresponding to $\theta_{\text{err}} = 0$.

A direct calculation (see Appendix 6.E) shows that a $|r\rangle\langle 1|$ error on the first data qubit can lead to *any* combination of Pauli Z -errors on data qubits through the propagation described in Fig. 6.4(b), thus allowing $\lceil d/4 \rceil$ decay events to cause a logical error. The only exception are the cases $\theta_{\text{err}} = 0$ and $\theta_{\text{err}} = \pi$, in which $\lceil d/2 \rceil$ decay events are required. Hence, the NH protocol can correct $\lfloor d/2 \rfloor$ errors under the data-ancilla blockade ($\theta_{\text{err}} = 0$), but only $\lfloor d/4 \rfloor$ errors under the all-to-all blockade ($\theta_{\text{err}} = \pi/2$).

With this understanding of the underlying error mechanism we now identify the

fastest possible gate protocol that is able to correct for $\lfloor d/2 \rfloor$ decay events in the all-to-all blockade model. Such a protocol requires *i)* $\theta_d \in \{0, \pi\}$ and *ii)* either $|c_1| = 1, c_2 = c_3 = c_4 = 0$ or $|c_2| = 1, c_1 = c_3 = c_4 = 0$, preventing the propagation of Rydberg leakage errors. From Eq. (6.4) and (6.5) we see that no *symmetric* protocol can simultaneously satisfy *i)* and *ii)*. Using quantum optimal control methods, we then find the shortest *asymmetric* pulses $\Omega_a(t) \neq \Omega_d(t)$ that satisfy *i)* and *ii)*. Interestingly, this protocol – which we call the *No Phase (NP)* protocol since the data qubit only accumulates an irrelevant phase $\theta_d = \pi$ – has a rather simple structure, shown in Fig. 6.2(f): On the ancilla qubit, two pulses with amplitude Ω_{\max} and duration $\tau_1 \approx 3.57/\Omega_{\max}$ are applied, where the second pulse has a phase shift of π compared to the first pulse, and there is an idle time $T - 2\tau_1$ in between them, where $T \approx 9.20/\Omega_{\max}$. On the data qubit the laser pulse is instead always applied with amplitude Ω_{\max} , but there are two phase jumps of π , switching the sign of Ω , at times τ_2 and $T - \tau_2$, with $\tau_2 = (T - 2\pi/\Omega_{\max})/4$. Fig. 6.4(a) shows that the NP protocol (solid lines) indeed achieves significantly lower logical error rates than the NH protocol, and, in the $d = 3$ case, is able to correct for one decay event ($\nu = 1.85 \approx 2$). We note that also the original π - 2π - π protocol [64] satisfies conditions *i)* and *ii)*, but has a 30% longer Rydberg time and thus a larger logical error rate than the NP protocol (see Appendix 6.F).

6.5 Conclusion

In conclusion we have established that, due to the propagation of Rydberg leakage errors, gate protocols which minimize the two-qubit gate fidelity do not necessarily achieve the lowest possible logical error rates. For the data-ancilla and all-to-all blockade model we identified the relevant error mechanisms and mitigated them by introducing two new protocols for performing stabilizer measurements with Rydberg atoms, which significantly reduce the logical error rate. Interestingly both protocols require breaking the symmetry between ancilla and data atoms, either by an asymmetric blockade model or by an asymmetric laser pulse. While in our numerical results we consider Rydberg decay as the only error source, we expect that our protocols also mitigate Rydberg leakage errors arising due to other error sources, such as Rydberg dephasing. The precise effect of other error sources, as well as the effects of the optical traps, which can exert a repulsive force on atoms in the Rydberg state, will be subject to future work. In a broader context, the results of this chapter demonstrate the necessity to optimize stabilizer measurements on the physical level to achieve the lowest possible logical error rate and points the way towards an efficient realization of surface codes with neutral atoms.

6.A Numerical Calculation of Error Probabilities

To calculate the error probabilities λ_Q in Eq. (6.3) we first numerically integrate the Lindblad master equation given by H and the $L_i^{(q)}$ with the initial condition

$\rho(0) = R$ for each 5-qubit Pauli string R , obtaining the result $\mathcal{F}(R) := \rho(T)$, where T is the duration of the laser pulses. We then calculate the error channel \mathcal{E}_{err} , without the application of the Pauli gates used for randomized compiling, as

$$\mathcal{E}_{\text{err}}(R) = U^\dagger \mathcal{D}^{\otimes 5}(\mathcal{F}(R))U. \quad (6.6)$$

\mathcal{E}_{err} can be expressed using its χ matrix as

$$\mathcal{E}_{\text{err}}(\rho) = \sum_{Q, Q'} \chi_{Q, Q'} Q \rho Q' \quad (6.7)$$

where Q and Q' are summed over all 5-qubit Pauli strings. The twirled channel is then given by [189]

$$\tilde{\mathcal{E}}_{\text{err}}(\rho) := 4^{-5} \sum_P P \mathcal{E}_{\text{err}}(P \rho P) P = \sum_Q \lambda_Q Q \rho Q \quad (6.8)$$

where $\lambda_Q = \chi_{Q, Q}$.

Now we use that

$$\begin{aligned} \text{tr}(R \mathcal{E}_{\text{err}}(R)) &= \sum_{Q, Q'} \chi_{Q, Q'} \text{tr}(R Q R Q') \\ &= \sum_Q \lambda_Q \text{tr}((R Q)^2) \\ &= 2^5 \sum_Q s(R, Q) \lambda_Q \end{aligned} \quad (6.9)$$

where the second equality follows from $\text{tr}(R Q R Q') = \pm \text{tr}(Q Q') = \pm 2^5 \delta_{Q Q'}$ and $s(R, Q) = 1$ if R and Q commute and $s(R, Q) = -1$ if R and Q anti-commute.

Inverting Eq. (6.9) gives

$$\lambda_Q = 4^{-5} \sum_R s(R, Q) \text{tr}(R \mathcal{E}_{\text{err}}(R)) \quad (6.10)$$

so λ_Q can be calculated using Eq. (6.6).

6.B Decomposition of Error Probabilities into Decay Events

In the following we calculate λ_Q to first order in γ . For this, denote by $U(t_1, t_2)$ the evolution operator under $H(t)$ (without Rydberg decay) from time $t = t_1$ to $t = t_2$. Note that $U = U(0, T)$. For an initial density matrix $\rho(0)$, the solution of the Lindblad equation is to first order in γ given by

$$\begin{aligned} \rho(T) = U \rho(0) U^\dagger + \sum_{q, i} \int_0^T dt & \left[F_i^{(q)}(t) \rho(0) F_i^{(q)}(t)^\dagger \right. \\ & \left. - \left\{ F_i^{(q)}(t)^\dagger F_i^{(q)}(t), \rho(0) \right\} / 2 \right] \end{aligned} \quad (6.11)$$

with $F_i^{(q)}(t) = U(t, T)L_i^{(q)}U(0, t)$.

Thus, the error channel \mathcal{E}_{err} (see Eq. (6.6)) is given by

$$\mathcal{E}_{\text{err}}(\rho) = \rho + \sum_{q,i,k} \int_0^T dt \left[E_{i,k}^{(q)}(t) \rho E_{i,k}^{(q)}(t)^\dagger - \left\{ E_{i,k}^{(q)}(t)^\dagger E_{i,k}^{(q)}(t), \rho \right\} / 2 \right] \quad (6.12)$$

with $E_{i,k}^{(q)} = U^\dagger D_k U(t, T) L_i^{(q)} U(0, t)$ where the D_k are the Kraus operators of $\mathcal{D}^{\otimes 5}$.

Now every $E_{i,k}^{(q)}(t)$ can be expanded as

$$E_{i,k}^{(q)}(t) = 2^{-5} \sum_Q \text{tr} \left(Q E_{i,k}^{(q)}(t) \right) Q \quad (6.13)$$

where Q is summed over all 5-qubit Pauli strings. From comparing Eq. (6.12) with Eq. (6.7) we can read off that for $Q \neq I^{\otimes 5}$

$$\lambda_Q = \chi_{Q,Q} = 4^{-5} \sum_{q,i,k} \int_0^T dt \left| \text{tr} \left(Q E_{i,k}^{(q)}(t) \right) \right|^2 \quad (6.14)$$

The interpretation of Eq. (6.14) is that in order to find the error probabilities λ_Q , at least to first order in γ , it is sufficient to consider single decay events. Each decay event is associated with a Lindblad operator $L_i^{(q)}$, specifying that qubit i decays from state $|r\rangle$ to state $|q\rangle$, with a time t at which the decay takes place, and with a Kraus operator D_k specifying how the channel $\mathcal{D}^{\otimes 5}$ acts. The index $k = (k_0, \dots, k_4)$ is summed over $\{0, 1, 2\}^5$, and the Kraus operators are given by $D_k = \bar{D}_{k_0} \otimes \dots \otimes \bar{D}_{k_4}$ with $\bar{D}_0 = |0\rangle\langle r|/\sqrt{2}$, $\bar{D}_1 = |1\rangle\langle r|/\sqrt{2}$ and $\bar{D}_2 = \Pi = |0\rangle\langle 0| + |1\rangle\langle 1|$.

In the main text and below, we show that for error strings Q with two vertically aligned Z -errors on the data qubits we obtain $\lambda_Q = \Theta(\gamma)$ (i.e. λ_Q is of order γ) by considering a single decay event and showing that $\text{tr} \left(Q E_{i,k}^{(q)}(t) \right) \neq 0$. Since all terms in Eq. (6.14) are nonnegative, this is indeed sufficient to show that $\lambda_Q = \Theta(\gamma)$.

6.C Propagation of $|r\rangle\langle 1|$ Errors under V_{CZ}

6.C.1 Symmetric Protocols

In the following we derive Eqs. (6.4) and (6.5). For this we consider a symmetric protocol, i.e. a protocol in which the same pulse $\Omega(t)$ is applied to both atoms. The action of such a pulse can be understood by considering the two two-level systems [18, 23]

$$H_1 = \frac{\Omega(t)}{2} |0r\rangle\langle 01| + \text{h.c.} \quad (6.15)$$

and

$$H_2 = \frac{\sqrt{2}\Omega(t)}{2} |W_+\rangle\langle 01| + \text{h.c.} \quad (6.16)$$

with $|W_\pm\rangle = (|1r\rangle \pm |r1\rangle)/\sqrt{2}$. V_{CZ} can be obtained by integrating the Schrödinger equation with H_1 and H_2 .

The pulse $\Omega(t)$ is chosen such that V_{CZ} acts as $V_{CZ}|01\rangle = e^{i\theta}|01\rangle$ and $V_{CZ}|11\rangle = -e^{2i\theta}|11\rangle$. Since H_1 and H_2 are traceless it follows that V_{CZ} must have determinant 1 when restricted to the $\{|01\rangle, |0r\rangle\}$ or $\{|11\rangle, |W_+\rangle\}$ subspaces. Thus it follows that $V_{CZ}|0r\rangle = e^{-i\theta}|0r\rangle$ and $V_{CZ}|W_+\rangle = -e^{-2i\theta}|W_+\rangle$. Additionally, since the same pulse is applied to both atoms but $|W_-\rangle$ is antisymmetric under the exchange of the atoms, $|W_-\rangle$ is unaffected by the pulse, i.e $V_{CZ}|W_-\rangle = |W_-\rangle$. Given the evolution of $|W_\pm\rangle$ under V_{CZ} we can now compute

$$\begin{aligned} V_{CZ}|1r\rangle &= (V_{CZ}|W_+\rangle + V_{CZ}|W_-\rangle)/\sqrt{2} \\ &= e^{-i\theta} (i \sin(\theta) |1r\rangle - \cos(\theta) |r1\rangle) \end{aligned} \quad (6.17)$$

and analogously

$$V_{CZ}|r1\rangle = e^{-i\theta} (i \sin(\theta) |r1\rangle - \cos(\theta) |1r\rangle). \quad (6.18)$$

Now we want to find an error E such that applying V_{CZ} after a $|r\rangle\langle 1|$ error is equivalent to applying first V_{CZ} and then E , at least under the condition that the before the $|r\rangle\langle 1|$ error we are in the computational subspace. Formally, we want to find E such that

$$V_{CZ}(|r\rangle\langle 1| \otimes I)\Pi^{\otimes 2} = EV_{CZ}\Pi^{\otimes 2} \quad (6.19)$$

Using that $[V_{CZ}, \Pi^{\otimes 2}] = 0$ and $(|r\rangle\langle 1| \otimes I)\Pi^{\otimes 2} = |r0\rangle\langle 10| + |r1\rangle\langle 11|$ we obtain

$$\begin{aligned} E\Pi^{\otimes 2} &= V_{CZ}|r0\rangle\langle 10|V_{CZ}^\dagger + V_{CZ}|r1\rangle\langle 11|V_{CZ}^\dagger \\ &= e^{-2i\theta}|r0\rangle\langle 10| - e^{-3i\theta}[\sin(\theta)|r1\rangle\langle 11| - \cos(\theta)|1r\rangle\langle 11|] \\ &= e^{-2i\theta}|r\rangle\langle 1| \otimes (I + Z)/2 - ie^{-3i\theta}\sin(\theta)|r\rangle\langle 1| \otimes (I - Z)/2 \\ &\quad + e^{-3i\theta}\cos(\theta)(I - Z)/2 \otimes |r\rangle\langle 1| \end{aligned} \quad (6.20)$$

For $E = c_1|r\rangle\langle 1| \otimes I + c_2|r\rangle\langle 1| \otimes Z + c_3I \otimes |r\rangle\langle 1| + c_4Z \otimes |r\rangle\langle 1|$ Eq. (6.19) is indeed satisfied with c_1, c_2, c_3 and c_4 given by Eq. (3) and (4).

6.C.2 The π - 2π - π Protocol

For completeness we show here that the π - 2π - π protocol [64] does not spread Rydberg excitation errors. On states outside of the computational subspace, the π - 2π - π protocol acts as follows (we assume the first qubit is the ancilla qubit, on which the two π pulses are applied, and the second the data qubit, on which the 2π pulse is applied);

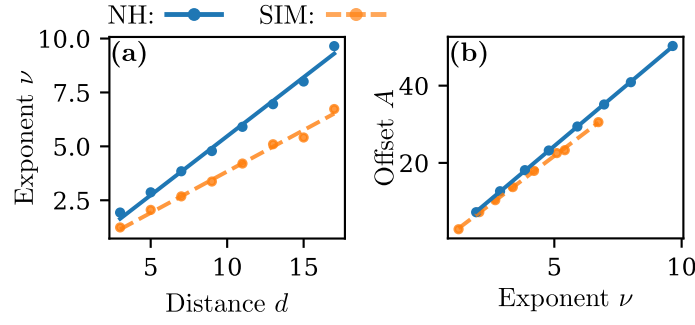


Figure 6.5: Fitting curve parameters for the SIM gate. (a) Exponent ν with which p_L increases with γ as a function of code distance d for the NH (blue, solid line) and the SIM (orange, dashed line) protocol. (b) Offset A (see text) for the NH (blue, solid line) and the SIM (orange, dashed line) protocol.

$$V_{CZ} |0r\rangle = -|0r\rangle \quad (6.21)$$

$$V_{CZ} |r0\rangle = |r0\rangle \quad (6.22)$$

$$V_{CZ} |1r\rangle = -|1r\rangle \quad (6.23)$$

$$V_{CZ} |r1\rangle = -|r1\rangle \quad (6.24)$$

Thus we obtain for a $|r\rangle \langle 1|$ error on the ancilla qubit

$$\begin{aligned} V_{CZ}(|r\rangle \langle 1| \otimes I)\Pi^{\otimes 2} &= |r0\rangle \langle 10| + |r1\rangle \langle 11| \\ &= (|r\rangle \langle 1| \otimes I)V_{CZ}\Pi^{\otimes 2} \end{aligned} \quad (6.25)$$

corresponding to $c_1 = 1$ and $c_2 = c_3 = c_4 = 0$.

6.D Error Analysis for the SIM protocol

6.D.1 Fit of the Logical Error Rates

To understand the behavior of the crossing point between the NH and the SIM protocol [see Fig. 2(b) in the main text] we fit for each distance d the logical error rate as $p_L = e^A \gamma^\nu$, with exponent ν and offset A . Fig. 6.5 shows a linear relationship $\nu = \alpha d$ between ν and d and an affine relationship $A = \log(c) - \log(\gamma_{\text{th}})\nu$ between A and ν , so that we obtain

$$p_L = c \left(\frac{\gamma}{\gamma_{\text{th}}} \right)^{\alpha d}. \quad (6.26)$$

From fitting the curves in Fig. 6.5 we obtain

$$\alpha = 0.55 \quad \gamma_{\text{th}} = 3.9 \times 10^{-3} \quad c = 0.036 \quad (6.27)$$

for the NH protocol and

$$\alpha' = 0.38 \quad \gamma'_{\text{th}} = 6.8 \times 10^{-3} \quad c' = 0.044 \quad (6.28)$$

for the SIM protocol.

The crossing point between protocols with different parameters $\gamma_{\text{th}}, c, \alpha$ and $\gamma'_{\text{th}}, c', \alpha'$ is then given by

$$\gamma_{\times} = (c/c')^{1/[(\alpha'-\alpha)d]} \left(\gamma'_{\text{th}}{}^{\alpha'} / \gamma_{\text{th}}{}^{\alpha} \right)^{1/(\alpha'-\alpha)} \quad (6.29)$$

which converges to $\gamma'_{\text{th}}{}^{\alpha'/(\alpha'-\alpha)} \gamma_{\text{th}}{}^{\alpha/(\alpha-\alpha')} = 1.1 \times 10^{-3} / \Omega_{\text{max}}$ as $d \rightarrow \infty$. This asymptotic crossing decay rate is shown by the gray dashed line in Fig.2(b) (main text).

6.D.2 Analytical Discussion

In the following we show that for the SIM protocol we have $\lambda_Q = \Theta(\gamma)$ for all 5-qubit Pauli errors $Q \neq I^{\otimes 5}$, i.e. that just one decay event can cause any Pauli error Q on all 5 qubits on the plaquette.

To show this it is sufficient to consider the decay of the ancilla qubit ($i = 0$) at $t = 2\pi/\Omega_{\text{max}}$, i.e. exactly in the middle of the 2π pulse applied on the data qubits. Below we show that for any error Q there exist q and k such that $\text{tr} \left(Q E_{0,k}^{(q)} \right) \neq 0$. Together with Eq. (6.14) this establishes $\lambda_Q = \Theta(\gamma)$.

Consider an initial state $|a, d_1, d_2, d_3, d_4\rangle$ of the ancilla and the data qubits, with $a, d_1, \dots, d_4 \in \{0, 1\}$. Until the decay event, the evolution is given by

$$U(0, t) |a, d_1, \dots, d_4\rangle = \begin{cases} (-i)^{d_1+\dots+d_4} |0, \bar{d}_1, \dots, \bar{d}_4\rangle & \text{if } a = 0 \\ -i |r, d_1, \dots, d_4\rangle & \text{if } a = 1 \end{cases} \quad (6.30)$$

where for $x \in \{0, 1\}$ we define $\bar{x} = 0$ if $x = 0$ and $\bar{x} = r$ if $x = 1$. After the decay, i.e. after applying $L_0^{(q)}$, we are in the state

$$L_0^{(q)} U(0, t) |a, d_1, \dots, d_4\rangle = -i \delta_{a,1} |q, d_1, \dots, d_4\rangle \quad (6.31)$$

where $\delta_{a,1} = 1$ if $a = 1$ and $\delta_{a,1} = 0$ if $a = 0$. At the end of the pulse we obtain $F_0^{(q)} = U(t, T) L_0^{(q)} U(0, t)$ as

$$F_0^{(q)} |a, d_1, \dots, d_4\rangle = \begin{cases} -\delta_{a,1} |r, 0, \dots, 0\rangle & \text{if } q = 1 \text{ and } d_1 = \dots = d_4 = 0 \\ -i \delta_{a,1} (-i)^{d_1+\dots+d_4} |q, \bar{d}_1, \dots, \bar{d}_4\rangle & \text{otherwise} \end{cases} \quad (6.32)$$

Now let $Q = Q_0 \otimes \dots \otimes Q_4$ be a Pauli error. We consider the Kraus operator $D_k = \bar{D}_{k_0} \otimes \dots \otimes \bar{D}_{k_4}$ of $\mathcal{D}^{\otimes 5}$ (see Appendix 6.B) and choose k as follows: We always take $k_0 = 2$, and for $j = 1, \dots, 4$ we take $k_j = 0$ if $Q_j \in \{X, Y\}$ and $k_j = 1$ if

$Q_j \in \{I, Z\}$. Furthermore, we choose $q = 0$ if $Q_0 \in \{X, Y\}$ and $q = 1$ if $Q_0 \in \{I, Z\}$. Then we obtain

$$D_k F_0^{(q)} |a, d_1, \dots, d_4\rangle = (-i)^5 \delta_{a,1} \delta_{d_1,1} \dots \delta_{d_4,1} |q, k_1, \dots, k_4\rangle \quad (6.33)$$

and thus also

$$E_{0,k}^{(q)} |a, d_1, \dots, d_4\rangle = -(-i)^5 \delta_{a,1} \delta_{d_1,1} \dots \delta_{d_4,1} |q, k_1, \dots, k_4\rangle. \quad (6.34)$$

Hence we find

$$\text{tr} \left(Q E_{0,k}^{(q)} \right) = -(-i)^5 \langle 1, \dots, 1 | Q |q, k_1, \dots, k_4\rangle \quad (6.35)$$

which is nonzero by the choice of q and k_1, \dots, k_4 .

6.E Propagation of a $|r\rangle \langle 1|$ Error on a Spectator Qubit under All-to-All Blockade

In the following we show that a $|r\rangle \langle 1|$ error on the first data qubit after the first CZ gate can cause *any* Pauli-Error $Q = Q_0 \otimes \dots \otimes Q_4$ with $Q_j \in \{I, Z\}$ on the 5 qubits of the plaquette by the error propagation shown in Fig. 3(c) (main text). The only exceptions are the cases $\theta_{\text{err}} = 0$ and $\theta_{\text{err}} = \pi$, for which only errors with $Q_2 = Q_3 = Q_4$ are possible, so that up to $\lfloor d/2 \rfloor$ decay events can be corrected.

By propagating through the three subsequent V_{CZ} gates, the $|1\rangle \langle r|$ error on the first data qubit causes an error

$$E = (|r\rangle \langle 1|)_1 \text{CZ}^{(0,2)} \text{CZ}^{(0,3)} \text{CZ}^{(0,4)} E_{sq} \quad (6.36)$$

where $(|r\rangle \langle 1|)_1$ denotes a $|r\rangle \langle 1|$ error on qubit 1, $\text{CZ}^{(i,j)}$ denotes a CZ gate between qubits i and j and

$$E_{sq} = R_Z(-3\theta_d) \otimes I \otimes R_Z(\theta_{\text{err}})^{\otimes 3}. \quad (6.37)$$

The error E can cause a Pauli error Q if there is a Kraus operator D of the channel $\mathcal{D}^{\otimes 5}$ such that $\text{tr}(DEQ) \neq 0$. We now only consider $D = \Pi \otimes |1\rangle \langle r| \otimes \Pi^{\otimes 3}$ and Pauli errors of the form $Q = Z^{z_0} \otimes \dots \otimes Z^{z_4}$. We obtain for $a, d_1, \dots, d_4 \in \{0, 1\}$ that

$$DE |a, d_1, \dots, d_4\rangle = \delta_{d_1,1} e^{i\alpha} |a, d_1, \dots, d_4\rangle \quad (6.38)$$

with

$$\alpha = \pi a(d_2 + d_3 + d_4) - 3\theta_d a + \theta_{\text{err}}(d_2 + d_3 + d_4). \quad (6.39)$$

With that, we obtain

$$\text{tr}(DEQ) = (-1)^{z_1} \sum_{a=0}^1 e^{ia(\pi z_0 - 3\theta_d)} \sum_{d_2, d_3, d_4=0}^1 e^{i\beta} \quad (6.40)$$

with

$$\beta = \sum_{j=2}^4 [\pi(z_j + a) + \theta_{\text{err}}] d_j. \quad (6.41)$$

We now obtain

$$\sum_{d_2, d_3, d_4=0}^1 e^{i\beta} = \prod_{i=2}^4 \sum_{d=0}^1 e^{i[\pi(z_j+a)+\theta_{\text{err}}]d}. \quad (6.42)$$

The sum $\sum_{d=0}^1 \exp\{i[\pi(z_j + a) + \theta_{\text{err}}]d\}$ vanishes if and only if $\pi(z_j + a) + \theta_{\text{err}} = (2k + 1)\pi$ for some integer k . Since $z_j, a \in \{0, 1\}$ this is only possible if $\theta_{\text{err}} \in \{0, \pi\}$. This establishes that for $\theta_{\text{err}} \notin \{0, \pi\}$ indeed every error $Q = Z^{z_0} \otimes Z^{z_4}$ is possible. In contrast, if $\theta_{\text{err}} \in \{0, \pi\}$ then $\sum_{d=0}^1 \exp\{i[\pi(z_j + a) + \theta_{\text{err}}]d\}$ only doesn't vanish for $z_j = a$ (for $\theta_{\text{err}} = 0$) or $z_j = a \oplus 1$ (for $\theta_{\text{err}} = \pi$), where \oplus denotes addition modulo 2. In either case, it follows that for $\text{tr}(DEQ) \neq 0$ it is required that $z_2 = z_3 = z_4$.

6.F Comparison between TO and π -2 π - π Gate under All-to-All Blockade

In the following we compare the TO and the π -2 π - π protocols, two of the most popular protocols in experimental implementations, under the all-to-all blockade. As discussed in the main text, the TO protocol is only able to correct $\lfloor d/4 \rfloor$ decay events, while the π -2 π - π can correct $\lfloor d/2 \rfloor$ decay events. However, the TO protocol has an almost 50% smaller Rydberg time than the π -2 π - π protocol.

Fig. 6.6(a) shows the logical error rate under the data-ancilla blockade for the TO and the π -2 π - π protocol for distances between $d = 3$ and $d = 13$ and $10^{-4} \leq \gamma/\Omega_{\text{max}} \leq 2 \times 10^{-3}$. For large decay rates γ the TO protocol has the lower logical error rate, due to the smaller Rydberg time. However, for small decay rates γ the π -2 π - π protocol has the lower logical error rate, due to its ability to correct $\lfloor d/2 \rfloor$ decay events. The black stars mark the points where both protocols have the same logical error rates. With increasing distance d the crossing point moves to larger decay rates γ , but converges to a finite values as $d \rightarrow \infty$.

To determine the crossing point γ_{\times} we proceed analogously to Sec 6.D.1 and fit a linear relationship $\nu = \alpha d$ between ν and d [6.6(b)] and an affine relationship $A = \log(c) - \log(\gamma_{\text{th}})\nu$ between A and ν [6.6(a)]. From the fits in Fig 6.6(b/c) we extract

$$\alpha = 0.41 \quad \gamma_{\text{th}} = 4.5 \times 10^{-3} \quad c = 0.038 \quad (6.43)$$

for the TO protocol and

$$\alpha' = 0.58 \quad \gamma'_{\text{th}} = 2.5 \times 10^{-3} \quad c' = 0.038 \quad (6.44)$$

for the π -2 π - π protocol. This gives an asymptotic crossing point $\gamma'_{\text{th}} \frac{\alpha'}{\alpha' - \alpha} \gamma_{\text{th}}^{\alpha/(\alpha - \alpha')} = 5.6 \times 10^{-3} / \Omega_{\text{max}}$ as $d \rightarrow \infty$, comparable to current experimental error rates $10^{-3} \Omega_{\text{max}} \lesssim \gamma \lesssim 10^{-4} \Omega_{\text{max}}$.

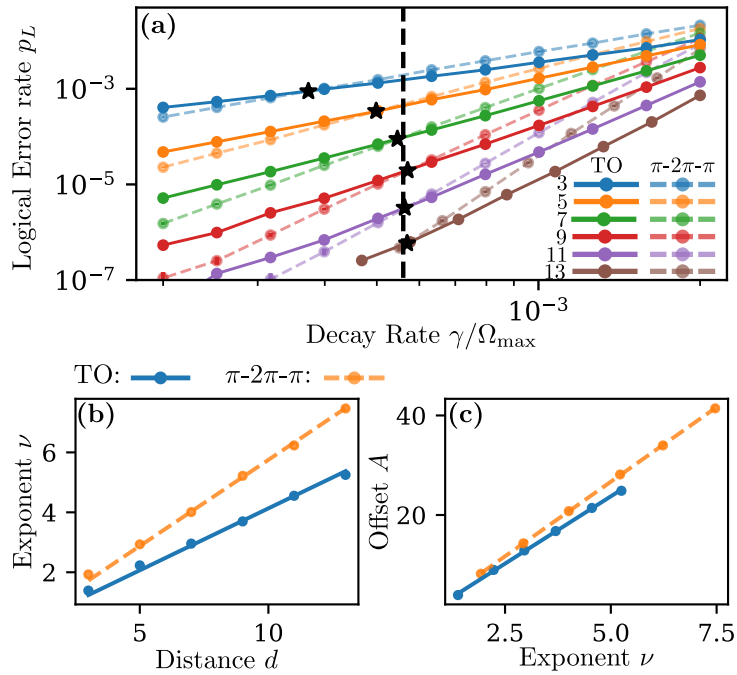


Figure 6.6: Comparison between TO and $\pi-2\pi-\pi$ protocol under the all-to-all blockade. (a) Comparison of the logical error rate p_L for the TO (solid curve) and the $\pi-2\pi-\pi$ (dashed curve) protocol. Stars mark the crossover points between the two protocols, the solid dashed line marks the value γ_{\times} for which both protocols give the same p_L in the $d \rightarrow \infty$ limit. (b) Exponent ν with which p_L increases with γ as a function of code distance d for the TO (blue, solid line) and the $\pi-2\pi-\pi$ (orange, dashed line) protocol. (c) Offset A (see text) for the TO (blue, solid line) and the $\pi-2\pi-\pi$ (orange, dashed line) protocol.

7 Non-Local Multi-Qubit Gates via a Driven Cavity

High-fidelity gates are essential for quantum computing, but looking towards scalable fault-tolerant computation, it is additionally highly desirable to have non-local quantum gates between two or more qubits. For example, the availability of an all-to-all connectivity can vastly reduce the circuit depth of typical quantum circuits, compared to a geometrically local connectivity [192]. Furthermore, the ability to perform non-local multi-qubit gates would enable the usage of quantum error correction (QEC) codes with non-local stabilizers, such as low density parity check (LDPC) codes [29, 193–196], which have a significantly lower overhead than the currently leading approach of surface codes [168]. In many physical platforms, however, neither non-local nor multi-qubit gates are natively available, but have to be costly synthesized from a sequence of local single- and two-qubit operations. For neutral atoms interacting via Rydberg states, we have seen in Chapter 3 that it is possible to realize multi-qubit gates. However, still only local gates are possible, since the interaction strength between the Rydberg states decays rapidly with their distance (see Sec. 2.5.1).

One way to realize non-local two-qubit gates is via qubit shuttling, which has been demonstrated for trapped ions [179] and neutral atoms [67, 197]. Evaluating the cost of non-local operations in this case is nontrivial, as the architecture can perform certain parallel moves simultaneously, but unequal moves must be performed serially. The shuttling time overhead for atoms in a planar lattice of linear dimension L , relevant to performing operations in certain LDPC codes, is $O(\sqrt{L})$ [78]. Alternatively, non-local gates have been previously proposed or realized with neutral atoms or ions by mediating interactions between qubits via a quantized bosonic mode, using motional modes of trapped ions [22, 46, 198, 199] or optical cavity modes for neutral atom spin qubits [77, 200–206]. For deterministic gates, prior art finds the fidelity error is $O(C^{-1/2})$ where C is the cooperativity of the cavity supporting the mode [203]. Expending additional detector resources, heralded non-local gates are achievable with error $O(C^{-1})$ but with a failure probability of $O(C^{-1/2})$ [205]. Another scheme using heralded photon transfers has an improved success probability but places stringent requirements on the level structure of the qubits so that all scattering and photon loss events are detectable [77]. In contrast, non-local entangled states can be prepared as fixed points of dissipative maps with an $O(C^{-1})$ fidelity error [207], though a fixed phase relation must be maintained between the fields addressing the qubits. While some of the proposals above can be

extended to N -qubit Toffoli gates [205, 206], for large scale digital quantum simulations and computing a unified approach that provides native implementations of larger families of multi-qubit gates would be highly desirable.

In all proposals above, entangling quantum gates are realized by a direct drive of the qubits via a free space mode, e.g. a laser, to turn the interaction between the qubits on or off. In this chapter, we explore a different approach based on simply driving the cavity mode directly with a classical field that is modulated in time, without requiring an external drive of the qubits. We find that this approach enables two new protocols for the implementation of large families of deterministic non-local multi-qubit quantum gates. Applied to just two qubits, both protocols provide, together with single qubit gates, a universal gate set for quantum computing, with two-qubit gate errors scaling as $\mathcal{O}(C^{-1/2})$, similar to the protocols driving the qubits directly. Applied to more than two qubits, however, each protocol provides a family of deterministic, multi-qubit non-local gates requiring minimal control, showing a unique combination of desirable features such as versatility in gate design, speed, and robustness.

The first protocol (A) operates in the limit of a strong drive on the cavity. It implements a family of geometric phase gates $U_A = \exp(i\theta\hat{n}^2)$, where \hat{n} is the number operator of qubits in state $|1\rangle$, by displacing the state of the cavity in a closed loop in phase space. Any angle θ can be achieved by choosing an appropriate drive of the cavity. A particularly important application of protocol A is the generation of multi-qubit GHZ states [156, 208] using the same procedure as in Sec. 3.7, a task for which viable protocols for qubits coupled via a cavity are rare and require a direct drive on the qubits [209]. One distinguishing feature of protocol A is its speed: In many previous proposals, the cavity is far detuned from the qubit frequency to avoid a large number of photons in the cavity and thus a large error through photon losses. This comes at the cost of a long gate duration of the order Δ/g^2 , where Δ is the detuning of the cavity and g is the coupling between the qubits and the cavity. In protocol A, the cavity is also far detuned, but a driving strength which is of the order of Δ and adapted to the photon loss rate allows for gate durations of order g^{-1} . An additional advantage of protocol A is its robustness: Similar to the Mølmer-Sørensen gate for trapped ions [22], U_A is independent of the initial state of the cavity mode, which is of particular importance if the cavity mode is in the microwave regime and may exhibit significant thermal population. Furthermore, protocol A is inherently robust against pulse imperfections in the drive of the cavity, since only the area enclosed and not the exact trajectory in phase space determines U_A .

The second protocol (B) operates in the limit of a weak drive and thus in the opposite limit of protocol A. It makes use of an adiabatic evolution of the joint cavity-qubit system to implement a family of phase gates $U_B = \exp[ic_1/(c_2 - \hat{n})]$, where c_1 and c_2 are parameters depending on the intensity, duration and detuning of the applied drive. The distinguishing feature of protocol B is its versatility: Since U_B depends *nonlinearly* on c_2 , the repeated application of U_B with different values of c_1 and c_2 can be used to synthesise *arbitrary* phase gates $\exp(i\varphi(\hat{n}))$. This can for example be

used to implement phase-rotation gates $\exp(i\alpha\sigma_z^{(1)} \otimes \dots \otimes \sigma_z^{(N)})$, which appear in many variational quantum algorithms for fermionic systems [210, 211]. It can also be used to implement $C_k Z$ gates, enabling generalized Toffoli gates which are frequently used as primitives in QEC to perform majority voting circuits for syndrome extraction and for measurement free QEC [212–214]. Note that synthesizing multi-controlled Z gates using only single- and two-qubit gates either requires circuits of large depths or additional ancilla qubits [215], both of which can be avoided using protocol B.

There are several main implications of the results of this chapter. While there are proposals for N -qubit Toffoli gates on qubits coupled via a cavity [205, 206], our protocols give the first native implementation for a large family of other multi-qubit gates. In particular, protocol A introduces for the first time a way to implement geometric phase gates for more than two qubits on these systems, while Protocol B even allows for the implementation of native *arbitrary* phase gates without decomposing them into single- and two-qubit gates. This significantly enhances the prospect of realizing non-local stabilizers and quantum error correction schemes such as LDPC codes with reduced qubit overheads compared to current leading schemes, in particular if our protocols are parallelized in architectures that exploit multiple modes (e.g. frequency, polarization, spatial modes for overlapping cavities) as necessary for parallel operations to support QEC. For near term applications, protocol A enhances the toolbox for the generation of large high-fidelity entangled states such as GHZ states, while the arbitrary phase gates implementable by protocol B are of significant interest for quantum simulation. All of these tasks can for the first time be accomplished without the need of an external drive of the qubits. Additionally, both protocols applied to just two qubits form, together with single qubit gates, a universal gate set for quantum computation. These protocols may in principle also be applied to other leading qubit platforms for quantum computing that exploit delocalized boson modes, such as trapped ions coupled via a motional mode.

The chapter is structured as follows: In Sec 7.1 we introduce the Hamiltonian considered in this work. In Secs. 7.2 and 7.3 we present protocols A and B, respectively, and derive their fidelities in the presence of the relevant losses. Finally, in Sec. 7.4 we estimate the achievable infidelities for our protocols for three different systems: atoms coupled via an optical cavity, Rydberg atoms coupled via a microwave cavity and polar molecules coupled via a microwave cavity.

This chapter has been previously published in Ref. [25].

7.1 Setup

The setup we have in mind is rather general and is shown in Fig. 7.1. It consists of N three-level systems with computational basis states $|0\rangle$ and $|1\rangle$ and an excited state $|e\rangle$, with transition frequencies ω_0 for the $|1\rangle \leftrightarrow |0\rangle$ and ω_e for the $|1\rangle \leftrightarrow |e\rangle$ transition. A cavity mode with annihilation (creation) operators $a(a^\dagger)$ and frequency ω_c couples the states $|1\rangle$ and $|e\rangle$ with coupling strength g . We assume that all

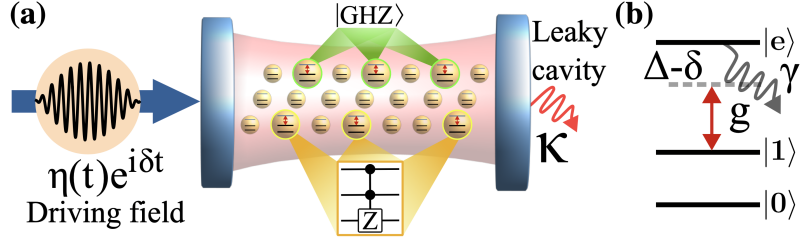


Figure 7.1: Setup. (a) A register of qubits is coupled to a common cavity with decay rate κ . By simply driving the cavity with a single classical field $\eta(t)$ detuned by δ from the resonance frequency of the cavity, a non-local entangled state like $|\text{GHZ}\rangle$ is generated, or, with a sequence of drives, non-local gates like a C_2Z gate are implemented. (b) Level scheme for each qubit consisting of the computational basis states $|0\rangle$ and $|1\rangle$ (with infinite lifetime), and an ancillary excited state $|e\rangle$ (with lifetime $1/\gamma$). The $|1\rangle \leftrightarrow |e\rangle$ transition is coupled to the cavity with coupling strength g and detuned from the cavity resonance by $\Delta - \delta$.

qubits couple with the identical coupling strength g to the cavity mode. The effects of inhomogeneities in the coupling strength are discussed in Appendices 7.A.5 and 7.B.3.

The cavity mode is driven by a (complex) classical field of strength $\eta(t)$ according to

$$H_{\text{drive}} = i(\eta(t)e^{-i\omega_L t} + \text{c.c.})(\hat{a}^\dagger - \hat{a}). \quad (7.1)$$

This classical field is detuned from the cavity and the $|1\rangle \leftrightarrow |e\rangle$ transition by $\delta = \omega_c - \omega_L$ and $\Delta = \omega_e - \omega_L$, respectively. The Hamiltonian in the rotating wave approximation and in the rotating frame defined by

$$\hat{U}_r(t) = \exp \left[it(\omega_L(\hat{a}^\dagger \hat{a} + \hat{n}_e) + \sum_j \omega_0 |0_j\rangle \langle 0_j|) \right] \quad (7.2)$$

then reads ($\hbar = 1$)

$$H(t) = \delta \hat{a}^\dagger \hat{a} + (\Delta - i\gamma/2)\hat{n}_e + [(g\hat{S}^- + i\eta(t))\hat{a}^\dagger + \text{h.c.}], \quad (7.3)$$

with $\hat{n}_e = \sum_j |e_j\rangle \langle e_j|$ the population of state $|e\rangle$ with lifetime $1/\gamma$, and $\hat{S}^+ = \sum_j |e_j\rangle \langle 1_j|$, $\hat{S}^- = (\hat{S}^+)^\dagger$ collective raising and lowering operators, respectively.

The system evolves under the Lindblad master equation $\dot{\rho} = -iH\rho + i\rho H^\dagger + L\rho L^\dagger - \{L^\dagger L, \rho\}/2$ with the jump operator $L = \sqrt{\kappa}\hat{a}$ and $1/\kappa$ the lifetime of excitations in the cavity mode. The decay of $|e\rangle$ is treated as population leakage, described by a non-hermitian term in H . Thus, expressions for the fidelity of the gate protocols derived below will be exact if none of the decay channels of $|e\rangle$ can repopulate $|0\rangle$ or $|1\rangle$, and otherwise will provide a lower bound. For both protocols, a time-dependent pulse $\eta(t)$ of duration T and with $\eta(0) = \eta(T) = 0$ is applied, while g , δ and Δ are kept constant in time.

To make our gates address only a subset of qubits in a register, we can map the $|1\rangle$ state for qubits that should be spectators to an ancillary state $|a\rangle$ that does not

couple to the bosonic mode either due to being far off resonant or by virtue of selection rules which forbid direct coupling to $|e\rangle$. Alternatively, a spatially addressable off-resonant laser beam can be used to apply an ac-Stark shift to the qubits, shifting the $|1\rangle \leftrightarrow |e\rangle$ transition far enough out of resonance with the cavity to neglect the coupling [216, 217].

7.2 Protocol A

In this section we discuss the first of our two protocols, Protocol A, which for $N = 2$ forms a universal gate set for quantum computation – together with single qubit gates –, while for arbitrary N it can be used to generate GHZ states.

Protocol A operates in the limit of a large detuning Δ between the cavity and the $|1\rangle \leftrightarrow |e\rangle$ transition and of a cavity driving strength η of the same order (i.e., $\Delta, \eta \rightarrow \infty$ and $\Delta = \mathcal{O}(\eta)$). We take δ to be of order $\mathcal{O}(g)$ and choose the pulse duration T to be of the order of $\mathcal{O}(g^{-1})$, such that it does not diverge in the limit $\Delta, \eta \rightarrow \infty$. In the following, we start by deriving an effective Hamiltonian valid in the limits given above, by first applying a time-dependent basis transformation on the cavity in Sec. 7.2.1, followed by a time-dependent basis transformation on the qubits in Sec. 7.2.2 to eliminate the state $|e\rangle$. The resulting effective Hamiltonian is similar to that of a Mølmer-Sorensen-Gate for trapped ions [22] and is then used in Sec. 7.2.3 to derive a family of geometric gates $U_A = \exp(i\theta\hat{n}^2)$. The fidelity of the gate for arbitrary N as a function of γ and κ is calculated analytically in Sec. 7.2.4. Section 7.2.5 verifies the analytical results against numerical simulations of the full Lindblad dynamics, finding excellent agreement.

7.2.1 Basis Transformation on the Cavity

To motivate the first basis transformation, acting on the cavity, we note that due to the limit $\eta \rightarrow \infty$ the cavity typically contains many ($\sim |\eta|^2/\delta^2$) photons. However, due to the simultaneous limit $\Delta \rightarrow \infty$ the number of photons only weakly depends on n , the number of qubits in state $|1\rangle$. It is thus useful to switch into a time-dependent frame of the cavity which reduces the number of photons. For this, we choose a frame which is given by the evolution that the cavity would undergo if it were not coupled to the qubits. This corresponds to the case $n = 0$, where all qubits are in state $|0\rangle$.

Such a frame is given by the simple displacement $D(\alpha) = \exp(\alpha\hat{a}^\dagger - \alpha^*\hat{a})$, where $\alpha(t)$ is the solution of

$$\dot{\alpha} = -\eta - (i\delta + \kappa/2)\alpha, \quad \alpha(t=0) = 0. \quad (7.4)$$

If $n = 0$, a cavity starting in the empty state $|0\rangle$ will be in the coherent state $|\psi_{\text{cav}}(t)\rangle = |-\alpha(t)\rangle$ at time t , so that $D(\alpha)|\psi_{\text{cav}}(t)\rangle = |0\rangle$. Note that the cavity remains in a pure state at all times, even if it undergoes decay.

Given the evolution of ρ for $n = 0$, we now treat the evolution of the joint cavity-qubit system for a general n . For this, we now proceed with the basis transformation $\tilde{\rho}(t) = D(\alpha(t))\rho(t)D(\alpha(t))^\dagger$. For general n , the evolution of $\tilde{\rho}$ is then given by (see Appendix 7.A.1)

$$\tilde{H} = \delta\hat{a}^\dagger\hat{a} + (\Delta - i\gamma/2)\hat{n}_e + g[(\hat{a}^\dagger - \alpha^*)\hat{S}^- + \text{h.c.}] \quad (7.5)$$

and $\tilde{L} = L = \sqrt{\kappa}\hat{a}$. Hence, the drive of the cavity mode is converted into an effective drive of the qubits with strength $-ig\alpha$. Because the decay in the original frame is compensated by a κ -dependent choice of α , in this new frame there are no excitations in the cavity mode and no decay events if $n = 0$ – even if in the original frame there may be many excitations and decay events.

7.2.2 Basis Transformation on the Qubits and Derivation of the Effective Hamiltonian

In order to derive an effective Hamiltonian on the computational states $|0\rangle, |1\rangle$, and the cavity, and to eliminate the state $|e\rangle$, we now use the limit $\Delta \rightarrow \infty$. For this, we consider $\tilde{H}^{(0)} = \Delta\hat{n}_e - (g\alpha^*S^- + \text{h.c.})$, which is the part of \tilde{H} which scales with Δ . (Recall that as $\Delta \rightarrow \infty$ we also consider the limit $\eta \rightarrow \infty$, and thus $|\alpha| \rightarrow \infty$). We perform a time-dependent basis transformation on the qubits so that the new basis states are the instantaneous eigenvectors of $\tilde{H}^{(0)}$. Such a basis transformation is given by (see Appendix 7.A.2)

$$\hat{U} = \exp\left[\frac{\lambda}{2}\left(-e^{i\mu}\hat{S}^+ + e^{-i\mu}\hat{S}^-\right)\right] \quad (7.6)$$

with $\cos\lambda = \Delta/\sqrt{4g^2|\alpha|^2 + \Delta^2}$ and $\mu = \arg(\alpha)$. In this new basis, the Hamiltonian is given by $\bar{H} = \hat{U}\tilde{H}\hat{U}^\dagger + i\dot{\hat{U}}\hat{U}^\dagger$. Crucially, the inertial term $i\dot{\hat{U}}\hat{U}^\dagger$ is of order $\mathcal{O}(1)$, i.e. it does not diverge as $\Delta \rightarrow \infty$. Since however the gap between the eigenspaces of $H^{(0)}$ diverges as $\Delta \rightarrow \infty$ and we consider a pulse duration T independent of Δ , the inertial term does not couple different eigenspaces of H_0 , and only changes the energy of each eigenspace. Thus we have $\bar{H} = U\tilde{H}\hat{U}^\dagger + \mathcal{O}(1)\hat{n} + \mathcal{O}(1)\hat{n}_e$. A direct calculation (see Appendix 7.A.2) now shows

$$\bar{H} = \delta\hat{a}^\dagger\hat{a} + \left(\varepsilon_1 - i\frac{\gamma_1}{2}\right)\hat{n} + \left(\varepsilon_e - i\frac{\gamma_e}{2}\right)\hat{n}_e + (\zeta\hat{a}^\dagger + \zeta^*\hat{a})(\hat{n} - \hat{n}_e) \quad (7.7)$$

where

$$\varepsilon_{e/1} = (\Delta \pm \sqrt{\Delta^2 + 4g^2|\alpha|^2})/2 + \mathcal{O}(1) \quad (7.8)$$

$$\zeta = \frac{g^2\alpha}{\sqrt{4g^2|\alpha|^2 + \Delta^2}} \quad (7.9)$$

$$\gamma_{e/1} = \frac{\gamma}{2}\left(1 \pm \sqrt{1 - 4|\zeta|^2/g^2}\right) \quad (7.10)$$

where the expressions above are evaluated with the $+$ sign for ε_e and γ_e and the $-$ sign for ε_1 and γ_1 . The $\mathcal{O}(1)$ term in $\varepsilon_{e/1}$ arises from the inertial term, and below

we will see that its exact value does not influence the gate. We note that Eqs. (7.8)–(7.10) are time-dependent. In Sec. 7.2.3 below we use the time-dependency of ζ to implement the desired quantum gate.

If we assume that none of the qubits start in state $|e\rangle$, the terms in Eq. (7.7) proportional to \hat{n}_e can be neglected. Furthermore, the $\varepsilon_1 \hat{n}$ term just corresponds to a frequency shift of the qubits, which can be compensated for either by single qubit z -rotation at the end of the gate, or by a change of reference frame. We are thus left with the effective Hamiltonian

$$H_{\text{eff}} = \delta \hat{a}^\dagger \hat{a} + \left(-i \frac{\gamma_1}{2} + \zeta \hat{a}^\dagger + \zeta^* \hat{a} \right) \hat{n}. \quad (7.11)$$

This effective Hamiltonian simply describes a driven cavity, where the driving strength $\zeta \hat{n}$ depends on the number n of qubits in state $|1\rangle$. It is thus analogous to the Hamiltonian for a Mølmer-Sørensen gate [22].

The finite lifetime γ of the state $|e\rangle$ leads to an effective error rate $\gamma_1 \hat{n}$. Note that since the basis transformation in this section only affected the space of the qubits, the Lindblad operator $L_{\text{eff}} = L = \sqrt{\kappa} \hat{a}$ is unchanged. We discuss the influence of these error sources in Sec. 7.2.4 below.

7.2.3 Implementation of a Quantum Gate

In this section we use the effective Hamiltonian (7.11) to derive a shape of $\zeta(t)$ which implements a quantum gate $U_A = \exp(i\theta \hat{n}^2)$ on the qubits only and leaves the system in a state with no entanglement between the cavity and the qubits. We first consider the loss free case $\gamma = \kappa = 0$, while the infidelity for finite values of γ and κ is calculated in the next section.

We choose ζ to be of the form

$$\zeta(t) = -\delta f(t) + i \dot{f}(t), \quad (7.12)$$

where f can be any *real* function satisfying $f(0) = f(T) = 0$, $\dot{f}(0) = \dot{f}(T) = 0$, and $\delta^2 f(t)^2 + \dot{f}(t)^2 < g^2/4$ for all t . These constraints arise because

- i)* To find a pulse $\eta(t)$ in the original Hamiltonian (7.3) which leads to the desired $\zeta(t)$ in the effective Hamiltonian (7.11), Eqs. (7.9) and (7.4) have to be inverted to first find $\alpha(t)$ and then $\eta(t)$. Equation (7.9) is only invertible if $|\zeta(t)| < g/2$, which imposes the constraint $\delta^2 f(t)^2 + \dot{f}(t)^2 < g^2/4$ on the choice of f , while Eq. (7.4) can be solved for $\eta(t)$ for any differentiable $\alpha(t)$.
- ii)* However, we require $\alpha(0) = \alpha(T) = 0$, so that the new frame introduced in Sec. 7.2.2 coincides with the lab frame at $t = 0$ and $t = T$. This is guaranteed by $f(0) = f(T) = 0$ and $\dot{f}(0) = \dot{f}(T) = 0$.

Now we show that the choice $\zeta(t) = -\delta f(t) + i\dot{f}(t)$ indeed leads to the implementation of U_A with the phase θ given by

$$\theta = \delta \int_0^T dt f(t)^2. \quad (7.13)$$

While this derivation is analogous to that of a Mølmer-Sorensen gate [22], we rederive it here in a way which allows for the easy addition of the effects of finite γ and κ in the next section.

We first assume that the qubits start in a computational basis state $|q\rangle$ ($q \in \{0, 1\}^N$) with exactly $n = \sum_{j=1}^N q_j$ qubits in state $|1\rangle$ (i.e. $\hat{n}|q\rangle = n|q\rangle$). Additionally, we assume that the cavity starts in a coherent state $|\beta(0)\rangle$. Since any initial state of the joint cavity-qubit system can be written as a superposition of states of the form $|\psi(0)\rangle = |\beta(0)\rangle \otimes |q\rangle$, those states suffice to uniquely determine the dynamics of the system under H_{eff} for any initial state.

We now make the Ansatz $|\psi(t)\rangle = e^{i\varphi_n(t)} |\beta_n(t)\rangle \otimes |q\rangle$, which indeed satisfies the Schrödinger equation for H_{eff} if

$$\dot{\beta}_n = -i\delta\beta_n - in\zeta \quad (7.14)$$

$$\dot{\varphi}_n = -n\text{Re}(\zeta^*\beta_n), \quad (7.15)$$

Making the choice $\zeta(t) = -\delta f(t) + i\dot{f}(t)$, the solution to Eq. (7.14) is given by

$$\beta_n(t) = \beta(0)e^{-i\delta t} + nf(t). \quad (7.16)$$

Plugging this into Eq. (7.15) yields

$$\begin{aligned} \varphi_n(T) &= -n\text{Re} \left[\int_0^T dt (-\delta f(t) - i\dot{f}(t)) (\beta(0)e^{-i\delta t} + nf(t)) \right] \\ &= -n\text{Re} \left[\int_0^T dt \left(-n\delta f(t)^2 + \dot{h}(t) \right) \right] \end{aligned} \quad (7.17)$$

where

$$h(t) = -i \left(\beta(0)f(t)e^{-i\delta t} + \frac{1}{2}nf(t)^2 \right). \quad (7.18)$$

Using that $h(0) = h(T) = 0$, we obtain $\varphi_n(T) = n^2\theta$.

Thus, the final state at time $t = T$ is $|\psi(T)\rangle = e^{i\theta n^2} |\beta(0)e^{-i\delta T}\rangle \otimes |q\rangle = |\beta(0)e^{-i\delta T}\rangle \otimes (U_A |q\rangle)$. Since the final state of the cavity is independent of n , there is no entanglement between the qubits and the cavity at time T . Furthermore, since U_A is *independent* of $\beta(0)$, and any arbitrary initial state of the cavity can be written as a superposition of different coherent states $|\beta(0)\rangle$, the implemented unitary is in fact independent of the initial state of the cavity.

7.2.4 Performance in the Presence of Losses

In this section we calculate the gate fidelity for the implementation of U_A in the presence of losses. In contrast to the previous section we restrict ourselves to an initial state $|0\rangle$ of the cavity. We start by solving the Lindblad equation with the effective Hamiltonian H_{eff} and the jump operator L . This allows us to find the quantum channel \mathcal{E} acting on the qubits which is obtained when the cavity is traced out after the gate. Given \mathcal{E} , we then find an expression for the infidelity. In the limit $\gamma, \kappa \rightarrow 0$ and $T \rightarrow \infty$, the infidelity is found analytically to be

$$1 - F = \left(\frac{\kappa}{4(1 + 2^{-N})\delta} + \frac{\gamma\delta}{2g^2} \right) N\theta. \quad (7.19)$$

To our knowledge this is the first analytical solution of $1 - F$ for Hamiltonians of the type of Eq. (7.11) in the presence of the relevant losses.

To solve the Lindblad equation for H_{eff} of Eq. (7.11) and L , we proceed analogously to Sec. 7.2.3 by first providing an Ansatz for the density matrix of the joint cavity-qubit system and then verifying that this Ansatz provides the correct solution of the time-dependent Lindblad equation.

To determine \mathcal{E} , it is sufficient to consider initial operator of the form $\rho(0) = |0\rangle\langle 0| \otimes |q\rangle\langle q'|$ of the joint cavity-qubit system, where $|q\rangle$ and $|q'\rangle$ ($q, q' \in \{0, 1\}^N$) are computational basis states with exactly $n = \sum_j q_j$ and $m = \sum_j q'_j$ qubits in state $|1\rangle$.

We now make the Ansatz

$$\rho(t) = \frac{e^{i\varphi_{nm}}}{\langle \beta_n | \beta_m \rangle} |\beta_n\rangle\langle \beta_m| \otimes |q\rangle\langle q'|. \quad (7.20)$$

In Appendix 7.A.3 we show that this Ansatz solves the Lindblad equation if

$$\dot{\beta}_n = -(i\delta + \kappa/2)\beta_n - in\zeta \quad (7.21)$$

$$\dot{\varphi}_{nm} = (m - n)(\zeta\beta_m + \zeta^*\beta_n) + i(m + n)\gamma_1/2. \quad (7.22)$$

The quantum operation on the Hilbert space of the qubits is given by

$$\mathcal{E}(|q\rangle\langle q'|) = \text{tr}_{\text{cav}}(\rho(T)) = e^{i\varphi_{nm}(T)} |q\rangle\langle q'|. \quad (7.23)$$

This latter expression for \mathcal{E} is used in the next subsection to determine the fidelity F .

With Eq. (7.23), the averaged gate fidelity can be computed as

$$\begin{aligned} F &= \int d\psi \langle \psi | e^{-i\theta\hat{n}^2} \mathcal{E}(|\psi\rangle\langle \psi|) e^{i\theta\hat{n}^2} |\psi\rangle \\ &= \frac{1}{2^N(2^N + 1)} \left[\sum_{n=0}^N \binom{N}{n} e^{i\varphi_{nn}} + \sum_{n,m=0}^N \binom{N}{n} \binom{N}{m} e^{i\varphi_{nm} - i(n^2 - m^2)\theta} \right] \end{aligned} \quad (7.24)$$

where the integral is taken over the whole computational subspace, and the second expression follows from [134].

Equation (7.24) now allows us to calculate the gate fidelity for arbitrary values of δ , T , γ and κ by inserting the solutions of Eqs. (7.21) and (7.22), given by

$$\beta_n(t) = -in \int_0^t dt' \zeta(t') e^{-(i\delta + \kappa/2)(t-t')} \quad (7.25)$$

and

$$\varphi_{nm}(T) = \int_0^T [(m-n)(\zeta(t)\beta_m(t)^* + \zeta(t)^*\beta_n(t)) + i(m+n)\gamma_-(t)/2] dt \quad (7.26)$$

respectively. In the limit $\gamma, \kappa \rightarrow 0$ and $T \rightarrow \infty$ this can be evaluated to Eq. (7.19) (see Appendix 7.A.4). From Eq. (7.19) we observe that δ can be used to trade between the infidelity arising from the decay of photons in the cavity (proportional to κ) and decay of the ancillary state $|e\rangle$ (proportional to γ). The infidelity is minimized for $\delta = \sqrt{\kappa/[2(1+2^{-N})\gamma]}g$, which gives

$$1 - F = \frac{N\theta}{\sqrt{2(1+2^{-N})C}} \quad (7.27)$$

where $C = g^2/(\gamma\kappa)$ denotes the cooperativity of the cavity.

7.2.5 CZ gate: Numerical Results

In the following we confirm our analysis above and find the infidelity of the U_A gate away from the limit $\Delta, \eta \rightarrow \infty$ via a numerical simulation of the full Lindblad equation for the specific case of the CZ gate ($N = 2$). The latter is implemented, up to single qubit gates, for $\theta = \pi/2$. To achieve this, we choose $f(t) = \sqrt{4\pi/(3\delta T)} \sin^2(\pi t/T)$, which satisfies the requirement $\delta \int_0^T f(t)^2 dt = \pi/2$ (see Eq. (7.13)). We numerically verify that there is a δ with $|\zeta(t)| < g/2$ for all t as long as $Tg \geq 8.3$.

For the chosen f , the infidelity $1 - F$ is shown in Fig. 7.2(a) as a function of the pulse duration T for several values of the cooperativity C and ratios γ/κ . The solid lines show the infidelity in the limit $\Delta \rightarrow \infty$ calculated analytically using Eqs. (7.24)-(7.26). The choice of δ has been optimized to achieve the best fidelity at each value of the pulse duration T . As $T \rightarrow \infty$ the infidelity approaches its asymptotic value, which is as predicted by Eq. (7.19) independent of γ/κ and only depends on the cooperativity C . For shorter pulse durations, there is a slight dependency on γ/κ , with the best infidelity always being achieved at $\gamma/\kappa \sim 1$. Note that the asymptotic value of the infidelity as $T \rightarrow \infty$ is often already closely approached for durations $T \sim 20g^{-1}$, underlining the fast speed of protocol A.

The dots in Fig. 7.2(a) show the infidelity which is achieved at a finite value of Δ , chosen such that $\max_t \eta(t) = 30g$. These values were found through a numerical

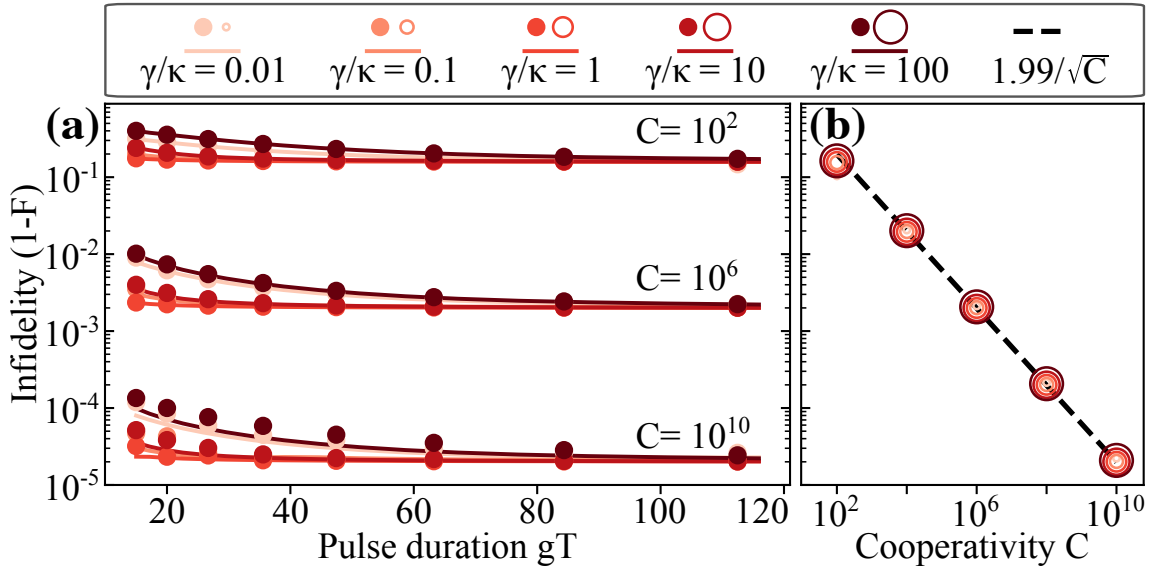


Figure 7.2: Protocol A. (a) Infidelity of a CZ gate vs pulse duration T for different values of C and γ/κ . Solid lines show the infidelity (analytic result) in the $\Delta \rightarrow \infty$ limit, circles show the infidelity (numerical calculation) at a finite value of Δ , chosen such that $\max_t |\eta(t)| = 30g$. For each T , C and γ/κ , δ is optimized to obtain the minimal $1-F$. (b) Numerical (circles) and analytical (dashed line) value of the infidelity vs C in the $\Delta, T \rightarrow \infty$ limit for different values of γ/κ .

integration of the Lindblad equation given by H [Eq. (7.3)] and the jump operator L . Only small deviations between the numerical and the analytical results can be observed, showing that a maximum driving strength of $30g$ is sufficient to implement protocol A with high fidelity.

Finally, Fig. 7.2(b) compares the asymptotic value of the infidelity from Fig. 7.2(a) with its analytical prediction $1 - F = 1.99/\sqrt{C}$ from Eq. (7.27). A good agreement is observed for all values of C and γ/κ .

This concludes our discussion of protocol A. We have demonstrated that by driving the strongly detuned cavity with a strong drive η , the unitary $U_A = \exp(i\theta\hat{n}^2)$ can be implemented through the proper choice of $\eta(t)$. We derived the infidelity of protocol A and showed that it agrees with numerical simulations. Together with global single qubit gates, protocol A can be used to generate GHZ states on N qubits using the same procedure as in Sec. 3.7.

7.3 Protocol B

In contrast to protocol A, protocol B is an adiabatic protocol that operates in the limit $\eta \rightarrow 0$, with detunings $\Delta, \delta = \mathcal{O}(g)$, and a pulse duration $T = \mathcal{O}(\eta^{-2})$. In Sec. 7.3.1 we discuss protocol B in the absence of losses, followed by the calculation of the infidelity for finite values of γ and κ in Sec. 7.3.2. We confirm our analysis

through a numerical simulation in Sec. 7.3.3. In Sec. 7.3.4 we discuss how several repetitions of protocol B can be used to implement *arbitrary* phase gates.

7.3.1 Loss Free Case

We start by assuming $\gamma = \kappa = 0$. We consider an initial state $|\psi(0)\rangle = |0\rangle \otimes |q\rangle$, with the cavity starting in state $|0\rangle$ and the qubits in a computational basis state $|q\rangle$ ($q \in \{0, 1\}^N$), with exactly $n = \sum_j q_j$ qubits in state $|1\rangle$. Note that $|\psi(0)\rangle$ is an eigenstate of the Hamiltonian H [Eq. (7.3)] for $\eta = 0$. If now η is varied slowly enough, the system will stay in an eigenstate of H and accumulate a dynamical phase. Since at the final time we have again $\eta(T) = 0$, we obtain $|\psi(T)\rangle = e^{i\varphi_n} |0\rangle \otimes |q\rangle$, where the dynamical phase is given by

$$\varphi_n = - \int_0^T \langle \psi_n(t) | H(t) | \psi_n(t) \rangle dt. \quad (7.28)$$

Using second order perturbation theory, one obtains (see Appendix 7.B.1)

$$\varphi_n = - \frac{I}{\delta - ng^2/\Delta}, \quad (7.29)$$

where $I = \int_0^T |\eta(t)|^2 dt$ is the pulse energy. Thus, the pulse implements a unitary

$$U_B = \exp \left[-i \frac{I}{(\delta - \hat{n}g^2/\Delta)} \right]. \quad (7.30)$$

7.3.2 Performance in the Presence of Losses

For $\gamma, \kappa \neq 0$ the quantum operation on the space of the qubits can be approximated by (see Appendix 7.B.2)

$$\mathcal{E}(|q\rangle \langle q'|) = c_{nm} e^{i(\varphi_n - \varphi_m)} |q\rangle \langle q'|. \quad (7.31)$$

Again, $|q\rangle$ and $|q'\rangle$ are computational basis states of the qubits with exactly $n = \sum_j q_j$ and $m = \sum_j q'_j$ qubits in state $|1\rangle$, respectively. The coefficients c_{nm} are given by

$$c_{nm} = 1 - [(\gamma_n + \gamma_m + (s_n - s_m)^2)]/2, \quad (7.32)$$

with

$$\gamma_n = \frac{\gamma ng^2}{(\Delta\delta - ng^2)^2} I = - \frac{\gamma}{\Delta} \frac{ng^2}{\Delta\delta - ng^2} \varphi_n \quad (7.33)$$

$$s_n = \frac{\sqrt{\kappa}\Delta}{\Delta\delta - ng^2} \sqrt{I} = \pm \frac{\sqrt{\kappa}\Delta}{\sqrt{|\Delta\delta - ng^2|}} \sqrt{|\varphi_n|}. \quad (7.34)$$

where in the last equality the sign is $+$ if $\Delta/(\Delta\delta - ng^2) > 0$ and $-$ otherwise.

The fidelity can be calculated analogously to Eq. (7.24) as

$$F = \frac{1}{2^N(2^N + 1)} \left[\sum_{n=0}^N \binom{N}{n} c_{nn} + \sum_{n,m=0}^N \binom{N}{n} \binom{N}{m} c_{nm} \right]. \quad (7.35)$$

To implement a CZ gate ($N = 2$), up to single qubit gates, I has to be chosen such that $|\varphi_2 - 2\varphi_1 + \varphi_0| = \pi$. Given this choice, the values of δ and Δ that maximize F can be found numerically as $\delta = 0.529\sqrt{\kappa/\gamma}g$, $\Delta = -2.09\sqrt{\gamma/\kappa}g$, which gives $1 - F = 1.79/\sqrt{C}$.

The scaling of the optimal δ and Δ with γ and κ can be explained as follows: Inserting the second expressions from Eq. (7.33) and (7.34) into Eq. (7.35) shows that for any given phases $\varphi_0, \dots, \varphi_N$, the infidelity is of the form $1 - F = \gamma h_1(\delta\Delta)/|\Delta| + \kappa h_2(\delta\Delta)|\Delta|$, where h_1 and h_2 are positive functions independent of γ and κ which only depend on δ and Δ through the product $\delta\Delta$. At a fixed value of $\delta\Delta$, the optimal choice of Δ is thus $|\Delta| = \sqrt{\gamma/\kappa} \sqrt{h_1(\delta\Delta)/h_2(\delta\Delta)}$, and the infidelity is $1 - F = \sqrt{2\gamma\kappa h_1(\delta\Delta)h_2(\delta\Delta)}$. Since h_1 and h_2 are independent of γ and κ , the optimal value of the product $\delta\Delta$ is also independent of γ and κ . Since $\Delta \propto \sqrt{\gamma/\kappa}$ it follows $\delta \propto \sqrt{\kappa/\gamma}$.

7.3.3 CZ Gate: Numerical Results

To confirm our formula for the infidelity and to determine the infidelity for finite pulse durations T , we numerically solve the Lindblad equations for different pulse durations T and different values of γ and κ . To achieve adiabaticity, $\eta(t)$ is chosen as a flat-top pulse, rising to its maximum value η_{\max} with a \sin^2 -shaped flank of duration $T_0 \leq T/2$, staying at η_{\max} for a duration $T - 2T_0$, and then falling back to 0 in a \sin^2 -shaped flank. T_0 and η_{\max} are numerically chosen to satisfy $|\varphi_2 - 2\varphi_1 + \varphi_0| = \pi$ with the minimal possible slope $\max_t |\dot{\eta}(t)|$.

Figure 7.3(a) shows the infidelity as a function of T for a CZ gate using protocol B for different values of C and γ/κ . We find that $1 - F$ approaches its asymptotic value $1.79/\sqrt{C}$ for pulse durations $10^2 g^{-1} \lesssim T \lesssim 10^3 g^{-1}$, while for smaller T it increases due to diabatic errors. The different behavior for different γ/κ ratios arises due to a nontrivial behavior of $|\varphi_2 - 2\varphi_1 + \varphi_0|$ away from the perturbative approximation made above.

7.3.4 Implementation of Arbitrary Phase Gates

In the following we show how $N - 1$ repetitions of protocol B can be used to implement an *arbitrary* symmetric phase gate $\exp(i\varphi(\hat{n}))$ for *any* function $\varphi(\hat{n})$, up to single qubit gates and a global phase.

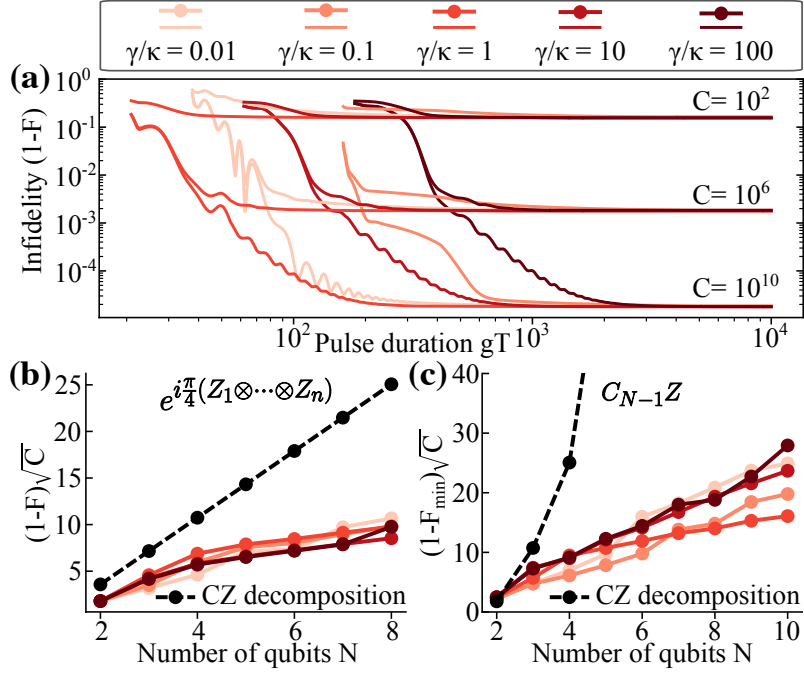


Figure 7.3: Protocol B. (a) Infiltrity (numerical calculation) for a CZ gate as a function of pulse duration T for different values of C and γ/κ . (b) Infiltrity of a phase-rotation gate with $\alpha = \pi/4$ in the $T \rightarrow \infty$ limit as a function of N . Also shown is the infiltrity of the same gate implemented using a decomposition into CZ and single-qubit gates using the circuit from Ref. [210]. (c) Infiltrity of a $C_{N-1}Z$ gate vs N when implemented using protocol B and by decomposition into CZ and single qubit gates using an ancilla-free Gray-code [215].

To see this, let us consider applying protocol B $N - 1$ times, with different detunings $\delta_1, \dots, \delta_{N-1}$ and $\Delta_1, \dots, \Delta_{N-1}$ and different pulse energies I_1, \dots, I_{N-1} in each pulse. We require that $\Delta_k - \delta_k$ is independent of k , so that the different pulses can be implemented by only changing the amplitude, duration and detuning of the external drive of the cavity, while the detuning between the cavity frequency and the $|1\rangle \leftrightarrow |e\rangle$ transition stays constant. Each of these pulses now implements a phase gate $\exp(i\varphi_k(\hat{n}))$ with $\varphi_k(\hat{n})$ given through Eq. (7.29). Taking all pulses together and adding a global phase θ_g and a single qubit phase θ_s , the implemented phase gate is

$$\varphi(\hat{n}) = \theta_g + \hat{n}\theta_s - \sum_{k=1}^{N-1} \frac{I_k}{\delta_k - \hat{n}g^2\Delta_k} \quad (7.36)$$

Observe that the $\varphi(\hat{n})$ depend *linearly* on the $N + 1$ variables θ_g, θ_s and I_1, \dots, I_{N-1} . Thus, since there are $N + 1$ possible values of n (from 0 to N), Eq. (7.36) has a unique solution of the θ_g, θ_s and I_1, \dots, I_{N-1} as a function of $\varphi(\cdot)$ and the δ_k and Δ_k . Hence there are pulse energies I_1, \dots, I_{N-1} to implement $\exp(i\varphi(\hat{n}))$ up to single qubit gates and a global phase. Note that such I_1, \dots, I_{N-1} can be found for *any* choice of the δ_k and Δ_k . In Appendix 7.B.4 we give a method based on linear programming to find the δ_k and Δ_k which minimize the gate infiltrity.

We exemplify the procedure described above for two classes of multi-qubit gates: Phase-rotation gates $\exp(-i\alpha Z_1 \otimes \dots \otimes Z_n)$ – corresponding to phases $\varphi_n = -\alpha(-1)^n$ – and N -qubit multi-controlled-Z gates ($C_{N-1}Z$ gates), i.e. phase gates with $\varphi_N = \pi$ and $\varphi_n = 0$ for $n < N$. The infidelity for both multi-qubit gates as a function of N is shown in Fig. 7.3(b,c) for different values of γ/κ . Here, we take $\delta_k - \Delta_k = 2.09g/\sqrt{\kappa/\gamma} + 0.529g\sqrt{\kappa/\gamma}$ (the optimal choice for $N = 2$), and choose the $\delta_1, \dots, \delta_{N-1}$ to maximize the fidelity (See Appendix 7.B.4). Note that for $C_{N-1}Z$ gates we consider the minimal fidelity $F_{\min} = \min_{|\psi\rangle} \langle \psi | C_{N-1}Z \mathcal{E}(|\psi\rangle \langle \psi|) C_{N-1}Z |\psi\rangle$ instead of the average gate fidelity for a fair comparison between different N . An approximately linear scaling of the infidelity with N is observed for both gates in Fig. 7.3(b,c). Our protocol outperforms implementations using decompositions into individual CZ and (perfect) single qubit gates in both cases for any $N > 2$.

This concludes our discussion of protocol B. We showed that by driving the cavity with a weak and slowly changing pulse $\eta(t)$, a multi-qubit quantum gate can be implemented by adiabatic evolution. Like for protocol A, the infidelity in the limit $T \rightarrow \infty$ only depends on the cooperativity and not on the ratio γ/κ . We also showed how $N - 1$ repetitions of protocol B with different pulse parameters can be used to implement *any* symmetric phase gate.

7.4 Fidelity Estimates in Realistic Systems

In this section we provide estimates for the achievable gate fidelity and pulse duration for protocols A and B for three different physical systems. We discuss atoms coupled to an optical cavity in Sec. 7.4.1, Rydberg atoms coupled to a microwave cavity in Sec. 7.4.2, and polar molecules coupled to a microwave cavity in Sec. 7.4.3.

7.4.1 Neutral Atoms Coupled to an Optical Cavity

As a first example, we consider neutral ^{87}Rb atoms trapped in optical tweezers and coupled to a fiber Fabry-Perot cavity as pioneered in Refs. [218–220]. As qubit states, we choose the electronic groundstates $|0\rangle = |5^2S_{1/2} F = 1 m_F = 0\rangle$ and $|1\rangle = |5^2S_{1/2} F = 2 m_F = 0\rangle$, while the ancillary state $|e\rangle$ is the electronically excited state $|e\rangle = |5^2P_{3/2} F = 3 m_F = 0\rangle$. The linewidth of the $|1\rangle \leftrightarrow |e\rangle$ transition ($\lambda = 780$ nm) is $\gamma = 2\pi \times 6$ MHz (FWHM).

For the cavity we assume a finesse $\mathcal{F} \approx 2 \times 10^5$, a waist radius $w_r \approx 2 \mu\text{m}$ and a length $L \approx 40 \mu\text{m}$ [218–220] resulting in a cooperativity of $C = 3\lambda^2\mathcal{F}/(2\pi^3w_r^2) \approx 1500$ with a coupling strength of $g = \sqrt{3\lambda^2c\gamma/(2\pi^2w_r^2L)} \approx 2\pi \times 400$ MHz and $\kappa = \pi c/L\mathcal{F} \approx 2\pi \times 20$ MHz (FWHM), so that $\gamma/\kappa \approx 0.3$. These values for the cavity parameters are within experimental reach [218].

With the numbers above, for protocol A a CZ gate on two atoms can be achieved with a fidelity of $1 - F \approx 5.1\%$ in the limit $T, \Delta \rightarrow \infty$. Finite values for Δ can be

chosen as long as $\Delta < \omega_0$, with the latter the energy separation between the states $|0\rangle$ and $|1\rangle$ (which is about 6.8 GHz for the states given above). For example, for a detuning $\Delta = 1$ GHz, the infidelity only slightly increases to $1 - F = 6.4\%$ for a choice of a finite (fast) pulse duration $T = 80$ ns. Other choices of Δ and T are possible [see Fig. 7.2(a)].

For protocol B, the infidelity in the limit $T \rightarrow \infty$ is given by $1 - F = 4.6\%$. Similar infidelities can be achieved for finite pulse durations, e.g. $1 - F = 5.0\%$ for $T = 120$ ns. These gate speeds compare favorably to those for current fast neutral atom gates [11, 64], however the fidelity is limited by the cooperativity C . We note while these infidelities are comparatively large, they are sufficient for specific tasks, e.g. for linking error corrected qubits [221].

7.4.2 Rydberg Atoms Coupled to a Microwave Cavity

Higher fidelities at the expense of longer gate durations can be achieved by taking both $|1\rangle$ and $|e\rangle$ to be Rydberg states e.g. $|1\rangle = |90\ ^2P_{3/2}\rangle$ and $|e\rangle = |90\ ^2S_{1/2}\rangle$ in Cs with lifetime 2 ms and 820 μs , respectively, while $|0\rangle$ is chosen as a long-lived state in the ground manifold of the atoms. In this case, the $|1\rangle \leftrightarrow |e\rangle$ transition has the frequency $\omega_e \approx 2\pi \times 5$ GHz, and is thus in the microwave regime.

The states $|1\rangle$ and $|e\rangle$ may be coupled via a superconducting microwave resonator with reasonable coupling strength $g \approx 2\pi \times 4$ MHz [222]. Quality factors $Q > 3 \times 10^8$ have been reported for microwave stripline resonators [223], yielding $\kappa = \omega_e/Q \approx 2\pi \times 17$ Hz, and thus a cooperativity $C = 5 \times 10^9$, with $\gamma/\kappa \simeq 12$.

We include the decay of the state $|1\rangle$ in our analysis, which is important as the latter is now a Rydberg state with a lifetime comparable to that of $|e\rangle$. Therefore, the minimal infidelity is not achieved anymore as $\Delta, T \rightarrow \infty$, but at finite values of T . For protocol A, as an example we choose $\Delta = 2\pi \times 400$ MHz, which is much smaller than the spacing of $|1\rangle$ and $|e\rangle$ to adjacent Rydberg states (approximately 5 GHz). The minimal infidelity of $1 - F = 2.3 \times 10^{-4}$ is then achieved at $T = 800$ ns. Furthermore, protocol A could be used to generate a GHZ state on 40 qubits with an infidelity below 10^{-2} , in a duration of $T = 800$ ns (the same duration as for a CZ gate).

Since protocol B is much slower than protocol A, due to its adiabatic nature, it is also affected more strongly by the decay of $|e\rangle$. However, the minimal achievable infidelity of $1 - F = 2.1 \times 10^{-3}$ at $T = 6.0 \mu\text{s}$ still significantly outperforms the infidelities from the previous section (Sec. 7.4.1).

7.4.3 Polar Molecules Coupled to a Microwave Cavity

As a final platform we consider ultracold polar molecules coupled to a microwave resonator [224–226]. Following Ref. [224], we assume Ca^{79}Br molecules [227] trapped

electrostatically in the vicinity of a superconducting microwave stripline resonator. We chose the computational basis states $|0\rangle = |N = 1, m_N = 0, F = 1, m_F = 0\rangle$, $|1\rangle = |N = 1, m_N = 0, F = 2, m_F = 1\rangle$ to be different hyperfine levels of the first excited rotational manifold of the molecule, where N is the rotational quantum number. The ancillary state $|e\rangle$ is then chosen in the second excited rotational level, $|e\rangle = |N = 2, m_N = 0, F = 2, m_F = 1\rangle$. These states are chosen to ensure that $|0\rangle, |1\rangle$ and $|e\rangle$ are simultaneously trappable [224].

For this choice of states the frequency of the $|1\rangle \leftrightarrow |e\rangle$ transition is given by $\omega_e = 2\pi \times 11$ GHz and is thus in the microwave regime. Coupling strengths up to $g = 2\pi \times 400$ kHz can be achieved with realistic experimental parameters [224]. Assuming $Q = 3 \times 10^8$ (as in Sec. 7.4.2) yields $\kappa = \omega_e/Q \approx 2\pi \times 37$ Hz, while the decay from $|e\rangle$ is $\gamma \lesssim 10^{-2}$ Hz [228] and can be neglected. If we assume $\gamma = 0$, arbitrarily low fidelities can be reached if we allow for arbitrarily long gate times. At finite pulse duration, protocol A can achieve an infidelity of $1 - F = 1.0 \times 10^{-5}$ already at a pulse duration of $T = 80 \mu\text{s}$, at $\Delta = 2\pi \times 1.2$ MHz $\gg g$. Again, other choices of T and Δ are possible, see Fig. 7.2(a).

At the same pulse duration, the infidelity of protocol B is given by $1 - F = 8.7 \times 10^{-5}$. This is almost one order of magnitude worse than protocol A, but nevertheless still sufficient for most quantum information processing tasks.

7.5 Conclusion

We have presented two new protocols for implementing a large family of non-local multi-qubit quantum gates on qubits coupled to a common cavity mode. These protocols are implemented by applying a classical drive to the cavity mode, while no external drive on the qubits is required. Applied to just two qubits, both protocols form, together with single qubit gates, a universal gate set for quantum computing. Applied on more than two qubits, protocol A can be used to generate a GHZ state, while protocol B can be used to implement arbitrary phase gates, such as phase-rotation or multi-controlled Z gates. We evaluated the fidelity of both protocols in the presence of a finite lifetime of the ancillary state $|e\rangle$ of the qubits and of the photons in the cavity, finding that the infidelity scales as $\mathcal{O}(C^{-1/2})$. For Rydberg atoms or polar molecules coupled via a microwave cavity, we expect that our protocols can achieve infidelities below 10^{-3} with realistic parameters, while for neutral atoms coupled via optical cavities infidelities of the order of a few percent can be reached.

Our protocols allow for the first time the realization of a large family of deterministic non-local multi-qubit quantum gates with applications in digital quantum simulations, metrology, cryptography and error correction, by controlling the system via only a simple classical drive of the cavity. In a quantum computing architecture, our protocol could be applied in several manners, either as the only entangling gate

of the architecture, or in conjunction with other, local, entangling protocols. For example, in an array of Rydberg atoms, entangling operations between nearby atoms could be performed using the Rydberg blockade mechanism, while entangling atoms further apart could be done with our protocols. It is also possible to use our protocols only for certain error correction tasks, while other entangling operations are done by local gates. Finally, our protocols could also be extended to overlapping cavities [77] to connect even more atoms.

In this chapter we modeled each qubit as a three level system and the cavity as a single bosonic mode. We expect that our protocols are generalizable to more complicated models with e.g. several excited states, a nonzero coupling from $|0\rangle$ to $|e\rangle$, or several bosonic modes (e.g. light modes of different polarizations) supported in the cavity. For example, the derivations of both protocols can be extended in a straightforward manner to include the coupling of $|1\rangle$ to a second excited state $|e'\rangle$. Such an additional coupling would only effect the parameter θ in protocol A and the dependency of $\varphi(\hat{n})$ on \hat{n} in protocol B. Finding the optimal gate parameters and the achievable fidelities for more general models of the qubit and the cavity will be subject to future work.

We expect that our protocols may significantly benefit from optimization of the time-dependent pulse-shape $\eta(t)$. In particular, while the infidelity for the various gates in the limit $T \rightarrow \infty$ is independent of the exact choice of η , we expect that the infidelity at finite T could be improved by applying quantum optimal control techniques to optimize the pulse-shape of $\eta(t)$ [135, 136], making our protocols both higher-fidelity and faster.

7.A Supporting Calculations for Protocol A

7.A.1 First Basis Transformation on the Cavity

Here we discuss the first time-dependent basis transformation on the subsystem of the cavity and derive Eq. (7.5). For a function $\alpha(t)$ consider the displacement operator $D(\alpha(t)) = \exp(\alpha(t)\hat{a}^\dagger - \alpha^*(t)\hat{a})$. Recall that it satisfies $D(\alpha)\hat{a}D(\alpha)^\dagger = \hat{a} - \alpha$ and $D(\alpha)\hat{a}^\dagger D(\alpha)^\dagger = \hat{a}^\dagger - \alpha^*$, and furthermore

$$\begin{aligned} \frac{d}{dt}D(\alpha) &= [\dot{\alpha}\hat{a}^\dagger - \dot{\alpha}^*\hat{a} + i\text{Im}(\dot{\alpha}^*\alpha)]D(\alpha) \\ &= D(\alpha)[\dot{\alpha}\hat{a}^\dagger - \dot{\alpha}^*\hat{a} - i\text{Im}(\dot{\alpha}^*\alpha)]. \end{aligned} \quad (7.37)$$

Now we define $\tilde{\rho} = D(\alpha)\rho D(\alpha)^\dagger$. It satisfies

$$\begin{aligned} \dot{\tilde{\rho}} &= -i(H'\tilde{\rho} - \tilde{\rho}(H')^\dagger) + L'\tilde{\rho}(L')^\dagger - \frac{1}{2}\{(L')^\dagger L', \tilde{\rho}\} \\ &\quad + \left(\frac{d}{dt}D(\alpha)\right) D(\alpha)^\dagger \tilde{\rho} + \tilde{\rho} D(\alpha) \left(\frac{d}{dt}D(\alpha)^\dagger\right) \end{aligned} \quad (7.38)$$

where $H' = D(\alpha)HD(\alpha)^\dagger$ and $L' = D(\alpha)LD(\alpha)^\dagger$.

We calculate

$$H' = \delta\hat{a}^\dagger\hat{a} + (\Delta - i\gamma/2)\hat{n}_e + g(\hat{a}^\dagger\hat{S}^- + \hat{a}\hat{S}^+) + (i\eta - \delta\alpha)\hat{a}^\dagger - (i\eta^* + \delta\alpha^*)\hat{a} - g\alpha^*\hat{S}^- - g\alpha\hat{S}^+ + \delta|\alpha|^2 + i(\eta\alpha^* - \eta^*\alpha) \quad (7.39)$$

and

$$L'\tilde{\rho}(L')^\dagger - \frac{1}{2}\{(L')^\dagger L, \tilde{\rho}\} = L\tilde{\rho}L^\dagger - \frac{1}{2}\{L^\dagger L, \tilde{\rho}\} + \frac{\kappa}{2}(-\alpha^*\hat{a}\rho - \alpha\rho\hat{a}^\dagger + \alpha^*\rho\hat{a} + \alpha\hat{a}^\dagger\rho) \quad (7.40)$$

as well as

$$\left(\frac{d}{dt}D(\alpha)\right)D(\alpha)^\dagger\tilde{\rho} + \tilde{\rho}D(\alpha)\left(\frac{d}{dt}D(\alpha)^\dagger\right) = [\dot{\alpha}\hat{a}^\dagger - \dot{\alpha}^*\hat{a}, \tilde{\rho}] \quad (7.41)$$

Plugging Eqs. (7.39)–(7.41) into Eq. (7.38) gives

$$\dot{\tilde{\rho}} = -i\tilde{H}\tilde{\rho} + i\tilde{\rho}\tilde{H}^\dagger + L\rho L^\dagger - \frac{1}{2}\{L^\dagger L, \rho\} \quad (7.42)$$

with

$$\begin{aligned} \tilde{H} = & \delta\hat{a}^\dagger\hat{a} + (\Delta - i\gamma/2)\hat{n}_e + g(\hat{a}^\dagger\hat{S}^- + \hat{a}\hat{S}^+) \\ & - g\alpha^*\hat{S}^- - g\alpha\hat{S}^+ + [(i\eta - (\delta - i\kappa/2)\alpha + i\dot{\alpha})\hat{a}^\dagger + \text{h.c.}] \end{aligned} \quad (7.43)$$

Now we take $\alpha(t)$ such that

$$\dot{\alpha} = -\eta - (i\delta + \kappa/2)\alpha \quad (7.44)$$

which is satisfied by

$$\alpha(t) = \int_0^t dt' \eta(t') e^{-(i\delta + \kappa/2)(t-t')}. \quad (7.45)$$

With this choice, \tilde{H} becomes simply

$$\tilde{H} = \delta\hat{a}^\dagger\hat{a} + (\Delta - i\gamma/2)\hat{n}_e + g(\hat{a}^\dagger\hat{S}^- + \hat{a}\hat{S}^+) - g\alpha^*\hat{S}^- - g\alpha\hat{S}^+ \quad (7.46)$$

thus completing our derivation of Eq. (7.5)

7.A.2 Second Basis Transformation on the Qubits

In this appendix we perform the time dependent basis transformation $\tilde{H} = U\tilde{H}U^\dagger + i\dot{U}U^\dagger$ for

$$U = \exp\left[\frac{\lambda}{2}\left(-e^{i\mu}\hat{S}^+ + e^{-i\mu}\hat{S}^-\right)\right] \quad (7.47)$$

and

$$\tilde{H} = \delta \hat{a}^\dagger \hat{a} + (\Delta - i\gamma/2) \hat{n}_e + g \hat{a}^\dagger \hat{S}^- + g \hat{a} \hat{S}^+ - g \alpha \hat{S}^+ - g \alpha^* \hat{S}^-. \quad (7.48)$$

We calculate

$$U = \left[|0\rangle \langle 0| + \cos\left(\frac{\lambda}{2}\right) (|1\rangle \langle 1| + |e\rangle \langle e|) + \sin\left(\frac{\lambda}{2}\right) (-e^{i\mu} |e\rangle \langle 1| + e^{-i\mu} |1\rangle \langle e|) \right]^{\otimes N} \quad (7.49)$$

which gives

$$\begin{aligned} U \hat{S}^+ U^\dagger &= (U \hat{S}^- U^\dagger)^\dagger = \cos^2\left(\frac{\lambda}{2}\right) \hat{S}^+ - e^{-2i\mu} \sin^2\left(\frac{\lambda}{2}\right) \hat{S}^- \\ &\quad + e^{-i\mu} \sin\left(\frac{\lambda}{2}\right) \cos\left(\frac{\lambda}{2}\right) (\hat{n} - \hat{n}_e) \end{aligned} \quad (7.50)$$

and

$$\begin{aligned} U \hat{n}_e U^\dagger &= \cos^2\left(\frac{\lambda}{2}\right) \hat{n}_e + \sin^2\left(\frac{\lambda}{2}\right) \hat{n} \\ &\quad + \sin\left(\frac{\lambda}{2}\right) \cos\left(\frac{\lambda}{2}\right) (e^{-i\mu} \hat{S}^- + e^{i\mu} \hat{S}^+), \end{aligned} \quad (7.51)$$

Now first consider $H^{(0)} = \Delta \hat{n}_e - g \alpha \hat{S}^+ - g \alpha^* \hat{S}^-$, the part of \tilde{H} that scales with Δ . We choose λ and μ so that $U H^{(0)} U^\dagger$ is diagonal. We find

$$\begin{aligned} U H^{(0)} U^\dagger &= \left[\Delta \cos^2\left(\frac{\lambda}{2}\right) + \frac{g}{2} (\alpha e^{-i\mu} + \text{c.c.}) \sin(\lambda) \right] \hat{n}_e \\ &\quad + \left[\Delta \sin^2\left(\frac{\lambda}{2}\right) - \frac{g}{2} (\alpha e^{-i\mu} + \text{c.c.}) \sin(\lambda) \right] \hat{n} \\ &\quad + \left[\frac{\Delta}{2} e^{i\mu} \sin(\lambda) + e^{2i\mu} \sin^2\left(\frac{\lambda}{2}\right) g \alpha^* - g \alpha \cos^2\left(\frac{\lambda}{2}\right) \right] \hat{S}^+ \\ &\quad + \left[\frac{\Delta}{2} e^{-i\mu} \sin(\lambda) + e^{-2i\mu} \sin^2\left(\frac{\lambda}{2}\right) g \alpha - g \alpha^* \cos^2\left(\frac{\lambda}{2}\right) \right] \hat{S}^- \end{aligned} \quad (7.52)$$

The coefficients of \hat{S}^+ and \hat{S}^- vanish for $\mu = \arg(\alpha)$ and λ such that $\Delta \sin\left(\frac{\lambda}{2}\right) \cos\left(\frac{\lambda}{2}\right) = g \alpha (\cos^2\left(\frac{\lambda}{2}\right) - \sin^2\left(\frac{\lambda}{2}\right))$, which is satisfied for $\cos \lambda = \Delta / \sqrt{\Delta^2 + 4g^2|\alpha|^2}$. We denote by ε_- and ε_+ the coefficients of \hat{n} and \hat{n}_e , respectively, and find

$$\begin{aligned} \varepsilon_- &= \Delta \sin^2\left(\frac{\lambda}{2}\right) - 2g|\alpha| \sin\left(\frac{\lambda}{2}\right) \cos\left(\frac{\lambda}{2}\right) \\ &= \frac{1}{2} \left(\Delta - \sqrt{\Delta^2 + 4g^2|\alpha|^2} \right) \end{aligned} \quad (7.53)$$

$$\begin{aligned} \varepsilon_+ &= \Delta \cos^2\left(\frac{\lambda}{2}\right) + 2g|\alpha| \sin\left(\frac{\lambda}{2}\right) \cos\left(\frac{\lambda}{2}\right) \\ &= \frac{1}{2} \left(\Delta + \sqrt{\Delta^2 + 4g^2|\alpha|^2} \right) \end{aligned} \quad (7.54)$$

Now we consider $\tilde{H} - H^{(0)} = \delta\hat{a}^\dagger\hat{a} - i\frac{\gamma}{2}\hat{n}_e + g\hat{a}\hat{S}^+ + g\hat{a}^\dagger\hat{S}^-$ and calculate $U(\tilde{H} - H^{(0)})U^\dagger$ term by term (the notation $\mathcal{O}(1)$ refers to the limit $\Delta \rightarrow \infty$).

$$U\hat{a}^\dagger\hat{a}U^\dagger = \hat{a}^\dagger\hat{a} \quad (7.55)$$

$$\begin{aligned} U\hat{n}_eU^\dagger &= \frac{1 - \cos \lambda}{2}\hat{n} + \frac{1 + \cos \lambda}{2}\hat{n}_e + \mathcal{O}(1)\hat{S}^+ + \mathcal{O}(1)\hat{S}^- \\ &= \frac{\hat{n} + \hat{n}_e}{2} - \frac{\Delta(\hat{n} - \hat{n}_e)}{2\sqrt{\Delta^2 + 4g^2|\alpha|^2}} + \mathcal{O}(1)\hat{S}^+ + \mathcal{O}(1)\hat{S}^- \end{aligned} \quad (7.56)$$

$$U\hat{S}^+U^\dagger = \frac{\alpha^*}{\sqrt{\Delta^2 + 4g^2|\alpha|^2}}(\hat{n} - \hat{n}_e) + \mathcal{O}(1)\hat{S}^+ + \mathcal{O}(1)\hat{S}^- \quad (7.57)$$

so that in total we find

$$\begin{aligned} U\tilde{H}U^\dagger &= \delta\hat{a}^\dagger\hat{a} + (\varepsilon_1 - i\gamma_1/2)\hat{n} + (\varepsilon_e - i\gamma_e/2)\hat{n}_e \\ &+ (\zeta\hat{a}^\dagger + \zeta^*\hat{a})(\hat{n} - \hat{n}_e) + \mathcal{O}(1)\hat{S}^+ + \mathcal{O}(1)\hat{S}^- \end{aligned} \quad (7.58)$$

where

$$\gamma_\pm = \frac{\gamma}{2} \left(1 \pm \frac{\Delta}{\sqrt{\Delta^2 + 4g^2|\alpha|^2}} \right), \quad (7.59)$$

$$\zeta = \frac{g^2\alpha}{\sqrt{\Delta^2 + 4g^2|\alpha|^2}}. \quad (7.60)$$

Now using the fact that $i\dot{U}U^\dagger$ is $\mathcal{O}(1)$ and acts on the qubits only (i.e. contains no a or a^\dagger terms) we obtain Eq. (7.7) from the main text for \tilde{H} .

7.A.3 Analytic Solution of Time Evolution under H_{eff}

In this appendix we find the analytic solution of the Lindblad equation $\dot{\rho} = -iH\rho + i\rho H^\dagger + L\rho L^\dagger - \frac{1}{2}\{L^\dagger L, \rho\}$ under $H = \delta\hat{a}^\dagger\hat{a} + (-i\gamma_1(t)/2 + \zeta(t)\hat{a}^\dagger + \zeta(t)^*\hat{a})\hat{n}$ and $L = \sqrt{\kappa}\hat{a}$ for an arbitrary drive $\zeta(t)$ and time dependent decay rate $\gamma_1(t)$. For this, we assume an initial state $\rho(0) = |\beta_n(0)\rangle\langle\beta_m(0)| \otimes |q\rangle\langle q'|$, where β_n and β_m are coherent states and $|q\rangle(|q'\rangle)$ are computational basis states with $n(m)$ qubits in state $|1\rangle$. Note that initial states of this form are a basis of space of all possible initial density matrices, so solving the Lindblad equation for the initial state $\rho(0)$ suffices to solve it for an arbitrary initial state.

In the following we show that the solution to the Lindblad equation is given by

$$\rho(t) = e^{i\varphi_{nm}(t)} \frac{|\beta_n(t)\rangle\langle\beta_m(t)| \otimes |q\rangle\langle q'|}{\langle\beta_m(t)|\beta_n(t)} \quad (7.61)$$

where $\dot{\beta}_n = -(i\delta + \kappa/2)\beta_n - in\zeta$, i.e.

$$\beta_n(t) = \beta_n(0)e^{-(i\delta + \kappa/2)t} - in \int_0^t dt' \zeta(t') e^{-(i\delta + \kappa/2)(t-t')} \quad (7.62)$$

and

$$\begin{aligned} \varphi_{nm}(t) = \int_0^t dt' [(m-n)(\zeta(t')\beta_m(t')^* \\ + \zeta(t')^*\beta_n(t')) + i(m+n)\gamma_1(t')/2]. \end{aligned} \quad (7.63)$$

Tracing out the cavity then gives the reduced density matrix $\rho_{\text{eff}} = e^{i\varphi_{nm}(t)} |q\rangle \langle q'|$ discussed in the main text.

To show Eq. (7.61), we make the Ansatz $\rho = \rho_{nm} \otimes |q\rangle \langle q'|$ with ρ_{nm} of the form $\rho_{nm}(t) = c_{nm}(t) |\beta_n(t)\rangle \langle \beta_m(t)|$. The Lindblad equation gives

$$\dot{\rho}_{nm} = -iH_n \rho_{nm} + i\rho_{nm} H_m^\dagger + L\rho_{nm} L^\dagger - \frac{1}{2} \{L^\dagger L, \rho_{nm}\}, \quad (7.64)$$

with $H_n = \delta\hat{a}^\dagger\hat{a} + (-i\gamma_1/2 + \zeta\hat{a}^\dagger + \zeta^*\hat{a})n$.

We start by calculating the left side of Eq. (7.64). It is a property of coherent states that

$$\frac{d}{dt} |\beta_n(t)\rangle = \dot{\beta}_n \hat{a}^\dagger |\beta_n\rangle - \frac{1}{2} \frac{d|\beta_n|^2}{dt} |\beta_n\rangle \quad (7.65)$$

so that

$$\begin{aligned} \dot{\rho}_{nm} = & c_{nm} \dot{\beta}_n \hat{a}^\dagger |\beta_n\rangle \langle \beta_m| + c_{nm} \dot{\beta}_m^* |\beta_n\rangle \langle \beta_m| \hat{a} \\ & + \left(\dot{c}_{nm} - \frac{c_{nm}}{2} \frac{d(|\beta_n|^2 + |\beta_m|^2)}{dt} \right) |\beta_n\rangle \langle \beta_m| \end{aligned} \quad (7.66)$$

Now we evaluate the right side of Eq. (7.64):

$$H_n \rho_{nm} / c_{nm} = [(\delta\beta_n + n\zeta) \hat{a}^\dagger + n\zeta^* \beta_n - in\gamma_1/2] |\beta_n\rangle \langle \beta_m| \quad (7.67)$$

$$\rho_{nm} H_m^\dagger / c_{nm} = [(\delta\beta_m^* + m\zeta^*) \hat{a} + m\zeta \beta_m^* + im\gamma_1/2] |\beta_n\rangle \langle \beta_m| \quad (7.68)$$

$$L\rho_{nm} L^\dagger / c_{nm} = \kappa \beta_n \beta_m^* |\beta_n\rangle \langle \beta_m| \quad (7.69)$$

$$\{L^\dagger L, \rho_{nm}\} / c_{nm} = [\kappa \beta_n \hat{a}^\dagger + \kappa \beta_m^* \hat{a}] |\beta_n\rangle \langle \beta_m| \quad (7.70)$$

Together, Eq. (7.67)-(7.70) give

$$\begin{aligned} & -iH_n \rho_{nm} + i\rho_{nm} H_m^\dagger + L\rho_{nm} L^\dagger - \frac{1}{2} \{L^\dagger L, \rho_{nm}\} \\ = & c_{nm} (-i\delta\beta_n - in\zeta - \kappa\beta_n/2) \hat{a}^\dagger |\beta_n\rangle \langle \beta_m| \\ & + c_{nm} (i\delta\beta_m^* + im\zeta^* - \kappa\beta_m^*/2) |\beta_n\rangle \langle \beta_m| \hat{a} \\ & + c_{nm} (-in\zeta^* \beta_n + im\zeta \beta_m^* + \kappa\beta_n \beta_m^* \\ & - (n+m)\gamma_1/2) |\beta_n\rangle \langle \beta_m| \end{aligned} \quad (7.71)$$

Equating Eq. (7.66) and Eq. (7.71) gives Eq. (7.62), as well as

$$\begin{aligned} \dot{c}_{nm}/c_{nm} = & \frac{1}{2} \frac{d(|\beta_n|^2 + |\beta_m|^2)}{dt} \\ & - in\zeta^*\beta_n + im\zeta\beta_m^* + \kappa\beta_n\beta_m^* - (n+m)\gamma_1/2 \end{aligned} \quad (7.72)$$

Now we take $c_{nm} = e^{i\varphi_{nm}}/\langle\beta_m|\beta_n\rangle$. Using $\langle\beta_m|\beta_n\rangle = \exp(-\frac{1}{2}(|\beta_n|^2 + |\beta_m|^2) + \beta_m^*\beta_n)$ we obtain

$$\begin{aligned} i\dot{\varphi}_{nm} &= \frac{\dot{c}_{nm}}{c_{nm}} + \frac{d}{dt} \left(-\frac{1}{2}(|\beta_n|^2 + |\beta_m|^2) + \beta_m^*\beta_n \right) \\ &= -in\zeta^*\beta_n + im\zeta\beta_m^* + \kappa\beta_n\beta_m^* - (n+m)\gamma_1/2 + \dot{\beta}_m^*\beta_n + \beta_m^*\dot{\beta}_n \\ &= i(m-n)\zeta^*\beta_n + i(m-n)\zeta\beta_m^* - (n+m)\gamma_1/2 \end{aligned} \quad (7.73)$$

where in the last equality we inserted $\dot{\beta}_n = -(i\delta + \kappa/2)\beta_n - in\zeta$. Integrating Eq. (7.73) gives Eq. (7.63).

7.A.4 Calculation of the Fidelity in the Limit $T \rightarrow \infty$

In the following we show that in the limit $T \rightarrow \infty$ and to first order in γ and κ the infidelity of protocol A is given by

$$1 - F = \left(\frac{\kappa}{4(1 + 2^{-N})\delta} + \frac{\gamma\delta}{2g^2} \right) N\theta. \quad (7.74)$$

In the limit $T \rightarrow \infty$ the solution to $\dot{\beta}_n = -(i\delta + \kappa/2)\beta_n - in\zeta$ can be obtained by an adiabatic approximation. For this, we insert $\dot{\beta}_n = 0$ and obtain

$$\beta_n = \frac{-in\zeta}{i\delta + \kappa/2} \approx -\frac{n\zeta}{\delta} \left(1 + i\frac{\kappa}{2\delta} \right). \quad (7.75)$$

With Eq. (7.22) we obtain

$$\varphi_{nm} = (n^2 - m^2)\theta + (m-n)^2 \frac{i\kappa}{2\delta} \theta + i(m+n) \int_0^T dt \gamma_1(t)/2 \quad (7.76)$$

where $\theta = \frac{1}{\delta} \int_0^T dt |\zeta(t)|^2$. Since in the limit $T \rightarrow \infty$ we have $\zeta \rightarrow 0$ we approximate

$$\gamma_1 = \frac{\gamma}{2} \left(1 - \sqrt{1 - 4|\zeta|^2/g^2} \right) \approx \frac{\gamma|\zeta|^2}{g^2} \quad (7.77)$$

so that

$$\frac{\varphi_{nm}}{\theta} = n^2 - m^2 + (m-n)^2 \frac{i\kappa}{2\delta} + (m+n) \frac{i\gamma\delta}{2g^2} \quad (7.78)$$

Inserting this into Eq. (7.24) and using that

$$\sum_{n,m=0}^N \binom{N}{n} \binom{N}{m} (m-n)^2 = 4^N \frac{N}{2} \quad (7.79)$$

and

$$\sum_{n=0}^N \binom{N}{n} (n+n) = 2^N N, \quad (7.80)$$

$$\sum_{n,m=0}^N \binom{N}{n} \binom{N}{m} (n+m) = 4^N N, \quad (7.81)$$

we obtain Eq. (7.74).

7.A.5 Effects of Coupling Inhomogeneities on the Fidelity

In this section we calculate the effect different couplings g_1, \dots, g_N of each qubit to the cavity on the gate fidelity. We assume that the g_1, \dots, g_N are independent and identically distributed random variables and have the quadratic mean $\bar{g} = \sqrt{\mathbb{E}[g_j^2]}$. Furthermore assume that the drive $\eta(t)$, and thus $\alpha(t)$, is chosen as given in the main text, with the homogeneous coupling g replaced by \bar{g} .

To be able to obtain analytical solutions we restrict ourselves to the case $T \rightarrow \infty$, but expect a similar scaling for finite T .

Following the same steps as in the main text, an effective Hamiltonian can be found as

$$H_{\text{eff}} = \delta a^\dagger a + \sum_{q \in \{0,1\}^N} (\zeta_q a^\dagger + \zeta_q^* a) |q\rangle \langle q| \quad (7.82)$$

where

$$\zeta_q = \sum_{j=1}^N q_j \frac{g_j^2 \alpha}{\sqrt{4g_j^2 |\alpha|^2 + \Delta^2}} \approx \frac{\alpha}{\Delta} \sum_{j=1}^N q_j g_j^2 \quad (7.83)$$

where the last approximation holds in the $T \rightarrow \infty$ limit, where $|\alpha| \ll \Delta$.

Starting in the initial state $|\psi(0)\rangle = |0\rangle \otimes |q\rangle$ for a computational basis state $q \in \{0,1\}^N$, the state at the final time T is given by $|\psi(T)\rangle = e^{i\varphi_q(T)} |\beta_q\rangle \otimes |q\rangle$, where $\beta_q = -i\delta\beta_q - i\zeta_q$ and $\dot{\varphi}_q = -\text{Re}(\zeta_q^* \beta_q)$. In the limit $T \rightarrow \infty$ we obtain $\beta_q(t) = -\zeta_q(t)/\delta$ and

$$\begin{aligned} \varphi_q(T) &= \left(\sum_j q_j g_j^2 \right)^2 \int_0^T dt \frac{|\alpha(t)|^2}{\Delta \delta} \\ &= \left(\sum_j q_j g_j^2 \right)^2 \frac{\theta}{\bar{g}^4} \\ &\approx n\theta^2 + \frac{2n\theta}{\bar{g}^2} \sum_j q_j (g_j^2 - g^2) \end{aligned} \quad (7.84)$$

where $n = \sum_j q_j$ is the number of qubits in state $|1\rangle$. Crucially, $\beta_q(T) = 0$, so that the action of the gate can still be described by a unitary operation, given by

$U = \sum_q e^{i\varphi_q(T)} |q\rangle \langle q|$. In the following, we will evaluate the averaged fidelity for the difference $U_A^\dagger U$ between the gate U_A which we aim to implement, and the gate U which is actually implemented.

The averaged fidelity can be evaluated as [134]

$$\begin{aligned} 1 - F &= \frac{1}{2^N(2^N + 1)} \left(2^N + \left| \sum_{q \in \{0,1\}^N} e^{i(\varphi_q(T) - n\theta^2)} \right|^2 \right) \\ &\approx 1 + \frac{1}{2^N(2^N + 1)} \left[\left(\sum_q (\varphi_q - n^2\theta) \right)^2 - 2^N \sum_q (\varphi_q - n^2\theta)^2 \right] \end{aligned} \quad (7.85)$$

We obtain the upper bounds

$$\begin{aligned} 1 - F &\leq \frac{1}{2^N} \sum_q (\varphi_q - n^2\theta)^2 \\ &= \frac{4\theta^2}{\bar{g}^4} \frac{1}{2^N} \sum_{q \in \{0,1\}^N} \left(n \sum_j q_j (g_j^2 - \bar{g}^2) \right)^2 \end{aligned} \quad (7.86)$$

The expected value of the infidelity can be upper bounded, using the independence of the g_j , as

$$\mathbb{E}[1 - F] \leq \frac{4\theta^2}{\bar{g}^4} \sum_q n^2 \sum_j q_j^2 \mathbb{E}[(g_j^2 - \bar{g}_j^2)^2] \quad (7.87)$$

$$= \frac{4\theta^2}{\bar{g}^4} \text{Var}[g_1^2] \frac{1}{2^N} \sum_{n=0}^N \binom{N}{n} n^3 \quad (7.88)$$

$$= N^2(N + 3) \frac{\theta^2}{2\bar{g}^4} \text{Var}[g_1^2]. \quad (7.89)$$

Note that since we assume that the g_j are independent and identically distributed, the $\text{Var}[g_1^2]$ can be replaced by $\text{Var}[g_j^2]$ for any j .

7.B Supporting Calculations for Protocol B

7.B.1 Eigenenergies of H in Perturbation Theory

In this appendix we calculate perturbations of the eigenenergies of H in the limit $\eta \rightarrow 0$ and prove Eq. (7.29). To find the eigenenergy for a computational basis state $|q\rangle$ with n qubits in state $|1\rangle$ it is sufficient to consider the three states $|0, q\rangle$, $|1, q\rangle$ and $|\chi\rangle = \hat{S}^+ |0, q\rangle / \sqrt{n}$, where the first entry in a ket vector denotes the number of

excitations in the cavity mode, and the second entry denotes the state of the qubits. Projected onto these three states, H is given by

$$H = \underbrace{\delta |1, q\rangle \langle 1, q| + \Delta |\chi\rangle \langle \chi| + g\sqrt{N}(|1, q\rangle \langle \chi| + |\chi\rangle \langle 1, q|)}_{H_0} + \underbrace{i\eta |1, q\rangle \langle 0, q| - i\eta^* |0, q\rangle \langle 1, q|}_V. \quad (7.90)$$

Denote by $|p_\pm\rangle$ the eigenstates of H_0 and by E_\pm their corresponding energies. The second order perturbation of the eigenenergy of $|0, q\rangle$ is

$$\varepsilon_n = - \sum_j \frac{|\langle 0, q| V |p_j\rangle|^2}{E_j} = -\eta^2 \langle 1, q| H_0^{-1} |1, q\rangle = -\frac{|\eta|^2 \Delta}{\Delta\delta - ng^2}. \quad (7.91)$$

This completes the proof of Eq. (7.29). We note that the perturbed eigenstate is given by

$$|\psi_q(t)\rangle = |0, q\rangle - i \frac{\eta(t) (\Delta |1, q\rangle - g\sqrt{n} |\chi\rangle)}{\Delta\delta - ng^2}. \quad (7.92)$$

7.B.2 Effect of Losses

In this appendix we calculate process \mathcal{E} of protocol B to first order in γ and κ in the adiabatic limit and prove Eq. (7.32). We assume an initial state $\rho(0) = |0, q\rangle \langle 0, q|$. Let $U(t)$ be unitary evolution in the absence of noise, and let $\tilde{\rho}(t) = U(t)^\dagger \rho(t) U(t)$. Then

$$\dot{\tilde{\rho}} = -\frac{\gamma}{2} U^\dagger \hat{n}_e U \tilde{\rho} - \frac{\gamma}{2} \tilde{\rho} U^\dagger \hat{n}_e U + \kappa U^\dagger \hat{a} U \tilde{\rho} U^\dagger \hat{a}^\dagger U - \frac{\kappa}{2} U^\dagger \hat{a}^\dagger \hat{a} U \tilde{\rho} - \frac{\kappa}{2} \tilde{\rho} U^\dagger \hat{a}^\dagger \hat{a} U. \quad (7.93)$$

To first order in γ and κ we thus find using the adiabatic approximation $U(t) |0, q\rangle = e^{-i\varphi_n(t)} |\psi_q(t)\rangle$ with $\varphi_n(t) = \int_0^t dt' \varepsilon_n(t')$ that

$$\begin{aligned} \tilde{\rho}(T) = |0, q\rangle \langle 0, q| + \int_0^T dt \Big[& -\frac{1}{2} e^{-i\varphi_n(t)} U^\dagger(t) (\gamma \hat{n}_e + \kappa \hat{a}^\dagger \hat{a}) |\psi_q(t)\rangle \langle 0, q| \\ & -\frac{1}{2} e^{i\varphi_m(t)} |0, q\rangle \langle \psi_{q'}(t)| (\gamma \hat{n}_e + \kappa \hat{a}^\dagger \hat{a}) U(t) \\ & + \kappa e^{-i(\varphi_n(t) - \varphi_m(t))} U^\dagger(t) \hat{a} |\psi_q(t)\rangle \langle \psi_{q'}(t)| \hat{a}^\dagger U(t) \Big]. \end{aligned} \quad (7.94)$$

We obtain

$$\begin{aligned} c_{nm} & := e^{i(\varphi_n(t) - \varphi_m(t))} \langle q| \mathcal{E}(|q\rangle \langle q'|) |q'\rangle \\ & = \sum_{k=0}^{\infty} \langle k, q| \tilde{\rho}(T) |k, q'\rangle \end{aligned} \quad (7.95)$$

Up to second order in η only terms with $k = 0$ contribute, so we obtain

$$c_{nm} = 1 + \int_0^T dt \left[-\frac{1}{2} \langle \psi_q(t) | (\gamma \hat{n}_e + \kappa \hat{a}^\dagger \hat{a}) | \psi_q(t) \rangle \right. \\ \left. - \frac{1}{2} \langle \psi'_q(t) | (\gamma \hat{n}_e + \kappa \hat{a}^\dagger \hat{a}) | \psi'_q(t) \rangle \right. \\ \left. + \kappa \langle \psi_q(t) | \hat{a} | \psi_q(t) \rangle \langle \psi'_q(t) | \hat{a}^\dagger | \psi'_q(t) \rangle \right]. \quad (7.96)$$

Using that $\langle \psi_q | \hat{n}_e | \psi_q \rangle = |\eta|^2 g^2 n / (\Delta\delta - ng^2)^2$, $\langle \psi_q | \hat{a}^\dagger \hat{a} | \psi_q \rangle = |\eta|^2 \Delta^2 / (\Delta\delta - ng^2)^2$ and $\langle \psi_q(t) | \hat{a} | \psi_q(t) \rangle = -i\eta\Delta / (\Delta\delta - ng^2)$ we find

$$c_{nm} = 1 - \frac{\gamma_n + \gamma_m}{2} - \frac{s_n^2 + s_m^2 - 2s_n s_m}{2} \quad (7.97)$$

with

$$\gamma_n = \frac{\gamma n g^2}{(\Delta\delta - ng^2)^2} I \quad s_n = \frac{\sqrt{\kappa} \Delta}{\Delta\delta - ng^2} \sqrt{I}. \quad (7.98)$$

This proves Eq. (7.32).

7.B.3 Effects of Coupling Inhomogeneities on the Fidelity

Analogously to Sec. 7.A.5 we now calculate the effect of inhomogeneities in the coupling strength in protocol B. We assume again that the g_1, \dots, g_N are independent and identically distributed random variables and have the quadratic mean $\bar{g} = \sqrt{\mathbb{E}[g_j^2]}$.

Repeating the derivation in the main text with couplings g_1, \dots, g_N which are different for each qubit gives a phase

$$\varphi_q = -\frac{I}{\delta - \frac{1}{\Delta} \sum_{j=1}^N q_j g_j^2} \quad (7.99)$$

$$\approx -\frac{I}{\delta - n\bar{g}^2/\Delta} - \frac{I\Delta}{(\delta\Delta - n\bar{g}^2)^2} \sum_j q_j (g_j^2 - \bar{g}^2) \quad (7.100)$$

which is accumulated when starting with the qubits in state $|q\rangle$ (for $q \in \{0, 1\}^N$). Here, as in Sec. 7.A.5, we use $n = \sum_j q_j$. Analogously to Eq. (7.87) we obtain

$$1 - F \leq \frac{1}{2^N} \sum_{q \in \{0,1\}^N} \left[\frac{I\Delta}{(\delta\Delta - n\bar{g}^2)^2} \sum_j q_j (g_j^2 - \bar{g}^2) \right]^2 \quad (7.101)$$

so that

$$\mathbb{E}[1 - F] \leq \text{Var}[g_1^2] \frac{1}{2^N} \sum_{n=0}^N \binom{N}{n} n \left[\frac{I\Delta}{(\delta\Delta - n\bar{g}^2)^2} \right]^2 \quad (7.102)$$

7.B.4 Using Protocol B for Arbitrary Phase Gates

In this appendix we discuss how protocol B can be used to implement phase gates $\exp(i\varphi(\hat{n}))$ for arbitrary $\boldsymbol{\varphi} = (\varphi(0), \dots, \varphi(N))$ (Here and in the following a bold font is used to indicate vector quantities). We aim to do this by applying K pulses with detunings $\delta_1, \dots, \delta_K$ and $\Delta_1, \dots, \Delta_K$, as well as driving fields $\eta_1(t), \dots, \eta_K(t)$ and corresponding pulse energies $\mathbf{I} = (I_1, \dots, I_K)$ with $I_k = \int_0^{T_k} |\eta_k(t)|^2 dt$. With this, we implement a phase gate with $\boldsymbol{\varphi} = A\mathbf{I}$, where A is a $(N+1) \times K$ matrix with

$$A_{nk} = -\frac{1}{\delta_k - ng^2/\Delta_k}. \quad (7.103)$$

By adding the infidelities of the individual pulses we obtain an average gate infidelity $\mathbf{b} \cdot \mathbf{I}$, where

$$b_k = \frac{1}{2^N(2^{N+1})} \left(\sum_{n=0}^N \binom{N}{n} \epsilon_k^{(n,n)} + \sum_{n,m=0}^N \binom{N}{n} \binom{N}{m} \epsilon_k^{(n,m)} \right) \quad (7.104)$$

with

$$\begin{aligned} \epsilon_k^{(n,m)} = & \gamma g^2 \left(\frac{n}{(\Delta_k \delta_k - ng^2)^2} + \frac{m}{(\Delta_k \delta_k - mg^2)^2} \right) \\ & + \kappa \Delta^2 \left(\frac{1}{\Delta_k \delta_k - ng^2} - \frac{1}{\Delta_k \delta_k - mg^2} \right)^2. \end{aligned} \quad (7.105)$$

Thus, for a fixed set of detunings $\delta_1, \dots, \delta_K$ and $\Delta_1, \dots, \Delta_K$, finding the optimal values of \mathbf{I} becomes a linear programming problem:

$$\begin{aligned} & \text{Find } \mathbf{I} \\ & \text{that minimizes } \mathbf{b} \cdot \mathbf{I} \\ & \text{subject to } A\mathbf{I} = \boldsymbol{\varphi} \\ & \text{and } \mathbf{I} \geq 0 \end{aligned}$$

The solution to this linear program can be readily found using the simplex method, which is implemented in various software packages [161].

Since the solution of the given linear program is always on an extremal point of the simplex given by $A\mathbf{I} = \boldsymbol{\varphi}$ and $\mathbf{I} \geq 0$, there are exactly $N+1$ indices k such that $I_k \neq 0$. To find the optimal pulse detunings one can thus take the following approach: First take $K \gg N$ and take the $\delta_1, \dots, \delta_K$ to form a uniformly spaced grid. Take $\Delta_k - \delta_k$ some constant independent of k to ensure that the different pulses can be implemented by only changing the pulse frequency, not the frequency of the cavity or the $|1\rangle \leftrightarrow |e\rangle$ transition. Now the linear program given above is solved, giving $N+1$ indices k_1, \dots, k_{N+1} at which $I_k \neq 0$. To implement the phase gate given by the $\boldsymbol{\varphi}$, $N+1$ pulses with detunings $\delta_{k_1}, \dots, \delta_{k_{N+1}}$ and $\Delta_{k_1}, \dots, \Delta_{k_{N+1}}$ as well as pulse energies $I_{k_1}, \dots, I_{k_{N+1}}$ have to be applied.

A reduction to $N - 1$ instead of $N + 1$ required pulses is obtained if one only aims to implement the phase gate $\exp(i\varphi(\hat{n}))$ up to a global phase and single qubit gates. Formally, this means replacing the constraint $A\mathbf{I} = \boldsymbol{\varphi}$ by

$$\forall n \geq 2 \quad (A\mathbf{I})_n - n(A\mathbf{I})_1 + (n - 1)(A\mathbf{I})_0 = \varphi_n \quad (7.106)$$

Since this condition is still linear in \mathbf{I} , the optimal \mathbf{I} can be found as before through a linear program.

With the procedure outlined above, \mathbf{I} is chosen to maximize the average gate fidelity. For implementing a $C_{N-1}Z$ gate, our goal is instead to maximize the minimal fidelity. This is not possible with our linear programming approach in a straight forward manner, so we resort to a heuristic approach. For this, we replace the b_k (Eq. (7.104)) by

$$b_k = \frac{1}{(N + 1)^2} \sum_{n,m=0}^N \epsilon_k^{(n,n)} \quad (7.107)$$

and solve the corresponding linear program. Compared to Eq. (7.104) this approach has the advantage that it weights the performance of the gate for all n and m equally, while Eq. (7.104) weights terms with $n, m \sim N/2$ higher than terms with extreme n and m . The resulting \mathbf{I} are then used to evaluate the minimal fidelity.

8 Conclusions and Outlook

In this thesis we have developed several new and optimized gate protocols for two- and multi-qubit quantum gates on neutral atoms interacting either via the van der Waals interaction of Rydberg states or by the coupling to a common cavity mode. For interactions mediated via Rydberg states, a large family of these protocols are *time-optimal* protocols, in which a global laser pulse with a smoothly varying phase is applied on two or more atoms to implement a given quantum gate as fast as possible. We used the numerical quantum optimal control method of GRAPE to find the time-optimal protocol for all two-qubit phase gates and several multi-qubit phase gates, and revealed the mathematical structure of time-optimal protocols using Pontryagin's maximum principle. Due to their simple structure, versatility, and high fidelity, time-optimal protocols have already been used to implement CZ gates and to generate GHZ states on up to ten atoms, and are expected to remain crucial building block for neutral atom quantum computers in the future. It is an interesting future research direction to use time-optimal pulses to replace certain parts of quantum circuits by native gates, or to generate special states other than GHZ states. In particular, the development of time-optimal protocols to generate so-called *magic states*, which are required for fault tolerant quantum computation (FTQC), is an exciting research goal.

While the speed of time-optimal protocol reduces the effect of many error sources, we also showed in this thesis that there are longer but *robust* gate protocols, which can achieve higher fidelities in the presence of certain error sources. Specifically, we developed pulse shapes which implement a CZ gate and are robust to deviations in the laser amplitude and laser detunings due to Doppler shifts induced by the thermal motion of the atoms. For Rydberg decay errors we instead showed that the time-optimal protocols for the CZ and C_2Z gate essentially already minimize the infidelity. There are several experimentally relevant error sources which we did not include in our discussion of robust gates, and developing approaches to mitigate them is an important future research direction. In particular, we considered only quasi-static fluctuations in the laser amplitude and detuning, and an extension of our results to time-dependent noise sources would be highly desirable. Furthermore, it remains open whether there is a semi-analytical description of robust pulses, similar to that of time-optimal pulses developed in Chapter 4.

Despite fast and robust gate protocols, errors are unavoidable in any quantum computation. The framework of FTQC uses redundancy to mitigate the effects of these errors. In this thesis, we showed that for a surface code on Rydberg atoms the protocols which minimize the gate infidelity on the physical level can differ significantly

from protocols that minimize the *logical* error rate. We identified Rydberg leakage errors as the source of this discrepancy and developed several protocols in which these errors are less detrimental. In the future, it will be important to integrate our results with approaches to correct other errors specific to neutral atoms, such as atom loss errors or leakage errors to other hyperfine states [84], into one monolithic FTQC protocol.

Finally, in this thesis we also developed two families of gate protocols that implement multi-qubit gates on neutral atoms interacting via a common cavity mode instead of the van der Waals interaction of Rydberg states. This allows for an all-to-all connectivity and non-local gates between the atoms. The distinguishing feature of our protocols is that they can be implemented by simply using a classical drive of the cavity mode, while no addressing of the atoms is necessary, opening up new experimental possibilities. In the future, variants of these protocols may be used to generate large non-local entangled states, such as GHZ states, with applications in quantum sensing, cryptography, and error correction.

The results presented in this thesis have brought the vision of a large scale neutral atom quantum computer capable at outperforming classical computers in practically relevant tasks closer to reality. However, many challenges still have to be overcome. Arguably one of the most important tasks is the implementation of larger FTQC protocols adapted to the dominant error channels encountered in neutral atoms. This includes the design of protocols that can simultaneously correct Pauli errors, Rydberg leakage errors, atom loss errors, and leakage errors to other hyperfine states, and that make optimal use of erasure errors and biased noise [14, 20]. The time-optimal and robust gate protocols developed in Chapters 3–5 as well as the discussion of Rydberg leakage errors in Chapter 6 form a good starting point for the design of such FTQC protocols. A second avenue is the exploration of low density parity check (LDPC) codes, which allow to encode more logical qubits in the same number of physical qubits than traditional surface codes [29, 78, 79]. Developing optimized approaches for implementing LDPC codes on neutral atoms, implementing logical gates on qubits encoded in LDPC codes, and understanding and improving the performance of LDPC codes under errors unique to the neutral atom architecture are all important future research directions, which can be tackled with the methods developed in this thesis.

Bibliography

- [1] M. A. Nielsen and I. L. Chuang. *Quantum Computation and Quantum Information*. Cambridge ; New York: Cambridge University Press, 2000.
- [2] B. Bauer, S. Bravyi, M. Motta, and G. K.-L. Chan. “Quantum Algorithms for Quantum Chemistry and Quantum Materials Science”. *Chemical Reviews* 120 (2020), pp. 12685–12717. DOI: 10.1021/acs.chemrev.9b00829.
- [3] A. Abbas, A. Ambainis, B. Augustino, A. Bärtschi, H. Buhrman, C. Coffrin, G. Cortiana, V. Dunjko, D. J. Egger, B. G. Elmegreen, N. Franco, F. Fratini, B. Fuller, J. Gacon, C. Gonciulea, S. Gribling, S. Gupta, S. Hadfield, R. Heese, G. Kircher, T. Kleinert, T. Koch, G. Korpas, S. Lenk, J. Marecek, V. Markov, G. Mazzola, S. Mensa, N. Mohseni, G. Nannicini, C. O’Meara, E. P. Tapia, S. Pokutta, M. Proissl, P. Reberntrost, E. Sahin, B. C. B. Symons, S. Tornow, V. Valls, S. Woerner, M. L. Wolf-Bauwens, J. Yard, S. Yarkoni, D. Zechiel, S. Zhuk, and C. Zoufal. *Quantum Optimization: Potential, Challenges, and the Path Forward*. 2023. URL: <http://arxiv.org/abs/2312.02279>.
- [4] D. J. Egger, C. Gambella, J. Marecek, S. McFaddin, M. Mevissen, R. Raymond, A. Simonetto, S. Woerner, and E. Yndurain. “Quantum Computing for Finance: State-of-the-Art and Future Prospects”. *IEEE Transactions on Quantum Engineering* 1 (2020), pp. 1–24. DOI: 10.1109/TQE.2020.3030314.
- [5] C. L. Degen, F. Reinhard, and P. Cappellaro. “Quantum Sensing”. *Reviews of Modern Physics* 89 (2017), p. 035002. DOI: 10.1103/RevModPhys.89.035002.
- [6] N. Gisin, G. Ribordy, W. Tittel, and H. Zbinden. “Quantum Cryptography”. *Reviews of Modern Physics* 74 (2002), pp. 145–195. DOI: 10.1103/RevModPhys.74.145.
- [7] M. Kjaergaard, M. E. Schwartz, J. Braumüller, P. Krantz, J. I.-J. Wang, S. Gustavsson, and W. D. Oliver. “Superconducting Qubits: Current State of Play”. *Annual Review of Condensed Matter Physics* 11 (2020), pp. 369–395. DOI: 10.1146/annurev-conmatphys-031119-050605.
- [8] C. D. Bruzewicz, J. Chiaverini, R. McConnell, and J. M. Sage. “Trapped-Ion Quantum Computing: Progress and Challenges”. *Applied Physics Reviews* 6 (2019), p. 021314. DOI: 10.1063/1.5088164.
- [9] L. Henriot, L. Beguin, A. Signoles, T. Lahaye, A. Browaeys, G.-O. Reymond, and C. Jurczak. “Quantum Computing with Neutral Atoms”. *Quantum* 4 (2020), p. 327. DOI: 10.22331/q-2020-09-21-327.

-
- [10] A. Browaeys and T. Lahaye. “Many-Body Physics with Individually Controlled Rydberg Atoms”. *Nature Physics* 16 (2020), pp. 132–142. DOI: 10.1038/s41567-019-0733-z.
- [11] M. Morgado and S. Whitlock. “Quantum Simulation and Computing with Rydberg-interacting Qubits”. *AVS Quantum Science* 3 (2021), p. 023501. DOI: 10.1116/5.0036562.
- [12] T. F. Gallagher. *Rydberg Atoms*. 1st ed. Cambridge University Press, 1994. DOI: 10.1017/CB09780511524530.
- [13] S. J. Evered, D. Bluvstein, M. Kalinowski, S. Ebadi, T. Manovitz, H. Zhou, S. H. Li, A. A. Geim, T. T. Wang, N. Maskara, H. Levine, G. Semeghini, M. Greiner, V. Vuletić, and M. D. Lukin. “High-Fidelity Parallel Entangling Gates on a Neutral-Atom Quantum Computer”. *Nature* 622 (2023), pp. 268–272. DOI: 10.1038/s41586-023-06481-y.
- [14] S. Ma, G. Liu, P. Peng, B. Zhang, S. Jandura, J. Claes, A. P. Burgers, G. Pupillo, S. Puri, and J. D. Thompson. “High-Fidelity Gates and Mid-Circuit Erasure Conversion in an Atomic Qubit”. *Nature* 622 (2023), pp. 279–284. DOI: 10.1038/s41586-023-06438-1.
- [15] D. Bluvstein, S. J. Evered, A. A. Geim, S. H. Li, H. Zhou, T. Manovitz, S. Ebadi, M. Cain, M. Kalinowski, D. Hangleiter, J. P. Bonilla Ataides, N. Maskara, I. Cong, X. Gao, P. Sales Rodriguez, T. Karolyshyn, G. Semeghini, M. J. Gullans, M. Greiner, V. Vuletić, and M. D. Lukin. “Logical Quantum Processor Based on Reconfigurable Atom Arrays”. *Nature* 626 (2024), pp. 58–65. DOI: 10.1038/s41586-023-06927-3.
- [16] R. Finkelstein, R. B.-S. Tsai, X. Sun, P. Scholl, S. Direkci, T. Gefen, J. Choi, A. L. Shaw, and M. Endres. “Universal Quantum Operations and Ancilla-Based Readout for Tweezer Clocks”. *arXiv:2402.16220* (2024). URL: <http://arxiv.org/abs/2402.16220>.
- [17] A. Cao, W. J. Eckner, T. L. Yelin, A. W. Young, S. Jandura, L. Yan, K. Kim, G. Pupillo, J. Ye, N. D. Oppong, and A. M. Kaufman. “Multi-Qubit Gates and ‘Schrödinger Cat’ States in an Optical Clock”. *arXiv:2402.16289* (2024). URL: <http://arxiv.org/abs/2402.16289>.
- [18] H. Levine, A. Keesling, G. Semeghini, A. Omran, T. T. Wang, S. Ebadi, H. Bernien, M. Greiner, V. Vuletić, H. Pichler, and M. D. Lukin. “Parallel Implementation of High-Fidelity Multiqubit Gates with Neutral Atoms”. *Physical Review Letters* 123 (2019), p. 170503. DOI: 10.1103/PhysRevLett.123.170503.
- [19] J. Preskill. “Fault-Tolerant Quantum Computation”. *Introduction to Quantum Computation and Information*. World Scientific, 1998, pp. 213–269. DOI: 10.1142/9789812385253_0008.
- [20] Y. Wu, S. Kolkowitz, S. Puri, and J. D. Thompson. “Erasure Conversion for Fault-Tolerant Quantum Computing in Alkaline Earth Rydberg Atom Arrays”. *Nature Communications* 13 (2022), p. 4657. DOI: 10.1038/s41467-022-32094-6.

- [21] S. B. Bravyi and A. Y. Kitaev. *Quantum Codes on a Lattice with Boundary*. 1998. URL: <http://arxiv.org/abs/quant-ph/9811052>.
- [22] K. Mølmer and A. Sørensen. “Multiparticle Entanglement of Hot Trapped Ions”. *Physical Review Letters* 82 (1999), pp. 1835–1838. DOI: 10.1103/PhysRevLett.82.1835.
- [23] S. Jandura and G. Pupillo. “Time-Optimal Two- and Three-Qubit Gates for Rydberg Atoms”. *Quantum* 6 (2022), p. 712. DOI: 10.22331/q-2022-05-13-712.
- [24] S. Jandura, J. D. Thompson, and G. Pupillo. “Optimizing Rydberg Gates for Logical-Qubit Performance”. *PRX Quantum* 4 (2023), p. 020336. DOI: 10.1103/PRXQuantum.4.020336.
- [25] S. Jandura, V. Srivastava, L. Pecorari, G. Brennen, and G. Pupillo. “Non-Local Multi-Qubit Quantum Gates via a Driven Cavity”. *arXiv:2303.13127* (2023). URL: <http://arxiv.org/abs/2303.13127>.
- [26] S. Jandura and G. Pupillo. “Surface Code Stabilizer Measurements for Rydberg Atoms”. *arXiv:2405.16621* (2024). URL: <http://arxiv.org/abs/2405.16621>.
- [27] S. Jandura and E. Y.-Z. Tan. “De Finetti Theorems for Quantum Conditional Probability Distributions with Symmetry”. *Annales Henri Poincaré* (2023). DOI: 10.1007/s00023-023-01357-3.
- [28] P. J. Ollitrault, S. Jandura, A. Miessen, I. Burghardt, R. Martinazzo, F. Tacchino, and I. Tavernelli. “Quantum Algorithms for Grid-Based Variational Time Evolution”. *Quantum* 7 (2023), p. 1139. DOI: 10.22331/q-2023-10-12-1139.
- [29] L. Pecorari, S. Jandura, G. K. Brennen, and G. Pupillo. “High-Rate Quantum LDPC Codes for Long-Range-Connected Neutral Atom Registers”. *arXiv:2404.13010* (2024). URL: <http://arxiv.org/abs/2404.13010>.
- [30] P. Benioff. “The Computer as a Physical System: A Microscopic Quantum Mechanical Hamiltonian Model of Computers as Represented by Turing Machines”. *Journal of Statistical Physics* 22 (1980), pp. 563–591. DOI: 10.1007/BF01011339.
- [31] \hat{U} . I. Manin and F. J. Dyson. *Mathematics as Metaphor*. Providence (R.I.): American mathematical society, 2007.
- [32] R. P. Feynman. “Simulating Physics with Computers”. *International Journal of Theoretical Physics* 21 (1982), pp. 467–488. DOI: 10.1007/BF02650179.
- [33] D. Deutsch. “Quantum Theory, the Church–Turing Principle and the Universal Quantum Computer”. *Proceedings of the Royal Society of London. A. Mathematical and Physical Sciences* 400 (1985), pp. 97–117. DOI: 10.1098/rspa.1985.0070.
- [34] D. Deutsch and R. Jozsa. “Rapid Solution of Problems by Quantum Computation”. *Proceedings of the Royal Society of London. Series A: Mathematical and Physical Sciences* 439 (1992), pp. 553–558. DOI: 10.1098/rspa.1992.0167.

-
- [35] E. Bernstein and U. Vazirani. “Quantum Complexity Theory”. *SIAM Journal on Computing* 26 (1997), pp. 1411–1473. DOI: 10.1137/S0097539796300921.
- [36] D. R. Simon. “On the Power of Quantum Computation”. *SIAM Journal on Computing* 26 (1997), pp. 1474–1483. DOI: 10.1137/S0097539796298637.
- [37] P. W. Shor. “Polynomial-Time Algorithms for Prime Factorization and Discrete Logarithms on a Quantum Computer”. *SIAM Journal on Computing* 26 (1997), pp. 1484–1509. DOI: 10.1137/S0097539795293172.
- [38] R. L. Rivest, A. Shamir, and L. Adleman. “A Method for Obtaining Digital Signatures and Public-Key Cryptosystems”. *Communications of the ACM* 21 (1978), pp. 120–126. DOI: 10.1145/359340.359342.
- [39] E. Farhi, J. Goldstone, and S. Gutmann. “A Quantum Approximate Optimization Algorithm”. *arXiv:1411.4028* (2014). URL: <http://arxiv.org/abs/1411.4028>.
- [40] A. W. Harrow, A. Hassidim, and S. Lloyd. “Quantum Algorithm for Linear Systems of Equations”. *Physical Review Letters* 103 (2009), p. 150502. DOI: 10.1103/PhysRevLett.103.150502.
- [41] J. Biamonte, P. Wittek, N. Pancotti, P. Rebentrost, N. Wiebe, and S. Lloyd. “Quantum Machine Learning”. *Nature* 549 (2017), pp. 195–202. DOI: 10.1038/nature23474.
- [42] I. L. Chuang, N. Gershenfeld, and M. Kubinec. “Experimental Implementation of Fast Quantum Searching”. *Physical Review Letters* 80 (1998), pp. 3408–3411. DOI: 10.1103/PhysRevLett.80.3408.
- [43] Y. Nakamura, Y. A. Pashkin, and J. S. Tsai. “Coherent Control of Macroscopic Quantum States in a Single-Cooper-pair Box”. *Nature* 398 (1999), pp. 786–788. DOI: 10.1038/19718.
- [44] M. H. Devoret, A. Wallraff, and J. M. Martinis. “Superconducting Qubits: A Short Review”. *arXiv:cond-mat/0411174* (2004). URL: <http://arxiv.org/abs/cond-mat/0411174>.
- [45] J. Clarke and F. K. Wilhelm. “Superconducting Quantum Bits”. *Nature* 453 (2008), pp. 1031–1042. DOI: 10.1038/nature07128.
- [46] J. I. Cirac and P. Zoller. “Quantum Computations with Cold Trapped Ions”. *Physical Review Letters* 74 (1995), pp. 4091–4094. DOI: 10.1103/PhysRevLett.74.4091.
- [47] S. Gulde, M. Riebe, G. P. T. Lancaster, C. Becher, J. Eschner, H. Häffner, F. Schmidt-Kaler, I. L. Chuang, and R. Blatt. “Implementation of the Deutsch–Jozsa Algorithm on an Ion-Trap Quantum Computer”. *Nature* 421 (2003), pp. 48–50. DOI: 10.1038/nature01336.
- [48] L. Childress and R. Hanson. “Diamond NV Centers for Quantum Computing and Quantum Networks”. *MRS Bulletin* 38 (2013), pp. 134–138. DOI: 10.1557/mrs.2013.20.

- [49] M. Veldhorst, H. G. J. Eenink, C. H. Yang, and A. S. Dzurak. “Silicon CMOS Architecture for a Spin-Based Quantum Computer”. *Nature Communications* 8 (2017), p. 1766. DOI: 10.1038/s41467-017-01905-6.
- [50] L. M. K. Vandersypen, H. Bluhm, J. S. Clarke, A. S. Dzurak, R. Ishihara, A. Morello, D. J. Reilly, L. R. Schreiber, and M. Veldhorst. “Interfacing Spin Qubits in Quantum Dots and Donors—Hot, Dense, and Coherent”. *npj Quantum Information* 3 (2017), p. 34. DOI: 10.1038/s41534-017-0038-y.
- [51] S. Slussarenko and G. J. Pryde. “Photonic Quantum Information Processing: A Concise Review”. *Applied Physics Reviews* 6 (2019), p. 041303. DOI: 10.1063/1.5115814.
- [52] F. Flamini, N. Spagnolo, and F. Sciarrino. “Photonic Quantum Information Processing: A Review”. *Reports on Progress in Physics* 82 (2019), p. 016001. DOI: 10.1088/1361-6633/aad5b2.
- [53] A. Stern and N. H. Lindner. “Topological Quantum Computation—From Basic Concepts to First Experiments”. *Science* 339 (2013), pp. 1179–1184. DOI: 10.1126/science.1231473.
- [54] V. Lahtinen and J. Pachos. “A Short Introduction to Topological Quantum Computation”. *SciPost Physics* 3 (2017), p. 021. DOI: 10.21468/SciPostPhys.3.3.021.
- [55] N. P. De Leon, K. M. Itoh, D. Kim, K. K. Mehta, T. E. Northup, H. Paik, B. S. Palmer, N. Samarth, S. Sangtawesin, and D. W. Steuerman. “Materials Challenges and Opportunities for Quantum Computing Hardware”. *Science* 372 (2021), eabb2823. DOI: 10.1126/science.abb2823.
- [56] F. Arute, K. Arya, R. Babbush, D. Bacon, J. C. Bardin, R. Barends, R. Biswas, S. Boixo, F. G. S. L. Brandao, D. A. Buell, B. Burkett, Y. Chen, Z. Chen, B. Chiaro, R. Collins, W. Courtney, A. Dunsworth, E. Farhi, B. Foxen, A. Fowler, C. Gidney, M. Giustina, R. Graff, K. Guerin, S. Habegger, M. P. Harrigan, M. J. Hartmann, A. Ho, M. Hoffmann, T. Huang, T. S. Humble, S. V. Isakov, E. Jeffrey, Z. Jiang, D. Kafri, K. Kechedzhi, J. Kelly, P. V. Klimov, S. Knysh, A. Korotkov, F. Kostritsa, D. Landhuis, M. Lindmark, E. Lucero, D. Lyakh, S. Mandrà, J. R. McClean, M. McEwen, A. Megrant, X. Mi, K. Michielsen, M. Mohseni, J. Mutus, O. Naaman, M. Neeley, C. Neill, M. Y. Niu, E. Ostby, A. Petukhov, J. C. Platt, C. Quintana, E. G. Rieffel, P. Roushan, N. C. Rubin, D. Sank, K. J. Satzinger, V. Smelyanskiy, K. J. Sung, M. D. Trevithick, A. Vainsencher, B. Villalonga, T. White, Z. J. Yao, P. Yeh, A. Zalcman, H. Neven, and J. M. Martinis. “Quantum Supremacy Using a Programmable Superconducting Processor”. *Nature* 574 (2019), pp. 505–510. DOI: 10.1038/s41586-019-1666-5.
- [57] Y. Wu, W.-S. Bao, S. Cao, F. Chen, M.-C. Chen, X. Chen, T.-H. Chung, H. Deng, Y. Du, D. Fan, M. Gong, C. Guo, C. Guo, S. Guo, L. Han, L. Hong, H.-L. Huang, Y.-H. Huo, L. Li, N. Li, S. Li, Y. Li, F. Liang, C. Lin, J. Lin, H. Qian, D. Qiao, H. Rong, H. Su, L. Sun, L. Wang, S. Wang, D. Wu, Y. Xu, K. Yan, W. Yang, Y. Yang, Y. Ye, J. Yin, C. Ying, J. Yu, C. Zha, C. Zhang, H. Zhang, K. Zhang, Y. Zhang, H. Zhao, Y. Zhao, L. Zhou, Q. Zhu, C.-Y.

- Lu, C.-Z. Peng, X. Zhu, and J.-W. Pan. “Strong Quantum Computational Advantage Using a Superconducting Quantum Processor”. *Physical Review Letters* 127 (2021), p. 180501. DOI: 10.1103/PhysRevLett.127.180501.
- [58] L. Egan, D. M. Debroy, C. Noel, A. Risinger, D. Zhu, D. Biswas, M. Newman, M. Li, K. R. Brown, M. Cetina, and C. Monroe. “Fault-Tolerant Control of an Error-Corrected Qubit”. *Nature* 598 (2021), pp. 281–286. DOI: 10.1038/s41586-021-03928-y.
- [59] C. Ryan-Anderson, J. G. Bohnet, K. Lee, D. Gresh, A. Hankin, J. P. Gaebler, D. Francois, A. Chernoguzov, D. Lucchetti, N. C. Brown, T. M. Gatterman, S. K. Halit, K. Gilmore, J. A. Gerber, B. Neyenhuis, D. Hayes, and R. P. Stutz. “Realization of Real-Time Fault-Tolerant Quantum Error Correction”. *Physical Review X* 11 (2021), p. 041058. DOI: 10.1103/PhysRevX.11.041058.
- [60] L. Postler, S. Heußen, I. Pogorelov, M. Rispler, T. Feldker, M. Meth, C. D. Marciniak, R. Stricker, M. Ringbauer, R. Blatt, P. Schindler, M. Müller, and T. Monz. “Demonstration of Fault-Tolerant Universal Quantum Gate Operations”. *Nature* 605 (2022), pp. 675–680. DOI: 10.1038/s41586-022-04721-1.
- [61] M. H. Abobeih, Y. Wang, J. Randall, S. J. H. Loenen, C. E. Bradley, M. Markham, D. J. Twitchen, B. M. Terhal, and T. H. Taminiau. “Fault-Tolerant Operation of a Logical Qubit in a Diamond Quantum Processor”. *Nature* 606 (2022), pp. 884–889. DOI: 10.1038/s41586-022-04819-6.
- [62] S. Krinner, N. Lacroix, A. Remm, A. Di Paolo, E. Genois, C. Leroux, C. Hellings, S. Lazar, F. Swiadek, J. Herrmann, G. J. Norris, C. K. Andersen, M. Müller, A. Blais, C. Eichler, and A. Wallraff. “Realizing Repeated Quantum Error Correction in a Distance-Three Surface Code”. *Nature* 605 (2022), pp. 669–674. DOI: 10.1038/s41586-022-04566-8.
- [63] Y. Zhao, Y. Ye, H.-L. Huang, Y. Zhang, D. Wu, H. Guan, Q. Zhu, Z. Wei, T. He, S. Cao, F. Chen, T.-H. Chung, H. Deng, D. Fan, M. Gong, C. Guo, S. Guo, L. Han, N. Li, S. Li, Y. Li, F. Liang, J. Lin, H. Qian, H. Rong, H. Su, L. Sun, S. Wang, Y. Wu, Y. Xu, C. Ying, J. Yu, C. Zha, K. Zhang, Y.-H. Huo, C.-Y. Lu, C.-Z. Peng, X. Zhu, and J.-W. Pan. “Realization of an Error-Correcting Surface Code with Superconducting Qubits”. *Physical Review Letters* 129 (2022), p. 030501. DOI: 10.1103/PhysRevLett.129.030501.
- [64] D. Jaksch, J. I. Cirac, P. Zoller, S. L. Rolston, R. Côté, and M. D. Lukin. “Fast Quantum Gates for Neutral Atoms”. *Physical Review Letters* 85 (2000), pp. 2208–2211. DOI: 10.1103/PhysRevLett.85.2208.
- [65] L. Isenhower, E. Urban, X. L. Zhang, A. T. Gill, T. Henage, T. A. Johnson, T. G. Walker, and M. Saffman. “Demonstration of a Neutral Atom Controlled-NOT Quantum Gate”. *Physical Review Letters* 104 (2010), p. 010503. DOI: 10.1103/PhysRevLett.104.010503.

- [66] I. S. Madjarov, J. P. Covey, A. L. Shaw, J. Choi, A. Kale, A. Cooper, H. Pichler, V. Schkolnik, J. R. Williams, and M. Endres. “High-Fidelity Entanglement and Detection of Alkaline-Earth Rydberg Atoms”. *Nature Physics* 16 (2020), pp. 857–861. DOI: 10.1038/s41567-020-0903-z.
- [67] D. Bluvstein, H. Levine, G. Semeghini, T. T. Wang, S. Ebadi, M. Kalinowski, A. Keesling, N. Maskara, H. Pichler, M. Greiner, V. Vuletić, and M. D. Lukin. “A Quantum Processor Based on Coherent Transport of Entangled Atom Arrays”. *Nature* 604 (2022), pp. 451–456. DOI: 10.1038/s41586-022-04592-6.
- [68] T. M. Graham, Y. Song, J. Scott, C. Poole, L. Phuttitarn, K. Jooya, P. Eichler, X. Jiang, A. Marra, B. Grinkemeyer, M. Kwon, M. Ebert, J. Cherek, M. T. Lichtman, M. Gillette, J. Gilbert, D. Bowman, T. Ballance, C. Campbell, E. D. Dahl, O. Crawford, N. S. Blunt, B. Rogers, T. Noel, and M. Saffman. “Multi-Qubit Entanglement and Algorithms on a Neutral-Atom Quantum Computer”. *Nature* 604 (2022), pp. 457–462. DOI: 10.1038/s41586-022-04603-6.
- [69] A. Omran, H. Levine, A. Keesling, G. Semeghini, T. T. Wang, S. Ebadi, H. Bernien, A. S. Zibrov, H. Pichler, S. Choi, J. Cui, M. Rossignolo, P. Rembold, S. Montangero, T. Calarco, M. Endres, M. Greiner, V. Vuletić, and M. D. Lukin. “Generation and Manipulation of Schrödinger Cat States in Rydberg Atom Arrays”. *Science* 365 (2019), pp. 570–574. DOI: 10.1126/science.aax9743.
- [70] L. Pause, L. Sturm, M. Mittenbühler, S. Amann, T. Preuschoff, D. Schöffner, M. Schlosser, and G. Birkl. “Supercharged Two-Dimensional Tweezer Array with More than 1000 Atomic Qubits”. *Optica* 11 (2024), p. 222. DOI: 10.1364/OPTICA.513551.
- [71] H. J. Manetsch, G. Nomura, E. Bataille, K. H. Leung, X. Lv, and M. Endres. “A Tweezer Array with 6100 Highly Coherent Atomic Qubits”. *arXiv:2403.12021* (2024). URL: <http://arxiv.org/abs/2403.12021>.
- [72] Atom Computing. *Quantum Startup Atom Computing First to Exceed 1,000 Qubits*. 2023. URL: <https://atom-computing.com/quantum-startup-atom-computing-first-to-exceed-1000-qubits/>.
- [73] T. M. Graham, L. Phuttitarn, R. Chinnarasu, Y. Song, C. Poole, K. Jooya, J. Scott, A. Scott, P. Eichler, and M. Saffman. “Midcircuit Measurements on a Single-Species Neutral Alkali Atom Quantum Processor”. *Physical Review X* 13 (2023), p. 041051. DOI: 10.1103/PhysRevX.13.041051.
- [74] S. Anand, C. E. Bradley, R. White, V. Ramesh, K. Singh, and H. Bernien. “A Dual-Species Rydberg Array”. *arXiv:2401.10325* (2024). URL: <http://arxiv.org/abs/2401.10325>.
- [75] P. Scholl, A. L. Shaw, R. B.-S. Tsai, R. Finkelstein, J. Choi, and M. Endres. “Erasure Conversion in a High-Fidelity Rydberg Quantum Simulator”. *Nature* 622 (2023), pp. 273–278. DOI: 10.1038/s41586-023-06516-4.

-
- [76] Y. Li and J. Thompson. “High-Rate and High-Fidelity Modular Interconnects between Neutral Atom Quantum Processors”. *arXiv:2401.04075* (2024). URL: <http://arxiv.org/abs/2401.04075>.
- [77] J. Ramette, J. Sinclair, Z. Vendeiro, A. Rudelis, M. Cetina, and V. Vuletić. “Any-To-Any Connected Cavity-Mediated Architecture for Quantum Computing with Trapped Ions or Rydberg Arrays”. *PRX Quantum* 3 (2022), p. 010344. DOI: 10.1103/PRXQuantum.3.010344.
- [78] Q. Xu, J. P. Bonilla Ataides, C. A. Pattison, N. Raveendran, D. Bluvstein, J. Wurtz, B. Vasić, M. D. Lukin, L. Jiang, and H. Zhou. “Constant-Overhead Fault-Tolerant Quantum Computation with Reconfigurable Atom Arrays”. *Nature Physics* (2024). DOI: 10.1038/s41567-024-02479-z.
- [79] Y. Hong, M. Marinelli, A. M. Kaufman, and A. Lucas. “Long-Range-Enhanced Surface Codes”. *arXiv:2309.11719* (2023). URL: <http://arxiv.org/abs/2309.11719>.
- [80] I. Bloch, J. Dalibard, and W. Zwerger. “Many-Body Physics with Ultracold Gases”. *Reviews of Modern Physics* 80 (2008), pp. 885–964. DOI: 10.1103/RevModPhys.80.885.
- [81] M. Marinescu, H. R. Sadeghpour, and A. Dalgarno. “Dispersion Coefficients for Alkali-Metal Dimers”. *Physical Review A* 49 (1994), pp. 982–988. DOI: 10.1103/PhysRevA.49.982.
- [82] D. J. Griffiths. *Introduction to Quantum Mechanics*. Englewood Cliffs (N.J.): Prentice Hall, 1995.
- [83] C.-J. Lorenzen and K. Niemax. “Quantum Defects of the $n^2P_{1/2,3/2}$ Levels in ^{39}KI and ^{85}RbI ”. *Physica Scripta* 27 (1983), pp. 300–305. DOI: 10.1088/0031-8949/27/4/012.
- [84] I. Cong, H. Levine, A. Keesling, D. Bluvstein, S.-T. Wang, and M. D. Lukin. “Hardware-Efficient, Fault-Tolerant Quantum Computation with Rydberg Atoms”. *Physical Review X* 12 (2022), p. 021049. DOI: 10.1103/PhysRevX.12.021049.
- [85] S. Ma, A. P. Burgers, G. Liu, J. Wilson, B. Zhang, and J. D. Thompson. “Universal Gate Operations on Nuclear Spin Qubits in an Optical Tweezer Array of Yb 171 Atoms”. *Physical Review X* 12 (2022), p. 021028. DOI: 10.1103/PhysRevX.12.021028.
- [86] I. S. Madjarov. “Entangling, Controlling, and Detecting Individual Strontium Atoms in Optical Tweezer Arrays”. PhD thesis. California Institute of Technology, 2021. URL: https://thesis.library.caltech.edu/14061/7/Thesis_Ivaylo_Madjarov.pdf.
- [87] M. A. Norcia, M. N. Winchester, J. R. K. Cline, and J. K. Thompson. “Superradiance on the Millihertz Linewidth Strontium Clock Transition”. *Science Advances* 2 (2016), e1601231. DOI: 10.1126/sciadv.1601231.

- [88] N. Chen, L. Li, W. Huie, M. Zhao, I. Vetter, C. H. Greene, and J. P. Covey. “Analyzing the Rydberg-based Optical-Metastable-Ground Architecture for Yb 171 Nuclear Spins”. *Physical Review A* 105 (2022), p. 052438. DOI: 10.1103/PhysRevA.105.052438.
- [89] T. P. Softley. *Atomic Spectra*. Reprinted. Oxford Chemistry Primers. Oxford: Oxford University Press, 2008.
- [90] R. Grimm, M. Weidemüller, and Y. B. Ovchinnikov. “Optical Dipole Traps for Neutral Atoms”. *Advances In Atomic, Molecular, and Optical Physics*. Vol. 42. Elsevier, 2000, pp. 95–170. DOI: 10.1016/S1049-250X(08)60186-X.
- [91] M. Endres, H. Bernien, A. Keesling, H. Levine, E. R. Anschuetz, A. Krajenbrink, C. Senko, V. Vuletic, M. Greiner, and M. D. Lukin. “Atom-by-Atom Assembly of Defect-Free One-Dimensional Cold Atom Arrays”. *Science* 354 (2016), pp. 1024–1027. DOI: 10.1126/science.aah3752.
- [92] D. Barredo, S. de Léséleuc, V. Lienhard, T. Lahaye, and A. Browaeys. “An Atom-by-Atom Assembler of Defect-Free Arbitrary Two-Dimensional Atomic Arrays”. *Science* 354 (2016), pp. 1021–1023. DOI: 10.1126/science.aah3778.
- [93] D. Barredo, V. Lienhard, S. de Léséleuc, T. Lahaye, and A. Browaeys. “Synthetic Three-Dimensional Atomic Structures Assembled Atom by Atom”. *Nature* 561 (2018), pp. 79–82. DOI: 10.1038/s41586-018-0450-2.
- [94] T. M. Graham, E. Oh, and M. Saffman. “Multiscale Architecture for Fast Optical Addressing and Control of Large-Scale Qubit Arrays”. *Applied Optics* 62 (2023), p. 3242. DOI: 10.1364/AO.484367.
- [95] H. Levine. “Quantum Information Processing and Quantum Simulation with Programmable Rydberg Atom Arrays”. PhD thesis. Cambridge, Massachusetts: Harvard University, 2021.
- [96] N. Schlosser, G. Reymond, I. Protsenko, and P. Grangier. “Sub-Poissonian Loading of Single Atoms in a Microscopic Dipole Trap”. *Nature* 411 (2001), pp. 1024–1027. DOI: 10.1038/35082512.
- [97] K.-N. Schymik, S. Pancaldi, F. Nogrette, D. Barredo, J. Paris, A. Browaeys, and T. Lahaye. “Single Atoms with 6000-Second Trapping Lifetimes in Optical-Tweezer Arrays at Cryogenic Temperatures”. *Physical Review Applied* 16 (2021), p. 034013. DOI: 10.1103/PhysRevApplied.16.034013.
- [98] T. Xia, M. Lichtman, K. Maller, A. W. Carr, M. J. Piotrowicz, L. Isenhower, and M. Saffman. “Randomized Benchmarking of Single-Qubit Gates in a 2D Array of Neutral-Atom Qubits”. *Physical Review Letters* 114 (2015), p. 100503. DOI: 10.1103/PhysRevLett.114.100503.
- [99] H.-Z. Wu, Z.-B. Yang, and S.-B. Zheng. “Implementation of a Multiqubit Quantum Phase Gate in a Neutral Atomic Ensemble via the Asymmetric Rydberg Blockade”. *Physical Review A* 82 (2010), p. 034307. DOI: 10.1103/PhysRevA.82.034307.

-
- [100] K. Singh, C. E. Bradley, S. Anand, V. Ramesh, R. White, and H. Bernien. “Mid-Circuit Correction of Correlated Phase Errors Using an Array of Spectator Qubits”. *Science* 380 (2023), pp. 1265–1269. DOI: 10.1126/science.ade5337.
- [101] N. Šibalić, J. Pritchard, C. Adams, and K. Weatherill. “ARC: An Open-Source Library for Calculating Properties of Alkali Rydberg Atoms”. *Computer Physics Communications* 220 (2017), pp. 319–331. DOI: 10.1016/j.cpc.2017.06.015.
- [102] S. Whitlock. “Robust Phase-Controlled Gates for Scalable Atomic Quantum Processors Using Optical Standing Waves”. *Quantum* 7 (2023), p. 941. DOI: 10.22331/q-2023-03-09-941.
- [103] H. Levine, D. Bluvstein, A. Keesling, T. T. Wang, S. Ebadi, G. Semeghini, A. Omran, M. Greiner, V. Vuletić, and M. D. Lukin. “Dispersive Optical Systems for Scalable Raman Driving of Hyperfine Qubits”. *Physical Review A* 105 (2022), p. 032618. DOI: 10.1103/PhysRevA.105.032618.
- [104] E. Brion, L. H. Pedersen, and K. Mølmer. “Adiabatic Elimination in a Lambda System”. *Journal of Physics A: Mathematical and Theoretical* 40 (2007), pp. 1033–1043. DOI: 10.1088/1751-8113/40/5/011.
- [105] T. M. Graham, M. Kwon, B. Grinkemeyer, Z. Marra, X. Jiang, M. T. Lichtman, Y. Sun, M. Ebert, and M. Saffman. “Rydberg-Mediated Entanglement in a Two-Dimensional Neutral Atom Qubit Array”. *Physical Review Letters* 123 (2019), p. 230501. DOI: 10.1103/PhysRevLett.123.230501.
- [106] W. Xu, A. V. Venkatramani, S. H. Cantú, T. Šumarac, V. Klüsener, M. D. Lukin, and V. Vuletić. “Fast Preparation and Detection of a Rydberg Qubit Using Atomic Ensembles”. *Physical Review Letters* 127 (2021), p. 050501. DOI: 10.1103/PhysRevLett.127.050501.
- [107] L. Isenhower, M. Saffman, and K. Mølmer. “Multibit C k NOT Quantum Gates via Rydberg Blockade”. *Quantum Information Processing* 10 (2011), pp. 755–770. DOI: 10.1007/s11128-011-0292-4.
- [108] D. Petrosyan, F. Motzoi, M. Saffman, and K. Mølmer. “High-Fidelity Rydberg Quantum Gate via a Two-Atom Dark State”. *Physical Review A* 96 (2017), p. 042306. DOI: 10.1103/PhysRevA.96.042306.
- [109] L. S. Theis, F. Motzoi, F. K. Wilhelm, and M. Saffman. “High-Fidelity Rydberg-blockade Entangling Gate Using Shaped, Analytic Pulses”. *Physical Review A* 94 (2016), p. 032306. DOI: 10.1103/PhysRevA.94.032306.
- [110] M. Saffman, I. I. Beterov, A. Dalal, E. J. Paez, and B. C. Sanders. “Symmetric Rydberg Controlled-Z Gates with Adiabatic Pulses”. *Physical Review A* 101 (2020), p. 062309. DOI: 10.1103/PhysRevA.101.062309.
- [111] F. Robicheaux, T. M. Graham, and M. Saffman. “Photon-Recoil and Laser-Focusing Limits to Rydberg Gate Fidelity”. *Physical Review A* 103 (2021), p. 022424. DOI: 10.1103/PhysRevA.103.022424.

- [112] D. D. B. Rao and K. Mølmer. “Robust Rydberg-interaction Gates with Adiabatic Passage”. *Physical Review A* 89 (2014), p. 030301. DOI: 10.1103/PhysRevA.89.030301.
- [113] I. I. Beterov, M. Saffman, E. A. Yakshina, D. B. Tretyakov, V. M. Entin, S. Bergamini, E. A. Kuznetsova, and I. I. Ryabtsev. “Two-Qubit Gates Using Adiabatic Passage of the Stark-tuned Förster Resonances in Rydberg Atoms”. *Physical Review A* 94 (2016), p. 062307. DOI: 10.1103/PhysRevA.94.062307.
- [114] Y. Chew, T. Tomita, T. P. Mahesh, S. Sugawa, S. de Léséleuc, and K. Ohmori. “Ultrafast Energy Exchange between Two Single Rydberg Atoms on the Nanosecond Timescale”. *arXiv:2111.12314* (2021). DOI: 10.48550/arXiv.2111.12314.
- [115] I. I. Beterov, D. B. Tretyakov, V. M. Entin, E. A. Yakshina, I. I. Ryabtsev, M. Saffman, and S. Bergamini. “Application of Adiabatic Passage in Rydberg Atomic Ensembles for Quantum Information Processing”. *Journal of Physics B: Atomic, Molecular and Optical Physics* 53 (2020), p. 182001. DOI: 10.1088/1361-6455/ab8719.
- [116] M. Müller, I. Lesanovsky, H. Weimer, H. P. Büchler, and P. Zoller. “Mesoscopic Rydberg Gate Based on Electromagnetically Induced Transparency”. *Physical Review Letters* 102 (2009), p. 170502. DOI: 10.1103/PhysRevLett.102.170502.
- [117] C.-Y. Guo, L.-L. Yan, S. Zhang, S.-L. Su, and W. Li. “Optimized Geometric Quantum Computation with a Mesoscopic Ensemble of Rydberg Atoms”. *Physical Review A* 102 (2020), p. 042607. DOI: 10.1103/PhysRevA.102.042607.
- [118] A. Mitra, M. J. Martin, G. W. Biedermann, A. M. Marino, P. M. Poggi, and I. H. Deutsch. “Robust Mølmer-Sørensen Gate for Neutral Atoms Using Rapid Adiabatic Rydberg Dressing”. *Physical Review A* 101 (2020), p. 030301. DOI: 10.1103/PhysRevA.101.030301.
- [119] A. Mitra, S. Omanakuttan, M. J. Martin, G. W. Biedermann, and I. H. Deutsch. “Neutral-Atom Entanglement Using Adiabatic Rydberg Dressing”. *Physical Review A* 107 (2023), p. 062609. DOI: 10.1103/PhysRevA.107.062609.
- [120] M. J. Martin, Y.-Y. Jau, J. Lee, A. Mitra, I. H. Deutsch, and G. W. Biedermann. “A Mølmer-Sørensen Gate with Rydberg-Dressed Atoms”. *arXiv:2111.14677* (2021). URL: <http://arxiv.org/abs/2111.14677>.
- [121] S. Liu, J.-H. Shen, R.-H. Zheng, Y.-H. Kang, Z.-C. Shi, J. Song, and Y. Xia. “Optimized Nonadiabatic Holonomic Quantum Computation Based on Förster Resonance in Rydberg Atoms”. *Frontiers of Physics* 17 (2022), p. 21502. DOI: 10.1007/s11467-021-1108-3.
- [122] Y. He, J.-X. Liu, F.-Q. Guo, L.-L. Yan, R. Luo, E. Liang, S.-L. Su, and M. Feng. “Multiple-Qubit Rydberg Quantum Logic Gate via Dressed-States Scheme”. *arXiv:2010.14704* (2021). DOI: 10.48550/arXiv.2010.14704.

-
- [123] J.-L. Wu, Y. Wang, J.-X. Han, S.-L. Su, Y. Xia, Y. Jiang, and J. Song. “Unselective Ground-State Blockade of Rydberg Atoms for Implementing Quantum Gates”. *Frontiers of Physics* 17 (2022), p. 22501. DOI: 10.1007/s11467-021-1104-7.
- [124] J.-L. Wu, Y. Wang, J.-X. Han, S.-L. Su, Y. Xia, Y. Jiang, and J. Song. “Resilient Quantum Gates on Periodically Driven Rydberg Atoms”. *Physical Review A* 103 (2021), p. 012601. DOI: 10.1103/PhysRevA.103.012601.
- [125] C.-P. Shen, J.-L. Wu, S.-L. Su, and E. Liang. “Construction of Robust Rydberg Controlled-Phase Gates”. *Optics Letters* 44 (2019), p. 2036. DOI: 10.1364/OL.44.002036.
- [126] M. Mohan, R. De Keijzer, and S. Kokkelmans. “Robust Control and Optimal Rydberg States for Neutral Atom Two-Qubit Gates”. *Physical Review Research* 5 (2023), p. 033052. DOI: 10.1103/PhysRevResearch.5.033052.
- [127] A. Pagano, S. Weber, D. Jaschke, T. Pfau, F. Meinert, S. Montangero, and H. P. Büchler. “Error Budgeting for a Controlled-Phase Gate with Strontium-88 Rydberg Atoms”. *Physical Review Research* 4 (2022), p. 033019. DOI: 10.1103/PhysRevResearch.4.033019.
- [128] T. Propson, B. E. Jackson, J. Koch, Z. Manchester, and D. I. Schuster. “Robust Quantum Optimal Control with Trajectory Optimization”. *Physical Review Applied* 17 (2022), p. 014036. DOI: 10.1103/PhysRevApplied.17.014036.
- [129] J. K. Nauth and V. M. Stojanović. “Quantum-Brachistochrone Approach to the Conversion from W to Greenberger-Horne-Zeilinger States for Rydberg-atom Qubits”. *Physical Review A* 106 (2022), p. 032605. DOI: 10.1103/PhysRevA.106.032605.
- [130] C. Lin, D. Sels, and Y. Wang. “Time-Optimal Control of a Dissipative Qubit”. *Physical Review A* 101 (2020), p. 022320. DOI: 10.1103/PhysRevA.101.022320.
- [131] A. Garon, S. J. Glaser, and D. Sugny. “Time-Optimal Control of $SU(2)$ Quantum Operations”. *Physical Review A* 88 (2013), p. 043422. DOI: 10.1103/PhysRevA.88.043422.
- [132] N. Khaneja, T. Reiss, C. Kehlet, T. Schulte-Herbrüggen, and S. J. Glaser. “Optimal Control of Coupled Spin Dynamics: Design of NMR Pulse Sequences by Gradient Ascent Algorithms”. *Journal of Magnetic Resonance* 172 (2005), pp. 296–305. DOI: 10.1016/j.jmr.2004.11.004.
- [133] R. H. Dicke. “Coherence in Spontaneous Radiation Processes”. *Physical Review* 93 (1954), pp. 99–110. DOI: 10.1103/PhysRev.93.99.
- [134] L. H. Pedersen, N. M. Møller, and K. Mølmer. “Fidelity of Quantum Operations”. *Physics Letters A* 367 (2007), pp. 47–51. DOI: 10.1016/j.physleta.2007.02.069.

- [135] S. J. Glaser, U. Boscain, T. Calarco, C. P. Koch, W. Köckenberger, R. Kosloff, I. Kuprov, B. Luy, S. Schirmer, T. Schulte-Herbrüggen, D. Sugny, and F. K. Wilhelm. “Training Schrödinger’s Cat: Quantum Optimal Control: Strategic Report on Current Status, Visions and Goals for Research in Europe”. *The European Physical Journal D* 69 (2015), p. 279. DOI: 10.1140/epjd/e2015-60464-1.
- [136] F. K. Wilhelm, S. Kirchhoff, S. Machnes, N. Wittler, and D. Sugny. “An Introduction into Optimal Control for Quantum Technologies”. *arXiv:2003.10132* (2020). DOI: 10.48550/arXiv.2003.10132.
- [137] F. Motzoi, J. M. Gambetta, P. Reberstrost, and F. K. Wilhelm. “Simple Pulses for Elimination of Leakage in Weakly Nonlinear Qubits”. *Physical Review Letters* 103 (2009), p. 110501. DOI: 10.1103/PhysRevLett.103.110501.
- [138] J. Kelly, R. Barends, B. Campbell, Y. Chen, Z. Chen, B. Chiaro, A. Dunsworth, A. G. Fowler, I.-C. Hoi, E. Jeffrey, A. Megrant, J. Mutus, C. Neill, P. J. J. O’Malley, C. Quintana, P. Roushan, D. Sank, A. Vainsencher, J. Wenner, T. C. White, A. N. Cleland, and J. M. Martinis. “Optimal Quantum Control Using Randomized Benchmarking”. *Physical Review Letters* 112 (2014), p. 240504. DOI: 10.1103/PhysRevLett.112.240504.
- [139] S.-Y. Huang and H.-S. Goan. “Optimal Control for Fast and High-Fidelity Quantum Gates in Coupled Superconducting Flux Qubits”. *Physical Review A* 90 (2014), p. 012318. DOI: 10.1103/PhysRevA.90.012318.
- [140] M. Werninghaus, D. J. Egger, F. Roy, S. Machnes, F. K. Wilhelm, and S. Filipp. “Leakage Reduction in Fast Superconducting Qubit Gates via Optimal Control”. *npj Quantum Information* 7 (2021), p. 14. DOI: 10.1038/s41534-020-00346-2.
- [141] Y. Baum, M. Amico, S. Howell, M. Hush, M. Liuzzi, P. Mundada, T. Merkh, A. R. Carvalho, and M. J. Biercuk. “Experimental Deep Reinforcement Learning for Error-Robust Gate-Set Design on a Superconducting Quantum Computer”. *PRX Quantum* 2 (2021), p. 040324. DOI: 10.1103/PRXQuantum.2.040324.
- [142] V. Nebendahl, H. Haffner, and C. F. Roos. “Optimal Control of Entangling Operations for Trapped Ion Quantum Computing”. *Physical Review A* 79 (2009), p. 012312. DOI: 10.1103/PhysRevA.79.012312.
- [143] T. Choi, S. Debnath, T. A. Manning, C. Figgatt, Z.-X. Gong, L.-M. Duan, and C. Monroe. “Optimal Quantum Control of Multimode Couplings between Trapped Ion Qubits for Scalable Entanglement”. *Physical Review Letters* 112 (2014), p. 190502. DOI: 10.1103/PhysRevLett.112.190502.
- [144] M. H. Goerz, T. Calarco, and C. P. Koch. “The Quantum Speed Limit of Optimal Controlled Phasegates for Trapped Neutral Atoms”. *Journal of Physics B: Atomic, Molecular and Optical Physics* 44 (2011), p. 154011. DOI: 10.1088/0953-4075/44/15/154011.

-
- [145] M. M. Müller, D. M. Reich, M. Murphy, H. Yuan, J. Vala, K. B. Whaley, T. Calarco, and C. P. Koch. “Optimizing Entangling Quantum Gates for Physical Systems”. *Physical Review A* 84 (2011), p. 042315. DOI: 10.1103/PhysRevA.84.042315.
- [146] M. H. Goerz, E. J. Halperin, J. M. Aytac, C. P. Koch, and K. B. Whaley. “Robustness of High-Fidelity Rydberg Gates with Single-Site Addressability”. *Physical Review A* 90 (2014), p. 032329. DOI: 10.1103/PhysRevA.90.032329.
- [147] J. Cui, Rick van Bijnen, T. Pohl, S. Montangero, and T. Calarco. “Optimal Control of Rydberg Lattice Gases”. *Quantum Science and Technology* 2 (2017), p. 035006. DOI: 10.1088/2058-9565/aa7daf.
- [148] A. Smith, B. E. Anderson, H. Sosa-Martinez, C. A. Riofrío, I. H. Deutsch, and P. S. Jessen. “Quantum Control in the Cs 6S_{1/2} Ground Manifold Using Radio-Frequency and Microwave Magnetic Fields”. *Physical Review Letters* 111 (2013), p. 170502. DOI: 10.1103/PhysRevLett.111.170502.
- [149] B. E. Anderson, H. Sosa-Martinez, C. A. Riofrío, I. H. Deutsch, and P. S. Jessen. “Accurate and Robust Unitary Transformations of a High-Dimensional Quantum System”. *Physical Review Letters* 114 (2015), p. 240401. DOI: 10.1103/PhysRevLett.114.240401.
- [150] N. K. Lysne, K. W. Kuper, P. M. Poggi, I. H. Deutsch, and P. S. Jessen. “Small, Highly Accurate Quantum Processor for Intermediate-Depth Quantum Simulations”. *Physical Review Letters* 124 (2020), p. 230501. DOI: 10.1103/PhysRevLett.124.230501.
- [151] B. Riaz, C. Shuang, and S. Qamar. “Optimal Control Methods for Quantum Gate Preparation: A Comparative Study”. *Quantum Information Processing* 18 (2019), p. 100. DOI: 10.1007/s11128-019-2190-0.
- [152] M. Hughes, M. D. Frye, R. Sawant, G. Bhole, J. A. Jones, S. L. Cornish, M. R. Tarbutt, J. M. Hutson, D. Jaksch, and J. Mur-Petit. “Robust Entangling Gate for Polar Molecules Using Magnetic and Microwave Fields”. *Physical Review A* 101 (2020), p. 062308. DOI: 10.1103/PhysRevA.101.062308.
- [153] R. Fletcher. *Practical Methods of Optimization*. 2nd ed. Chichester ; New York: Wiley, 1987.
- [154] V. Buchemavari, S. Omanakuttan, Y.-Y. Jau, and I. Deutsch. “Entangling Quantum Logic Gates in Neutral Atoms via the Microwave-Driven Spin-Flip Blockade”. *Physical Review A* 109 (2024), p. 012615. DOI: 10.1103/PhysRevA.109.012615.
- [155] L. Pezzè, A. Smerzi, M. K. Oberthaler, R. Schmied, and P. Treutlein. “Quantum Metrology with Nonclassical States of Atomic Ensembles”. *Reviews of Modern Physics* 90 (2018), p. 035005. DOI: 10.1103/RevModPhys.90.035005.
- [156] M. Hein, J. Eisert, and H. J. Briegel. “Multi-Party Entanglement in Graph States”. *Physical Review A* 69 (2004), p. 062311. DOI: 10.1103/PhysRevA.69.062311.

- [157] E. M. Kessler, P. Kómár, M. Bishof, L. Jiang, A. S. Sørensen, J. Ye, and M. D. Lukin. “Heisenberg-Limited Atom Clocks Based on Entangled Qubits”. *Physical Review Letters* 112 (2014), p. 190403. DOI: 10.1103/PhysRevLett.112.190403.
- [158] L. S. Pontryagin and L. W. Neustadt. *The Mathematical Theory of Optimal Processes*. English ed. Classics of Soviet Mathematics. New York: Gordon and Breach Science Publishers, 1986.
- [159] U. Boscain, M. Sigalotti, and D. Sugny. “Introduction to the Pontryagin Maximum Principle for Quantum Optimal Control”. *PRX Quantum* 2 (2021), p. 030203. DOI: 10.1103/PRXQuantum.2.030203.
- [160] A. D. Lewis. “The Maximum Principle of Pontryagin in Control and in Optimal Control”. 2006. URL: <https://mast.queensu.ca/~andrew/teaching/pdf/maximum-principle.pdf>.
- [161] E. Jones, T. Oliphant, P. Peterson, et al. *SciPy: Open Source Scientific Tools for Python*. 2001. URL: <http://www.scipy.org/>.
- [162] K. Sahay, J. Jin, J. Claes, J. D. Thompson, and S. Puri. “High-Threshold Codes for Neutral-Atom Qubits with Biased Erasure Errors”. *Physical Review X* 13 (2023), p. 041013. DOI: 10.1103/PhysRevX.13.041013.
- [163] C. Fromonteil, D. Bluvstein, and H. Pichler. “Protocols for Rydberg Entangling Gates Featuring Robustness against Quasistatic Errors”. *PRX Quantum* 4 (2023), p. 020335. DOI: 10.1103/PRXQuantum.4.020335.
- [164] S. Kuhr, W. Alt, D. Schrader, I. Dotsenko, Y. Miroshnychenko, A. Rauschenbeutel, and D. Meschede. “Analysis of Dephasing Mechanisms in a Standing-Wave Dipole Trap”. *Physical Review A* 72 (2005), p. 023406. DOI: 10.1103/PhysRevA.72.023406.
- [165] M. Saffman. “Quantum Computing with Atomic Qubits and Rydberg Interactions: Progress and Challenges”. *Journal of Physics B: Atomic, Molecular and Optical Physics* 49 (2016), p. 202001. DOI: 10.1088/0953-4075/49/20/202001.
- [166] T. G. Tiecke, J. D. Thompson, N. P. de Leon, L. R. Liu, V. Vuletić, and M. D. Lukin. “Nanophotonic Quantum Phase Switch with a Single Atom”. *Nature* 508 (2014), pp. 241–244. DOI: 10.1038/nature13188.
- [167] A. Jenkins, J. W. Lis, A. Senoo, W. F. McGrew, and A. M. Kaufman. “Ytterbium Nuclear-Spin Qubits in an Optical Tweezer Array”. *Physical Review X* 12 (2022), p. 021027. DOI: 10.1103/PhysRevX.12.021027.
- [168] A. G. Fowler, M. Mariantoni, J. M. Martinis, and A. N. Cleland. “Surface Codes: Towards Practical Large-Scale Quantum Computation”. *Physical Review A* 86 (2012), p. 032324. DOI: 10.1103/PhysRevA.86.032324.
- [169] P. W. Shor. “Scheme for Reducing Decoherence in Quantum Computer Memory”. *Physical Review A* 52 (1995), R2493–R2496. DOI: 10.1103/PhysRevA.52.R2493.

-
- [170] D. Gottesman. *Stabilizer Codes and Quantum Error Correction*. 1997. URL: <http://arxiv.org/abs/quant-ph/9705052>.
- [171] E. Knill and R. Laflamme. “Theory of Quantum Error-Correcting Codes”. *Physical Review A* 55 (1997), pp. 900–911. DOI: 10.1103/PhysRevA.55.900.
- [172] A. M. Steane. “Efficient Fault-Tolerant Quantum Computing”. *Nature* 399 (1999), pp. 124–126. DOI: 10.1038/20127.
- [173] A. Kubica, A. Haim, Y. Vaknin, H. Levine, F. Brandão, and A. Retzker. “Erasure Qubits: Overcoming the T_1 Limit in Superconducting Circuits”. *Physical Review X* 13 (2023), p. 041022. DOI: 10.1103/PhysRevX.13.041022.
- [174] A. M. Kaufman, B. J. Lester, and C. A. Regal. “Cooling a Single Atom in an Optical Tweezer to Its Quantum Ground State”. *Physical Review X* 2 (2012), p. 041014. DOI: 10.1103/PhysRevX.2.041014.
- [175] J. D. Thompson, T. G. Tiecke, A. S. Zibrov, V. Vuletić, and M. D. Lukin. “Coherence and Raman Sideband Cooling of a Single Atom in an Optical Tweezer”. *Physical Review Letters* 110 (2013), p. 133001. DOI: 10.1103/PhysRevLett.110.133001.
- [176] A. Cooper, J. P. Covey, I. S. Madjarov, S. G. Porsev, M. S. Safronova, and M. Endres. “Alkaline-Earth Atoms in Optical Tweezers”. *Physical Review X* 8 (2018), p. 041055. DOI: 10.1103/PhysRevX.8.041055.
- [177] M. A. Norcia, A. W. Young, and A. M. Kaufman. “Microscopic Control and Detection of Ultracold Strontium in Optical-Tweezer Arrays”. *Physical Review X* 8 (2018), p. 041054. DOI: 10.1103/PhysRevX.8.041054.
- [178] A. Bermudez, X. Xu, R. Nigmatullin, J. O’Gorman, V. Negnevitsky, P. Schindler, T. Monz, U. G. Poschinger, C. Hempel, J. Home, F. Schmidt-Kaler, M. Biercuk, R. Blatt, S. Benjamin, and M. Müller. “Assessing the Progress of Trapped-Ion Processors Towards Fault-Tolerant Quantum Computation”. *Physical Review X* 7 (2017), p. 041061. DOI: 10.1103/PhysRevX.7.041061.
- [179] J. M. Pino, J. M. Dreiling, C. Figgatt, J. P. Gaebler, S. A. Moses, M. S. Allman, C. H. Baldwin, M. Foss-Feig, D. Hayes, K. Mayer, C. Ryan-Anderson, and B. Neyenhuis. “Demonstration of the Trapped-Ion Quantum CCD Computer Architecture”. *Nature* 592 (2021), pp. 209–213. DOI: 10.1038/s41586-021-03318-4.
- [180] R. Belyansky, J. T. Young, P. Bienias, Z. Eldredge, A. M. Kaufman, P. Zoller, and A. V. Gorshkov. “Nondestructive Cooling of an Atomic Quantum Register via State-Insensitive Rydberg Interactions”. *Physical Review Letters* 123 (2019), p. 213603. DOI: 10.1103/PhysRevLett.123.213603.
- [181] M. Abramowitz and I. A. Stegun, eds. *Handbook of Mathematical Functions: With Formulas, Graphs, and Mathematical Tables*. 9. Dover print.; [Nachdr. der Ausg. von 1972]. Dover Books on Mathematics. New York, NY: Dover Publ, 2013.

- [182] T. Tamir. “Characteristic Exponents of Mathieu Functions”. *Mathematics of Computation* 16 (1962), pp. 100–106. DOI: 10.1090/S0025-5718-1962-0135739-3.
- [183] E. Dennis, A. Kitaev, A. Landahl, and J. Preskill. “Topological Quantum Memory”. *Journal of Mathematical Physics* 43 (2002), pp. 4452–4505. DOI: 10.1063/1.1499754.
- [184] O. Higgott. “PyMatching: A Python Package for Decoding Quantum Codes with Minimum-Weight Perfect Matching”. *ACM Transactions on Quantum Computing* 3 (2022), pp. 1–16. DOI: 10.1145/3505637.
- [185] N. Delfosse, V. Londe, and M. E. Beverland. “Toward a Union-Find Decoder for Quantum LDPC Codes”. *IEEE Transactions on Information Theory* 68 (2022), pp. 3187–3199. DOI: 10.1109/TIT.2022.3143452.
- [186] J. Roffe, D. R. White, S. Burton, and E. Campbell. “Decoding across the Quantum Low-Density Parity-Check Code Landscape”. *Physical Review Research* 2 (2020), p. 043423. DOI: 10.1103/PhysRevResearch.2.043423.
- [187] C. Gidney. “Stim: A Fast Stabilizer Circuit Simulator”. *Quantum* 5 (2021), p. 497. DOI: 10.22331/q-2021-07-06-497.
- [188] J. J. Wallman and J. Emerson. “Noise Tailoring for Scalable Quantum Computation via Randomized Compiling”. *Physical Review A* 94 (2016), p. 052325. DOI: 10.1103/PhysRevA.94.052325.
- [189] M. R. Geller and Z. Zhou. “Efficient Error Models for Fault-Tolerant Architectures and the Pauli Twirling Approximation”. *Physical Review A* 88 (2013), p. 012314. DOI: 10.1103/PhysRevA.88.012314.
- [190] K. Singh, S. Anand, A. Pocklington, J. T. Kemp, and H. Bernien. “Dual-Element, Two-Dimensional Atom Array with Continuous-Mode Operation”. *Physical Review X* 12 (2022), p. 011040. DOI: 10.1103/PhysRevX.12.011040.
- [191] P. M. Ireland, D. M. Walker, and J. D. Pritchard. “Interspecies Förster Resonances for Rb-Cs Rydberg d-States for Enhanced Multi-Qubit Gate Fidelities”. *Physical Review Research* 6 (2024), p. 013293. DOI: 10.1103/PhysRevResearch.6.013293.
- [192] A. Holmes, S. Johri, G. G. Guerreschi, J. S. Clarke, and A. Y. Matsuura. “Impact of Qubit Connectivity on Quantum Algorithm Performance”. *Quantum Science and Technology* 5 (2020), p. 025009. DOI: 10.1088/2058-9565/ab73e0.
- [193] D. Gottesman. “Fault-Tolerant Quantum Computation with Constant Overhead”. *Quantum Information and Computation* 14 (2014), pp. 1339–1371. DOI: 10.26421/QIC14.15-16-5.
- [194] N. P. Breuckmann and J. N. Eberhardt. “Quantum Low-Density Parity-Check Codes”. *PRX Quantum* 2 (2021), p. 040101. DOI: 10.1103/PRXQuantum.2.040101.

-
- [195] L. Z. Cohen, I. H. Kim, S. D. Bartlett, and B. J. Brown. “Low-Overhead Fault-Tolerant Quantum Computing Using Long-Range Connectivity”. *Science Advances* 8 (2022), eabn1717. DOI: 10.1126/sciadv.abn1717.
- [196] S. Bravyi, A. W. Cross, J. M. Gambetta, D. Maslov, P. Rall, and T. J. Yoder. “High-Threshold and Low-Overhead Fault-Tolerant Quantum Memory”. *Nature* 627 (2024), pp. 778–782. DOI: 10.1038/s41586-024-07107-7.
- [197] J. Beugnon, C. Tuchendler, H. Marion, A. Gaëtan, Y. Miroshnychenko, Y. R. P. Sortais, A. M. Lance, M. P. A. Jones, G. Messin, A. Browaeys, and P. Grangier. “Two-Dimensional Transport and Transfer of a Single Atomic Qubit in Optical Tweezers”. *Nature Physics* 3 (2007), pp. 696–699. DOI: 10.1038/nphys698.
- [198] C. A. Sackett, D. Kielpinski, B. E. King, C. Langer, V. Meyer, C. J. Myatt, M. Rowe, Q. A. Turchette, W. M. Itano, D. J. Wineland, and C. Monroe. “Experimental Entanglement of Four Particles”. *Nature* 404 (2000), pp. 256–259. DOI: 10.1038/35005011.
- [199] J. J. García-Ripoll, P. Zoller, and J. I. Cirac. “Speed Optimized Two-Qubit Gates with Laser Coherent Control Techniques for Ion Trap Quantum Computing”. *Physical Review Letters* 91 (2003), p. 157901. DOI: 10.1103/PhysRevLett.91.157901.
- [200] T. Pellizzari, S. A. Gardiner, J. I. Cirac, and P. Zoller. “Decoherence, Continuous Observation, and Quantum Computing: A Cavity QED Model”. *Physical Review Letters* 75 (1995), pp. 3788–3791. DOI: 10.1103/PhysRevLett.75.3788.
- [201] S.-B. Zheng and G.-C. Guo. “Efficient Scheme for Two-Atom Entanglement and Quantum Information Processing in Cavity QED”. *Physical Review Letters* 85 (2000), pp. 2392–2395. DOI: 10.1103/PhysRevLett.85.2392.
- [202] A. Beige, D. Braun, B. Tregenna, and P. L. Knight. “Quantum Computing Using Dissipation to Remain in a Decoherence-Free Subspace”. *Physical Review Letters* 85 (2000), pp. 1762–1765. DOI: 10.1103/PhysRevLett.85.1762.
- [203] A. S. Sørensen and K. Mølmer. “Measurement Induced Entanglement and Quantum Computation with Atoms in Optical Cavities”. *Physical Review Letters* 91 (2003), p. 097905. DOI: 10.1103/PhysRevLett.91.097905.
- [204] S.-B. Zheng. “Unconventional Geometric Quantum Phase Gates with a Cavity QED System”. *Physical Review A* 70 (2004), p. 052320. DOI: 10.1103/PhysRevA.70.052320.
- [205] J. Borregaard, P. Kómár, E. M. Kessler, A. S. Sørensen, and M. D. Lukin. “Heralded Quantum Gates with Integrated Error Detection in Optical Cavities”. *Physical Review Letters* 114 (2015), p. 110502. DOI: 10.1103/PhysRevLett.114.110502.
- [206] P. Lewalle, L. S. Martin, E. Flurin, S. Zhang, E. Blumenthal, S. Hacohe-Gourgy, D. Burgarth, and K. B. Whaley. “A Multi-Qubit Quantum Gate Using the Zeno Effect”. *Quantum* 7 (2023), p. 1100. DOI: 10.22331/q-2023-09-07-1100.

- [207] M. J. Kastoryano, F. Reiter, and A. S. Sørensen. “Dissipative Preparation of Entanglement in Optical Cavities”. *Physical Review Letters* 106 (2011), p. 090502. DOI: 10.1103/PhysRevLett.106.090502.
- [208] D. Leibfried, M. D. Barrett, T. Schaetz, J. Britton, J. Chiaverini, W. M. Itano, J. D. Jost, C. Langer, and D. J. Wineland. “Toward Heisenberg-Limited Spectroscopy with Multiparticle Entangled States”. *Science* 304 (2004), pp. 1476–1478. DOI: 10.1126/science.1097576.
- [209] Y. Zhao, R. Zhang, W. Chen, X.-B. Wang, and J. Hu. “Creation of Greenberger-Horne-Zeilinger States with Thousands of Atoms by Entanglement Amplification”. *npj Quantum Information* 7 (2021), p. 24. DOI: 10.1038/s41534-021-00364-8.
- [210] P. K. Barkoutsos, J. F. Gonthier, I. Sokolov, N. Moll, G. Salis, A. Fuhrer, M. Ganzhorn, D. J. Egger, M. Troyer, A. Mezzacapo, S. Filipp, and I. Tavernelli. “Quantum Algorithms for Electronic Structure Calculations: Particle-hole Hamiltonian and Optimized Wave-Function Expansions”. *Physical Review A* 98 (2018), p. 022322. DOI: 10.1103/PhysRevA.98.022322.
- [211] H. R. Grimsley, S. E. Economou, E. Barnes, and N. J. Mayhall. “An Adaptive Variational Algorithm for Exact Molecular Simulations on a Quantum Computer”. *Nature Communications* 10 (2019), p. 3007. DOI: 10.1038/s41467-019-10988-2.
- [212] G. A. Paz-Silva, G. K. Brennen, and J. Twamley. “Fault Tolerance with Noisy and Slow Measurements and Preparation”. *Physical Review Letters* 105 (2010), p. 100501. DOI: 10.1103/PhysRevLett.105.100501.
- [213] D. Crow, R. Joynt, and M. Saffman. “Improved Error Thresholds for Measurement-Free Error Correction”. *Physical Review Letters* 117 (2016), p. 130503. DOI: 10.1103/PhysRevLett.117.130503.
- [214] H. E. Ercan, J. Ghosh, D. Crow, V. N. Premakumar, R. Joynt, M. Friesen, and S. N. Coppersmith. “Measurement-Free Implementations of Small-Scale Surface Codes for Quantum-Dot Qubits”. *Physical Review A* 97 (2018), p. 012318. DOI: 10.1103/PhysRevA.97.012318.
- [215] S. Balauca and A. Arusoiaie. “Efficient Constructions for Simulating Multi Controlled Quantum Gates”. *Computational Science – ICCS 2022*. Ed. by D. Groen, C. de Mulatier, M. Paszynski, V. V. Krzhizhanovskaya, J. J. Dongarra, and P. M. A. Sloot. Vol. 13353. Cham: Springer International Publishing, 2022, pp. 179–194. DOI: 10.1007/978-3-031-08760-8_16.
- [216] H. Labuhn, S. Ravets, D. Barredo, L. Béguin, F. Nogrette, T. Lahaye, and A. Browaeys. “Single-Atom Addressing in Microtraps for Quantum-State Engineering Using Rydberg Atoms”. *Physical Review A* 90 (2014), p. 023415. DOI: 10.1103/PhysRevA.90.023415.
- [217] Y. Wang, A. Kumar, T.-Y. Wu, and D. S. Weiss. “Single-Qubit Gates Based on Targeted Phase Shifts in a 3D Neutral Atom Array”. *Science* 352 (2016), pp. 1562–1565. DOI: 10.1126/science.aaf2581.

-
- [218] D. Hunger, T. Steinmetz, Y. Colombe, C. Deutsch, T. W. Hänsch, and J. Reichel. “A Fiber Fabry–Perot Cavity with High Finesse”. *New Journal of Physics* 12 (2010), p. 065038. DOI: 10.1088/1367-2630/12/6/065038.
- [219] M. Uphoff, M. Brekenfeld, G. Rempe, and S. Ritter. “Frequency Splitting of Polarization Eigenmodes in Microscopic Fabry–Perot Cavities”. *New Journal of Physics* 17 (2015), p. 013053. DOI: 10.1088/1367-2630/17/1/013053.
- [220] G. Barontini, L. Hohmann, F. Haas, J. Estève, and J. Reichel. “Deterministic Generation of Multiparticle Entanglement by Quantum Zeno Dynamics”. *Science* 349 (2015), pp. 1317–1321. DOI: 10.1126/science.aaa0754.
- [221] J. Ramette, J. Sinclair, N. P. Breuckmann, and V. Vuletić. *Fault-Tolerant Connection of Error-Corrected Qubits with Noisy Links*. 2023. URL: <http://arxiv.org/abs/2302.01296>.
- [222] J. D. Pritchard, J. A. Isaacs, M. A. Beck, R. McDermott, and M. Saffman. “Hybrid Atom-Photon Quantum Gate in a Superconducting Microwave Resonator”. *Physical Review A* 89 (2014), p. 010301. DOI: 10.1103/PhysRevA.89.010301.
- [223] C. U. Lei, L. Krayzman, S. Ganjam, L. Frunzio, and R. J. Schoelkopf. “High Coherence Superconducting Microwave Cavities with Indium Bump Bonding”. *Applied Physics Letters* 116 (2020), p. 154002. DOI: 10.1063/5.0003907.
- [224] A. André, D. DeMille, J. M. Doyle, M. D. Lukin, S. E. Maxwell, P. Rabl, R. J. Schoelkopf, and P. Zoller. “A Coherent All-Electrical Interface between Polar Molecules and Mesoscopic Superconducting Resonators”. *Nature Physics* 2 (2006), pp. 636–642. DOI: 10.1038/nphys386.
- [225] P. Rabl, D. DeMille, J. M. Doyle, M. D. Lukin, R. J. Schoelkopf, and P. Zoller. “Hybrid Quantum Processors: Molecular Ensembles as Quantum Memory for Solid State Circuits”. *Physical Review Letters* 97 (2006), p. 033003. DOI: 10.1103/PhysRevLett.97.033003.
- [226] R. Sawant, J. A. Blackmore, P. D. Gregory, J. Mur-Petit, D. Jaksch, J. Aldegunde, J. M. Hutson, M. R. Tarbutt, and S. L. Cornish. “Ultracold Polar Molecules as Qudits”. *New Journal of Physics* 22 (2020), p. 013027. DOI: 10.1088/1367-2630/ab60f4.
- [227] W. J. Childs, D. R. Cok, G. L. Goodman, and L. S. Goodman. “Hyperfine and Spin–Rotational Structure of CaBr $X^2\Sigma$ ($v = 0$) by Molecular-beam Laser-rf Double Resonance”. *The Journal of Chemical Physics* 75 (1981), pp. 501–507. DOI: 10.1063/1.442057.
- [228] S. Y. Buhmann, M. R. Tarbutt, S. Scheel, and E. A. Hinds. “Surface-Induced Heating of Cold Polar Molecules”. *Physical Review A* 78 (2008), p. 052901. DOI: 10.1103/PhysRevA.78.052901.